CRANFIELD INSTITUTE OF TECHNOLOGY
SCHOOL OF WATER SCIENCES
SCHOOL OF INDUSTRIAL AND
MANUFACTURING SCIENCE

Ph. D. Thesis
Academic years 1987-1990

Paul H. M. Feron

Hydrodynamics and Mass Transfer in Obstructed Narrow Channels

Supervisor: George S. Solt
May 1991

ABSTRACT

The objective of this research was to carry out a comprehensive investigation on hydrodynamics and mass transfer of different idealised geometries representing typical conditions which might occur in the narrow cells common in membrane process plant.

The method used was to represent these cells by a ten times scale model, adjusting velocity and viscosity to match the Reynolds numbers which might occur in actual membrane equipment, typically between 100 and 1000. The geometries investigated had rods of circular cross-section placed at right angles to the direction of flow: the spacing, positioning and diameter of the rods were varied.

Observations of flow patterns indicated that in most geometries flow instability arose at Reynolds numbers of 200-300, i.e. an order of magnitude below the value at which it would arise in the empty channel.

Pressure drop measurements showed that to a reasonable approximation the pressure loss per rod was constant for any given rod diameter. Flow instability did not significantly affect the rate of increase of pressure loss with increasing flow velocity.

Mass transfer measurements and shear rate measurements using the diffusion limited current technique were made on these geometries. In contrast with pressure drop, mass transfer generally showed an upturn at higher values of the Reynolds number than the value at which flow instability set in. Local mass transfer and shear rate were correlated by means of a simple theoretical model. Excellent agreement was achieved for steady flow but agreement was only qualitative for unsteady flow.

The conclusions which have emerged point the way to development of actual geometries superior to those currently in use with respect to their pressure loss/mass transfer characteristics. These would improve the performance of membrane equipment, and possibly other mass and heat transfer processes in which geometry of this kind is encountered.

LIST OF CONTENTS

LIST OF FIGURES

Fig. 8.7: Mass transfer between rods (calculation and measurement); Suspended staggered rods, l_{rr} = 24 mm, d_{rw} = 1 mm

LIST OF PLATES

LIST OF TABLES

LIST OF SYMBOLS

Roman — Unit

a,b : Exponents

a_1,a_2 : Constants in Eq. 2.11

A : Constant in kinetic contribution to pressure drop [m^{-2}]

A_1,A_2 : Constants in Eq. 4.2

A_e : Constant in empty channel pressure gradient e.g. Eq. 2.28

A_{el} : Electrode area [m^2]

B : Constant in viscous contribution to pressure drop [m^{-1}]

B_1,B_2 : Constants in Eq. 4.3

c : Concentration [$mole/m^3$]

c_b : Concentration in bulk [$mole/m^3$]

C_1 : Constant in Eq. 3.1

C_2 : Constant in Eq. 3.1 [K]

C_d : Drag coefficient = $\Delta p/\frac{1}{2}\rho V^2$

d : Rod diameter [m]

d_h : Hydraulic diameter = 4 times volume divided by wetted area [m]

$(d_h)_e$: Hydraulic diameter of empty channel = $2wh/(w+h)$ [m]

$(d_h)_f$: Hydraulic diameter of 'filled' channel [m]

d_{rw} : Gap between rod and wall [m]

D : Diffusion coefficient [m^2/s]

E : Porosity

f : Frequency [Hz]

f_e : Friction factor based on empty channel parameters = $(\Delta p/l)/(2\rho v^2/(d_h)_e)$

f_f : Friction factor based on obstructed channel parameters = $(\Delta p/l)/(2\rho(v_{eff})^2/(d_h)_f)$

F : Faraday constant =96487 C/mole [As/mole]

h : Channel height [m]

H : Heat transfer coefficient [$W/(m^2K)$]

I : Electrical current [A]

j : Chilton-Colburn mass transfer factor = $Sh/(ReSc^{1/3})$

k : Mass transfer coefficient [m/s]

k_x : Local mass transfer coefficient [m/s]

K : Mixing factor

l : Length [m]

l_f : Fibre separation distance [m]

l_{rr} : Inter-rod distance [m]

l_{st} : Mesh step [m]

Nu_e : Nusselt number = $H(d_h)_e/\lambda$

p : Pressure differential [Pa]

$(p^*)_e$: Dimensionless pressure gradient based on empty channel parameters = $(\Delta p/l)(d_h)_e^3/(2\rho\nu^2)$

$(p^*)_f$: Dimensionless pressure gradient based on obstructed channel parameters = $(\Delta p/l)(d_h)_f^3/(2\rho\nu^2)$

Po : Dimensionless energy dissipation
$(\Delta pV/l)(d_h)_e^4/(2\rho\nu^3)$

Pr : Prandtl number

Q : Volumetric flow rate [m^3/s]

Re : Reynolds number

Re^* : Modified Reynolds number = $VS''/(AE\nu)$

Re_{cc} : Reynolds number based on velocity in channel centre and rod diameter = $U_{cc}d/\nu$

Re_{ch} : Change-over Reynolds number (Eq. 2.11)

Re_d : Reynolds number based on superficial velocity and rod diameter = Vd/ν

Re_e : Reynolds number based on empty channel parameters = $V(d_h)_e/\nu$

Re_f : Reynolds number based on obstructed channel parameters = $V_{eff}(d_h)_f/\nu$

S : Shear rate [s^{-1}]

S^* : Dimensionless shear rate = $2S((d_h)_e)^2/\nu$

S' : Specific surface area of separator = separator surface area / volume [m^{-1}]

S'' : Total surface area divided by the channel volume [m^{-1}]

Sc : Schmidt number = ν/D

Sh : Sherwood number

Sh_e : Sherwood number based on empty channel parameters = $k(d_h)_e/D$

Sh_x : Local Sherwood number = $k_x(d_h)_e/D$

Sh_f : Sherwood number based on filled channel parameters = $k(d_h)_f/D$

S_e	: Empty channel cross-section	[m^2]
S_{min}	: Cross-section at narrowest point	[m^2]
T	: Temperature	[K]
u	: Velocity in x-direction	[m/s]
v	: Velocity in y-direction	[m/s]
V	: Superficial velocity = volume flow rate / cross-sectional area of empty channel	[m/s]
V_i	: Interstitial velocity = V/E	[m/s]
w	: Channel width	[m]
x	: Coordinate along channel wall	[m]
x^*	: Dimensionless x-coordinate = $x/(d_h)_e$	
y	: Coordinate normal to the wall	[m]

Greek		Unit
α	: Dimensionless constant in Eq. 2.15	
β	: Dimensionless constant in Eq. 2.15	
γ	: Reynolds-analogy constant	
η	: Dynamic viscosity	[kg/(ms)]
λ	: Heat conduction coefficient	[W/(mk)]
ν	: Kinematic viscosity	[m^2/s]
ρ	: Density	[kg/m^3]

ACKNOWLEDGEMENTS

The work described in this thesis was made possible by a grant of the Science and Engineering Research Council and I would like to acknowledge their support. The idea for this research came from George Solt who also supervised me throughout the past three years. I wish to thank him for keeping me on the Ph.D-track. The teachings of the 'Blue Peter principles' by Andrzej Nowosielski, Simon Judd and Simon Funge-Smith were greatly appreciated.
Various people knowingly and unknowingly contributed to the research and I would like to express my gratitude for this:
- Tony Scott fabricated the model geometries and the flow channels were made in the SIMS workshop under the supervision of Andrew Baldwin.
- David Binks [SME] assisted me in the course of the flow visualisation experiments, Prof. Ian Smith [SME] advised me on the pressure measurements and Dr. A.A. Wragg (Exeter University) taught me the ins-and-outs of electro-chemical mass transfer measurements.
- John Nixon designed the electronic circuits for the electro-chemical mass transfer measurements which were consequently built by Don Woolnough.
- Nigel Emery and Wen Tong gave practical help and Ian Richardson helped with computer matters.
Finally, I have to thank Rita Edwards for maintaining a steady supply of British tea.

Paul Feron May 1991

1. INTRODUCTION

Flat sheet and spiral wound membrane modules incorporate a structure whose function is to keep the membranes apart. Historically these separators first became important for membrane mass transfer in electrodialysis (ED) plants (flat sheet configuration) but they are now particularly widespread in spiral wound reverse osmosis (RO) and ultrafiltration (UF) modules. They have also been successfully applied in electrochemical reactors. The first separator used for electrodialysis plants was a corrugated perforated sheet but nowadays the most common separator materials are extruded meshes (VEXAR), based on the original 'NETLON' design, although other mesh-like structures (woven, punched and expanded materials) have been used as well. Surprisingly, the basic separator design (shown in Figure 1.1) has remained unaltered throughout the last two decades despite several efforts (see Chapter 2) to improve on it.

Separators intended for use in membrane operations must

1) be mechanically strong
2) be chemically inert
3) be dimensionally uniform and stable
4) minimise membrane shadowing
5) not exaggerate the fouling tendency
6) be cheap.

Membrane operations are limited by concentration polarisation phenomena. Concentration polarisation is the build-up of a concentration gradient near the membrane leading to a concentration at the membrane surface which is substantially different from the bulk concentration. This leads in the first instance to a decrease in the driving force but other more detrimental effects might occur. Separators can create flow conditions which reduce the effects of polarisation by increasing the mass transfer from the bulk to the wall layer. The mechanisms involved will be examined in this thesis but one must expect the momentum transfer to the wall layer to increase as well. Hence separators enhance mass transfer compared to the equivalent empty channel but at the expense of an increased flow resistance and thus an increased pumping power input. The relationship between mass transfer and pumping power input can be expressed in dimensionless form by the quantities $Sh_e/Sc^{1/3}$ and $f_eRe_e^3(=Po)$ where Sh_e is the Sherwood number, Sc is the Schmidt number, Re_e is the Reynolds number and f_e is the friction factor. The use of these and similar dimensionless forms in the economic evaluation of separators having an idealised geometry has been demonstrated in SON74, ISA76 and LEI77 for ED and in SHE79 for UF. Similar economic evaluation of meshes has not been reported in spite of the availability of a (limited) body of data (HIC68, MEL72, SCH80, KUR83 and SCH87) which could enable a membrane module designer to perform the evaluation. Such an analysis leads to an

optimisation of the membrane module operating conditions with reference to the meshes analysed but gives no information as to the way the design of a separator could be improved. The effort presented in this thesis has been directed towards achieving a better understanding of the hydrodynamics and mass transfer in channels containing obstacles for $100<Re_e<1250$. This should produce ideas for an improved separator design. Meshes and other obstacles in a narrow flow channel are often referred to as 'turbulence promoters'. The flow conditions (Reynolds numbers) encountered in commercial membrane modules are, however, such that turbulent flow, i.e. chaotic flow, rarely occurs. For ED, for instance, it appears that Re_e is typically around 250. In that case laminar flow prevails and at most the flow is unstable and exhibits a sinusoidal pattern. Therefore it is suggested here that 'convection promoters' is a better term as it describes the phenomena more accurately.

This thesis is set up as follows: The relevant literature is reviewed in Chapter 2. One result of this is the selection of geometries to be examined. The research methods used are flow visualisation (Chapter 3), pressure drop measurement (Chapter 4) and electrochemical mass transfer measurement (Chapters 5, 6 and 7). In Chapter 8 the mass transfer mechanisms are discussed and finally Chapter 9 gives the main conclusions.

2. REVIEW OF TRANSFER PHENOMENA IN LAMINAR CHANNEL FLOW

2.1 Introduction

An improved understanding of the flow and associated transfer phenomena in thin channels filled with obstacles is not only relevant to membrane operations but also to compact heat exchangers and electro-chemical reactors. In all of these applications the small size of the channels would, at normal flow rates, lead to laminar flow conditions (Hagen-Poiseuille flow) in the case of an unobstructed channel. For the empty channel of infinite width the pressure drop can be expressed as a friction factor, f_e, in the following way:

$$f_e = (\Delta p/l)/(2\rho V^2/(d_h)_e) = 24/Re_e \qquad (2.1)$$

where Δp = pressure drop

l = length of section

V = superficial flow velocity

ρ = density

$(d_h)_e$ = hydraulic diameter of empty channel = two times the channel height h for infinitely wide channnel

Re_e = Reynolds number based on empty channel i.e. $V(d_h)_e/\nu$ where ν is the kinematic viscosity

An alternative to the use of a friction factor is a dimensionless pressure gradient $(p^*)_e$:

$$(p^*)_e = f_e(Re_e)^2 = (\Delta p/l)(d_h)_e^3/(2\rho\nu^2) = 24Re_e \qquad (2.2)$$

The dimensionless pressure gradient has the advantage that for a given liquid and a constant temperature, it directly expresses pressure drop as a function of flow rate. But, unlike the friction factor, it covers quite a large range of values. In the literature one encounters friction factors mostly and only recently [KAR88] the use of dimensionless pressure gradient has been introduced. This thesis will mostly employ the dimensionless pressure gradient to describe pressure drop versus flow rate characteristics.

Average mass transfer in the empty channel of infinite width can be expressed by a Sherwood number Sh_e defined by [LEV28]:

$$Sh_e = k(d_h)_e/D = 1.85Sc^{1/3}Re_e^{1/3}((d_h)_e/l)^{1/3} \qquad (2.3)$$

where k = mass transfer coefficient

D = diffusion coefficient

Sc = Schmidt number = ν/D

Mass transfer in the empty channel can now be expressed as a function of the dimensionless energy dissipation Po $(fRe_e^3 = (p^*)_e Re_e = (\Delta pV/l)(d_h)_e^4/(2\rho\nu^3))$:

$$Sh_e = 1.09Po^{1/6}((d_h)_e/l)^{1/3}Sc^{1/3} \qquad (2.4)$$

For completeness the popular correlations for turbulent flow conditions in the empty channel are given here as well [SKE74]:

$$(p^*)_e = 0.0791Re_e^{1.75} \qquad (2.5)$$

$$Sh_e = 0.023Sc^{1/3}Re_e^{0.8} \qquad (2.6)$$

which can be written as a function of the dimensionless energy dissipation in the following manner:

$$Sh_e = 0.0481Po^{0.291}Sc^{1/3} \qquad (2.7)$$

In the literature on separator filled channels one finds a number of different definitions of length scale and velocity scale and hence a number of different definitions of the Reynolds numbers and Sherwood numbers. For instance Belfort and Guter [BEL72], Sonin and Isaacson [SON74, ISA76], Shen and Probstein [SHE79], Light and Tran [LIG81], Zhong et. al. [ZHO83] and Miyoshi et. al. [MIY88] use the channel height h as the length scale, Winograd et. al. [WIN73] use h/2 as the length scale, whereas Leitz and Marinčič [LEI77] and Letord-Quéméré et. al. [LET86] favour the following length scale: 2wh/(w+h) which is the definition of the hydraulic diameter, $(d_h)_e$, of the empty channel of finite width w and height h.

A different approach has been followed by Schwager et. al. [SCH80] and Schock and Miquel [SCH87] in analogy to the description of packed columns. They have used the definition of the hydraulic diameter of the channel filled with the separator i.e. 4 times volume of flow channel divided by the wetted surface as the length scale. This leads to the following expression [SCH87]:

$$(d_h)_f = E / (1/(d_h)_e + (1-E)S'/4) \qquad (2.8)$$

where:

$(d_h)_e$ = hydraulic diameter of empty channel

E = porosity = 1 - separator volume/channel volume

S' = specific surface of separator = separator surface / separator volume

For the velocity scale an interstitial velocity $V_i = V/E$ is chosen. This takes into account the speed up effect due to the reduced average cross sectional area. The Reynolds number for the filled channel can now be defined as

$$Re_f = V_i(d_h)_f/\nu \qquad (2.9)$$

Due to the use of these different definitions a direct comparison of separators is not always possible. In the review of the literature, results based on empty channel definitions will be indicated by the subscript e and

results based on separator filled channels will be indicated by the subscript f.

Previous investigations can be broadly divided into two categories according to the types of structures examined:

1) mesh-type structures
2) idealised geometries.

Most of these investigations have concentrated on the measurement of pressure drop and mass transfer and expressed these in terms of friction factors and Sherwood numbers. Mass transfer was nearly always measured by a limiting current technique using either electrodialysis or a redox reaction on an electrode, the only exception being [SCH87] in which RO was used. The results of these mass transfer measurements were expressed as correlations of the following kind:

$$Sh = constant Re^{a} Sc^{b} \qquad (2.10)$$

where the constant might contain a function related to the geometry. For the Schmidt number exponent b=1/3 seems to be the best choice [WIN73, SCH80, KUR83]. For the Reynolds number exponents in the range 0.33-1.10 have been offered.

Paragraphs 2.2 and 2.3 discuss results of mesh-type structures and idealised geometries, respectively. Special attention has been paid to present these results in a uniform fashion in order to facilitate comparison between

results from different sources. This approach was not followed in a recent review of the effect turbulence promoters have on mass transfer by Chang and Park [CHA86].

2.2 Mesh-type Structures

Although the first separator used in ED-stacks was a corrugated perforated pvc sheet [e.g. WIL63] the de-facto standard has become the extruded mesh for both ED/sheet flow-stacks and UF/RO spiral wound modules. Since its introduction several researchers have analysed its hydrodynamics and mass transfer properties. The first reported study on separator comparison was by Klyachko and Ushakov [KLY67] for electrodialysis in which pressure drop correlations were given for two perforated corrugated pvc sheet separators, two expanded material separators and two 'net' separators in the form f_f:

$$f_f \begin{cases} = a_1/Re_f & Re_f<Re_{ch} \\ = a_2/Re_f^2 & Re_f>Re_{ch} \end{cases} \qquad (2.11)$$

Results from limiting current measurements were also given but did not allow conversion into a Sherwood number correlation.

The first comprehensive study was carried out by Belfort and Guter [BEL72] who examined 21 different separators (including woven, extruded, corrugated perforated and expanded materials) for ED-stacks. Firstly, the separators

were characterised by 1) the porosity, 2) dead flow area (for which an ingenious photographic technique was developed), 3) their effect on the electrical resistance of the channel, 4) a pressure coefficient defined as the point where the drag coefficient ($C_d=\Delta p/\frac{1}{2}\rho V^2$) starts to deviate from the relationship ConstantRe^{-1} (similar to Klyachko and Ushakov). Secondly a selected number of separators was subjected to an in-situ ED evaluation i.e. the separators were inserted into an ED-stack and limiting current, current efficiency, power consumption were determined. Also flow visualisation was employed using a number of scaled-up models representing typical mesh geometries. It was noted that the flow became unsteady at Re_e between 180 and 270. Also in this Re_e-region the limiting current was seen to increase rapidly from a plateau, leading the authors to suggest a link between the two. Unfortunately the pressure drop- and limiting current-data were not expressed in a friction factor and Sherwood number form which would enable comparison with other data.

A rapid increase in the limiting current after a change in slope in the pressure drop versus flowrate graph was also noted in KLY67 and by Ichiki and Asawa [ICH77] (see Figure 2.1). The latter attributed this phenomenon to the onset of transitional flow although no flow visualisation experiments were reported to confirm this. Apart from single meshes, two or three layers of meshes with thinner

filaments were also investigated by Ichiki and Asawa and they were found to produce similar limiting currents at a given pressure drop but at a lower flow rate. Also the laminated mesh structures resulted in a lower electrical channel resistance due to their higher porosity. The data from the pressure drop and limiting current measurements could be converted into correlation involving empty channel parameters (Re_e, Sh_e, f_e and $(p^*)_e$). For the thin filament meshes the limiting current increase occurred in the Re_e-region 180-420, for the other meshes in the Re_e-region 440-560.

Zhong et. al. [ZH083] in an investigation of 31 meshes for ED-stacks also noted the capability of two or three layers of meshes with thin filaments to produce high limiting currents at fairly low Reynolds number. They distinguished three different regions in the pressure drop vs flow rate graph: laminar, transitional and turbulent. The boundary between these regions was dependent on the type of separator: laminar→transitonal for Re_e=22-122, transitional→turbulent for Re_e=360-2000. It is, however, unlikely that the flow would have become unsteady in the Re_e-range quoted for the laminar-transitional boundary.

Hicks and Mandersloot [HIC68] were the first to report both pressure drop and mass transfer data which allowed transformation into suitable dimensionless numbers. In their research on a packed bed of porous spheres,

perforated corrugated pvc sheet and expanded aluminium mesh, they assumed the pressure drop to consist of a viscous contribution $A\eta V$ and a kinetic contribution $B\rho V^2$. (On a historical note, in many papers this approach is attributed to Osborne Reynolds [REY00] who indeed mentioned this in relation with turbulent pipe flow but following Ergun [ERG49] a reference by Brillouin [BRI07] indicates that earlier work, on pendulums by Coulomb (1801) and 's Gravesande (1719, 1748), already mentioned resistance both due to liquid inertia and liquid viscosity).

Hicks and Mandersloot suggested a relation between heat/mass transfer and pressure drop based on the following:

1) Average heat/mass transfer in turbulent flow varies according to the square root of the average shear rate regardless of the origin of the turbulence, i.e. a high flow rate or a turbulence promotor [LEV62].
2) The average shear rate is determined by the viscous part of the pressure drop.

This resulted in the following expression for the Chilton/Colburn mass transfer factor j:

$$j = Sc^{2/3}k/V = \text{constant}(Re^*)^{-1/2} \qquad (2.12)$$

where $Re^* = VS''/(AE\nu)$ is a modified Reynolds number in which A is the constant in the viscous contribution in the pressure drop equation, S''

is the total surface area divided by the channel or bed volume ($E/S'' = (d_h)_f/4$)

Their experimental results for the three different geometries appeared to be correlated by:

$$j = 0.121(Re^*)^{-0.49} \qquad (2.13)$$

Equation 2.12 can be rewritten as a Sherwood number:

$$Sh_f = k(d_h)_f/D = \text{constant} \propto^{1/2} Re_f^{1/2} Sc^{1/3} \qquad (2.14)$$

where $\propto$ is defined by dimensionless pressure gradient:

$$(p^*)_f = \propto Re_f + \beta Re_f^2 \qquad (2.15)$$

The main advantage of this description is that it takes into account the effect of different orientation of the separator, which can have a large effect as illustrated by Figure 2.2. This figure gives the dimensionless pressure gradient as a function of Reynolds number for an expanded mesh at different orientation. Equation 2.14 calculates the heat/mass transfer for all the surface area in the channel including the inert surface area and hence it probably overestimates the mass transfer.

Equation 2.14 predicts that mass transfer varies with the square root of the flow rate. Winograd et. al. [WIN73] in

an article on turbulence promoters predicted an identical dependence based on a rather different model. They assumed that near a turbulence promoter both the hydrodynamic and the mass transfer boundary layer thicknesses are instantaneously reduced by a certain amount, after which they are allowed to develop again according to a model similar to laminar flow over a flat plate. Using the nomenclature in this thesis, the result of this so-called mesh-step model can be expressed as:

$$Sh_e = 0.753 Re_e^{1/2} Sc^{1/3} ((d_h)_e / l_{st})^{1/2} (K/(2-K))^{1/2} \quad (2.16)$$

where l_{st} = the distance between consecutive promoters, i.e. the mesh-step.

K = mixing factor = (boundary layer thickness before disruption - boundary layer thickness after disruption) / boundary layer thickness before disruption

The model has been checked using the ferri/ferro-cyanide limiting current technique for several arrays of rods of 0.9 mm diameter placed at distance of 0.2 mm from the cathode in a 2.3 mm thick and 100 mm wide channel, for Re_e in the range 20-1600. The experimental results gave a reasonable agreement with the model for both the square root dependence on flow rate and inverse inter-rod distance. One can notice from their Figure 6, however, that the mass transfer measurements as a function of

Reynolds number increase faster than Equation 2.16 predicts for Re_e>500-700. This deviation might be attributed to the onset of unsteadiness. Also Winograd et. al. noticed that the model was not valid for $l_{st}/(d_h)_e$<2 in which case the dependence of mass transfer on inter-rod distance was much weaker. Unfortunately the dimensions of most commercial meshes is such that they fall into this region. It was shown that for these the square root dependence on flow rate was still valid but the influence of the mesh-step was unapparent. This was most effectively shown by the nearly identical mass transfer results of two meshes consisting of squares where the second was fabricated out of the first by cutting out larger squares thus doubling the mesh-step. Winograd et. al. suggested that the selection of a suitable mesh for electrodialysis could be based on characteristics like pressure drop, membrane shadowing and membrane sagging only as the mass transfer characteristics were nearly identical. The results of the mass transfer measurements can be written in the form of an empty channel correlation:

$$Sh_e = \text{constant} \cdot Re_e^{1/2} Sc^{1/3} \qquad (2.17)$$

where the constant is in the range 0.38-0.54 for $100<Re_e<1600$

A square root dependence of the mass transfer rate on the flow rate was also found in studies on candidate meshes

for electrodialysis by Zhong et. al. [ZHO83] and by Kuroda et. al. [KUR83]. The former also examined the influence of the mesh-step on mass transfer by cutting larger squares out of one of their meshes and confirmed the inverse square root dependence given by Winograd's model (Equation 2.16) for $l_{st}/(d_h)_e>3$. Kuroda's mass transfer results for 4 meshes using the ferri/ferro cyanide limiting current technique can be written in a form identical to Equation 2.17 but with the constant in the range 0.55 -0.75 for $50<Re_e<700$. The higher values could have been due to the fact that the results were average values of 40 small electrodes (10X20 mm) and not results from one large electrode. Kuroda et. al. also presented results from pressure drop measurements which can be written in the following manner:

$$(p^*)_e = \text{constant} \cdot Re_e^{1.5} \qquad (2.18)$$

with the constant in the range 3.9-12. The exponent equal to 1.5 was thought to be indicative of transitional flow but no flow visualisation experiments were carried out to confirm this.

Miyoshi et. al. [MIY88] also measured limiting currents in an electrodialysis experiment and found that Equation 2.17 fitted their results with the constant in the region 0.25-0.50 for $20<Re_e<900$. They described the effect of the separator on mass transfer by means of an eddy diffusivity

which led to an increase of the effective diffusion coefficient. In an earlier paper [MIY82] they derived an expression for the velocity profile assuming the kinematic viscosity consists of a molecular contribution and a contribution due to the mixing effect of the separator. Using this expression they were then able to relate the constant in Equation 2.17 to the geometrical parameters of the mesh. This constant also contained a term which indicated a dependence on the length of the channel identical to the empty channel (Equation 2.3) the use of which is questionable.

Schwager et. al. [SCH80] presented experimental results on cloth separators intended for use in electrolytic cells, using filled channel correlations:

$$(p^*)_f = 75Re_f + 0.175Re_f \qquad (2.19)$$

$$Sh_f = 0.26Re_f^{0.6}Sc^{1/3} \qquad (2.20)$$

for $1<Re_f<3000$ and $800<Sc<18500$

They found that the results were in reasonable quantitative agreement with a surface renewal model based on forced convection mass transfer to a flat plate in an infinite liquid. This predicts for the mass transfer:

$$Sh_f = 0.68Re_f^{1/2}Sc^{1/3}((d_h)_f/l_f)^{1/2} \qquad (2.21)$$

where l_f is the separation distance between the fibres. This result is almost identical with the theoretical result for laminar channel entrance flow with simultaneously developing mass transfer and hydrodynamic boundary layers e.g. [WRA62] where the constant is 0.66. The model is also similar to Winograd's, the only difference being the fact that Winograd allows for incomplete disruption of the boundary layers through his empirical mixing factor K. Qualitative confirmation of the surface renewal effect is given by the photographic results from Schwager et. al. using the photographic technique originally developed by Belfort and Guter [BEL72].

Although mesh-structures have found widest use in reverse osmosis in spiral wound modules, to date there has been surprisingly little interest in their effect on mass transfer and pressure drop in this application. Light and Tran [LIG81] have compared the performance of the standard VEXAR separator with custom-designed separators consisting of an array of rods of half the channel thickness placed in the channel centre. They found that for a non-fouling feed exhibiting a limiting flux the VEXAR material was able to achieve higher flux values than the custom-designed materials albeit at higher pressure losses. In contrast when they used a fouling feed not exhibiting a limiting flux they found that the VEXAR material

exaggerated the fouling tendency, possibly due to the presence of stagnant areas.

Schock and Miquel [SCH87] presented mass transfer and pressure loss correlations for separators used in reverse osmosis spiral wound modules, using filled channel parameters:

$$Sh_f = 0.065 Re_f^{0.875} Sc^{0.25} \qquad (2.22)$$

$$(p^*)_f = 1.56 Re_f^{1.7} \qquad (2.23)$$

$100 < Re_f < 1000$

Equation 2.23 was valid for the feed separators. For the permeate separators, which are much more dense in order to withstand the high operating pressures, the Re_f-exponent was found to be 1.2 but the constant varied between 3 and 26. A salient feature of the mass transfer Equation 2.22 is the Schmidt number exponent being equal to 0.25. This was an assumed relationship not backed up by any experiments. Several researchers have examined the Schmidt number dependence for mass transfer in a separator filled channel [WIN73, SCH80, KUR83] and concluded that the exponent was equal to 1/3. As Schock and Miquel carried out their experiments at Sc=660, it is suggested here that their mass transfer correlation ought to be modified to include a Schmidt number dependence having the overwhelming experimental support:

$$Sh_f = 0.0378Re_f^{0.875}Sc^{1/3} \qquad (2.24)$$

It has to be mentioned, however, that the discrepancy between Equation 2.22 and 2.24 is still only 10% at Sc=2000.

For the calculation of the hydraulic diameter of the filled channel, Schock and Miquel derived Equation 2.8. Because filaments are commonly of a thickness equal to half the channel height (h), Equation 2.8 can be simplified to Equation 2.25 (channel has an infinite width):

$$(d_h)_f = 2hE/(5-4E) \qquad (2.25)$$

Although not explicitly mentioned, this appears to be the equation Schock and Miquel have used. It is depicted in Figure 2.3 together with some data from the literature and it has to be regarded as an estimate for the filled channel hydraulic diameter because it also assumes the filaments to have only point contacts with both the membrane and each other. If one assumes the filaments to have a square cross section and their thickness to be half the channel height, the relationship between filled channel hydraulic diameter and the porosity can be written as:

$$(d_h)_f = 2hE/(3-2E) \qquad (2.26)$$

which is also shown in Figure 2.3. For a given porosity (hence volume available to flow) the square filaments shadow part of the wall leading to a reduction of the wetted area and hence to an increase in the hydraulic diameter. Despite their shortcomings both equations have the advantage that the filled channel hydraulic diameter can be calculated from a simple measurement of the channel height and the separator porosity. Graphs of dimensionless pressure gradient and Sherwood number using the filled channel description are given in Figure 2.4 and 2.5 respectively. For the dimensionless pressure gradient it appears that the correlation of Schwager et. al. and Schock and Miquel are slightly lower than the Ergun-equation generally used for packed columns [ERG52]

$$(p^*)_f = 33Re_f + 0.58Re_f^2 \qquad (2.27)$$

The pressure gradient correlation of Schwager et. al gives higher values than Schock and Miquel's for the Re_f-range under consideration as does their mass transfer correlation.

Flow conditions inside separator filled channels have received little attention in the past. Apart from Belfort and Guter [BEL72], Melbourne [MEL72] appears to be the only one to have used flow visualisation to characterise the flow. He carried out a series of experiments using scaled-up versions of two NETLON separators, one

representing the geometry used in a commercial ED-plant and one representing a more open separator. In the present research the experiments with the scaled-up NETLON separator were duplicated broadly confirming Melbourne's findings. Figure 2.6 gives an impression of the flow conditions near the channel wall. For low Re_e (=50) the flow is more or less straight down the channel in the direction of the average pressure gradient, undulating as directed by the separator. For intermediate Re_e (=150) the flow aligns itself with the filaments of the separator until it reaches the channel side where it is 'reflected' to the other channel side. Melbourne did detect some 'screw-like' motion near the channel middle which was attributed to the interaction between the two sheets of flow in the shear layer. At high Re_e (=300) the flow is unsteady and vortical. It is of interest to remark that commercial electrodialysis plants operate in the region of intermediate Re_e where little mixing occurs.

At this point it is useful to compare Melbourne's results with those found by Focke and Knibbe [FOC86] inside corrugated plate geometries used as heat exchangers. For an angle between the corrugations and the channel axis equal to 45^o the flow in corrugated plate geometries was predominantly down the corrugation, albeit that unlike the mesh flow visualisation the flow spiralled down the corrugation. At the channel side the flow was 'reflected' and continued in the other channel half, as in the mesh

flow visualisation. They also found that for the angle equal to 80^{o} the reflection did not occur on the channel side but near the point where the crests of opposing corrugations had contact points. This resulted in a helical flow pattern (i.e. shorter zig-zag motion) which became unsteady for Re_e=290. Results from mass transfer and friction factor measurements were reported by Focke et. al in a different account [FOC85]. In this they showed that both friction factor and mass transfer in the corrugated plate geometries reached a maximum when the angle between the channel axis and the corrugation was between 70^{o} and 80^{o}. They also concluded from their mass transfer measurements that the spiralling character of the flow was essential in ensuring a fairly uniform mass transfer. The implications of Focke's results for flow in channels with mesh-type structures could be of interest but are not investigated further in this thesis.

2.3 Idealised Geometries in Two-dimensional Channel Flow

Research into the transfer phenomena occurring in flow through channels filled with idealised geometries is important for a wide variety of process plant. For membrane operations (spiral wound and stack modules) and electro-chemical reactors it could give clues about a better design of the mesh separator commonly used. It could also improve the design of heat exchangers. All of these have, in common, a large transfer area concentrated

in a small volume which leads to laminar flow conditions, hence low transfer rates. Transfer rate enhancement is therefore essential to make this compact process plant an economical proposition. It is widely known that the presence of obstacles in a channel can lead to transfer enhancement. The use of idealised geometries flow will simplify the analysis of the transfer phenomena, hopefully without nullifying their relevance to more complicated geometries.

Sonin and Isaacson developed an optimisation method for the design of electrodialysis plant [SON74] which they applied in an ensuing article [ISA76] using data valid for cylindrical rods placed in the channel centre. Table 2.1 presents these data using the empty channel definitions:

Table 2.1: Sherwood number and dimensionless pressure gradient at various inter-rod spacings l_{rr} [ISA76]

$l_{rr}/(d_h)_e$	$(p^*)_e$	$Sh_e/Sc^{1/3}$	Re_e-range
35	$21Re_e+0.015Re_e^2$	$0.25Re_e^{0.45}$	550->1450
17	$28Re_e+0.026Re_e^2$	$0.54Re_e^{0.38}$	750->1450
8.8	$35Re_e+0.049Re_e^2$	$0.30Re_e^{0.51}$	750->1800
2.2	$81Re_e+0.13Re_e^2$	$0.068Re_e^{0.80}$	750->2500
1.1	$145Re_e+0.26Re_e^2$	$0.24Re_e^{0.62}$	550->2500

The data presented in Table 2.1 were only valid over a limited range. Three regions could be distinguished in their Sherwood versus Reynolds number graph. Below Re_e in

the range 250 to 440 (dependent on geometry) the Sherwood number was only slightly higher than for the empty channel. Above this the Sherwood increased sharply until it reached the range for which data are shown in the Table 2.1. Isaacson and Sonin concluded that this was the region in which the geometries were most effective in promoting mass transfer. Their economic optimisation pointed at the geometry with $l_{rr}/(d_h)_e$=2.2 as being the most efficient (l_{rr} is the inter-rod distance). Isaacson and Sonin pointed out that this value was in agreement with the results of [WIN73], discussed in Paragraph 2.2

An apparently identical geometry was used by Shen and Probstein [SHE79] in an ultrafiltration module. Although a three-region structure was not apparent in their Sherwood versus Reynolds graphs their results did confirm that there was little gain in plant efficiency from a reduction in $l_{rr}/(d_h)_e$ to below say 2.

A summary of an extensive investigation into mass tranfer and hydrodynamics in electro-chemical cells was reported by Leitz and Marincic [LEI77]. The geometries were cylindrical, rectangular and triangular rods which were wider spaced than in the previously mentioned investigations: $l_{rr}/(d_h)_e$>5.5. In addition to the inter-rod distance, rod diameter and position in the channel were varied for the cylindrical rods, for the triangular rods position only and for the rectangular rods the length

in the direction of the flow only. Triangular and rectangular rods were half the channel thickness and the latter were located on the channel wall. Flow through channels with rectangular and cylindrical rods became unsteady at Re_e=250, for the triangular rods at Re_e=200. The pressure gradient was found to consist of a laminar part, equal to the pressure gradient in the empty channel and a turbulent part. For the cylindrical and triangular rods the correlation was:

$$(p^*)_e = A_e Re_e + 0.175((d_h)_e/l_{rr})((S_e/S_{min})^2-1)Re_e^2 \quad (2.28)$$

where S_e : empty channel cross section

S_{min}: cross-section at narrowest point

l_{rr} : inter-rod distance

For the rectangular geometries:

$$(p^*)_e = A_e Re_e + 2.082((d_h)_e)/l_{rr})Re_e^2 \quad (2.29)$$

In both equations, $A_e Re_e$ represents the pressure gradient in the empty channel and can be looked up in, for instance, SHA78 as a function of the channel aspect ratio. For the cylindrical rods the pressure gradient has been calculated from Equation 2.28 using the geometrical data from ISA76 and compared with the latter data in Figure 2.7. A reasonable agreement can be detected, also for the lowest values of $l_{rr}/(d_h)_e$.

Mass transfer was measured using the ferri/ferro-cyanide

diffusion limited current technique on a partly segmented electrode consisting of one thousand closely spaced micro-elecrodes (50 rows of 20 electrodes) and eleven Sherwood number versus Reynolds number correlations were presented for the various geometries with the following general form:

$$Sh_e = \text{constant} \cdot Sc^{1/3} Re_e^{a} ((d_h)_e / l_{rr})^{b} \qquad (2.30)$$

with a=0.343-1.094 and b=0.153-0.531

The interested reader is referred to [LEI77] for the complete set and only two correlations are given here. First for the alternating rectangular rods:

$$Sh_e = 1.45 Sc^{1/3} Re_e^{0.378} ((d_h)_e / l_{rr})^{0.309} \qquad (2.31)$$

and secondly for the cylindrical rods of half the channel thickness placed in the channel centre:

$$Sh_e = 0.272 Sc^{1/3} Re_e^{0.631} ((d_h)_e / l_{rr})^{0.357} \qquad (2.32)$$

The mass transfer and pressure gradient correlations were then incorporated into a mass transfer vs power requirement ($Sh_e/Sc^{1/3}$ vs $Po^{1/3}$) graph from which the optimum conditions could be determined. It appeared that circular rods were superior throughout the whole range i.e. for low mass transfer/low power consumption (hence low flow rates) a cylindrical rod of large diameter (say two thirds of the channel height) was superior and for

high mass transfer/power consumption (hence high flow rates) a cylindrical rod of small diameter (say one fifth of the channel height) was the optimum. Because the optimum interrod spacing found for the cylindrical rods was the lowest taken into account ($(d_h)_e/l_{rr}$=5.5), it might not have been the absolute optimum and referring to ISA76 it might be as low as $(d_h)_e/l_{rr}$=2-3. Again the correlation for the cylindrical rods (Equation 2.32) can be compared with the correlation given in ISA76 and this is done in Figure 2.8. There is good agreement between the two sets of correlations except for $l_{rr}/(d_h)_e$=2.2 where Equation 2.32 underestimates mass transfer.

Storck and Hutin [STO80,STO81] investigated transfer phenomena in channels with cylindrical rods placed in the channel centre and small wires and meshes located on the wall. For all geometries, except the cylindrical rods, Re_e was larger than 2000. For this geometry the mass transfer correlation derived from experiments with the ferri/ferro-cyanide diffusion limited current technique could be written as:

$$Sh_e = 2.42Sc^{1/3}Re_e^{0.61}((d_h)_e/l_{rr})^{0.5}(d/(d_h)_e)^{1.5} \quad (2.33)$$

for $750<Re_e<6200$, $l_{rr}/(d_h)_e$=1.5,3,4.5,6 and $(d/(d_h)_e$=0.3 and 0.48, the former relates to a rod diameter d of half the channel thickness, the latter to 0.8 the channel thickness.

For $l_{rr}/(d_h)_e$=1.5 and 3 the correlation found by Stork and Hutin is compared with the correlation found by Leitz and Marincic in Figure 2.9 and the latter underestimates the correlation in [STO80] although the agreement is good for $l_{rr}/(d_h)_e$=3. In [STO81] mass transfer profiles measured from an array of micro-electrodes are presented, and it appeared that for the cylindrical rods having a diameter equal to half the channel thickness there are two peaks, one directly underneath the rod due to the increased fluid velocity and one further downstream due to a wake effect. Pressure gradients were given in terms of a graph of the friction factor, again mostly in the turbulent regime.

Mass transfer profiles measured with the diffusion limited current technique were reported by Watson and Thomas [WAT67] for small detached cylindrical rods (one eighth to one quarter of the channel height) located near the channel wall. They also exhibited a maximum underneath the rod and a maximum further downstream. Watson and Thomas suggested that it was beneficial to pair the rods with a separation distance of 8-10 rod diameters.

Kang and Chang [KAN82] were the first to use numerical simulation for the analysis of flow and mass transfer around obstacles in channel flow. They solved the steady state flow and mass transfer problem by the finite difference approach using the stream function and vorticity for Re_e=100-1000. Their geometries consisted of

rectangles with a height equal to half the channel thickness, located either on one channel wall only ('cavity' promoter) or on both walls in an alternating manner ('zig-zag promoter'). For the zig-zag promoter two eddies exist, one large one behind a rectangle and a smaller one in front. These eddies grow in size with increasing Reynolds number. The calculated flow patterns were checked by flow visualisation and agreed well apart from the onset of unsteadiness at Re_e=420-500 in the visualisation experiments. Local Sherwood numbers were also determined by the numerical simulations and agreed reasonably well with measurements presented in a follow-on article by Kim et. al. [KIM83]. Again, the diffusion limited current technique was employed for this purpose. Kang and Chang attributed the mass transfer improvement to two factors:

1) the increase in shear rate due to presence of obstacles leading to much thinner boundary layers, hence higher mass transfer, and
2) the presence of recirculation zones which augmented the convective flow to the surface. Although the shear stress was zero at a stagnation point, mass transfer in this region was high.

Focke [FOC83] used the diffusion limited current technique with a segmented electrode, to measure average and local mass transfer in channels with one or more semi-circular rods attached to the channel wall. The effect of these

rods was two-fold:

1) They increased the velocities near them leading to a mass transfer maximum at the position of the promoter
2) The recirculation zone behind them became turbulent at Reynolds number much lower than could be expected for empty channel flow. The increased mixing due to this local turbulence caused a complete disruption of the boundary layer and a second maximum in mass transfer somewhere near the flow reattachment point. Due to the 'seeding' of the mass transfer boundary layer with turbulence mass transfer was promoted further downstream as well.

Focke presented the following correlation for an array of alternating semicircular rods of half the channel height:

$$Sh_e = 0.43Sc^{1/3}Re_e^{0.65}((d_h)_e/l_{rr})^{0.4} \qquad (2.34)$$

for $400<Re_e<5000$, $l_{rr}/(d_h)_e = 1.64, 4.91, 14.7$

and showed that this equation resembled the expression for turbulent channel entrance flow more closely than the laminar channel entrance used in SCH80.

Miyashita et. al. [MIY81, MIY83] investigated turbulent flow in channels with cylindrical rods located at a certain distance from one wall. Rod diameter and distance from the wall were varied and they measured local mass transfer, local shear stress and turbulence intensity.

They found that mass transfer increased due to both an increase in turbulence intensity and in shear stress. Miyashita's observations are therefore similar to Focke's who included the laminar region as well.

Miyashita's research was carried out with a view to improve compact heat exchangers and a similar research was carried out by Oyakawa and Mabuchi [OYA83] with a staggered arrangement of rods with a diameter of 0.4 times the channnel height in turbulent channel flow. The rod to wall distance and the rod-rod distance were made variable. Their flow visualisation experiments indicated that as the rod to wall distance was decreased the flow pattern changed from a von Karman-vortex flow for the cylinder in the middle to a flow with an unsteady recirculation zone attached to the channel wall at a rod to wall distance of 0.03 times the channel height. When the rods were suspended, heat transfer measurements indicated a maximum underneath the rods and this maximum increased with decreasing rod-wall distance. A second maximum occurred some distance behind the rod closest to the wall. The authors linked this maximum to an increase in intensity of the vortices near the wall. As the rod-wall distance was further decreased, a third maximum appeared at the point of reattachment of the flow and this maximum was highest for zero rod-wall distance when the two other maxima disappeared.

Shiina et. al. [SHI82] studied the influence of cylindrical obstacles located on the channel wall on the flow patterns for $70<Re_e<2400$. The diameter of the rods was one third of the channel thickness and a circulation zone was observed which grew in length with increasing Re_e until Re_e=600-700 when vortices started to be shed from the cylinder. At this point heat transfer improved and a spacing of 7 rod diameters was found to take the best advantage of vortices being shed. In a second paper Shiina [SHI83] analysed the vortex shedding frequencies for single cylindrical obstacles of different diameters located in either the channel centre or on the channel wall. He found that for low rod-diameter/channel height ratios (d/h) the transition occurred at high Re_e for rods located in the channel centre. However, when using a Reynolds number Re_{cc} ($u_{cc}d/\nu$, u_{cc} is velocity in channel centre, d is rod diameter) the transition occurred in the relatively narrow range $170<Re_{cc}<260$ with the lower limit for d/h=1/4 and the upper limit for d/h=1/2. Good agreement was obtained between the shedding frequencies in uniform flow and channel flow for $Re_{cc}<300$. Above this the shedding frequencies appeared to be higher which Shiina attributed to deviations from the parabolic flow profile. For the rods located on the wall similar conclusions were reached but instead of u_{cc} the velocity scale had to be taken as the velocity at the edge of the rod. In a third paper Shiina [SHI84] examined shedding frequencies from square and trapezoid obstacles. The latter were in

reasonable agreement with the cylindrical obstacles but the former gave smaller shedding frequencies and the flow visualisation showed that the intensity and scale of the vortices shed by the square obstacles were much less. Similar observations were also reported by Gerrard [GER78] for squares in an unbounded flow.

Numerical simulation was used by Karniadakis et. al. [KAR88] for flow and heat transfer in a channel filled with an array of cylindrical obstructions with diameter of 1/8 and 1/5 of the channel height. They concluded that the presence of these small obstacles caused the flow to became unstable at Reynolds numbers much smaller than for the empty channel and furthermore that the nature of the unstable flow resembled unsteady flow in the empty channel. In both cases unsteadiness appears as so-called Tollmien-Schlichting waves which can be predicted by a stability analysis of the linearised Navier-Stokes equation. The Reynolds-analogy, which states that momentum transfer and heat transfer are similar in the case of the transfer being determined by a convective-diffusive balance, was thought to be applicable to the unstable flow. It is generally used for turbulent channel flow and can be expressed as follows:

$$S^* = \gamma Re_e Nu_e \qquad (2.35)$$

where S^* : dimensionless shear stress

γ : Reynolds-analogy constant

Re_e : Reynolds number

Nu_e : Nusselt number

The constant γ is independent of Reynolds number and flow geometry but varies according to $Pr^{-1/3}$. The pressure drop consists of the shear stress and the contribution due to the cylinder drag and it was shown that the latter was much smaller. This meant that for a given Nusselt number the energy dissipation ($(p^*)_e Re_e$) varied proportionally to the square of the Reynolds number. Therefore it was advantageous to look for geometries for which the flow became unstable at low Reynolds number as this meant that pressure drop, shear stress and energy dissipation were reduced.

2.4 Discussion and Scope of Present Study

The mass transfer- and pressure gradient correlations presented in the previous paragraphs indicate that the presence of obstacles in channel flow can lead to an intensification of mass and momentum transport to the channel wall. Several mechanisms are thought to have been responsible. First, an obstacle will impart a velocity component normal to the wall thus increasing the convection to the wall. Near the wall the velocity can be taken to vary linearly with the distance to the wall:

$$u(x,y) = (\partial u/\partial y)_{y=0} \cdot y = S \cdot y \qquad (2.36)$$

Where x : coordinate along the wall

y : coordinate normal to the wall

S : shear rate.

Conservation of mass gives for the velocity component normal to the wall:

$$v = -\tfrac{1}{2}(\partial S/\partial x) \cdot y^2 \qquad (2.37)$$

where the negative sign indicates flow to the wall. Hence an increase in the shear rate in the flow direction will augment the normal component, and a decrease will reduce the normal flow.

Mass transfer is governed by the balance of diffusion and convection which is formulated mathematically in Appendix A (Equation A1). The diffusion in the direction of the flow can usually be neglected if the Reynolds number is not too low and the flow does not separate from the wall, leading to Equation A3 in which the flow is considered to be steady. The solution of Equation A2 with the velocity profiles given in Equations 2.36 and 2.37 and concentration boundary conditions $c=0$ at $y=0$ and $c=c_b$ at $y=\infty$ has been obtained by a variety of methods [LIG50, ACR60, KES62, LEB70] and is given in Equation 2.38 using dimensionless variables.

$$Sh_x = 0.641 Sc^{1/3} | d/((_0\int^{x^*} (S^*)^{\frac{1}{2}} dx')^{2/3})/dx^* | \qquad (2.38)$$

where Sh_x : local Sherwood number

x^* : dimensionless x-coordinate $(x/(d_h)_e)$

S^* : dimensionless shear rate = $2S((d_h)_e)^2/\nu$

For the average Sherwood number Sh_e one can write

$$Sh_e = 0.641 Sc^{1/3} | (_0\int^{x^*} (S^*)^{\frac{1}{2}} dx')^{2/3}/x^* | \qquad (2.39)$$

Equations 2.38 and 2.39 give mass transfer as a function of the shear rate. So shear rate measurements can be used to predict mass transfer but only if 1) the flow is steady, 2) the Reynolds number is high enough to neglect streamwise diffusion and 3) the flow is without zones of separation which would invalidate the use of the velocity profiles given in Equations 2.36 and 2.37. Also the use of these velocity profiles is only permitted if the concentration boundary layer is small enough which is the case for high Schmidt numbers. For the empty channel where $S^*=24Re_e$ Equation 2.39 leads to the mass transfer correlation for the empty channel (Equation 2.3).

For steady flow in channels with obstacles located on the wall there usually exists a zone directly behind the obstacle where the flow is recirculating. The main flow separates from the wall in front of the obstacle, goes

round it and reattaches at some point further downstream. The previous analysis is invalid in this flow but some general remarks can be made. Mass transfer in the recirculation zone is bound to be small as the flow velocities are small. At the point of reattachment mass transfer is high because of the high velocity normal to the wall. Conversely at separation points the mass transfer must be low because the velocity direction is away from the wall. One might suspect that the development of the mass transfer boundary layer is interrupted by the physical presence of the obstacle on the wall which forces the liquid to flow away from the wall. This second effect of the obstacle on mass transfer will probably be enhanced by the transition of the flow from laminar to turbulent.

It is well known that mass transfer in turbulent conditions can be described by a surface renewal effect i.e. the mass transfer boundary layer is periodically renewed by the penetration of an eddy [PIN74]. Flow through channels in which obstacles are present undergoes the transition from laminar to turbulent at lower Re_e than the empty channel and the surface renewal effect might be prevalent in mass transfer. Previous studies also link zones of high turbulence intensity with zones of high mass transfer.

Several idealised geometries consisting of circular rods were chosen (Figure 2.10) to investigate the suggested

mass transfer mechanisms:

1) An array of suspended, centered rods having dimensions of approximately half the channel thickness has been analysed extensively in various studies and a study of these provides a valuable benchmark. The chosen values of the inter-rod distance l_{rr} covered the region of interest as suggested by Isaacson and Sonin [ISA76].

2) An array of attached rods was chosen as it was thought to be especially relevant to describe a separator's prime function i.e. to keep the membranes apart.

3) An array of thin suspended rods was suggested by Watson and Thomas [WAT67] as an effective way to promote mass transfer at a decreased pressure drop and further investigation of this was considered worthwhile. Watson and Thomas suggested an optimum inter-rod distance l_{rr} of 8-10 rod diameters which was covered by our geometries. Three values of the rod-wall distance were chosen. The array was staggered to minimise possible interference of the rods on opposite sides of the channel.

The research methods used to investigate the hydrodynamics of the chosen geometries were flow-visualisation (Chapter 3) and pressure drop measurements (Chapter 4) and mass transfer was measured using the diffusion limited current technique (Chapters 5, 6 and 7).

3. FLOW VISUALISATION STUDIES

3.1 Experimental Equipment and Materials

Few studies have used flow visualisation as a research tool in this field [BEL72, MEL72]. However, a study of channel flow patterns should lead to a better understanding of the transfer phenomena, and flow visualisation became the first stage of the study.

A tray of rectangular cross-section was milled out of a PERSPEX sheet and polished with progessively finer grades of 'wet and dry' paper. Finally BRASSO copper polish was used to yield a hydrodynamically as well as optically smooth surface. The tray together with a PERSPEX lid with machined grooves carrying O-rings formed the model flow channel. Plate 5.2 gives a picture of the tray used for the mass transfer studies. Although this tray was made out of PVC it is nearly identical to the PERSPEX one used for the flow visualisation studies.

The geometries were made in PERSPEX by mounting rods in between strips with a thickness equal to the tray depth to form a structure which could be inserted into the flow tray. The gap between the sides of the structure and the tray filled with liquid which remained stagnant while the flow passed between the sides. This allowed a clear view across the cell. The cell was mounted into a bracket which

allowed assembly in the horizontal plane, and operation in the vertical, to avoid accumulation of air bubbles in certain regions. Tray and lid were clamped together by a series of bolts which minimised cell deformation during operation.

The model's channel dimensions were 1000X100X13 mm which is approximately ten times thicker than a channel in a typical membrane module ($(d_h)_e$=23 mm). A 50 mm section at the inlet was filled with plastic wool held in place by means of a perforated plate in order to provide a proper flow distribution.

The channel was incorporated into a flow loop shown in Figure 3.1. An encapsulated 1 kW tungsten/halogen floodlight illuminated the middle of the channel and observations were recorded on photograph using a camera and on video tape using a video recorder with a still picture facility. A hardboard enclosure excluded other light to yield maximum contrast. A full description of the equipment and materials and their origins is given in Appendix B.

3.2 Experimental Methods

Flow rate reduction and high viscosity liquids (a sugar solution or a glycerol/water mixture) were used to give Reynolds numbers similar to real membrane channels. Before

each experiment the kinematic viscosity of the operating liquid was measured over a range of temperatures using a viscometer previously calibrated with water and water/glycerol mixtures. The data were fitted to the following relationship:

$$\nu = \exp(C_1 + C_2/T) \qquad (3.1)$$

(ν is kinematic viscosity and T is absolute temperature) and the constants C_1 and C_2 were determined by linear regression of the suitably transformed data ($\ln(\nu)$ vs 1/T). During each experiment the temperature in the storage tank was measured and the kinematic viscosity (necessary for the determination of the Reynolds number) calculated using Equation 3.1.

Following Merzkirch [MER74] a variety of media was tested for flow visualisation:

1) Hydrogen bubbles

   These were generated at a thin copper wire suspended over the channel height using as fluid water-glycerol mixtures with added sodium sulphate. The method produced good results but proved laborious as a new wire had to be installed for every experiment. Therefore it was only used during the testing period.

2) Dye injection

   Fluorescein sodium dissolved in a sample of the operating liquid (a sugar solution) was found to be an excellent flow indicator. The dye was injected via a

needle through a rubber bung fitted into the channel lid, using a gear pump to ensure steady flow regardless of the pressure in the channel. The needle diameter was such that vortex shedding from it did not occur. Several injection positions were used throughout the experiments, all of them in the lid centre and all of them at least 300 mm from the inlet section which meant, according to theory (e.g. SHA78), that the flow in the empty channel was fully developed provided the entrance flow profile was uniform. The injection velocity was similar to the mean channel velocity and the amount of mass and momentum injected was very small compared to the mass and momentum transport rate in the average flow. As the channel wall is the transfer area and hence is of special interest, dye was also injected into the flow near the wall. In this case the lowest possible injection velocity was chosen.

3) Aluminium powder

Laboratory reagent fine aluminium powder, sieved to the size range 45-57 μm, has a negligible settling velocity compared to the fluid velocities in the channel. Over a period of time it settled in the storage tank and had to be resuspended by hand-stirring before each experiment.

4) Air bubbles

These were introduced by deliberate splashing in the storage tank and yielded an instant but only approximate idea of the flow regime.

Exposure times for the dye experiments were generally 1/60 seconds and shorter, for the aluminium powder experiments between 1/4 and 1/15 seconds, longer to provide streaks. These exposure times were dependent on flow conditions with high flow rates needing the shortest exposure times which were limited by the amount of lighting.

3.3 Experimental Results

Throughout this account the Reynolds number Re_e is based on the hydraulic diameter of the empty channel $(d_h)_e$ using the superficial velocity V. This choice is made for convenience and does not necessarily mean that it is the best method for comparison of the various geometries. A similar convention has been adopted by other workers [BEL72, LEI77, CAR83]. An estimate for the accuracy with which the Reynolds number could be determined is given in Appendix D.

For all geometries investigated the flow exhibited oscillations, i.e. it became unsteady at Re_e one order of magnitude lower than for the empty channel. The Re_e at which oscillations start to set in, is called the critical Re_e and is around 2600 [KA070] for the equivalent empty channel. In the present experiments it was determined using aluminium powder as the flow-regime indicator.

3.3.1 Centered Rods

The flow patterns appeared to be identical for all the inter-rod distances l_{rr} investigated (see Figure 2.10 for l_{rr}-range). For steady conditions there exists a wake, consisting of two counter-rotating vortices behind the rod. The flow pattern near the wall is not greatly affected by the presence of the rod. With increasing Re_e the vortices grow in length to about two rod diameters, beyond which point oscillations start to set in, giving rise to a sinusoidally shaped tail originating from the wake behind the rod. This occurs at a critical Re_e approximately equal to 260, independent of l_{rr}. Plates 3.1 and 3.2 shows the transition from steady to unsteady flow by injection of dye into the channel centre.

At higher Re_e the oscillations increase in amplitude, thereby periodically drawing fluid away from the channel wall at the plane where the wake ends (see Plate 3.3; top). A moving vortex as illustrated by Plate 3.3 (bottom) could be observed for Re_e higher than 450. Also, observations of the flow near the wall were made using a microscope arrangement attached to the video-camera. A noticeable backflow on the wall occurred at the point where the oscillating wake caused the flow to be directed away from the wall. Finally, it should also be noted that these unsteady phenomena were intermittent, i.e., they were interrupted by brief quiescent periods.

An arrangement with a single rod and two rods with a varying inter-rod distance was also investigated giving similar flow patterns for l_{rr}>30 mm as the arrays of rods, i.e., two counter-rotating vortices behind the rods for steady flow, and for unsteady flow a sinusoidal pattern in the channel middle and a moving vortex on the wall. However further downstream the moving vortex disappeared but the sinusoidal pattern in the channel middle remained intact until the channel outlet albeit slightly dampened. Critical Re_e for the single rod was around 300 and also for the first rod in the two-rod arrangement. Critical Re_e for the second rod was equal to 290 in all cases but for l_{rr}=30 mm it was 260.

3.3.2 Attached Staggered Rods

The present results show critical Re_e for these geometries is around 180 for l_{rr}=20 mm and around 240 for higher values of l_{rr}, i.e. 40 to 100 mm (see Figure 2.10). For steady conditions the flow has a slowly rotating vortex behind each rod which increases in length until the flow becomes unsteady. Table 3.1 gives the maximum wake length for different values of the inter-rod distance l_{rr}.

Table 3.1: Maximum wake length measured from rod end to reattachment point for different inter-rod distances

l_{rr} (mm)	20	40	60	80	100
maximum wake length (mm)	14	25	35	42	42

At Re_e just above the critical one the flow exhibits oscillations in the wake, becoming more violent at higher Re_e with a considerable amount of fluid mixing between the wake and the main flow. Directly behind the rod the flow remains quiescent even at high Re_e. Aluminium powder observations give the flow the appearance of a regular procession of vortices rolling downstream and disappearing at the next rod on the opposite wall. Vortices also appear in front of the rods at high Re_e. Plate 3.4 shows the steady and unsteady flow conditions visualised with dye for l_{rr}=20 mm. For l_{rr}=40 mm Plates 3.5 and 3.6 show the flow conditions visualised by dye and aluminium powder, respectively. The reported vortex shedding phenomenom can be seen clearly in Plate 3.6.

3.3.3 Suspended Staggered Rods

The nine geometries (see Figure 2.10) all showed unsteadiness at Reynolds numbers far below the critical Re_e in the equivalent empty channel. Again at Re_e slightly higher than the critical one the flow exhibited oscillations which first occurred in the wake and became

more violent as the Re_e was further increased. At high Re_e vortices were shed and transported downstream. The critical Re_e are given in Table 3.2

Table 3.2: Critical Re_e for different rod-wall (d_{rw}) and inter-rod (l_{rr}) distances

d_{rw} / l_{rr}	1 mm	2 mm	3 mm
12 mm	230	230	410
24 mm	180	180	280
48 mm	230	190	210

Interesting differences in the flow conditions behind suspended rods were observed as the gap between rod and wall d_{rw} was decreased:

For d_{rw}=3 mm, the steady flow behind the rods has a nearly symmetrical wake consisting of two counter-rotating vortices extending to a maximum of two rod diameters. This was similar to the centered rods except for the case where l_{rr}=6 mm when the flow behind the rod is drawn down from the channel centre round the trailing face of the rod and continues downstream nearer to the channel wall. The wake in the latter case is asymmetric i.e. it has two counter rotating vortices of which the one closest to the channel middle was the larger. A slight asymmetry was also observed for l_{rr}=12, 24 mm but in this case the vortex

nearest the wall was slightly bigger. Above the critical Re_e the flow exhibited oscillations originating from the wake tail similar to the centered rods. Although the flow in the channel middle is unsteady the flow close to the wall is only affected at high Re_e. Plates 3.7, 3.8 and 3.9 show the transition to unsteady flow and its effect on the flow near the wall, visualised by dye injection for l_{rr}=12 mm. Plate 3.10 shows the effect of the higher critical Re_e on the flow near the wall for l_{rr}=6 mm, i.e., the flow near the wall is relatively undisturbed even at high Re_e.

For d_{rw}=2 mm, the steady flow through the gap between rod and wall is drawn up round the trailing face of the rod, and continues downstream nearer to the middle of the channel. Unlike the case when d_{rw}=3 mm, the wake behind the rods is asymmetric (see Plate 3.11; top). Beyond the point where the flow is drawn up through the gap, the flow is fairly quiescent near the wall. At Re_e above the critical one the fluid can clearly be seen to be drawn away from the wall indicating that separation could occur on the wall (see Plate 3.11; bottom and Plate 3.12; top). This effect was less pronounced for l_{rr}=6 mm where part of the dye injected near the wall remained near the wall for several inter-rod distances l_{rr} and the mixing of the dye appeared to be less vigorous (see Plate 3.12 bottom). Aluminium powder observations show the appearance of a moving vortex on the wall for unsteady flow (see Plate 3.13).

For d_{rw}=1 mm the flow pattern resembles that of an array of attached staggered rods for both steady and unsteady conditions. At Re_e below critical there exists a steady vortex on the wall behind the rod with the flow going underneath the rod, pulling away from the channel wall behind the rod and continuing downstream round the steady vortex. The length of this vortex is approximately 6mm for l_{rr}=6, 12 mm, and 12mm for l_{rr}=24 mm. This means that for l_{rr}=6 mm the space between the rods on a line parallel to the channel axis is occupied by the vortex. When the flow has become unsteady, the flow has the appearance of vortices rolling downstream in a regular but intermittent fashion. Also the shedding of vortices brings about considerable mixing between the liquid in the channel middle and the liquid close to the channel wall. Plates 3.14 and 3.15 give the transition from steady to unsteady flow for l_{rr}=6, 12 mm, respectively.

3.4 Discussion

3.4.1 Centered Rods

It is helpful to define another Reynolds number Re_d equal to Vd/ν. For the array of rods the flow became unsteady at Re_e around 260 (Re_d=79) which agrees with experiments in TAN65. The extensive work on flow phenomena caused by a cylinder in unbounded cross-flow, e.g. GER78, can be used as a guideline for our configuration of an array of

centered rods in a channel. The critical Re_d for a cylinder in unbounded flow is in the range 30 to 50. Even at Re_e slightly above the critical Re_e the flow with its sinusoidal pattern behind the rod is still similar to the unbounded flow situation. At higher Re_e, however, instead of developing a Von Karman vortex street, the flow remains sinusoidal in the channel middle but with an increasing amplitude as the Reynolds number increases. The effect of the confining walls is clearly visible. In Figure 3.2 the influence of the blockage ratio d/h on the critical Re_d is demonstrated using data from a variety of sources. Although the discrepancy in the data is considerable the graph illustrates the trend that the critical Reynolds number increases with increasing blockage ratio.

When the flow has become unsteady it appears to have a moving vortex on the channel wall with liquid being pushed away from the channel wall. The implication for a mass transfer boundary layer is that it gets interrupted when this vortex passes. This ought to be beneficial to mass transfer and maybe even more important than the increase in mixing which the onset of unsteadiness usually brings about.

3.4.2 Attached Staggered Rods

Laminar flow over a single backward facing step has been widely investigated and can be regarded as a benchmark for the attached staggered rods. Armaly et. al. [ARM83] have

analysed this flow problem using laser doppler anemometry and numerical techniques. For Re_e=240 which is the critical Reynolds number for most of the attached staggered rod arrays, their results indicate a wake length of 6 times the step height which is in excellent agreement with the maximimum wake length results for the larger inter-rod distance l_{rr} presented in Table 3.1. For low l_{rr} the effect of the rod on the other side is to inhibit further growth of the wake as the flow gets deflected by the rod.

Kang and Chang [KAN82] in their study on attached staggered rectangular obstacles observed critical Re_e between 420 and 500, approximately double the present results. They also presented a graph of wake length versus Reynolds number for a geometry with a separation distance slightly larger than the l_{rr}=60 mm case in which the maximum wake length was found to be 4.5 times the obstacle height, slightly lower than the result in Table 3.1.

The critical Re_e determined by the present experiments is also lower than the value given by Shiina [SHI83] for a single (d=h/2) attached to one channel wall viz. Re_e=530 to 670. The wake length for Re_e=240 according to experimental results reported in [SHI82] is 6 times the rod diameter, in excellent agreement with Table 3.1 for larger l_{rr}. The flow patterns presented by Shiina et. al. [SHI82, SHI83] are very similar to the patterns presented

in Plates 3.4-3.6 with vortex shedding being the dominant feature at Re_e above the critical one.
The low critical Re_e encourages mixing and hence ought to improve mass transfer. Also the rods act as physical barriers to the development of a mass transfer boundary layer and should already be effective in steady flow.

3.4.3 Suspended Staggered Rods

The conclusion from Table 3.2 is that critical Re_e's cannot be predicted by simple means. For instance, one might have expected that the shedding of vortices from the rod was related to a local Reynolds number based on the local velocity stemming from an assumed parabolic velocity profile and rod diameter. If this Reynolds number exceeds 50 (onset of unsteadiness in unbounded flow) the flow ought to become unsteady. This meant that increasing the rod-wall distance d_{rw}, i.e., increasing the local velocity at the rod position, should lead to a lower critical Re_e which is not borne out by the results presented in Table 3.2. Larger d_{rw} do not necessarily reduce the critical Re_e and the inter-rod distances play a part also. Also the flow visualisation results indicate quite large departures from the parabolic velocity valid for the empty channel.

In [KAR88] diagrams of flow patterns resulting from a numerical study for a geometry with one row of cylinders (circular cross section) located near a channel wall

(d/h=0.2, d_{rw}/h=0.15, l_{rr}/d=16.6, i.e. comparable to this work's d_{rw}=2 mm, l_{rr}=48 mm geometry) were given for Re_e=333 and Re_e=600 (based on superficial flow velocity and hydraulic diameter of an empty two-dimensional channel). The critical Re_e was calculated to be around 400. No recirculation zone was apparent for the lower Re_e. At the higher Re_e the flow appears to have a moving vortex on the wall closest to the cylinder, consistent with our findings. Karniadakis et. al. suggest that the transition phenomena in this geometry resemble those in empty channel, viz. the development of Tollmien-Schlichting waves, but at a calculated Re_e an order of magnitude lower.

In [MAT75] the flow around a single obstruction of square cross section in a Poiseuille flow (d/h=0.2, d_{rw}/h=0.1 i.e. comparable to this work's d_{rw}=1 mm geometry) was simulated numerically for steady conditions (Re_e=133, based on superficial flow velocity and hydraulic diameter of an empty two-dimensional channel). A separation zone is clearly visible on the wall behind the rod and the flow pattern resembles the pattern found in our experiments.

Finally, all but one of the staggered suspended rod geometries showed the emergence of unsteadiness in the flow at Re_e in the range 180 to 280 which should improve mixing and hence mass transfer. The ability to disrupt flow near the channel wall appeared to be largely

determined by the rod-wall distance d_{rw} with the smallest distance already causing a disruption at sub-critical Re_e and the largest distance at higher Re_e.

3.4.4 Final Remarks

The most striking feature in the flow visualisation experiments was the early transition from laminar steady flow to unsteady flow. The unsteady flow had a very orderly appearance in the shape of oscillations originating from the obstacle's wake. Turbulent flow i.e. a chaotic flow was not noticed throughout the experiments. The unsteady phenomena were intermittent which is indicative of a transition from laminar to turbulent flow [SCH68, p.433]. The transition occurring at very low Re_e is perhaps not a complete surprise because the essential element of unbounded laminar flow around a bluff body viz. the wake or vortex, is maintained in channel flow. The wake is essential as it creates an inflexional velocity profile which affects the stability strongly [SCH68, p.445]. It is the presence of an inflexional velocity profile which causes the flow behind a cylinder in unbounded flow to become unsteady for Re_d in the range 30 to 50. The analogy between channel flow and unbounded flow is nevertheless incomplete because for all but one of the geometries the channel transition occurs in a fairly narrow range of Re_e-values regardless of the rod diameter. Clearly the constraining effect of the channel wall is

present as well. It appears to be possible to predict the transition by a flow stability analysis of the velocity profiles over the length of the repetitive cells in the channel. This was shown by Karniadakis et. al. [KAR88]. The presence of wakes, at Re_e below critical, is in line with simple qualitative deliberations on flow separation and vortex formation e.g. [SCH68, p.29]. Behind an obstacle (and in the case of the attached rods to a lesser extent in front) the flow decelerates leading to an adverse pressure gradient. The flow very close to the obstacle or to the wall has not enough kinetic energy to overcome the adverse pressure gradient due to the friction with the wall and hence separates away from it.

Finally, all the geometries appear to be able to cause flow disruption on the channel wall above a certain Re_e which depends on the geometry. This lends credibility to the idea that the mass transfer boundary layer will be periodically destroyed and redeveloped after this, i.e, the 'surface-renewal' mechanism ought to be applicable in our geometries. For the attached geometries, this mechanism might already be applicable at Re_e below critical.

4. PRESSURE GRADIENT STUDIES

4.1 Experimental Equipment and Materials

The second method used to characterise the geometries hydrodynamically is by the determination of the hydraulic resistance they impose upon the flow. For this purpose a PERSPEX flow channel and lid identical to the one described in Paragraph 3.1 but with a reduced width was fabricated in which the geometries could be fitted fairly tightly. The new channel was finished in the same manner as the previous one. Two pressure taps made from PERSPEX tube were fitted in the channel middle 480 mm apart, the first one 300 mm from the channel entrance. The separation distance represented a whole number of inter-rod distances for most of the geometries examined by flow visualisation. The expected differential pressure between the two taps was estimated to be of the order of a couple of hundred pascals. Therefore an inclined manometer with a range 0 to 600 Pa (for a manometer liquid of specific gravity 1.0) was used. The maximum value was checked by measurement of the internal dimensions of the manometer. The rest of the equipment was the same as in the flow visualisation experiments and the new channel with the manometer were incorporated in the flow loop depicted in Figure 3.1.

4.2 Experimental Method

The manometer liquid used in the experiments was carbon tetra-chloride (CCl_4: 1595 kg/m^3) because this did not mix with our operating liquid, i.e., sugar solutions of various densities (1080-1200 kg/m^3) [SMI89]. The pressure range was then equal to 0-600$(\rho_{CCl4} - \rho_{sugar})/\rho_{H2O}$ Pa. Before a series of experiments, the manometer was filled with the appropriate amount of CCl_4 and before each experiment care was taken to ensure that the tube connection between the cell and the manometer was free from air bubbles. To check for hysteresis effects each experiment was carried out in the sequence minimum flow rate → maximum flow rate → minimum flow rate. During the sequence 5-10 minutes was allowed at each reading for the manometer liquid - operating liquid interface to reach its equilibrium level.

Different sugar solutions were necessary to permit an accurate measurement of both pressure gradient and flow rate for all geometries and Re_e-range (100 to 1250).

4.3 Experimental Results

The measured pressure differentials were written dimensionless by:

$$(p^*)_e = (\Delta p/l)(d_h)_e^3/(2\rho\nu^2) = f_e Re_e^2 \qquad (4.1)$$

Δp pressure differential

l	distance between the presssure taps
ρ	density of operating liquid
ν	kinematic viscosity of operating liquid
$(d_h)_e$	hydraulic diameter of empty channel (23 mm)
f_e	empty channel friction factor
Re_e	Reynolds number for empty channel

Re_e was determined in the same manner as in the flow visualisation studies. An estimate of the accuracy in the pressure gradient results is given in Appendix D.
No significant discrepancies were found between the dimensionless pressure gradients calculated from two sets of experiments with different sugar solutions i.e. different values of the density. As is illustrated by Figure 4.1. a satisfactory overlap of the data was obtained, indicating that the data were consistent.
The dimensionless pressure gradient could be fitted to two types of curves (Equations 4.2 and 4.3) using a non-linear regression method (GraphPAD; ISI-software) and the resulting correlations always showed a correlation coefficient squared in excess of 0.99.

$$(p^*)_e = A_1 Re_e + A_2 Re_e^2 \qquad (4.2)$$

and

$$(p^*)_e = B_1 Re_e^{B_2} \qquad (4.3)$$

4.3.1 Centered Rods

The dimensionless pressure gradient data are shown in Figure 4.2 as a function of the Reynolds number. The resulting correlations are given in Table 4.1.

Table 4.1: Correlations for dimensionless pressure gradient of centered rods.

l_{rr} (mm)	$(p^*)_e = A_1 Re_e + A_2 Re_e^2$	$(p^*)_e = B_1 Re_e^{B_2}$
30	$144 Re_e + 0.45 Re_e^2$	$3.76 Re_e^{1.73}$
60	$73 Re_e + 0.24 Re_e^2$	$2.28 Re_e^{1.71}$
120	$27 Re_e + 0.132 Ree^2$	$0.653 Re_e^{1.80}$

4.3.2 Attached Staggered Rods

The dimensionless pressure gradient data are shown in Figure 4.3 as a function of the Reynolds number. The resulting correlations are given in Table 4.2.

Table 4.2: Correlations for dimensionless pressure gradient of attached staggered rods

l_{rr} (mm)	$(p^*)_e = A_1 Re_e + A_2 Re_e^2$	$(p^*)_e = B_1 Re_e^{B_2}$
20	$34 Re_e + 0.97 Re_e^2$	$1.41 Re_e^{1.95}$
40	$5.4 Re_e + 0.42 Re_e^2$	$0.46 Re_e^{1.99}$
60	$16 Re_e + 0.26 Re_e^2$	$0.50 Re_e^{1.92}$
80	$15 Re_e + 0.19 Re_e^2$	$0.39 Re_e^{1.91}$

4.3.3 Suspended Staggered Rods

The dimensionless pressure gradient data are shown in Figures 4.4, 4.5 and 4.6, respectively for d_{rw}= 3, 2, and 1 mm. The resulting correlations are given Tables 4.3, 4.4 and 4.5.

Table 4.3: Correlations for dimensionless pressure gradient of suspended staggered rods (d_{rw}=3 mm)

l_{rr} (mm)	$(p^*)_e=A_1Re_e+A_2Re_e^2$	$(p^*)_e=B_1Re_e^{B_2}$
6	$177Re_e + 0.36Re_e^2$	$6.23Re_e^{1.65}$
12	$115Re_e + 0.24Re_e^2$	$6.40Re_e^{1.58}$
24	$59Re_e + 0.124Re_e^2$	$3.13Re_e^{1.59}$

Table 4.4: Correlations for dimensionless pressure gradient of suspended staggered rods (d_{rw}=2 mm)

l_{rr} (mm)	$(p^*)_e=A_1Re_e+A_2Re_e^2$	$(p^*)_e=B_1Re_e^{B_2}$
6	$250Re_e + 0.54Re_e^2$	$10.4Re_e^{1.63}$
12	$90Re_e + 0.31Re_e^2$	$3.45Re_e^{1.69}$
24	$41Re_e + 0.148Re_e^2$	$1.42Re_e^{1.71}$

Table 4.5: Correlations for dimensionless pressure gradient of suspended staggered rods (d_{rw}=1 mm)

l_{rr} (mm)	$(p^*)_e=A_1Re_e+A_2Re_e^2$	$(p^*)_e=B_1Re_e^{B_2}$
6	$99Re_e + 0.50Re_e^2$	$2.12Re_e^{1.82}$
12	$86Re_e + 0.27Re_e^2$	$3.65Re_e^{1.66}$
24	$23Re_e + 0.141Re_e^2$	$0.59Re_e^{1.82}$

4.4 Discussion

For laminar flow in an infinite channel, the constants in Equations 4.2 and 4.3 are A_1=24, A_2=0 and B_1=24, B_2=1, respectively (Equation 2.2). In the past it has often been assumed that deviations from the linear dependency in the Reynolds number was an indication of the flow undergoing the transition to turbulence e.g. [ZHO83]. This is not necessarily the case as has been pointed out by Scheidegger in his monograph on porous media [SCH60]. He argued that deviations from Darcy's law, which states a linear relationship between pressure drop and flow rate, were due to omission of the non-linear terms from the Navier-Stokes equation. The point at which Darcy's law was not valid anymore varied tremendously and values in the Re_f-range 0.1 to 75 are quoted by Scheidegger. The curvature of the flow channels also appeared to be of importance in the case of porous media. For packed columms Heggs [HEG83] quotes a transition range 10 to 1000.

It has already been mentioned in Paragraph 2.2 that the second term in Equation 4.2 can be thought of as the contribution of the inertial forces to the pressure gradient (also called the form drag), the first term being the viscous contribution (drag due to skin friction). A deviation from the linear relationship can then be seen as the inertial forces becoming as important as the viscous forces, or even dominant in the pressure gradient. The Re_e-exponenents (B_2 in Equation 4.3) are between 1.5 and 2 indicating the inertial forces have a dominant role.

The dimensionless pressure gradient is not only a function of the Reynolds number but also of the geometry of the structure i.e. the inter-rod distance, the diameter of the rod which indicates the amount of blockage, and also the distance of the rod to the wall. This can be expressed as follows:

$$(p^*)_e = F(Re_e,\ l_{rr}/(d_h)_e,\ d/(d_h)_e,\ d_{rw}/(d_h)_e) \qquad (4.4)$$

The amount of pressure data is too small to enable the determination of the exact functional form F and only a limited quantitative discussion is given.

For most categories of the geometries the pressure drop appeared to vary proportionally to the number of rods in the channel, similar to tube banks and could be described as a linear function of $(d_h)_e/l_{rr}$, i.e., the 'promoter

frequency' as defined in LEI77. This can be interpreted as follows: each rod has a certain pressure loss which dominates the channel pressure gradient, i.e. the pressure drop over the distance between the rods is not significant within the limits investigated in this study.

4.4.1 Centered Rods

All the dimensionless pressure gradient data could be well correlated by:

$$(p^*)_e = ((d_h)_e/l_{rr})(190Re_e + 0.61Re_e^2) \qquad (4.5)$$

or

$$(p^*)_e = ((d_h)_e/l_{rr})(5.44Re_e^{1.72}) \qquad (4.6)$$

as illustrated in Figure 4.7.

Equations 4.5 and 4.6 can be assumed to be valid for $1.30<l_{rr}/(d_h)_e<5.22$ but not for larger values of the dimensionless inter-rod distance where one expects the pressure gradient to approach the empty channel correlation asymptotically. The correlation suggested by Leitz and Marinčič (Equation 2.28) satisfies this criterion. It is compared with the present data in Figure 4.8 and agreement is good, albeit that the present results are consistently higher.

4.4.2 Attached Staggered Rods

For l_{rr}=40, 60 and 80 mm ($l_{rr}/(d_h)_e$=1.74, 2.61, 3.48) the dimensionless pressure gradient data could be well correlated by:

$$(p^*)_e = ((d_h)_e/l_{rr})(32Re_e + 0.69Re_e^2) \qquad (4.7)$$

or

$$(p^*)_e = ((d_h)_e/l_{rr})(1.08Re_e^{1.94}) \qquad (4.8)$$

as illustrated in Figure 4.9. The dimensionless pressure gradient for l_{rr}=20 mm ($l_{rr}/(d_h)_e$=0.87), the shortest inter-rod distance was higher than these correlations, either due to the lower critical Re_e or to the extremely tortuous nature of the flowpath.

The contribution of the linear component in Equation 4.7 being small or, similarly the exponent in Equation 4.8 being close to 2, indicates that the inertial forces are the domininant feature in the pressure gradient. This is not surprising, given the tortuous nature of the flow path.

4.4.3 Suspended Staggered Rods

For d_{rw}=3 mm and l_{rr}= 12 and 24 mm ($l_{rr}/(d_h)_e$=0.522, 1.043) the dimensionless pressure gradients can be correlated by

$$(p^*)_e = ((d_h)_e/l_{rr})(61Re_e + 0.128Re_e^2) \qquad (4.9)$$

or

$$(p^*)_e = ((d_h)_e/l_{rr})(3.24Re_e^{1.59}) \qquad (4.10)$$

as illustrated in Figure 4.10. For l_{rr}= 6 mm ($l_{rr}/(dh)_e$=0.261), the shortest inter-rod distance, the pressure gradient is lower than prescribed by Equations 4.9 and 4.10. This is probably due to the higher critical Re_e (see Table 3.2).

For d_{rw}=2 mm and l_{rr}=6, 12, and 24 mm ($l_{rr}/(d_h)_e$=0.261, 0.522, 1.043) the dimensionless pressure gradients can be correlated by

$$(p^*)_e = ((d_h)_e/l_{rr})(52Re_e + 0.150Re_e^2) \qquad (4.11)$$

or

$$(p^*)_e = ((d_h)_e/l_{rr})(1.92Re_e^{1.68}) \qquad (4.12)$$

as illustrated in Figure 4.11.

For d_{rw}=1 mm and l_{rr}=6, 12 and 24 mm ($l_{rr}/(d_h)_e$=0.261, 0.522, 1.043) the dimensionless pressure gradients can be correlated by

$$(p^*)_e = ((d_h)_e/l_{rr})(38Re_e + 0.129Re_e^2) \qquad (4.13)$$

or

$$(p^*)_e = ((d_h)_e/l_{rr})(1.11Re_e^{1.73}) \qquad (4.14)$$

as illustrated in Figure 4.12.

It is interesting to note that judging from the correlations presented in this paragraph the geometry with d_{rw}=2 mm gives the largest pressure drop, with d_{rw}=3 mm causing a smaller pressure drop but still larger than d_{rw}=1 mm. If one assumed the geometries to be placed in a Hagen-Poiseuille flow (empty channel), the rods placed closest to the channel centre would give higher pressure drops because the local velocities are highest in the centre. However, the only occasion where this order is followed is for the largest inter-rod distance l_{rr}=24 mm and Re_e smaller than 500 as illustrated in Figure 4.13. This was to be expected because at this inter-rod distance the flow will resemble the empty channel most and at the lowest Reynolds number the influence of the rods on the

flow will be least. When the rods are close to the wall the pressure drop is smallest and clearly the effect of the low local velocities must be responsible for this. On the whole the influence of the rod-wall distance is minor and the inter-rod distance plays a far more important role.

4.4.4 Final Remarks

The onset of oscillations in the flow as shown in Chapter 3 does not lead to a sudden increase in the pressure gradient. The results appear to be well described by straight lines in log $(p^*)_e$ versus log Re_e graphs for $100<Re_e<1250$. There were only two occasions for which the effect of transition could be suggested as the explanation of a deviatory pressure gradient as discussed in the previous paragraphs.

For most geometries the pressure gradient measurements indicated that each rod had a certain pressure drop associated with it, which depended on the position of the rod in the channel and the diameter of the rod. Doubling the number of rods in the channel simply doubled the pressure drop.

It was noted that for a given porosity the pressure gradient was similar regardless of the type of structure with the pressure gradient decreasing with increasing

porosity. Again the pressure gradient data were fitted to the two types of correlations (Equations 4.2 and 4.3) assuming a linear relationship in 1-E and ensuring that for E=1 the pressure gradient is equal to the empty channel (Figure 4.14):

$$(p^*)_e = A_e Re_e + (1-E)(1100 Re_e + 5.34 Re_e^2) \qquad (4.15)$$

or

$$(p^*)_e = A_e Re_e + (1-E)(28.4 Re_e^{1.79}) \qquad (4.16)$$

where $A_e Re_e$ represents the empty channel pressure gradient (A_e=20.48 in our channel, A_e=24 for infinite channel [SHA78]). The maximum deviation of the data points is 25% which makes it useful as a rough guide to the pressure drop. Equations 4.15 and 4.16 on average overestimate the pressure gradient for the attached staggered rods and underestimate the pressure gradient for the staggered suspended rods.

The position of the rod in the channel has a minor influence on the pressure gradient, judging from Figure 4.15 which displays the correlations given in Equations 4.6, 4.8, 4.10, 4.12 and 4.14. Despite the different values of the Re_e-exponent, the pressure gradients, stripped of their dependence on the inter-rod distance, are not greatly affected by the position in the channel

and are similar for a given rod diameter. In contrast the effect of the rod diameter or blockage ratio $(d/(d_h)_e)$ is quite important with the 7 mm rods giving an approximately 4 times higher pressure gradient than the 3 mm rods. As only two rod diameters have been investigated the influence of the blockage ratio can only be estimated and a multiple linear regression on the data having undergone a logarithmic transformation resulted in:

$$(p^*)_e = ((d_h)_e/l_{rr})(d/(d_h)_e)^{1.57}(39.4Re_e^{1.70}) \qquad (4.17)$$

Figure 4.16 gives an indication of the representativeness of Equation 4.17. As the results presented in Tables 4.1 to 4.5 indicate quite a large variation in the Re_e-exponent, a single exponent correlation like e.g. Equation 4.17 must be regarded as an rough estimate for the pressure gradient.

Finally, Figures 4.17-4.19 display the pressure gradient in the 'filled channel' description (see Paragraph 2.1). It can be seen that this description does not lead to a single correlation for the geometries involved. Also drawn is the correlation developed for RO-separators by Schock and Miquel (Equation 2.23) which appears to lie approximately in the centre of gravity of the data. The attached staggered rods were the only structures for which a 'filled channel' description proved useful but only for l_{rr}=40, 60, 80 mm and for Re_f smaller than 400. Figure

4.20 shows that in these circumstances the pressure gradient results collapsed to a single curve:

$$(p^*)_f = 11.1Re_f + 0.18Re_f^2 \qquad (4.18)$$

or

$$(p^*)_f = 0.60Re_f^{1.82} \qquad (4.19)$$

5. MASS TRANSFER STUDIES

5.1 Diffusion Limited Current Technique

An electro-chemical method, viz the diffusion limited current technique (DLCT), is used to measure mass transfer. It is based on the phenomenon that for an electrolysis process the transfer of reacting species to an electrode is limited by the diffusion process only, under certain easily controllable conditions. As such it is an ideal method to study diffusion processes, also, because the mass transfer can be measured as an electric current. The solution, used mostly, is a mixture of potassium ferri- and ferro-cyanide in an excess of supporting electrolyte (usually sodium hydroxide) and the reaction of interest occurs at the cathode where ferricyanide is reduced to ferrocyanide:

$Fe(CN)_6^{3-} + e \rightarrow Fe(CN)_6^{4-}$

The current versus cathode potential graph shows a plateau for a range of the cathode potential. Below this range the current is mainly determined by Ohm's law, above it other reactions start to become important at the cathode. On the plateau one may assume that no accumulation of the reacting species occurs and the concentration at the wall has fallen to zero. As one may neglect the contribution to the current due to migration effect because of the presence of an excess of supporting electrolyte, the limiting current (I) can be expressed as a mass transfer

coefficient k:

$$k = I/(Fc_bA_{el}) \qquad (5.1)$$

where F = Faraday constant

c_b = bulk concentration of reacting species

A_{el} = area of electrode

Several monographs [MIZ71, WRA77, SEL78] describe the technique in detail and give extensive surveys of its applications. Beside these reviews several other references [AGG79, JEN77, BER83] proved to be of value because of their detailed discussion of experimental design and procedure and several points are highlighted below:

1) Exclusion of light from the solution because ferrocyanide decomposes under the influence of light, ultimately leading to formation of hydrogen cyanide which contaminates the solution and poisons the electrodes.
2) Exclusion of oxygen from the solution because this might poison the electrodes (BER83 also mentions hydrogen sulphide as a possible cause of electrode poisoning). Bubbling nitrogen through the solution before the experiments and maintaining a nitrogen blanket over the solution throughout the experiments will avoid this effect.
3) Attainment of the limiting current condition can be ensured by:

- making the anode area much larger than the cathode area
- reducing the concentration of ferricyanide with respect to ferrocyanide

4) Electrode preparation by:
- polishing to remove any oxide film
- degreasing with for instance carbon tetrachloride
- cathodic activation i.e. hydrogen evolution at a current density of 20 mA/cm^2 in 5% sodium hydroxide for 15-20 minutes. This step was not deemed necessary in BER83 for Reynolds numbers below 10^4.
- Rinsing electrodes with deionised water after each experiment to avoid the formation of deposits when exposed to air.

The DLCT can be used to obtain local mass transfer measurements if one uses a segmented electrode, e.g. FOC83 and KIM83, or if one uses mini-electrodes within a larger electrode but electrically isolated from it, e.g. WAT68. It is important to keep the area taken up by the insulation material as tiny as possible in order to give a representative measurement.

The principles of shear rate measurements using the DLCT are described by Hanratty and Campbell [HAN83]. They give a 'design equation' relating the mass transfer coefficient to the shear rate:

$$kl/D = 0.807(Sl^2/D)^{1/3} \qquad (5.2)$$

where k : mass transfer coefficient

l : length of electrode

D : diffusion coefficient

S : shear rate

Equation 5.2 is the solution of the mass transport equation given in Appendix A (Equation A2) with boundary conditions c=0 at the wall and $c=c_b$ at $y=\infty$ and using a linear velocity profile in the mass transfer boundary layer (Equation 2.36). It assumes the shear rate to be constant over the length of the electrode and therefore Equation 5.2 is a special case of Equation 2.39 written in a different form. In Equation 5.2 stream-wise diffusion has been neglected and Mitchell and Hanratty [MIT66] stated that this is permitted for $Sl^2/D>5000$ based on earlier work by Ling [LIN62]. Deviations from Equation 5.2 due to stream-wise diffusion were small at lower values, e.g. at $Sl^2/D=200$ less than 5%. Although derived for steady laminar flow, Equation 5.2 is also valid for unsteady flow provided that the fluctuations are small. In that case the entities in Equation 5.2 can be replaced by their average values [MIT66]. For extremely low values of the shear rate, e.g. near separation and reattachment points, Equation 5.2 is not valid anymore and the use of a sandwich or dual electrode can, apart from indicating the local flow direction, enable one to measure shear rates in

these conditions [SON69, LEB73, TAG79, CHO83] (also see Appendix A). Beside Hanratty and Campbell [HAN83] Lebouché and Martin [LEB75] have listed design equations for a variety of electrode shapes as well.

5.2 Experimental Equipment and Materials

The flow loop displayed in Figure 3.1 was rebuilt using inert and opaque materials as much as possible (Appendix B). The clamping bracket used for the flow visualisation studies and pressure gradient studies was used to incorporate a PVC flow cell. Similar to the cell described in Paragraph 2.1 the cell consisted of a tray and a lid. The internal dimensions of the flow channel were identical to the one described in Paragraph 3.1, enabling the use of the PERSPEX geometries previously employed. Two O-rings were deemed necessary to prevent leakage of the agressive operating liquid. Several modifications were made to the flow loop displayed in Figure 3.1. Firstly, flow rates were measured with three rotameters of different capacities in parallel to increase the accuracy over the whole range of Re_e. Except for the actual readings these flow meters were completely covered with black tape to avoid the interaction of light with the operating liquid. Secondly, a heating mat was glued to the outside of the storage tank to achieve above ambient temperatures of the operating liquid. Finally nitrogen gas was fed into the operating liquid through a gas sparger placed in the

storage tank in order to avoid interference of dissolved oxygen.

The design of the electrodes was aimed at meeting the following objectives:

1) Determination of the mass transfer correlation for the chosen geometries
2) Measurement of local mass transfer
3) Measurement of wall shear rate

The mass transfer correlation (first objective) can be derived from measurements taken from a single large cathode. For this purpose both cathode and anode were cut from 1 mm thick nickel sheet, with the cathode having a width equal to the flow channel's width (100 mm) and a length representing an even number of the inter-rod distance l_{rr} (240 mm) for most of the geometries investigated in the previous experiments. The anode dimensions were 100X300 mm. Both electrodes were pressed into a 1.2 mm recess in the flow cell filled with epoxy resin, the cathode in the tray and the anode in the lid. Proper care was taken to ensure that the electrode surface was flush with the surrounding PVC. Excess epoxy resin was wiped away as much as possible directly after glueing. Progressively finer grades of emery paper were used to polish the electrodes and cell surface. Electrical contacts were made using spring-loaded pins pressing against the underside of the electrode through a slit in the tray or lid.

To achieve the second objective 20 circular mini-electrodes of nickel were positioned in an array along the centre of the large cathode, at 10 mm intervals. As this procedure was very cumbersome it will be described in some detail. The circular mini-electrodes were manufactured from nickel wire of 1 mm diameter. To establish the electrical connection, a wire was wrapped around the nickel wire and the whole unit set in PERSPEX glue in a small PERSPEX tube with the nickel wire left sticking out a couple of millimeters. When set the unit was inserted into a 1.4 mm hole drilled in the cathode and glued in using epoxy resin. This appeared to be a trial and error procedure as the nickel wire was not always electrically isolated from the surrounding cathode after the epoxy resin had set. Furthermore the length of nickel wire sticking out through the cathode had to be reduced to achieve a smooth surface. Sanding down the nickel wire often resulted in an electrical connection being established between the nickel wire and the surrounding electrode. Nevertheless, at the end of repeated trials the 20 mini-electrodes were properly in position and the diameters of the wires were checked under a microscope confirming a value of 1 mm. Plate 5.1 gives two examples of the mini-electrodes.

To meet the third objective, the shear rate measurements, a dual electrode arrangement was deemed necessary as this would enable the determination of the direction of the

flow near the wall. The length of both elements was chosen such that measurements from the electrodes could be used to calculate the shear rate. A long electrode will ensure the validity of the design equation (Equation 5.2), will give a large current and is easier to manufacture. A short electrode will improve the spatial resolution. A suitable compromise appeared to be 1 mm. The width was 10 mm, thus minimising diffusion interference from the edges. The dual electrode was fabricated from 1 mm thick nickel sheet cut to form two 10X25 mm plates. These were glued together using epoxy resin and one side was smoothed and polished using progessively finer grades of emery paper. At this point it was checked whether the electrodes were electrically insulated. The whole unit was then glued into a slot in the PVC tray with the polished side flush with the surrounding area, 320 mm from the inlet. Excess epoxy resin was wiped away immediately after. After the resin had set the channel area, containing the dual electrode arrangement, was polished with emery paper. Again checks were made to ensure electrical isolation. Electrical contact was made with two spring-loaded pins pressing against the sides of the dual electrode outside the channel. As the electrode was fixed in the channel an arrangement had to be fabricated which enabled the movement of the geometries along the cell axis. This was done using a threaded PVC pin and a threaded hole in the perforated plate which formed part of the each geometry investigated. The pin was inserted into the flow channel

at the outlet and held in position by a single PVC nut. Sealing was provided with two O-rings which fitted into two grooves in the pin. The geometry could be moved axially by turning the pin, with one turn resulting in 1 mm travel. The PERSPEX geometries had to be shortened to allow for sufficient space to travel. Plastic wool held in place by a mesh was used to create a smooth entrance flow. Plate 5.2 shows the finished tray of the flow cell and the electrodes.

Current measurement of the multiple electrode system was facilitated by a data-acquisition system which comprised the following:

1) an electronic circuit [NIX89] which had the dual function of keeping the electrode voltage at a preset level regardless of the current being drawn, and providing an output voltage which varied proportionally to the current drawn (see Figure 5.1). This output voltage was then fed to
2) an analog to digital converter (ADC) which converted the voltage into an integer in the range 0 to 4095. The ADC was a circuity board which fitted into one of the empty slots of
3) a personal computer. The personal computer was used to set electrode scanning rate and sampling times and to produce data files which could be used for analysis and manipulation.

5.3 Experimental Methods

5.3.1 Preparation of Experiments

The flow cell was incorporated into the flow loop and before any measurements were taken the following preparations were made to ensure reproducible results:

1) Rinsing of the whole flow loop with a detergent (DECON90) followed by several rinses with de-ionised water
2) Cathodic activation of all electrodes, i.e. hydrogen evolution 15-20 minutes in a 5% solution of sodium hydroxide at a current density of 20 mA/cm^2 followed by several rinses with de-ionised water.

Before each experiment the electrodes were cleansed with 0.1 M hydrogen chloride to remove any oxide film, cyclohexane to remove any grease, and then rinsed thoroughly with de-ionised water. Also before all the experiments the PERSPEX geometries were washed in a detergent solution (DECON90) and rinsed thoroughly with de-ionised water. Finally, with the geometry and flow channel incorporated in the flow loop the flow channel was rinsed with de-ionised water. The flow channel was never left filled with the operating liquid but always filled with de-ionised water when not in use. Figure 5.2 gives examples of the current-voltage or polarisation curves. From this it can be seen that maintaining the voltage at

400 mV will result in the limiting current condition being achieved and this setting was used in every experiment.

5.3.2 Properties of Operating Liquid

A 1 M sodium hydroxide solution was used throughout the experiments with the ferri-/ferrocyanide concentration being between 0.005 and 0.01 M. The ferricyanide concentration was measured with a spectrophotometer at a wavelength of 420 nm. Similar wave length values were quoted by other workers viz. 410 nm [RUN69] and 419 nm [WRA89]. The calibration curve is shown in Figure 5.3 and samples of the operating liquid were taken daily and diluted to a concentration suitable for measurement. Figure 5.4 shows the day-to-day variation in the ferricyanide concentration and it is clear that the drop in the ferricyanide concentration was small. This was most likely due to the near complete shielding from light i.e. the solution was exposed to the light only when taking a rotameter reading. As the dimensionless results of measurements taken from the cell with the same geometry in it on the first and last day of the series of experiments were identical it was concluded that the experimental procedure was sufficient to produce reproducible results.

The value of the diffusion coefficient was determined from the Stokes-Einstein relation given by Bazan and Arvia [BAZ65]:

$$D\eta/T = 2.5 \cdot 10^{-15} \ [mkg/(s^2K)] \qquad (5.3)$$

where D : diffusion coefficient

η : dynamic viscosity

T : absolute temperature

Values between 2.27 and 2.67 have been offered for the numerical constant in Equation 5.3 [SEL78] but 2.5 seems the most favoured value for operating liquids having a similar composition to the present liquid [BER77]. An alternative to the use of Equation 5.3 can be found in GOR66 in which the numerical constant is a function of the ionic strength.

The relationship between viscosity and temperature was determined in an identical manner, as described in Paragraph 3.1, and in the experiments a measurement of the temperature sufficed to calculate the viscosity and diffusion coefficient. Because the Schmidt number (ν/D) undergoes a dramatic change as the temperature changes, an accurate measurement is very important and although the temperature in the flow loop was not controlled it was ascertained that the temperature during a data acquisition period was constant. Furthermore the temperature variation during each experiment was limited by the operation at slightly above ambient temperature (20°C-25°C). The resulting Schmidt number was in the range 1500-2000.

5.3.3 Current Measurements

Currents from the large electrode were measured using a digital multimeter. Possible hysteresis effects were assumed to be averaged out by taking measurements with the flow rate undergoing the sequence maximum flow → minimum flow → maximum flow. Sufficient time was allowed for the multimeter to reach its equilibrium value after each alteration in the flow rate. It was immaterial to the value of the large electrode current whether or not the mini-electrodes were brought into the limiting current condition.

Currents from the mini-electrodes and the dual electrode were measured using the data-acquisition system which was precalibrated in the electronics workshop with a precision multimeter. The ADC (16 channels) was supplied with a demo-program outlining the essential elements (setting sampling rate, setting number of samples and choosing channel) and a library of machine-coded operating routines in the QUICKBASIC environment. Two ADC's were purchased to enable scanning of the 20 micro-electrodes but it appeared to be impossible to scan the 20 micro-electrodes with the two ADC's due to a software fault in the machine-coded operating routines [RIC90]. As the originators of the software were unable to solve this problem at short notice it was decided to sacrifice some of the information contained in the 20 mini-electrodes and use only one ADC

with 16 channels. Checks on the latter system showed that it worked flawlessly. The QUICKBASIC demo-program was altered to a program which as well as setting up and executing the data acquisition, determined the value of the relevant parameters, e.g. mass transfer coefficient, Reynolds number, Sherwood number etc., and prepared a data file which could be read by the plotting and analysis program GRAPHPAD. A similar program was developed for the data acquisition from the dual electrode in the shear rate measurements.

6. MASS TRANSFER CORRELATIONS

6.1 Experimental Results

The values of the large electrode currents were transformed into the dimensionless mass transfer entity $Sh_e/Sc^{1/3}$ and plotted as a function of Re_e. Sh_e is the Sherwood number, $=k(d_h)_e/D$, and Sc is the Schmidt number, $=\nu/D$. The 1/3 exponent of the Schmidt number has been assumed rather than determined. Values for the mass transfer coefficient were determined from Equation 5.1. Where suitable a curve of the kind given in Equation 2.10 was fitted to the data using a non-linear regression method (GraphPAD; ISI-software), with a correlation coefficient in excess of 0.98. In Appendix D an estimate of the accuracy of the mass transfer results is given.

6.1.1 Centered Rods

The dimensionless mass transfer data are depicted in Figure 6.1 as a function of Reynolds number. A change in the slope of the graph can be detected for Re_e in the region 300 to 500. In this range the data can be represented by the correlations given in Table 6.1.

Table 6.1: Mass transfer correlations for the centered rods

l_{rr} (mm)	$Sh_e/Sc^{1/3}=aRe_e^b$	Re_e-range
30	$0.22Re_e^{0.69}$	$Re_e>500$
60	$0.11Re_e^{0.76}$	$Re_e>400$
120	$0.10Re_e^{0.72}$	$Re_e>300$

6.1.2 Attached Staggered Rods

The dimensionless mass transfer data are depicted in Figure 6.2 as a function of Reynolds number. Again a change in the slope of the graph can be detected and Table 6.2 gives the correlations for this range.

Table 6.2: Mass transfer correlations for the attached staggered rods

l_{rr} (mm)	$Sh_e/Sc^{1/3}=aRe_e^b$	Re_e-range
20	$0.43Re_e^{0.66}$	$Re_e>180$
40	$0.24Re_e^{0.68}$	$Re_e>200$
80	$0.18Re_e^{0.70}$	$Re_e>250$

6.1.3 Suspended Staggered Rods

The dimensionless mass transfer data are depicted in Figures 6.3, 6.4 and 6.5 as a function of Re_e. For all nine geometries a sudden rise in mass transfer occurred above a certain Reynolds number and above this the data were fitted to give the correlations presented in the Tables 6.3, 6.4 and 6.5.

Table 6.3: Mass transfer correlations for the suspended staggered rods (d_{rw}=3 mm).

l_{rr} (mm)	$Sh_e/Sc^{1/3}=aRe_e^b$	Re_e-range
6	$0.087Re_e^{0.74}$	$Re_e>700$
12	$0.16Re_e^{0.66}$	$Re_e>500$
24	$0.12Re_e^{0.69}$	$Re_e>300$

Table 6.4: Mass transfer correlations for the suspended staggered rods (d_{rw}=2 mm).

l_{rr} (mm)	$Sh_e/Sc^{1/3}=aRe_e^b$	Re_e-range
6	$0.036Re_e^{0.92}$	$Re_e>500$
12	$0.055Re_e^{0.85}$	$Re_e>500$
24	$0.062Re_e^{0.81}$	$Re_e>500$

Table 6.5: Mass transfer correlations for the suspended staggered rods (d_{rw}=1 mm).

l_{rr} (mm)	$Sh_e/Sc^{1/3}=aRe_e^b$	Re_e-range
6	$0.23Re_e^{0.71}$	$Re_e>500$
12	$0.040Re_e^{0.90}$	$Re_e>400$
24	$0.037Re_e^{0.89}$	$Re_e>300$

6.2 Discussion

The effect of flow instability can easily be discerned from the mass transfer measurements. In contrast to the pressure gradient measurements the data cannot be represented by a single correlation over the whole Re_e-region. All geometries have a threshold in Re_e above which the data can be represented by a power law correlation. In most cases this threshold Re_e is higher than the observed

critical Re_e (see Chapter 3). For the attached staggered geometries it is similar to the critical Re_e, presumably because the flow instability occurs in the wall-bounded vortex behind the rod and thus starts to interact with the mass transfer process at the critical Re_e. For the centered rods and the suspended staggered rods one has to increase the Reynolds number to the point where the flow instability reaches the wall.

6.2.1 Centered Rods

For the centered rods the exponent of the Reynolds number in the mass transfer correlations compares well with previous work e.g. [ISA76, SHE79, CAR83]. In [LEI77] and [STO80] slightly lower values of respectively 0.63 and 0.61 are given but it has to be borne in mind that a single value for the exponent cannot be regarded as realistic for all dimensionless inter-rod distances $l_{rr}/(d_h)_e$. For large values of this the mass transfer will probably tend to the empty channel correlation (exponent = 1/3) with the effect of the rod being negligible. Discrepancies might also be explained by the fact that different Reynolds number intervals are used to fit the data. The work by Isaacson and Sonin [ISA76], Shen and Probstein [SHE79] and Carlsson et. al. [CAR83] indicates that there is a maximum value for the exponent at $l_{rr}/(d_h)_e$ around 2 which is not at variance with the results presented in Paragraph 6.1.1. The latter results

gave the highest values for the exponents for $l_{rr}/(d_h)_e$=2.61.

Despite the reservations with regard to the use of single value of the exponent for the whole range of $l_{rr}/(d_h)_e$ it appeared that the mass transfer data could be correlated to give the following:

$$Sh_e/Sc^{1/3} = 0.183(Re_e)^{0.730}((d_h)_e/l_{rr})^{0.403} \qquad (6.1)$$

for Re_e>400.

Figure 6.6 illustrates the quality of this correlation graphically.

In Figure 6.7 the present results are compared with some results from [ISA76] and it can be seen that although $l_{rr}/(d_h)_e$ is slightly different the present mass transfer results are significantly higher. A possible explanation might be the fact that the diameter to channel height ratio of the rods used in [ISA76] was smaller (d/h=0.44) than in the present case (d/h=0.54).

6.2.2 Attached Staggered Rods

The value of the Re_e-exponent compares well with the correlation determined by Focke [FOC83] for a staggered arrangement of semi-circular obstructions (Equation 2.34). In Figure 6.8 this correlation is compared with the

present data and it is seen that the latter are lower than the correlation for $l_{rr}/(d_h)_e$=1.74, 2.61 but agrees well for $l_{rr}/(d_h)_e$=0.87. Because in FOC83 mass transfer also occurred at the obstructions, the present data could be expected to be lower and only the last result is at variance. It must be added that Focke did not investigate $l_{rr}/(d_h)_e$ below 1.64 and hence extrapolation of his correlation is tentative. As the mass transfer results for the attached staggered rods gave similar values for the Re_e-exponent they were fitted to an equation similar to Equation 6.1. The resulting correlation is:

$$Sh_e/Sc^{1/3} = 0.371(Re_e)^{0.667}((d_h)_e/l_{rr})^{0.563} \qquad (6.2)$$

for Re_e>200

Figure 6.9 shows the quality of the correlations graphically and the agreement is good.

Finally, it has to be mentioned here that the mass transfer for the attached staggered rods does not compare well with mass transfer for alternating attached rectangular obstructions as investigated in [LEI77] and [KIM83] who gave a much lower Re_e-exponent (0.378, 0.376 respectively).

6.2.3 Suspended Staggered Rods

The mass transfer results indicate in general that decreasing the rod-wall distance leads to an increase in mass transfer. Increasing the inter-rod distance leads to lower overall mass transfer. These observations are in agreement with the expectations that 1) a rod close to the wall will be able to disrupt the mass transfer boundary layer to a larger extent than a rod further way and 2) a larger distance between the rods will allow the development of a thicker mass transfer boundary layer and hence lead to lower overall mass transfer.

There are a few exceptions to these general observations. First, for the geometries with rod to wall distance d_{rw}=3 mm the mass transfer follows the pattern described previously at low Re_e but at high Re_e overall mass transfer for l_{rr}=6 mm is lower than for l_{rr}=12 mm. This has to be attributed to the higher critical Re_e for l_{rr}=12 mm which causes mass transfer to increase only at a higher Re_e.

Secondly, mass transfer for l_{rr}=24 mm is nearly identical both for d_{rw}=1 mm and d_{rw}=2 mm.

The geometry d_{rw}=1 mm, l_{rr}=6 mm is the one which gives highest mass transfer but also exhibits some interesting features. Mass transfer starts to increase at Re_e around

200 presumably due to the flow becoming unsteady. For Re_e between 300 and 500 mass transfer remains approximately constant and above 500 it starts to rise again. The reasons for the occurrence of the plateau and subsequent rise in the curve are not known and were not expected from the flow visualisation experiments.

6.3 Geometry Comparison

Figure 6.10 shows the mass transfer data for the 7 mm rods. Although the mass transfer correlations of the attached staggered rods give a lower value for the Re_e exponent than the centered rods, for a given inter-rod distance (hence porosity) the mass transfer is higher.

Figure 6.11, 6.12 and 6.13 show the comparison of mass transfer data for centered rods and the suspended staggered rods for geometries of similar porosity (See Appendix C). It can be seen that for each centered rod geometry, a suspended staggered rod geometry can be found which has better mass transfer but as the porosity decreases the rods in the suspended staggered rods geometries have to be closer to the wall to achieve this. Also at higher porosities the mass transfer results appear to converge because for P=1 the geometry will be the empty channel as one would expect.

Another salient feature is the lower dependence of mass transfer on the inter-rod distance in case of the

suspended staggered rods e.g. for d_{rw}=3 mm the mass transfer results are similar for all l_{rr}.

6.4 Mass Transfer versus Power Consumption

Having established the pressure gradient in Chapter 4 and the mass transfer in this chapter a geometry evaluation can now be made by expressing $Sh_e/Sc^{1/3}$ as a function of the dimensionless energy dissipation $Po = (p^*)_e Re_e$ $(=(\Delta pV/l)(d_h)_e^4/(\rho\nu^3))$. These 'energetic' correlations give for each geometry the mass transfer at a given (dimensionless) power input. The resulting correlations are given in Tables 6.6 to 6.10. A lower boundary on the values of Po is determined by the point above which the Sh_e vs Re_e graph exhibits a change in the slope and an upper boundary by the range of the mass transfer measurements which in general was limited to Re_e<1250.

Table 6.6: Energetic correlation, centered rods

l_{rr} (mm)	$Sh_e/Sc^{1/3}=aPo^b$	Po-range
30	$0.16Po^{0.25}$	$9.0 10^7<Po<1.1 10^9$
60	$0.084Po^{0.28}$	$2.6 10^7<Po<5.8 10^8$
120	$0.11Po^{0.26}$	$5.5 10^6<Po<3.0 10^8$

Table 6.7: Energetic correlation, attached staggered rods

l_{rr} (mm)	$Sh_e/Sc^{1/3}=aPo^b$	Po-range
20	$0.40Po^{0.22}$	$6.3\cdot10^6<Po<1.9\cdot10^9$
40	$0.29Po^{0.23}$	$3.5\cdot10^6<Po<8.4\cdot10^8$
60	$0.21Po^{0.24}$	$4.9\cdot10^6<Po<5.3\cdot10^8$

Table 6.8: Energetic correlation, suspended staggered rods, d_{rw}=3 mm

l_{rr} (mm)	$Sh_e/Sc^{1/3}=aPo^b$	Po-range
6	$0.052Po^{0.28}$	$2.1\cdot10^8<Po<9.8\cdot10^8$
12	$0.10Po^{0.26}$	$6.0\cdot10^7<Po<6.3\cdot10^8$
24	$0.089Po^{0.27}$	$8.1\cdot10^6<Po<3.3\cdot10^8$

Table 6.9: Energetic correlation, suspended staggered rods, d_{rw}=2 mm

l_{rr} (mm)	$Sh_e/Sc^{1/3}=aPo^b$	Po-range
6	$0.016Po^{0.35}$	$1.3\cdot10^8<Po<1.4\cdot10^9$
12	$0.037Po^{0.32}$	$6.2\cdot10^7<Po<7.2\cdot10^8$
24	$0.056Po^{0.30}$	$2.9\cdot10^7<Po<3.5\cdot10^8$

Table 6.10: Energetic correlation, suspended staggered rods, d_{rw}=1 mm

l_{rr} (mm)	$Sh_e/Sc^{1/3}=aPo^b$	Po-range
6	$0.19Po^{0.25}$	$8.5\cdot10^7<Po<1.1\cdot10^9$
12	$0.026Po^{0.34}$	$3.1\cdot10^7<Po<6.4108$
24	$0.044Po^{0.31}$	$5.6\cdot10^6<Po<3.1\cdot10^8$

Figure 6.14 shows the correlations from Table 6.6 and 6.7 for the 7 mm rods (centered and attached staggered). It appears that for both geometries it is advantageous to

decrease the inter-rod distance as this leads to an increase in mass transfer for a given power consumption, although the increase for the centered rods is relatively small. The centered rods with a large inter-rod distance will be usable at a lower power consumption than the centered rods with a small inter-rod distance. This is less evident for the attached staggered rods. Figure 6.14 shows further that the attached, staggered rods invariably lead to higher mass transfer than the centered rods for a given power consumption. This is at variance with Leitz and Marincic [LEI77] who concluded that the centered rods were superior to an array of alternating rectangular strips. Further to this, some experimental evidence can be found in the literature which suggests that rectangular obstructions cause less violent unsteady flow as a result of which one might expect less mass transfer enhancement. As already mentioned in Paragraph 2.3 Shiina [SHI84] investigated square obstructions in a channel and found lower vortex shedding frequencies and less violent fluctuations in the flow when compared to circular obstructions. Gerrard, in his review of flow around blunt obstacles in unbounded flow [GER78], also mentioned that square obstructions resulted in lower vortex shedding frequencies than circular obstructions.

Figures 6.15, 6.16, 6.17 show the results for the suspended staggered rods for d_{rw}= 3, 2 and 1 mm, respectively (Tables 6.8, 6.9 and 6.10). In this case with

the exception of the geometry with l_{rr}=6 mm and d_{rw}=1 mm the geometries with the large interrod distance are the most advantageous in terms of mass transfer for a given power input. They are also usable at low power input.

The comparison between all geometries shows that the attached staggered rods are superior in promoting mass transfer for a given power input ($200<Re_e<1250$). Their mass transfer results are higher and they are usable over a wide range power inputs. A special case has to be made for the suspended staggered geometry with l_{rr}=6 mm and d_{rw}=1 mm as it appears to produce mass transfer similar to the attached staggered rods albeit only in the high range of the dimensionless power input. The suspended staggered rods with inter-rod distance l_{rr}=24 mm are able to produce mass transfer similar to the centered rods but for smaller l_{rr} (with the aforementioned exception) they are worse. Also, the suspended staggered rods have a higher Reynolds number exponent than the centered rods. If one assumes these exponents do not change it follows that for higher Reynolds number (outside the range considered) the suspended staggered rods will result in higher mass transfer promotion than the centered rods.

In Figure 6.18 the correlations for the 7 mm rods are compared with a separator correlation determined from SCH87 (Equations 2.23 and 2.24). The correlations given in SCH87 are based on 'filled channel' parameters (Re_f, Sh_f)

and need to be converted to 'empty channel' parameters (Re_e, Sh_e). This can be done readily if the porosity of the separator is known (Equation 2.25). Because in SCH87 the separator porosities were mostly around 0.9 this value was chosen for the calculations. From Figure 6.18 it appears that, if one neglects membrane shadowing, the idealised geometries are capable of doubling mass transfer at low power input but are less effective at high power input. However, it needs to be stated here that the comparison between idealised geometries and mesh type separators is not a realistic one. Therefore, possible inferences need to be taken with some caution.

7. LOCAL MASS TRANSFER MEASUREMENTS

7.1 Introduction

Local mass transfer measurements were carried out with the array of mini-electrodes on the large electrode and the dual-electrode arrangement (see paragraph 5.2). The results of the latter can be used to calculate shear rates as explained in Paragraph 5.1. Also the difference in mass transfer between the first and second electrode indicates the local flow direction. If the differential mass transfer is negative the local flow direction opposes the average flow direction and a recirculation zone is thus detected.

There were 20 mini-electrodes at 10 mm intervals starting 30 mm from the leading edge of the large electrode. To get a representative mass transfer profile over the 200 mm section the inter-rod distance l_{rr} of the geometries should not be large otherwise only a small number of rod pitches will be covered by the measurement. On the other hand a small value of l_{rr} results in only a few measurement points in between the rods. To illustrate this for the centered rods: if l_{rr}=120 mm only one complete rod pitch will be covered by the mini-electrodes, if l_{rr}=30 mm only 3 measurements will be taken over a single rod pitch. Hence l_{rr}=60 mm seems to be a suitable compromise.
On the basis of this, representative geometries were

selected for each class depicted in Figure 2.10. Suspended, staggered rods with d_{rw}=3 mm were left out as they resulted in low overall mass transfer (see Paragraph 6.1.3). The following five geometries were subjected to an investigation of the local mass transfer:

1) centered rods, l_{rr}=60 mm
2) attached staggered rods, l_{rr}=40 mm
3) suspended staggered rods, l_{rr}=24 mm, d_{rw}=2 mm
4) suspended staggered rods, l_{rr}=24 mm, d_{rw}=1 mm
5) suspended staggered rods, l_{rr}=6 mm, d_{rw}=1 mm,

where the last geometry was chosen because it produced an unexpectedly high mass transfer (see Paragraph 6.1.3) The position of the mini-electrodes, with respect to the rods for the five geometries investigated, is shown in Figure 7.1. The mass transfer length of 200 mm represented, for all geometries, at least two complete rod pitches.

As explained in Paragraph 5.3.3 only 16 mini-electrodes could be scanned in one experiment due to the limitations of the ADC. The 16 actually recorded could be selected from any of the 20 positions. A scanning frequency of 15 Hz was found to be sufficiently fast to follow the current variations occuring when the flow had become unsteady and 1000 readings were taken from each electrode.

7.2 Results and Discussion

The mass transfer measurements were expressed as $Sh_e/Sc^{1/3}$ and the position of the electrode was written dimensionless as $x/(d_h)_e$ where x is the axial distance measured from a certain reference point.

Mass transfer results for the empty channel determined from the mini-electrodes are shown in Figure 7.2 for several values of Re_e where x is the axial distance measured from the start from the electrode. As expected mass transfer decreases downstream from the leading edge. The empty channel experimental results were somewhat higher than the results expected for an infinitely wide channel.

Mini-electrode mass transfer results for the channel with the geometries in it gave no significant decrease in mass transfer along the length of the large electrode for Reynolds numbers in the range for which the correlations given in Chapter 6 were valid. This is illustrated in Figure 7.3 for the centered rods (l_{rr}=60 mm). This figure gives the measured mass transfer to the mini-electrodes on the cathode. The channel with the rods is shown underneath the graph. It has the correct vertical dimension with respect to the horizontal dimension. The vertical arrows indicate the cathode. The mass transfer results show a drop in mass transfer along the large electrode for

Re_e=179 but not for Re_e=926. The absence of an entrance effect at these Reynolds numbers means that mini-electrode mass transfer measurements taken over the length of the large electrode can be assumed to represent and to be translated into mass tranfer between two consecutive rods. Hence the mass transfer results will be presented in the next paragraphs as though they were measured between two consecutive rods or, to be more precise, between two rods on a line parallel to the channel axis. Mass transfer in between the rods will be shown in a graphical form in which the dimensionless axial distance $x/(d_h)_e$ is measured from the centre of the first rod. A cross section of the channel with the rods in it is drawn underneath (to scale) and the cathode is indicated by arrows. A curve is fitted to the results using a cubic spline procedure (GraphPAD; ISI-software).

The mass transfer results from the dual electrode arrangement will be depicted in a similar fashion. Two series of measurements are shown in each graph: results from the first electrode, i.e. the electrode upstream with regard to the average flow direction, and the differential of the first and second electrode. The latter will reveal the zones of reversed flow near the wall.

The standard deviation in the current signal from the first electrode in the dual electrode arrangement was also

determined. This should give an indication of the intensity of the flow fluctuations near the wall.

7.2.1 Centered Rods, l_{rr}=60 mm

Figure 7.4 gives the results for mass transfer in between the rods for eight values of Re_e between 440 and 1228. For all Re_e in this range the profiles exhibit two maxima, one absolute maximum underneath the rods and a local maximum at around $x/(d_h)_e$=1.15. In front of this local maximum there is an absolute minimum at around $x/(d_h)_e$=0.65 and behind it there is a local minimum at $x/(d_h)_e$=1.75. These results are similar to those obtained by Storck and Hutin [STO81] on an identical geometry.

Figure 7.5 gives the mass transfer results in between two rods obtained from the dual electrode arrangement. The results from the first electrode show a maximum underneath the rod and a nearly constant mass transfer in between the rods at the lowest Reynolds number. As the Reynolds number is increased a minimum develops at $x/(d_h)_e$=1.05 which moves slightly upstream at higher Reynolds ($x/(d_h)_e$=0.75). The differential mass transfer electrode shows a similar pattern at all Reynolds numbers, with a dip developing at roughly the same position where the upstream electrode has its minimum mass transfer. The differential mass transfer has a zero or negative minimum for the values of Re_e

between 564 and 1197 which indicates that on average there exists a backflow near the wall and near the position where the mass transfer to the first electrode is at its minimum.

The standard deviation in the mass transfer as depicted in Figure 7.6 is at its highest (typically 0.25) around the points where the differential mass transfer measurement changes sign and the flow separates and reattaches. Along most of the wall, however, the standard deviation does not exceed 0.1.

7.2.2 Attached Staggered Rods, l_{rr}=40 mm

Figure 7.7 shows the mass transfer profile in between the rods for six values of Re_e between 194 and 1277. For these values of Re_e an absolute maximum in mass transfer can be observed for $x/(d_h)_e$ around 1.50, i.e., at an axial position just in front of the midpoint between two rods on a line parallel to the channel axis. Mass transfer minima occur behind the rods for $x/(d_h)_e$ around 0.35 and in front of the rods for $x/(d_h)_e$ around 2.80. Local maxima occur just behind the rods and just in front of the rods. The mass transfer profiles are roughly in agreement with results obtained using segmented electrodes with an array of square [KIM83] and semicylindrical [FOC83] obstacles attached to the walls. These workers also found a maximum just in front of the obstacle on the opposite wall, a minimum behind and in front of the attached obstacle with

the latter followed by a rise in mass transfer towards the obstacle.

Mass transfer measurements obtained from the dual electrode arrangement are shown in Figure 7.8. The results from the first electrode show a maximum at $x/(d_h)_e$=1.7 which is slightly in front of the midpoint between two rods on a line parallel to the cell axis. A maximum is also observed underneath the rods. This means that flow has leaked underneath the rod. A close examination of the dual electrode arrangement revealed that it was slightly recessed into the channel wall and thus not completely flush with the surroundings. A local maximum was observed at $x/(d_h)_e$=0.9, i.e. halfway between two adjacent rods. The mass transfer difference between the first and the second electrode showed a maximum at $x/(d_h)_e$=1.8 which is slightly behind the midpoint between two rods on a line parallel to the cell axis. The mass transfer difference gave negative values for a region behind the rods on the bottom wall ($x/(d_h)_e$<1.25) and in front of them ($x/(d_h)_e$>2.8). The zero crossings coincide with local minima for the single electrode measurements. The occurence of negative values indicating the presence of a recirculating zone, agrees with the visual observations in Paragraph 3.3.2. Very close behind a rod and also in front of the rod, the differential mass transfer measurements give positive results, especially noticeable at the higher Reynolds numbers. Possibly, the effect of the leakage flow

underneath the rods causes the recirculation zone behind the rods to be reduced in length.

Figure 7.9 depicts the standard deviation in mass transfer to the first electrode. Peaks occur at the points where the value of the differential measurement was close to zero i.e. near points of separation and reattachment the fluctuations are largest. Over most of the wall region between the rods the standard deviation was less than 0.1.

7.2.3 Suspended Staggered Rods, l_{rr}=24 mm, d_{rw}=2 mm

Figure 7.10 shows the mass transfer profile between the rods for six values of Re_e between 515 and 1204. Two mass transfer peaks of similar height could be observed, one slightly upstream of the rods and one around $x/(d_h)_e$=0.8 i.e. in front of the midpoint between two rods on a line parallel to the channel axis. Also two minima are observed, roughly symmetrical around the rods, at $x/(d_h)_e$=0.2 and $x/(d_h)_e$=1.8. Similar mass transfer patterns have been reported in [WAT68] for transitional and turbulent flow and in [MIY83] for turbulent flow using a non-staggered arrangement of suspended rods. Heat transfer computations reported in [KAR88] on a similar arrangement gave a peak directly underneath the rod, a sharp drop to a minimum directly behind the promoter and a slow rise until the next rod. A second maximum was not present.

The results from the mass transfer measurements from the dual electrode arrangement are shown in Figure 7.11. For the first electrode a distinct peak can be observed underneath the rods followed by a drop to a minimum around $x/(d_h)_e$=0.35. After this, mass transfer increases to reach a fairly flat maximum at $x/(d_h)_e$=1.1, corresponding to the midway point between two rods on a line parallel to the channel axis. A second minimum can be observed at $x/(d_h)_e$=1.7. The differential mass transfer shows a similar pattern albeit that the position of the extrema appears to be slightly shifted downstream compared to the results from the single electrode. No negative values were recorded which suggests that on average there is no backflow near the wall region.

The standard deviation in the mass transfer to the first electrode is shown in Figure 7.12. Peaks occur at the positions where mass transfer to the electrode has its minimum. For nearly all positions, however, the standard deviation never exceeds 0.1.

7.2.4 Suspended Staggered Rods, l_{rr}=24 mm, d_{rw}=1 mm

Figure 7.13 shows the mass transfer results for 7 values of Re_e between 523 and 1177. The pattern is similar for the suspended staggered rods with a 2 mm gap. Two maxima can be noticed, one absolute directly underneath the rods and one local around $x/(d_h)_e$=0.9 i.e slightly in front of

the midway point between two rods on a line parallel to the channel axis. Two minima can be seen, behind $(x/(d_h)_e=0.25)$ and in front $(x/(d_h)_e=1.75)$ of the rods.

The mass transfer results from the dual electrode arrangement shown in Figure 7.14 are also quite similar to the suspended staggered rods having a 2 mm gap. There is one absolute maximum just underneath the rods and a local maximum around the midpoint between two rods on a line parallel to the cell axis $(x/(d_h)_e=1.15)$. For unstable flow minima are found at $x/(d_h)_e=0.4$ (absolute) and $x/(d_h)_e=1.85$ (local). The differential mass transfer results are similar to the single electrode mass transfer results but are shifted downstream. Also the minimum in front of the rod is now the absolute minimum and the minimum behind the rod is a local minimum. For stable flow the differential mass transfer measurements give negative values for $x/(d_h)_e$ between 0.2 and 0.75., behind the rods, and for a small region when $x/(d_h)_e$ is around 1.9, in front of the rods. These regions indicate two recirculation zones of which only the first one was observed in the flow visualisation experiments. Negative values for the differential mass transfer measurements were not observed during unstable flow, although the value of the minimum in front of the rod was very small.

Figure 7.15 shows the mass transfer standard deviation to the first electrode in the dual-electrode arrangement. It

is highest just in front of the minima in the mass transfer to the first electrode (See also Figure 7.14). This maximum appears to increase with increasing Reynolds number. For most of the zone between the rods the standard deviation is less than 0.1.

7.2.5 Suspended Staggered Rods, l_{rr}=6 mm, d_{rw}=1 mm

Mini-electrode mass transfer measurements taken along the length of the electrode were converted to points in between two rods and are shown in Figure 7.16 for Re_e= 131, 487, 885 and 1198 respectively. Measurements taken closer to the downstream end of the large electrode did not appear to be lower than measurements taken at the upstream end. Hence a distinct entrance effect was not present. The mass transfer between the rods exhibited a maximum underneath the rods and a minimum in between them, at $x/(d_h)_e$ around 0.2 for the high Reynolds numbers and at $x/(d_h)_e$ around 0.1 for Re_e=131. As the Reynolds number increases the minimum changes from a fairly flat minimum at the lowest Reynolds number to a pronounced minimum at the highest Reynolds number.

7.3 Mass Transfer Fluctuations

Beside the intensity of the fluctuations in the flow, the frequency of the fluctuations might also be of importance in the mass transfer mechanism. Knowledge about the

typical time constants also gives information about the frequency response of the electrodes. Mass transfer fluctuations have been obtained from one mini-electrode, in each run, selected for its large standard deviation. The scanning rate was 15 Hz and the length was approximately 30 seconds. Table 7.1 gives the position of the electrode for each geometry.

Table 7.1: Position of the mini-electrode for each geometry

geometry	position behind rod centre (mm)	figure
centered l_{rr}=60 mm	15	7.17
attached staggered l_{rr}=40 mm	14	7.18
suspended staggered d_{rw}=2 mm, l_{rr}=24 mm	31.5	7.19
suspended staggered d_{rw}=1 mm, l_{rr}=24 mm	8	7.20

The comparison of the results for the 7 mm rods (centered and attached) reveals that for similar Reynolds numbers the mass transfer fluctuations effected by the attached staggered rods are of a higher frequency than the centered rod mass transfer fluctuations. For the 3 mm rods no major difference are noticed in the frequency of the fluctuations. For the lower Reynolds numbers the fluctuations are more obvious for d_{rw}=1 mm. This might have been due to the fact that the steady flow has an eddy located at the wall. Any oscillation is immediately

noticeable in the mass transfer fluctuation. However, the position of the mini-electrode relative to the rods might also have influenced this. Comparing the mass transfer fluctuations of all geometries it appears that the centered rods give rise to the slowest fluctuations, with the suspended staggered rods being somewhat faster and the attached staggered rods giving rise to the most frequent fluctuations.

7.4 Determination of Wall Shear Rate Pattern

The mass transfer to the dual electrode arrangement can be used to calculate shear rates at the wall as described in Paragraph 5.2 and Appendix A, provided several conditions are met.

Firstly, streamwise diffusion must be neglible and therefore the dimensionless quantity Sl^2/D (see Equation 5.2) has to be larger than 2000. This condition was met, except near separation and reattachment points where Equation 5.2 is not valid anyway. This meant that for stable flow the shear rate can be directly calculated from Equation 5.2 using either the mass transfer coefficient of the first electrode or the mass transfer coefficient of the second electrode. The latter option is chosen in a recirculation zone as the local flow direction opposes the average flow direction in this region. Near reattachment and separation points no shear rate values are calculated.

The shear rate is made dimensionless in the following fashion:

$$S^* = 2S(d_h)_e)^2/\nu \qquad (7.1)$$

This way of representation ensures that for the empty channel the dimensionless shear rate and the dimensionless pressure gradient are exactly equal.

For unstable flow the frequency response of the electrodes needs to be taken into account. In Appendix A the condition for an instaneous response to a shear rate variation is stated as:

$$f(0.807)^2 \cdot (kl/D)^{-2} \cdot l^2/D < 0.1 \qquad (7.2)$$

where f is the typical frequency of the fluctuation
From the single electrode mass transfer results a typical value for $Sh_e/Sc^{1/3}$ is 50, for Sc equal to 1700. This gives a value for kl/D of 26. Assuming $D=6 \cdot 10^{-10}$ m^2/s this results in f<0.06. In other words the electrode reacts instantaneously to variations having typical time constants larger than 16 seconds. The mass transfer fluctuations presented in Paragraph 7.4 indicate that the typical time constants associated with these can be much smaller, down to around 1 second. Therefore the frequency response to the shear rate fluctuations can be expected to be incomplete. As the electrodes are unable to follow the

fast shear rate fluctuations, it raises questions about the inability of the differential mass transfer measurements to detect a reversed flow region for the suspended staggered rods, d_{rw}=1 mm at high Reynolds numbers. A distinct negative differential mass transfer result was obtained for stable flow whereas this was absent in unstable flow (Figure 7.14). Calculating the shear rate from Equation 5.2 surely leads to a rather low estimate for the shear rate. The true standard deviation in the mass transfer cannot be detected but Equation 5.2 is the best estimate possible given the constraints imposed by the typical flow time constants.

Subparagraphs 7.4.1 to 7.4.4 present the shear rates for four geometries at several Reynolds numbers. The shear rate results are similar in that a maximum is always observed underneath a rod due to the local acceleration of the flow, followed by a drop to a minimum directly behind the rod due to the flow deceleration. They also broadly confirm the presence of recirculation zones for the attached staggered rods and the suspended staggered rods, d_{rw}=1 mm. An estimate of the accuracy of the shear rate calculation can be found in Appendix D.

7.4.1. Centered Rods; l_{rr}=60 mm

The calculated dimensionless shear rates are depicted in Figure 7.21. For all Reynolds numbers a maximum can be

observed underneath the rods. Coinciding with the onset of the unsteadiness in the flow a dip in the pattern develops around $x/(d_h)_e$=1. This dip deepens, leading to negative values of the shear rate, and moves forward for increasing Reynolds number. The negative values of the shear rate indicate, in the mean, a backflow on the wall. There is an excellent agreement between the patterns shown in Figure 7.21 and the numerical flow computations performed in KIE86 for a single cylinder in channel flow.

7.4.2. Attached Staggered Rods; l_{rr}=40 mm

The calculated dimensionless shear rates are shown in Figure 7.22. Recirculation zones, indicated by negative shear rate values, are present behind and in front of the rods. A sharply peaked maximum occurs underneath the rods due to a leakage flow which becomes more important as the Reynolds number is increased.

7.4.3. Staggered Suspended Rods; l_{rr}=24 mm, d_{rw}=2 mm

The calculated shear rates are shown in Figure 7.23. An absolute maximum is present underneath the rods and a local maximum around the midpoint between two rods on a line parallel to the channel axis. A minimum in the shear rate pattern is present behind the rods, similar to the shear rate pattern for the centered rods. Contrary to the

latter pattern, no negative shear rates were obtained and no backflow was noticed.

7.4.4. Staggered Suspended Rods; l_{rr}=24 mm, d_{rw}=1 mm

The calculated shear rates are depicted in Figure 7.24. A pronounced absolute maximum is present underneath the rods and a local maximum slightly downstream from the midpoint between two rods on a line parallel to the channel axis. For stable flow negative values of the shear rate indicate a recirculation zone behind the rods. When the flow has become unstable the shear rate in this zone becomes positive. The minima in the shear rate, however, tend to zero for the largest Reynolds numbers shown.

8. MASS TRANSFER MECHANISMS

8.1 Introduction

The mass transfer measurements in this study covered the range from steady laminar flow to unsteady flow. For laminar flow in the empty channel a mass transfer boundary layer is allowed to develop from the start and continues to grow without interruption and hence mass transfer decreases downstream. For turbulent flow mass transfer will be constant along the channel wall as a mass transfer boundary layer is frequently interrupted by turbulent eddies reaching the wall. In the case of laminar steady flow mass transfer decreases over several rod pitches for the centered and suspended rods similar to the empty channel. This is not the case with the attached staggered rods, which presumably destroyed the mass transfer boundary layer. When the flow has become unsteady mass transfer does not decrease downstream for all of the geometries investigated above a certain Reynolds number. This Reynolds number seemed to coincide with the Reynolds number where the overall mass transfer correlation showed an increase. Mass transfer in obstructed channel flow therefore clearly possesses characteristics both of laminar and of turbulent empty channel mass transfer.

The crucial element in any mechanistic model for mass transfer in obstructed channel flow is the ability of the

obstacle to produce flow patterns which result in a disruption of the mass transfer boundary layer. Winograd et. al. [WIN73] have proposed a model describing the process of boundary layer destruction and redevelopment (see Chapter 2). The model is akin to channel entrance transfer phenomena as it describes the simultaneous development of a hydrodynamic and mass transfer boundary layer. Here it is suggested that the development of the mass transfer boundary layer is entirely determined by the shear rate. For this case an expression for local mass transfer can be derived as shown in Appendix A and Paragraph 2.4.

$$Sh_x/Sc^{1/3} = 0.641\left|d\left(\left({}_0\int^{x^*}(S^*)^{\frac{1}{2}}dx'\right)^{2/3}\right)/dx^*\right| \qquad (8.1)$$

where $Sh_x = k_x(d_h)_e/D$

$x^* = x/(d_h)_e$

$S^* = 2S((d_h)_e)^2/\nu$

The rest of this chapter is devoted to the comparison of mass transfer calculated from Equation 8.1 using the shear rates presented in Paragraph 7.4 with the mass transfer as measured by the mini-electrodes.

8.2 Centered Rods; l_{rr}=60 mm

Figure 8.1 shows that excellent agreement between calculation and measurement is obtained for laminar steady flow along the whole length of the electrode. Figure 8.2

shows the mass transfer pattern in between the rods for unsteady flow. For the calculations the start of the mass transfer was chosen as the point where the dual electrode detected back flow. It appears that with increasing Reynolds number the calculated mass transfer becomes significantly less than the measured mass transfer.

8.3 Attached Staggered Rods; l_{rr}= 40 mm

As there are recirculation zones even at the lowest Reynolds number the application of Equation 8.1 over the whole length of the electrode was not performed as the equation was not valid near reattachment and separation points. Instead mass transfer was determined from Equation 8.1 with the starting point of the integration at a reattachment point. This idea was also explored by Nishimura et. al. [NIS85] in a study on mass transfer in flow through wavy walled channels. The results given in Figure 8.3 indicate an excellent agreement for steady laminar flow but calculated mass transfer is significantly lower than measured mass transfer for unsteady flow.

8.4 Suspended Staggered Rods; l_{rr}=24 mm, d_{rw}=2 mm

Figure 8.4 gives the calculated and measured mass transfer over the whole length of the large electrode for steady flow. Although the general trend is reproduced by the calculations the agreement between calculations and

measurents is less than in the case of the centered rods (Figure 8.1). The shear rate patterns showed a dip behind the rods but no separation was detected by the differential mass transfer measurements. Nevertheless, assuming that the mass transfer boundary layer was completely disrupted, Equation 8.1 was used to calculate mass transfer with the minimum in the shear rate as starting point. The results of these calculations are shown in Figure 8.5. The general pattern appears to agree with the measured mass transfer but measured mass transfer is higher for high Reynolds number.

8.5 Suspended Staggered Rods; l_{rr}=24 mm, d_{rw}=1 mm

For steady flow a recirculation zone was detected behind the rod closest to the wall by the flow observations and by the electrochemical mass transfer measurements. This recirculation zone did not result in a complete disruption of the boundary layer as the mass transfer along the large electrode showed a decreasing trend. Figure 8.6 shows the comparison between measured and calculated mass transfer along the length of the large electrode for steady flow. The starting point of the calculation was chosen as the point where the flow reattaches and the calculation was performed to either side as for the attached staggered rods. The comparison shows that calculated mass transfer is higher than the measured mass transfer but the pattern of the mass transfer in between two rods is reproduced.

For unsteady flow no flow separation on the wall was detected and again the minimum of the shear rate was chosen as the starting point of the integration. Hence it was assumed that at this point the mass transfer boundary layer was completely disrupted. The comparison between calculations and measurements is shown in Figure 8.7. The calculations are able to reproduce the general pattern of the mass transfer but at high Reynolds number measured mass transfer is higher than calculated mass transfer.

8.6 Discussion

The comparison between the mass transfer calculations based on the shear rate pattern and the mass transfer measurements were in quantitative agreement for steady flow. For unsteady flow there was only a qualitative agreement. As the Reynolds number was increased the measured mass transfer appeared to be systematically higher than the calculated mass transfer. Two possible explanations are offered here.

Firstly, as shown in Paragraph 7.4, the determination of the shear rate is not accurate as the electrodes in the dual electrode arrangement are not completely responsive to the high frequency variation occurring in the flow channel and hence to the mass transfer towards the electrodes. This means that the standard deviation in the measured mass transfer (typically 0.1 times the average

except in zones of flow separation and/or reattachment) is lower than in reality. The difference between the real and measured standard deviation increases as the Reynolds number increases because the fluctuations have a lower time constant and hence a higher frequency. As illustrated in Appendix A this means that shear rate calculations based on average mass transfer measurements have underestimated the true average shear rate. Using low estimates of the shear rates for the calculation of mass transfer leads to low estimates for mass transfer.

Secondly, the mass transfer model used assumes singular points or small zones where the mass transfer boundary layer is completely disrupted and from which it is allowed to develop until the next singular point or zone. The distance between these points is the distance between a reattachment point and a separation point. For the centered rods and suspended, staggered rods this is equal to the distance between two rods on a line parallel to the channel axis. The flow visualisation experiments have revealed that the unsteady flow can be regarded as succession of vortices as shown in Plates 3.2 and 3.2 for the centered rods. Depending on the strength of these vortices they may be able to cause intermittent disruption along the full length of the channel wall. In that case the length over which a boundary layer is allowed to develop is the distance between two vortices. This distance depends on the velocity with which the vortices

travel downstream and the frequency with which the vortices are generated. In between the vortices the boundary layer is probably still determined by the average shear rate. As the Reynolds number is increased the frequency with which these vortices are generated increases and hence the distance between the vortices decreases. This could explain the deviation between mass transfer calculations and measurements at high Reynolds number when using the simple model. A model based on this 'surface renewal' phenomenon has been useful in predicting mass transfer for turbulent channel flow [PIN74] and could probably also be successfully implemented in the unsteady flows encountered in this work.

9. CONCLUSIONS

The general objective of the study was to improve the understanding of the transfer phenomena occurring in obstructed thin channels. The combination of a literature survey, flow visualisation, pressure gradient measurement and mass transfer measurement has resulted in the following main conclusions which are strictly speaking only valid for the geometries investigated i.e. cylindrical rods placed in a regular fashion perpendicular to the flow in a rectangular channel (see Figure 2.10) and for $100<Re_e<1250$:

1) Flow observations:

Flow in an obstructed channel becomes unsteady at a Reynolds number one order of magnitude lower than in an unobstructed channel. The critical Reynolds number seems little influenced by the distances between the rods, the diameter of the rod and the position relative to the wall. Unsteadiness first becomes visible as slight oscillations on the steady flow pattern. As the Reynolds number is increased these oscillations increase in magnitude and at high Reynolds number vortices can be seen to be convected downstream.

2) Pressure loss:

For most geometries the pressure gradient varied inversely to the inter-rod distance l_{rr} i.e. the

pressure drop over a certain channel section varied proportionally to the number of rods present in that channel section. A smaller rod diameter gave rise to a smaller pressure drop. The position of the rod relative to the wall had comparitively little effect on the pressure drop. The dependence of the pressure gradient on Reynolds number could be expressed by a single correlation over the range of Reynolds numbers investigated and the onset of the unsteadiness in the flow did not lead to a departure of the trend in the pressure gradient. The shape of the pressure gradient correlations suggested that the inertial forces played a major role in the pressure drop. In contrast, for an empty channel the pressure drop is entirely determined by the viscous forces.

3) Overall mass transfer:

The overall mass transfer correlation showed an increase above a certain Reynolds number. This was attributable to the onset of unsteadiness in the flow. The attached staggered rods had the lowest Reynolds number for which mass transfer started to rise, probably because the vortex was attached to the wall and hence unsteadiness in the vortex had an immediate effect on the mass transfer. In the unsteady flow range the Sherwood number varies according to $(Re_e)^a$ where a=0.65 to 0.92 which is much higher than for the empty channel and approaches the exponent for turbulent flow.

The position of the rod relative to the wall is, in contrast to the pressure drop, of importance: a geometry with rods on or close to the wall results in higher mass transfer. The overall comparison of mass transfer results in the selection of the attached staggered rods as the geometry which gives highest mass transfer for a given pumping energy input. The centered rods give marginally higher mass transfer than the suspended staggered rods for a given energy input. For Reynolds numbers above the range considered the tendency indicates that this order will be reversed. A special case is taken by the suspended staggered rods with l_{rr}=6 mm and d_{rw}=1 mm which appears to give mass transfer similar to the attached staggered rods for a given pumping energy input.

4) Local mass transfer:

For the suspended staggered rods and the centered rods mass transfer is generally highest underneath the rod. Mass transfer decreases downstream for steady flow as the mass transfer boundary layer is allowed to build up for these geometries. When the flow is sufficiently unsteady the development of the boundary layer is interrupted in the zone behind the rod from where the oscillations start. This gives rise to a second maximum in mass transfer behind the rod. For the attached staggered rods a maximum in mass transfer is observed near the point where the flow reattaches with a

decrease in mass transfer to either side of the maximum. The attached staggered rods do not exhibit a decrease in mass transfer along the channel wall for steady flow. Clearly the physical presence of the rod on the wall interrupts the development of the boundary layer.

The intensity of the fluctuations in the flow always appears to be largest near separation/reattachment points.

Finally, it is observed that mass transfer varies considerably over one rod pitch with the ratio between maximum and minimum mass transfer varying between 5 and 10.

5) Mass transfer mechanism:

Mass transfer in steady flow appears to be entirely dictated by the wall shear rate pattern (Equation 8.1) for the suspended staggered and centered rods in the absence of recirculation zones. But also for the attached staggered rods it has been shown that the mass transfer pattern can be retrieved using Equation 8.1 if one assumes the boundary layer to start developing from the reattachment point. From the calculations described in Chapter 8 it could not be determined whether the average shear rate pattern also dictated the mass transfer in unsteady flow. A qualitative agreement between mass transfer measurement and calculation was achieved, though.

6) Relevance to membrane operations:

All the experiments described in this account were executed using a channel whose thickness was ten times that of a channel in a typical membrane module. It is assumed that, for a given Reynolds number, the observed phenomena will be present in the thinner channel as well.

Several effects might prevent the results from being directly applicable to membrane operations:

- Natural convection might be considerable in some membrane operations and, indeed, might have been present in the experiments described here. Nevertheless, the mass transfer experiments showed no proof of this.

- In RO and UF there is a flow through the wall which might interfere with the characteristics of the flow. For RO it is a small flow and the interference is probably small. For UF in the empty channel it has been shown in BEL85 that the flow across the channel wall leads to an increase in the transition Reynolds number.

- Liquids encountered in membrane operations are often macro-molecular solutions or colloidal suspensions and are therefore not always newtonian. Rheological aspects have not been taken into account in this work.

Finally, the experimental results have shown that several of the geometries used in this study can improve upon the mass tranfer achieved with conventional separators in membrane modules.

REFERENCES

ACR60 Acrivos, A.:'Solution of the laminar boundary layer energy equation at high Prandtl number', THE PHYSICS OF FLUIDS 3(1960)657-658

AGG79 Aggarwal, J.K., Talbot, L.:'Electro-chemical measurements of mass transfer in semi-cylindrical hollows', INT. J. HEAT & MASS TRANSFER 22(1979)61-75

AMB86 Ambari, A., Deslouis, C., Tribollet, B.:'Frequency response of the mass transfer rate in a modulated flow at electrochemical probes', INT. J. HEAT & MASS TRANSFER 29(1986)35-45

ARM83 Armaly, B.F., Durst. F., Pereira, J.C.F., Schönung, B.: 'Experimental and theoretical investigation of backward-facing step flow', JOURNAL OF FLUID MECHANICS 127(1983)473-496

BAZ65 Bazán, J.C., Arvia, A.J.:'The diffusion of ferro- and ferricyanide in aqueous solutions of sodium-hydroxide', ELECTROCHIMICA ACTA 10(1965)1025-1032

BEL72 Belfort, G., Guter, G.A.:'An experimental study of electrodialysis hydrodynamics', DESALINATION 10(1972)221-262

BEL85 Belfort, G., Nagata, N.:'Fluid mechanics and cross flow filtration: some thoughts', DESALINATION 53(1985)57-79

BER77 Berger, F.P., Hau, K.-F., F.-L.:'Mass transfer in turbulent pipe flow measured by the electrochemical method', INT. J. HEAT & MASS TRANSFER 20(1977)1185-1194

BER83 Berger, F.P, Ziai, A.:'Optimisation of experimental conditions for electrochemical mass transfer measurements', CHEM. ENG. RES. DES. 61(1983)377-382

BRI07 Brillouin, M.:'Leçons sur la viscosité des liquides et des gaz', Gauthier-Villars, Paris, 1907

CAR83 Carlsson, L. et. al.:'Design and performance of a modular,multipurpose electrochemical reactor', J. ELECTROCHEM. SOC. 130(1983)342-346

CHA86 Chang, H.N., Park, J.K.:'Effect of turbulence promoters on mass transfer', Chapter 1 in Handbook of heat and mass transfer (Volume 2), Gulf Publishing Co., 1986

CHO83 Chouikhi, S.M., Patrick, M.A., Wragg, A.A.:'Two phase turbulent wall transfer processes downstream of abrupt enlargements of pipe diameter', pp 53-66 in PHYSICAL MODELLING OF MULTIPHASE FLOW, BHRA Fluid Engineering, 1983

ERG49 Ergun, S., Orning, A.A.:'Flow through randomly packed columns and fluidised beds', IND. & ENG. CHEM. 41(1949)1179-1184

ERG52 Ergun, S.:'Fluid flow through packed columns', CHEMICAL ENGINEERING PROGRESS 48(1952)89-94

FOC83 Focke, W.W.:'On the mechanism of transfer enhancement of eddy promoters', ELECTROCHIMICA ACTA 28(1983)1137-1146

FOC85 Focke, W.W.:'The effect of the corrugation inclination angle on the thermo-hydraulic performance of plate heat exchangers', INT. J. HEAT & MASS TRANSFER 28(1985)1469-1479

FOC86 Focke, W.W., Knibbe, P.G.:'Flow visualisation in parallel-plate ducts with corrugated walls', JOURNAL OF FLUID MECHANICS 165(1986)73-77

FOR71 Fortuna, G., Hanratty, T.J.:'Frequency response of the boundary layer on wall transfer probes', INT. J. HEAT & MASS TRANSFER, 14(1971)1499-1507

GER78 Gerrard, J.H.:'The wakes of cylindrical bluff bodies at low Reynolds numbers', PHIL. TRANS. ROYAL SOC. LONDON 288(1978)351-382

GOR66 Gordon, S.L., Newman, J.S, Tobias, C.W.:'The role of ionic migration in electrolytic mass transport; diffusivities of $(Fe(CN)_6)^{3-}$ and $(Fe(CN)_6)^{4-}$ in KOH and NaOH solutions', BERICHTEN DER BUNSENGESELLSCHAFT 70(1966)414-420

HAN83 Hanratty, T.J., Campbell, J.A.:'Measurements of wall shear stress', pp 559-615 in FLUID MECHANICS MEASUREMENTS, Hemisphere Publishing Corporation, 1983

HEG83 Heggs, P.J.:'Experimental techniques and correlations for heat exchanger surfaces: packed beds', pp 341-368 in LOW REYNOLDS NUMBER FLOW HEAT EXCHANGERS, Hemisphere Publishing Co., 1983

HIC68 Hicks, R.E, Mandersloot, W.G.B.:'The effect of viscous forces on heat and mass transfer in systems with turbulence promoters and in packed beds', CHEMICAL ENGINEERING SCIENCE 23(1968)1201-1210

ICH77 Ichiki, T., Asawa, T.:'An experimental study of turbulence promoters in electrodialysis', Reports Res. Lab. Asahi Glass Co. Ltd. 27/2(1977)115-121

ISA76 Isaacson, M.S., Sonin, A.A.:'Sherwood number and friction factor correlations for electrodialysis systems, with application to process optimisation', IND. & ENG. CHEM.: PROC. DES. & DEV. 15(1976)313-321

JEN77 Jenkins, J.D., Gay, B.:'Experience in the use of the ferri-ferrocyanide redox couple for the determination of the transfer coefficient in models of shell- and tube heat exchangers' Session IIIa in proceedings of EUROMECH90, Nancy, 4-8 July 1977

KAN82 Kang, I.S., Chang, H.N.:'The effect of turbulence promoters on mass transfer - numerical analysis and flow visualisation', INT. J. HEAT & MASS TRANSFER 25(1982)1167-1181

KAO70 Kao, T.W., Park, C.:'Experimental investigations on the stability of channel flows. Part I: Flow of a single liquid in a rectangular channel', J. FLUID MECH. 43(1970)145-164

KAR88 Karniadakis, G.E., Mikić, B.B., Patera, A.T.:'Minimum dissipation tranport enhancement by flow destabilisation: Reynolds' analogy revisited', J. FLUID MECH. 192(1988)365-391

KES60 Kestin, J., Persen, L.N.:'The transfer of heat across a turbulent boundary layer at very high Prandtl numbers', INT. J. HEAT & MASS TRANSFER 5(1962)355-371

KIE86 Kiehm, P., Mitra, N.K., Fiebig, M.:'Navier-Stokes computation of two-dimensional laminar wakes of a circular cylinder' pp. 132-147 in 'Finite approximations in fluid mechanics', E.H. Hirschel(ed.), Vieweg, 1986

KIM83 Kim, D.H., Kim, I.H., Chang, H.N.:'Experimental study of mass transfer around a turbulence promoter by the limiting current method', INT. J. HEAT & MASS TRANSFER 26(1983)1007-1016

KLY68 Klyachko, V.A., Ushakov, L.D.:'Hydraulic principles for the design of electrodialysis desalination plants', DESALINATION 2(1967)279-282

KUR83 Kuroda, O., Takahashi, S., Nomura, M.:'Characteristics of flow and mass transfer in an electrodialysis compartment including spacer', DESALINATION 46(1983)225-232

LEB70 Lebouché, M.:'Transfer de matière en régime de couche limite bidimensionelle et à nombre Schmidt grand', C.R. ACAD. SC. PARIS SERIE A 270(1970)1757-1760

LEB73 Lebouché, M.:'Sur la mesure polarographique du gradient pariétal de vitesse dans les zones d'arrêt amont ou de décollement du cylindre', C.R. ACAD. SC. PARIS, SERIE A 276(1973)1245-1248

LEB75 Lebouché, M., Martin, M.:'Convection forcée autour du cylindre: sensibilité aux pulsations de l'écoulement externe', INT, J. HEAT & MASS TRANSFER 18(1975)1161-1175

LEI77 Leitz, F.B., Marinčić, L.:'Enhanced mass transfer in electrochemical cells using turbulence promoters', J. APPLIED ELECTROCHEMISTRY 7(1977)473-484

LET86 Letord-Quéméré, M.M., Legrand, J., Coeuret, F.:'Improvement of mass transfer in electrochemical cells by means of expanded materials', pp. 71-81 in 'Electrochemical Engineering', I. Chem. Eng. Symp. Ser. no.98, 1986

LEV28 Lévêque, M.A.:'Les lois de la transmission de chaleur par conversion', pp 305-342, 381-415 in ANNALES DES MINES, series 12, Nr. 13, 1928

LEV62 Levich, V.G.:'Physicochemical hydrodynamics', Prentice-Hall Inc., 1962

LIG50 Lighthill, M.J.:'Contributions to the theory of heat transfer through a laminar boundary layer', PROCEEDINGS OF THE ROYAL SOCIETY OF LONDON 202A(1950)359-377

LIG81 Light, W.G., Tran, T.V.:'Improvement of thin-channel design for pressure-driven membrane systems', IND. & ENG. CHEM.: PROC. DES. & DEV. 20(1981)33-40

LIN63 Ling, S.C.:'Heat transfer from a small isothermal spanwise strip on an insulated boundary', J. HEAT TRANSFER 85(1963)230-236

MAT75 Matida, Y., Kuwahara, K., Takama, H.:'Numerical study of steady two-dimensional flow past a square cylinder in a channel', J. PHYS. SOC. JAPAN 38(1975)1522-1529

MEL72 Melbourne, J.D.,:'Polarisation in electrodialysis', Ph.D thesis, University of Cambridge, 1972

MER74 Merzkirch, W.:'Flow visualisation', Academic Press, 1974

MIT66 Mitchell, J.E., Hanratty, T.J.:'A study of turbulence at a wall using an electrochemical wall shear stress meter', J. FLUID MECHANICS 26(1966)199-221

MIY81 Miyashita, H., Shiomi, Y., Wakabayashi, K.:'Augmentative mechanism of mass transfer using a turbulence promoter in rectangular duct', KAGAKU KOGAKU RONBUNSHU 7(1981)349-354

MIY82 Miyoshi, H., Fukumoto, T., Kataoka, T.:'A consideration on flow distribution in an ion exchange compartment with spacer', DESALINATION 42(1982)47-55

MIY83 Miyashita, H., Shiomi, Y.:'Transport phenomena among turbulence promoter at/on wall surface in rectangular duct', Proceedings of PACHAEC'83 2(1983)1-6

MIY88 Miyoshi, H., Fukumoto, T., Kataoka, T.:'A method for estimating the limiting current density in electrodialysis', SEPARATION SCIENCE AND TECHNOLOGY 23(1988)585-600

MIZ71 Mizushina, T.:'The electrochemical method in transport phenomena', ADVANCES IN HEAT TRANSFER 7(1971)87-161

NIS85 Nishimura, T., Ohori, Y., Kajimote, Y., Kawamura, Y.:'Mass transfer characteristics in a channel with symmetric wavy wall for steady flow', J. CHEM. ENG. JAPAN 18(1985)550-555

NIX89 Nixon, J., School of Industrial and Manufacturing Science , Cranfield Institute of Technology: personal communication, 1989

OYA83 Oyakawa, K., Mabuchi, I.:'Heat transfer in parallel duct with circular cylinders inserted in staggered arrangement', BULLETIN OF JSME 26(1983)545-553

PY69 Py, B., Gosse, J.:'Sur la réalisation d'une sonde polarographique pariétale sensible à la vitesse et la direction de l'écoulement', C.R. ACAD. SC. PARIS SERIE A 269(1969)401-404

PY73 Py. B.:'Etude tridimensionelle de la sous-couche visqueuse dans une veine rectangulaire par des mesure de transfert de matière en paroi', INT. J. HEAT & MASS TRANSFER 16(1973)129-144

PIN74 Pinczewski, W., Sideman, S.:'A model for mass(heat) transfer in turbulent tube flow. Moderate and high Schmidt(Prandtl) numbers', CHEM. ENG. SCI. 26(1974)1969-1976

REY00 Reynolds, O.:'Papers on mechanical and physical objects, Volume I, 1869-1882', Cambridge University Press, 1900

RIC90 Richardson, I.M., School of Industrial and Manufacturing Science, Cranfield Institute of Technology: personal communication, 1990

RUN69 Runchal, A.K.:'Transfer processes in steady two-dimensional separated flows', Ph.D-thesis, Imperial College, London, 1969

SCH60 Scheidegger, A.E.:'The physics of flow through porous media', University of Toronto Press, 1960

SCH68 Schlichting, H.:'Boundary layer theory', 6th edition McGraw-Hill, 1968

SCH80 Schwager, F., Robertson, P.M., Ibl, N.:'The use of eddy promoters for the enhancement of mass transport in electrolytic cells', ELECTROCHIMICA ACTA 25(1980)1655-1665

SCH87 Schock, G., Miquel, A.:'Mass transfer and pressure loss in spiral wound modules', DESALINATION 64(1987)339-352

SEL78 Selman, J.R., Tobias, C.W.:'Mass transfer measurements by the limiting current technique', pp 211-318 in ADVANCES IN CHEMICAL ENGINEERING, Academic Press, 1978

SHA63 Shair, F.H., Grove, A.S., Petersen, E.E., Acrivos, A.A.: 'The effect of confining walls on the stability of the steady wake behind a circular cylinder', JOURNAL OF FLUID MECHANICS 17(1963)546-550

SHA78 Shah, R.K., London, A.L.:'Laminar flow forced convection in ducts', Academic Press 1978

SHE79 Shen, J.S., Probstein, R.F.:'Turbulence promotion and hydrodynamic optimisation in an ultrafiltration process', IND. & ENG. CHEM.: PROC. DES. & DEV. 18(1979)547-554

SHI82 Shiina, Y, Takizuka, T., Okamoto, Y.:'Flow around turbulence promoters in parallel channel, (I): flow patterns around cylinder type turbulence promoters' JOURNAL OF NUCLEAR SCIENCE AND TECHNOLOGY 19(1982)720-728

SHI83 Shiina, Y:'Flow around turbulence promoters in parallel channel, (II): shedding vortex around cylinder' JOURNAL OF NUCLEAR SCIENCE AND TECHNOLOGY 20(1983)389-399

SHI84 Shiina, Y:'Shedding vortices around various types of turbulence promoters in parallel channel' JOURNAL OF NUCLEAR SCIENCE AND TECHNOLOGY 21(1984)836-843

SKE74 Skelland, A.H.P.:'Diffusional Mass Transfer' J. Wiley & Sons, 1974

SMI89 Smith, Prof. I., School of Mechanical Engineering, Cranfield Institute of Technology: personal communication, 1989

SON69 Son, J.S., Hanratty, T.J.:'Velocity gradients at the wall for flow around a cylinder at Reynolds numbers from $5*10^3$ to 10^5', J. FLUID MECHANICS 35(1969)353-368

SON74 Sonin, A.A., Isaacson, M.S.:'Optimisation of flow design in forced flow electrochemical systems, with special application to electrodialysis', IND. & ENG. CHEM.: PROC. DES. & DEV. 13(1974)241-248

STO80 Storck, A., Hutin, D.:'Energetic aspects of turbulence promotion applied to electrolysis processes', CAN. J. CHEM. ENG. 58(1980)92-102

STO81 Storck, A., Hutin, D.:'Mass transfer and pressure drop performance of turbulence promoters in electrochemical cells', ELECTROCHIMICA ACTA 26(1981)127-137

TAG79 Tagg, D.J., Patrick, M.A., Wragg, A.A.:'Heat and mass transfer downstream of abrupt nozzle expansions in turbulent flow', TRANS. INSTN. CHEM. ENG. 57(1979)176-181

TAN65 Taneda. S.:'Experimental investigation of vortex streets', J. PHYS. SOC. JAPAN 20(1965)1714-1721

WAT68 Watson, J.S., Thomas, D.G.:'Forced convection mass transfer part IV: Increased mass transfer in an aqueous medium caused by detached cylindrical turbulence promoters in a rectangular channel', A.I.Ch.E. J. 13(1967)676-677

WIL63 Wilson, J.R.:'Depolarisation in electrodialytic demineralisation', TRANS. INSTN. CHEM. ENG. 41(1963)3-12

WIN73 Winograd, Y., Solan, A., Toren, M.:'Mass transfer in narrow cells in the presence of turbulence promoters', DESALINATION 13(1973)171-186

WRA62 Wranglén, G., Nilsson, O.:'Mass transfer under forced laminar and turbulent convection at horizontal plane plate electrodes', ELECTROCHIMICA ACTA 7(1962)121-137

WRA77 Wragg, A.A.:'Applications of the limiting diffusion current technique in chemical engineering', pp 39-44, 49 in THE CHEMICAL ENGINEER, January 1977

WRA89 Wragg, A.A., Department of Engineering, Exeter University: personal communication, 1989

ZHO83 Zhong, X.W., Zhang, W.R., Hu, Z.Y., Li, H.C.:'Effect of characteristics of spacer in electrodialysis cells on mass transfer', DESALINATION 46(1983)243-252

APPENDICES

A. MASS TRANSFER THEORY AND APPLICATION TO MEASUREMENT OF SHEAR RATE

Transport of a species in a solution in the absence of any force fields is governed solely by the balance between convection and diffusion which in the case of constant material properties and time dependence can be written as:

$$\partial c/\partial t + (v\nabla c) = D(\nabla^2 c) \qquad (A1)$$

For two dimensions Equation A1 can be expressed in its components:

$$\partial c/\partial t + u\partial c/\partial x + v\partial c/\partial y = D\partial^2 c/\partial x^2 + D\partial^2 c/\partial x^2 \qquad (A2)$$

The diffusion coefficient D in the case of ionic solutions has a very small value which means that concentration gradients are predominant near the boundaries of the volume of interest i.e. the areas where mass and/or electrical charge is exchanged with the outside world. This leads to the concept of a concentration boundary layer. In steady channel flow Equation A2 can be simplified by omission of the time dependent contribution. Furthermore if one assumes that the fluid velocities are mainly in the direction of the channel axis (X-axis) one may neglect the contribution of streamwise diffusion i.e. in the X-direction. This leads to:

$$u\partial c/\partial x + v\partial c/\partial y = D\partial^2 c/\partial x^2 \qquad (A3)$$

The concentration boundary layer is usually very small and near a wall the velocity u in the concentration boundary layer can without great loss in accuracy be expressed by a linear relationship:

$$u = (\partial u/\partial y)_{y=0} \cdot y = S \cdot y \qquad (A4)$$

Conservation of mass then gives the following relationship for the velocity component perpendicular to the wall:

$$v = -\tfrac{1}{2}(\partial S/\partial x) \cdot y^2 \qquad (A5)$$

Equations A3, A4 and A5 form the mathematical description of a well known mass transfer problem which is complete by the introduction of the following boundary conditions for a wall where mass transfer starts at the positon x=0:

$c=0$, for $y=0$ and $x>=0$

$c=c_b$, for $y=\infty$

$\partial c/\partial y=0$ for $y=0$ and $x<=0$

The solution of this problem as given by various authors [LIG50, ACR60, KES62 and LEB70] leads to the following

expression for the local wall mass transfer coefficient k_x:

$$k_x = 0.807D^{2/3}d(({}_o\int^x S^{\frac{1}{2}}dx')^{2/3})/dx \quad \text{for } x>0 \qquad (A6)$$

This can be written in a dimensionless fashion:

$$Sh_x/Sc^{1/3} = 0.641d(({}_o\int^{x^*}(S^*)^{\frac{1}{2}}dx')^{2/3})/dx^* \quad \text{for } x^*>0 \qquad (A7)$$

where $x^* = x/(d_h)_e$

$S^* = S2((d_h)_e)^2/\nu$

It is straighforward to show that for the average mass transfer coefficient one may write:

$$k = 0.807D^{2/3}({}_o\int^x S^{\frac{1}{2}}dx')^{2/3}/x \quad \text{for } x>0 \qquad (A8)$$

which can also be written in a dimensionless fashion:

$$Sh_e/Sc^{1/3} = 0.641({}_o\int^{x^*}(S^*)^{\frac{1}{2}}dx')^{2/3}/x^* \quad \text{for } x^*>0 \qquad (A9)$$

For a constant shear rate Equations A7 and A9 lead to:

$$Sh_x/Sc^{1/3} = 0.427(S^*)^{1/3}(x^*)^{-1/3} \quad \text{for } x^*>0 \qquad (A10)$$

$$Sh_e/Sc^{1/3} = 0.641(S^*)^{1/3}(x^*)^{-1/3} \quad \text{for } x^*>0 \qquad (A11)$$

When the empty channel shear rate is substituted ($S^*=24Re_e$) into Equation (A11) the empty channel mass transfer correlation can be recovered (Equation 2.3).

As mass transfer is intimately connected with the value of the shear rate on the transferring area mass transfer measurements can be used to determine shear rates. From Equation A8 under the condition of constant shear rate the so-called design equation (Equation 5.1) can be derived:

$$kl/D = 0.807(Sl^2/D)^{1/3} \qquad (A12)$$

where l is the length of the transfer area. Equation A12 is considered to be valid for $Sl^2/D>5000$ in MIT66 and $S^*l^2/D>1000$ in PY69, the validity being limited by the effects of streamwise diffusion and natural convection. In LEB73 a correction factor for Equation A12 is given in case of a linear change in the shear rate over the length of the transfer area. The average mass transfer coefficient is given in Equation A13 and it can be seen the correction is a second order effect.

$$kl/D = 0.807(Sl^2/D)^{1/3}(1-((dS/dx)l/S)^2/144) \qquad (A13)$$

Also in LEB73 an equation for the mass transfer coefficient is given for the situation when the shear rate is exactly zero on the electrode. It can be derived from Equation A8 that in this case:

$$k = 0.571((dS/dx)D^2)^{1/3} \qquad (A14)$$

which can be written dimensionlessly as

$$Sh_e/Sc^{1/3} = 0.454(dS^*/dx^*)^{1/3} \qquad (A15)$$

Equations A12 and A13 are invalid near separation- and reattachment points because the shear rate goes to zero in these points. A single transfer area is also unable to determine the direction of the flow near the wall. To overcome the latter problem a double transfer area arrangement can be used [SON69, LEB73, TAG79, CHO83] i.e. two small transfer zones separated by a tiny inert zone. This is referred to as a dual electrode. The mass transfer to the downstream zone will inevitably be smaller than to the upstream zone because a boundary layer has already developed in the wake of the upstream zone. Hence the sign of the difference in mass transfer between the two areas gives the local flow direction. This difference can also be used to calculate the shear rate as shown in LEB73 which gives Equation A16 for the relation between mass transfer coefficient difference k and shear rate:

$$kl/D = 0.333(Sl^2/D)^{1/3}(1-0.806(dS/dx)1/S) \qquad (A16)$$

Equation A16 can be simplified if the change in shear rate over the transfer area (of length 2l) is neglected:

$$kl/D = 0.333(Sl^2/D)^{1/3} \qquad (A17)$$

The constant 0.333 is valid in case of neglible thickness of the inert zone between the active zones. In practice the value of the constant depends on the thickness of the inert zone and the value of the constant needs to be obtained by a calibration [PY73].
Mass transfer measurements can also be used to measure a time varying shear rate. Equation A12 can be rewritten as:

$$Sl^2/D = 5.90(kl/D)^3 \qquad (A18)$$

Hence the shear rate varies according to the mass tranfer coefficient cubed. If one assumes the mass transfer coefficient to consist of a constant term k_m and a fluctuating term k_f the average of the mass tranfer coefficient cubed $(k^3)_m$ can be approximated by

$$(k^3)_m = (k_m)^3(1+3(k^2)_m/(k_m)^2) \qquad (A19)$$

where the last term represents the mass transfer standard deviation squared. For a mass transfer standard deviation equal to say 0.1 the contribution of the fluctuations to the average mass transfer cubed 0.03 times the average and hence very small. The error introduced by using the cube of the average mass transfer coefficient instead of the average of instantaneous mass transfer coefficients cubed is very small in those circumstances. This analysis

assumes that the mass transfer coefficient is able to follow all the fluctuations in the shear rate. Several authors have reported on the time response of the mass transfer boundary layer to a variation in the shear rate [FOR71, HAN83 and AMB86]. From these it can be seen that the boundary layer follows the shear rate completely if the dimensionless frequency $f(l^2/(S^2D))^{1/3} < 0.1$. As the shear rate is usually not known beforehand Equation A16 or A12 can be used to provide an estimate for the shear rate and the condition for a good frequency response can then be written as:

$$f(0.807)^2(kl/D)^{-2}l^2/D < 0.1 \qquad (A20)$$

More information on the electrochemical measurement of the shear rate can be found in the review by Hanratty and Campbell [HAN83].

B. DETAILS OF EXPERIMENTAL EQUIPMENT AND MATERIALS

1. Flow visualisation studies

Equipment	Make/Supplier
Centrifugal pump Type no. 903	Stuart Turner Henley on Thames
Gear pump ('Micropump') max. flow rate: approx. 7 ml/min	Cole Palmer Instrument Co., Bishop's Stortford
Syringe needles 2060D (i.d .381 mm, o.d.: .711 mm)	Jencons Ltd. Leighton Buzzard
Variable area flow meter (type 10A3500/3600) max. flow rate 833.5 1/h (Sg 1.0)	Fischer & Porter Ltd. Workington
Photographic camera	Praktica MTL3
U-matic video recorder	JVC
Viscometer, suspended level	Fitzsimmons
Hydrometer (conf. to BS718)	BDH Ltd., Atherstone
Digital thermometer	BDH Ltd., Atherstone
Tungsten/halogen floodlight TH1000/1500 (1000 W)	Denmans Electrical Plc. Kempston
PERSPEX (sheet)	British Mica Co. Ltd. Bedford
PERSPEX (rods and pipes)	VT-Plastics Ltd. Bedford

Consumables	Make/Supplier
Fluorescein sodium (technical)	BDH Ltd., Atherstone
Aluminium powder, fine ('AnalaR')	BDH Ltd., Atherstone
Aluminium powder (200 mesh)	Aldrich Chemical Co. Ltd., Gillingham
Cane sugar	Tate and Lyle
Glycerol	Aldrich Chemical Co. Ltd., Gillingham
Photographic film	Ilford, XP1/400 ASA, HP5/400 ASA

2. Pressure gradient studies

Most equipment and materials identical to the flow visualisation studies with the addition of:

Equipment	Make/Supplier
Inclined U-tube manometer 0->600 Pa (Sg. 1.0)	Everyvalve Equipment Co. Potters Bar

Consumables	Make/Supplier
Carbon-Tetrachloride ('AnalaR')	BDH Ltd., Atherstone

3. Mass transfer studies

Equipment	Make/Supplier
Magnetic drive centrifugal pump TE-5C-MD	March May Ltd. Eaton Socon
Variable area flow meters (type 10A3500/3600) max. flow rates: 200 l/h, 109 l/h and 415 cc/min (Sg 1.0)	Fischer & Porter Ltd. Workington
Spectro-photometer	Philips, PU8620
PC/XT	Osborne
Digital multimeter	Thandar TM355
AVO-meter Eight, Mk.7	RS-Components Ltd. Corby
PC26A 16 Channel/12 Bit ADC	Amplicon Liveline Ltd. Brighton
Hydrometer (conf. to BS718)	BDH Ltd., Atherstone
Gas bubbler	BDH Ltd., Atherstone
Heating mat	BDH Ltd., Atherstone
Mercury thermometer (conf. to BS593)	BDH Ltd., Atherstone
Viscometer, Cannon-Fenske (conf. to BS188)	Gallenkamp Loughborough
Nickel sheet(99.98%) (large electrode)	Goodfellow, Cambridge

Nickel foil (99.997%) (shear rate electrode)	Aldrich Chemical Co. Ltd., Gillingham
Nickel wire (99.995%) (mini-electrodes)	Aldrich Chemical Co. Ltd., Gillingham
PVC (fittings and pipes)	Wilford Plastics Ltd. Luton
PVC (sheet)	VT-Plastics Ltd. Bedford
Polythene tank (20 l)	Gibbs and Dandy Ltd. Bedford
All electronic supplies	RS-Components Ltd. Corby

Consumables	Make/Supplier
Potassium ferri/ferrocyanide ('AnalaR')	BDH Ltd., Atherstone
Sodium hydroxide ('AnalaR')	BDH Ltd., Atherstone
Cyclohexane ('AnalaR')	BDH Ltd., Atherstone
Hydrochloric acid ('AnalaR')	BDH Ltd., Atherstone
Epoxy resin Araldite (normal/rapid)	Jencons Ltd. Leighton Buzzard
Disposable cuvettes (10 mm)	Sigma Chemical Co. Ltd. Poole

C. GEOMETRIC CHARACTERISTICS OF OBSTRUCTED CHANNELS

The obstructions in the channels are parallel cylindrical rods of diameter d being separated from each other by a distance l_{rr}, the interrod distance. The channel length and width are l and w, repectively. Figure C1 gives the cross section of these geometries and the whole channel can be thought to be built up from units of length l_{rr} with one rod present in it.

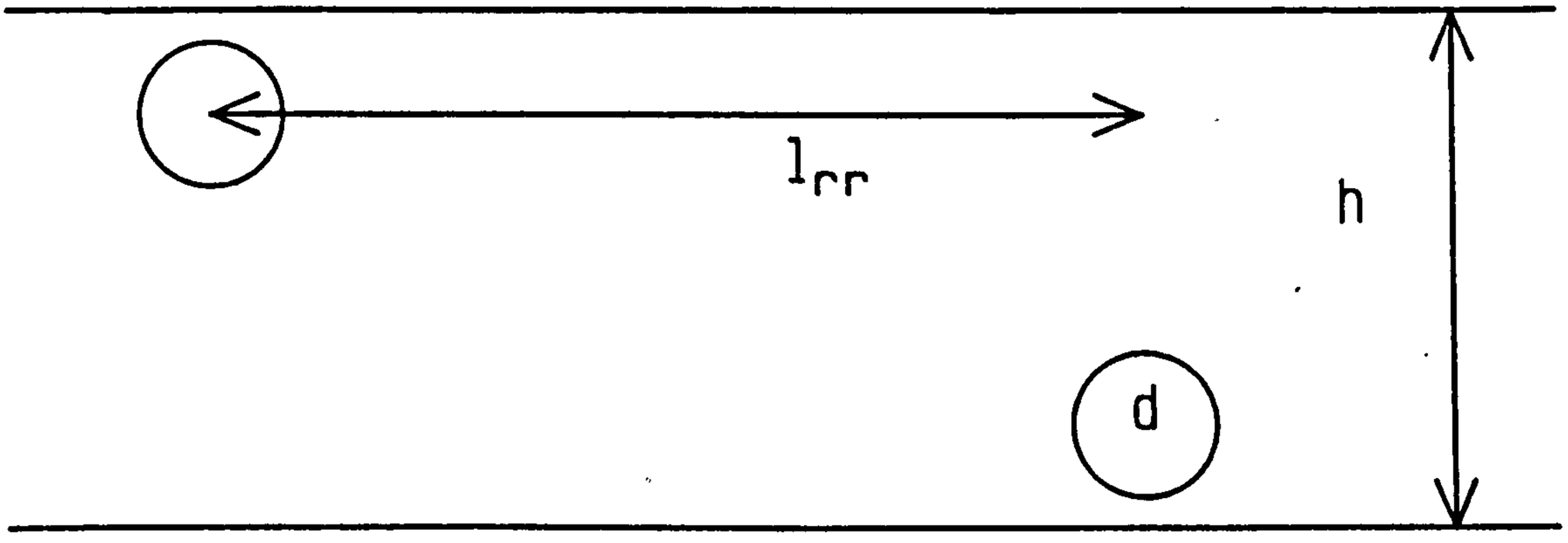

Fig. C1: Cross section of general geometry

The entities used to describe separators are usually the porosity E and the hydraulic diameter of the obstructed channel $(d_h)_f$. The porosity is defined as the fraction of the channel volume occupied by the liquid and can be written as:

$$E = 1 - \frac{\pi d^2}{4 l_{rr} h} \qquad (C1)$$

The hydraulic diameter is defined as 4 times the liquid volume divided by the wetted area. The latter consists of two contributions from the channel, top and bottom of channel ($2wl_{rr}$) and the two sides corrected for the end area of the rods ($2hl_{rr}-\pi/2d^2$) and the contribution from the rods (πdw). This leads to the following expression for the hydraulic diameter of the obstructed channel:

$$(d_h)_f = (d_h)_e \frac{E}{1+(1-E)((d_h)_e/d)(1-d/2w)} \qquad (C2)$$

where $(d_h)_e$ is the hydraulic diameter of the empty channel ($2hw/(w+h)$). For an infinitely wide channel Equation C2 can be written as the general equation developed for separators as given in SCH87 (Equation 2.8 in this thesis). Tables C1, C2 and C3 give the porosity and hydraulic diameter derived from Equations C1 and C2 for the centered rods, attached rods and suspended rods, respectively (w=100 mm, h=13 mm, $(d_h)_e$= 23 mm).

Table C1: Porosity and hydraulic diameter of centered rods (d=7 mm) for different inter-rod distances.

l_{rr} (mm)	E	$(d_h)_f$ (mm)
30	0.9013	15.79
60	0.9507	18.91
120	0.9753	20.81

Table C2: Porosity and hydraulic diameter of attached staggered rods (d=7 mm) for different inter-rod distances.

l_{rr} (mm)	E	$(d_h)_f$ (mm)
20	0.8520	13.34
40	0.9260	17.26
60	0.9507	18.91
80	0.9630	19.83

Table C3: Porosity and hydraulic diameter of suspended staggered rods (d=3 mm) for different inter-rod distances.

l_{rr} (mm)	E	$(d_h)_f$ (mm)
6	0.9094	12.42
12	0.9547	16.36
24	0.9773	19.20

D. ACCURACY OF RESULTS

Throughout this thesis results are expressed in a dimensionless form i.e. flow rate is expressed as a Reynolds number Re_e, pressure is expressed by $(p^*)_e$, mass transfer is expressed by the quantity $Sh_e/Sc^{1/3}$ where Sh_e is the Sherwood number and Sc the Schmidt number and shear rate is expressed by S^*. These four entities are calculated from measurements and estimates for the accuracy of the end-result based on the estimates for the error of each measurement will be given below:

1) $Re_e = V(d_h)_e/\nu = 2Q/(\nu(w+h))$

Q : flow rate
w : channel width (100 mm)
h : channel height (13 mm)
ν : kinematic viscosity

Flow rates were measured with rotameters for which the manufacturers specify an accuracy of 2% of the full scale reading. The rotameters were checked with the 'bucket and stopwatch' method and good agreement was found. As an estimate for the accuracy 5% was taken as a typical value based on reading of 0.4 times the maximum reading and using the manufacturers' specified accuracy.
The measurement error in the channel dimensions was typically 0.1 mm resulting in a approximate accuracy in (w+h)/2 of around 1%.
Kinematic viscosities were measured over a range of the temperature and fitted to a curve of the type given by Equation 3.1. The deviation of the measurements of the viscosity from the fitted curve was always less than 1% and this was taken to be the accuracy of the determination of the kinematic viscosity based on the measurement of temperature.
The accuracy of with which the Reynolds number could be determined is found by summation and is equal to 7%.

2) $(p^*)_e = (\Delta p/1)(d_h)_e^3/(2\rho\nu^2)$

In addition to the quantities already discussed the density ρ could be determined with an accuracy of 0.1% with a hydrometer.
The pressure drop was measured with an inclined U-tube manometer calibrated by the manufacturer. The calibration was found to be in accordance with the internal dimensions of the manometer. Based on the hysteresis effects mentioned Paragraph 4.2 the accuracy was estimated to be 2%.
The error in the length measurement was estimated to be 1 mm, giving rise to an accuracy of 0.5%.
The accuracy in the dimensionless pressure gradient is obtained by summation and estimated to be 7.5%.

3) $Sh_e/Sc^{1/3} = (k(d_h)_e)/D)/(\nu/D)^{1/3} =$

$I(d_h)_e/(NFc_bA_{el}D^{2/3}\nu^{1/3})$

I : electrode current
$(d_h)_e$: hydraulic diameter
N : number of electrons transferred
F : Faraday number
c_b : bulk concentration
A_{el} : area of electrode
D : diffusion coefficient

The accuracy of the current measurement was better than 0.5% and the concentration could be measured with an accuracy of less than 1% according to the calibration curve. The inaccuracy in the area measurement of the large electrode is negligible but for the mini-electrodes it was estimated to be 6%. The deviation in the latter was mainly due to the nickel being smeared out when smoothing the electrode surface.
The diffusion coefficient was calculated from the kinematic viscosity (see Paragraph 5.3.2) and therefore the accuracy with which the diffusion coefficient can be determined is equal to the accuracy of the kinematic viscosity. It has to be borne in mind that no allowances are made for a deviation in the equation which links the diffusion coefficient to the kinematic viscosity (Equation 5.3) which could be up to 10%.
The accuracy in the dimensionless entity $Sh_e/Sc^{1/3}$ is then estimated to be 3.5% for the large electrode and 9.5% for the mini-electrodes.

4) $S^* = 2S((d_h)_e)^2/\nu = 3.81k^3(d_h)_e^2l/(\nu D^2) =$

$3.81I^3(d_h)_e^2l/(\nu(NFc_bA_{el})^3D^2)$

Most of the measurement errors have been discussed previously except the error in the electrode length (3%) and the electrode area (3%). This results in an estimated accuracy equal to 15.5 %.

FIGURES

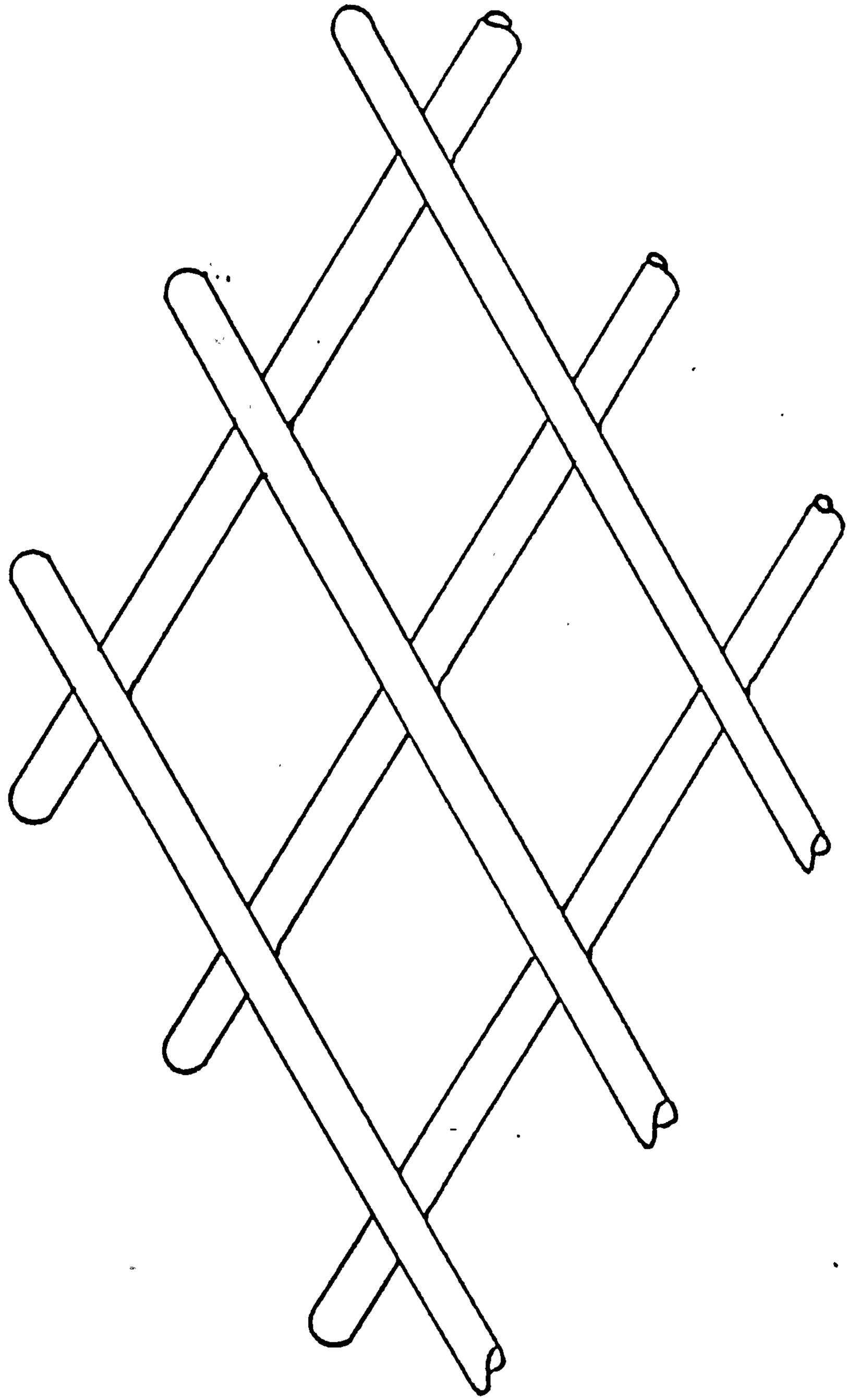

Fig. 1.1: Schematic representation of 'NETLON' separator

Fig. 2.1: Mass transfer and dimensionless pressure gradient
Data sample from Ichiki and Asawa

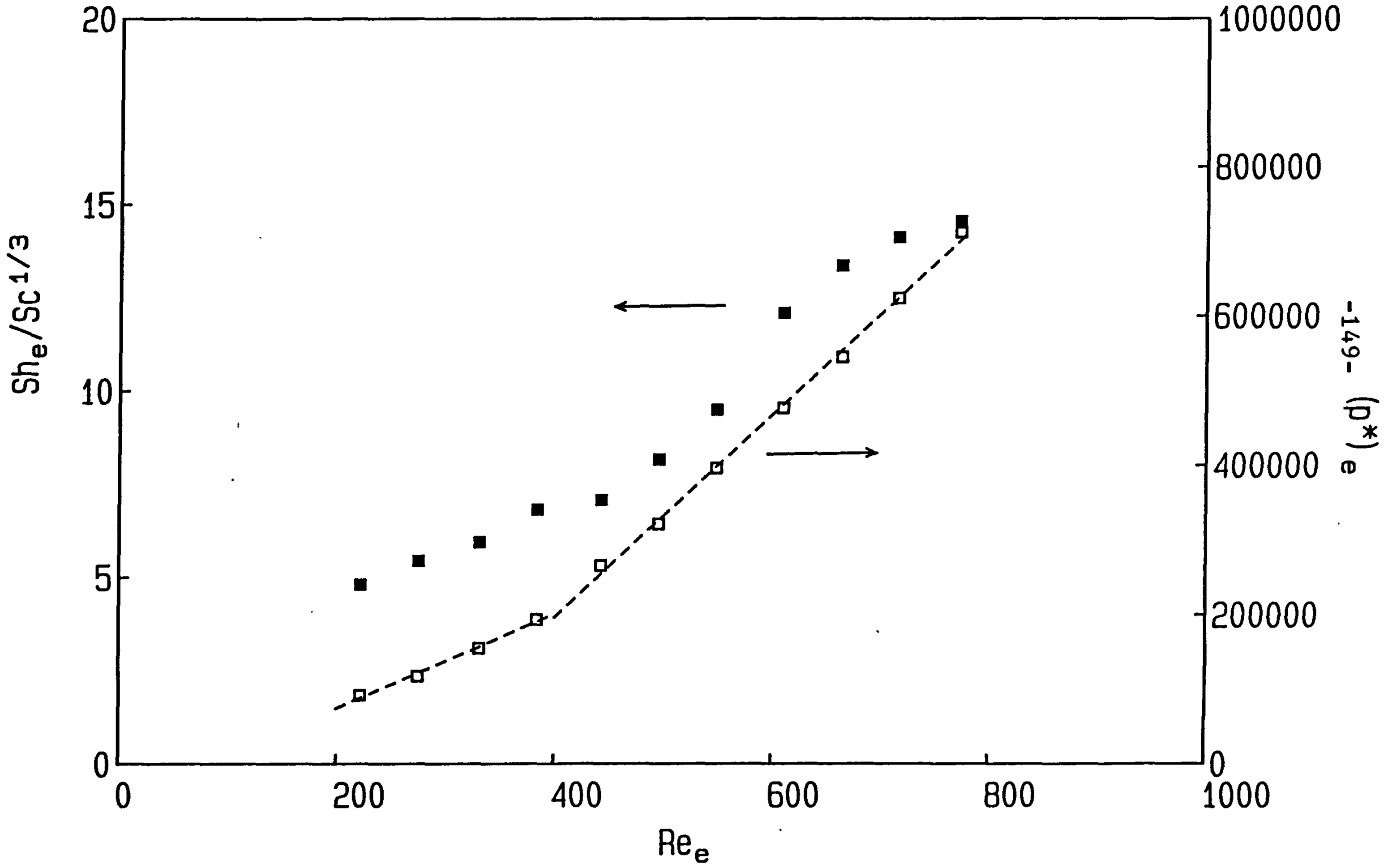

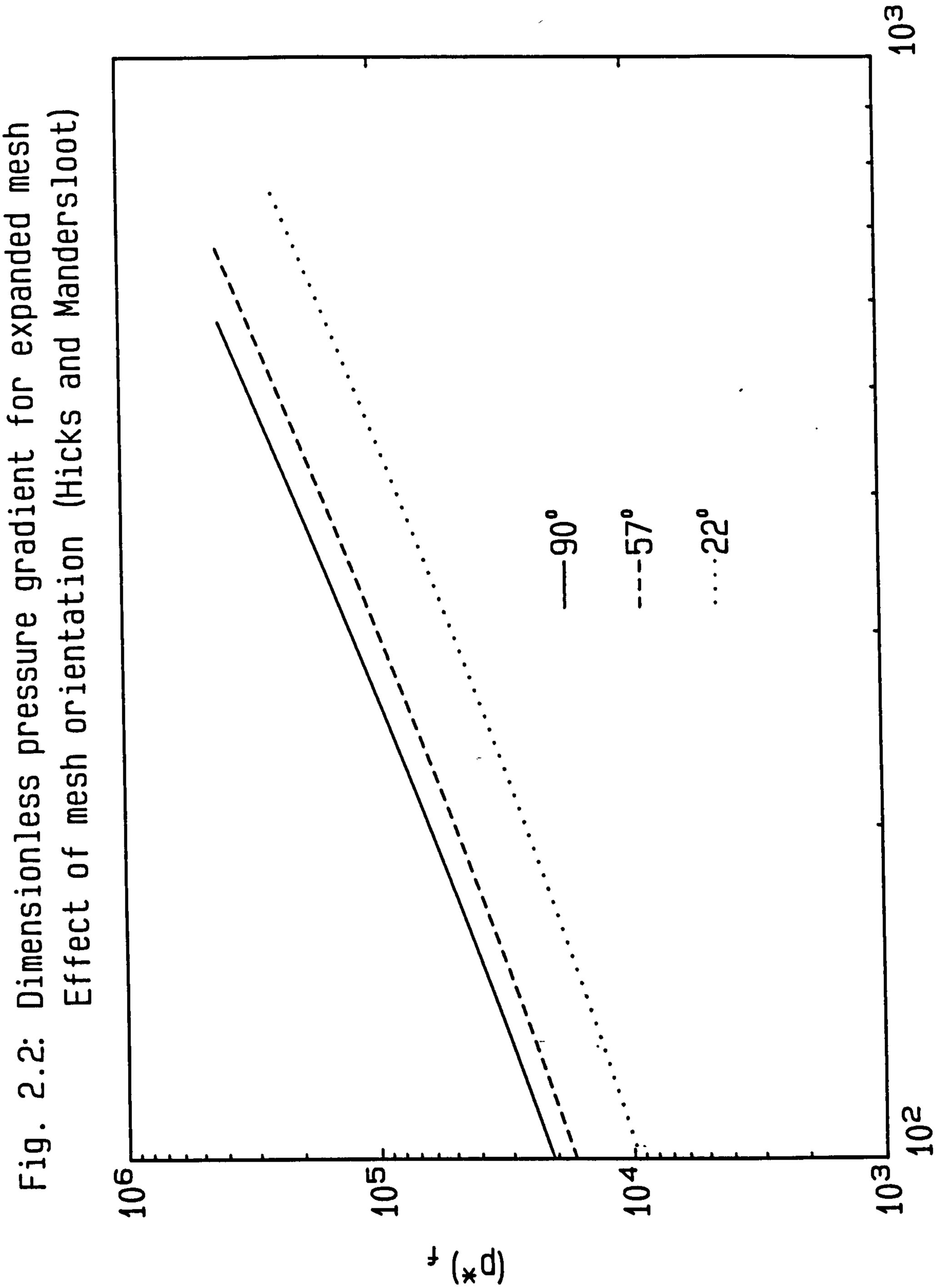

Fig. 2.2: Dimensionless pressure gradient for expanded mesh
Effect of mesh orientation (Hicks and Mandersloot)

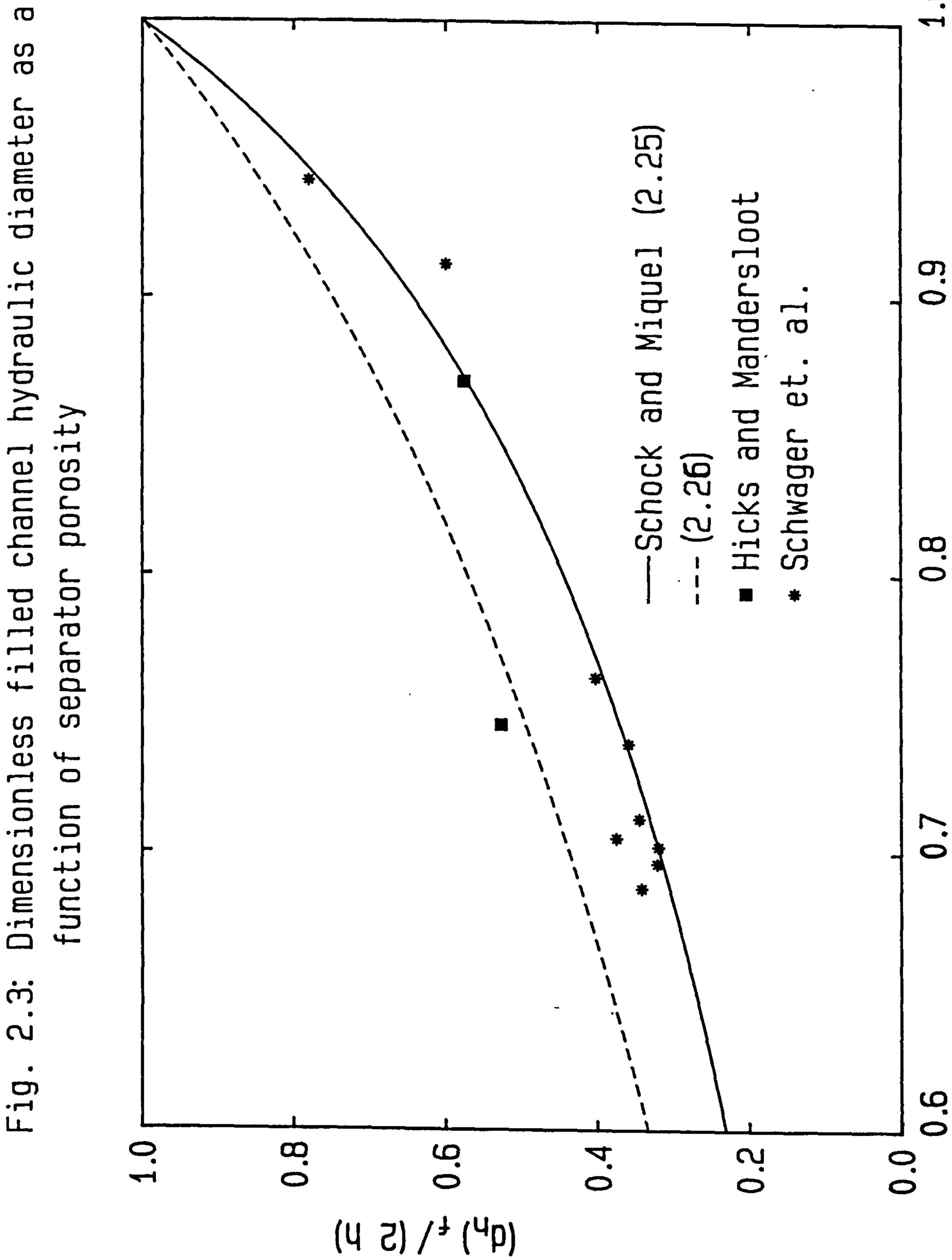

Fig. 2.3: Dimensionless filled channel hydraulic diameter as a function of separator porosity

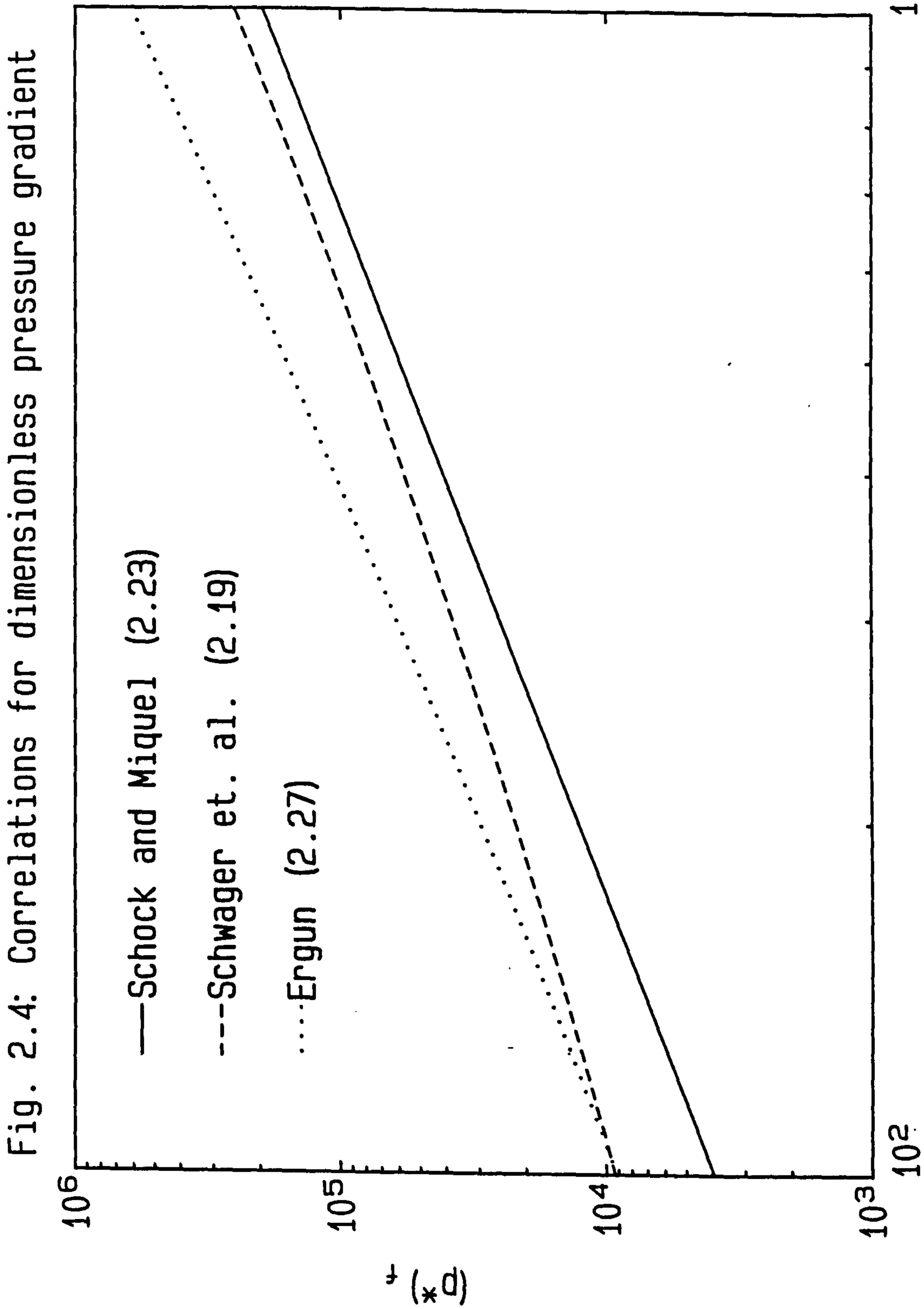
Fig. 2.4: Correlations for dimensionless pressure gradient
——Schock and Miquel (2.23)
---Schwager et. al. (2.19)
....Ergun (2.27)
$(p^*)_f$
Re_f
10^6
10^5
10^4
10^3
10^2
10^3

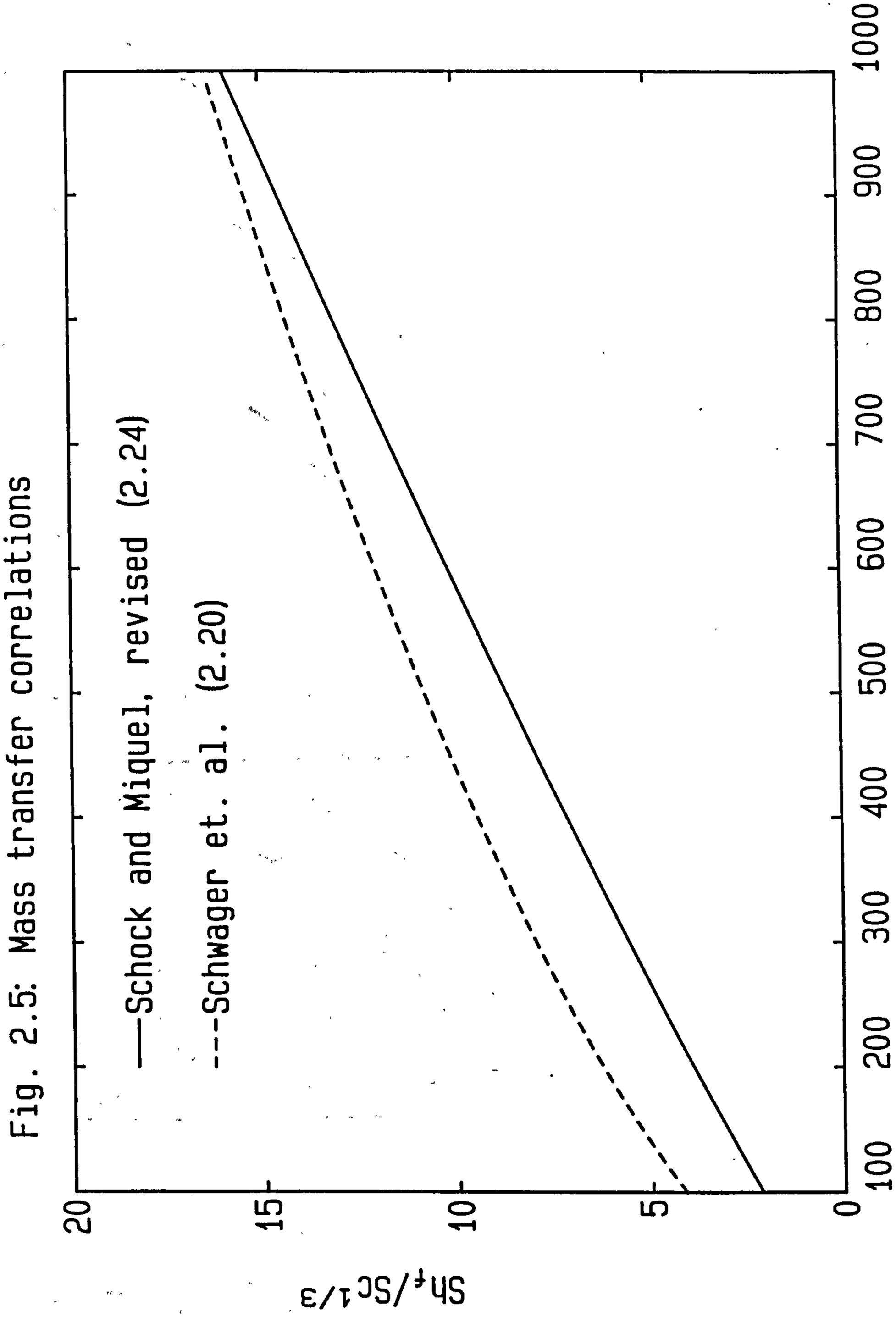

Fig. 2.5: Mass transfer correlations

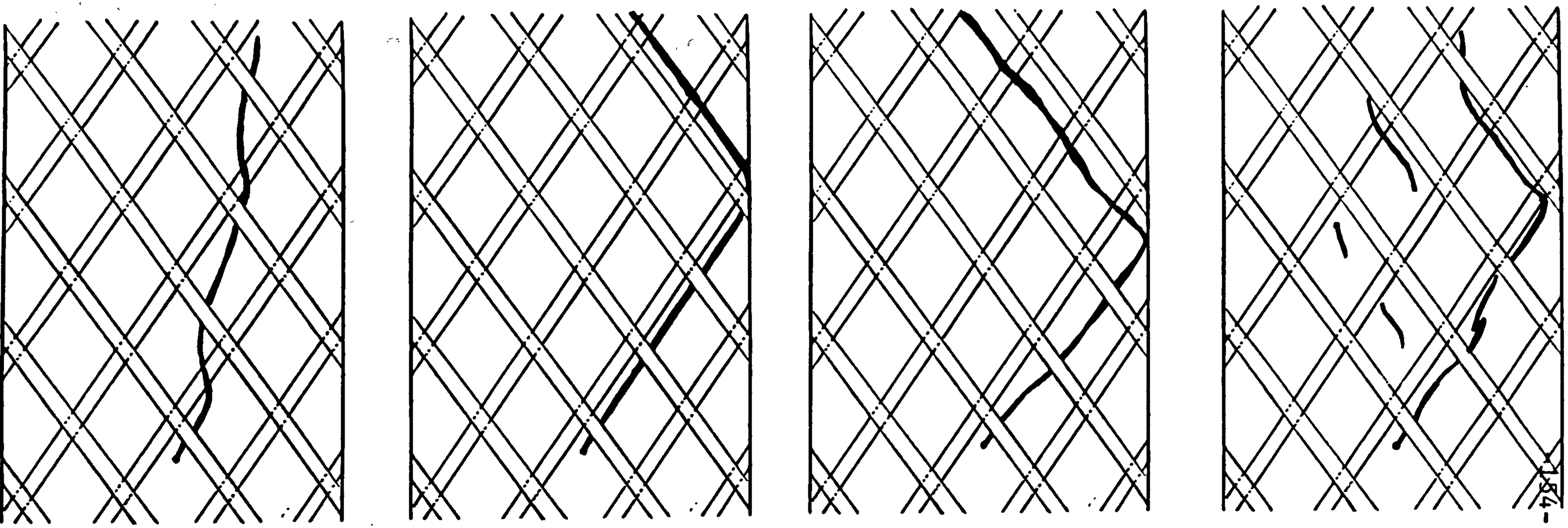

Re_e = 50 Re_e = 150 Re_e = 250 Re_e = 350

Fig. 2.6: Sketches of dye traces for 'NETLON' separator

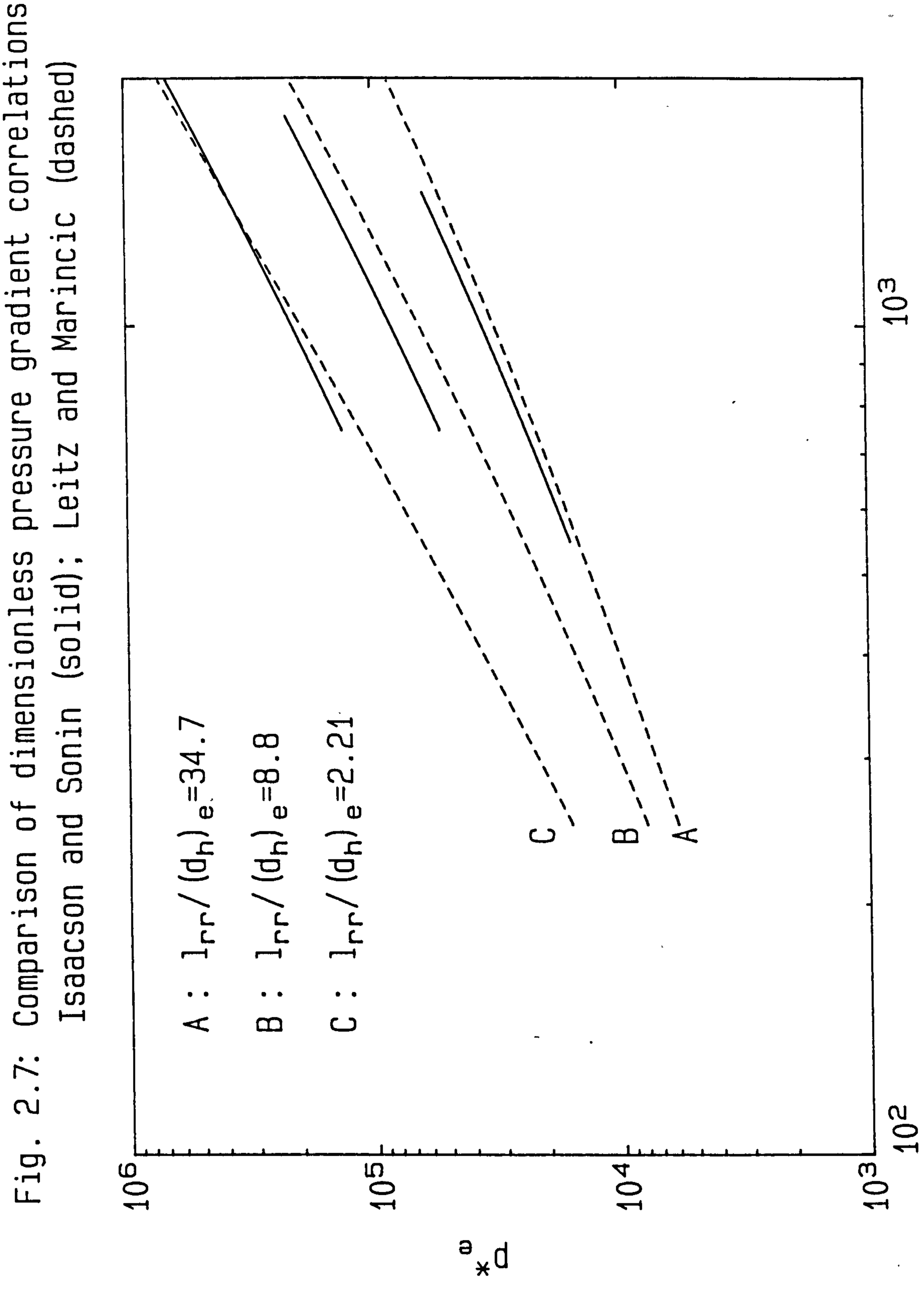
Fig. 2.7: Comparison of dimensionless pressure gradient correlations
Isaacson and Sonin (solid); Leitz and Marincic (dashed)
A : $l_{rr}/(d_h)_e$=34.7
B : $l_{rr}/(d_h)_e$=8.8
C : $l_{rr}/(d_h)_e$=2.21
C
B
A
10^6
10^5
10^4
10^3
10^2
Re_e
$p^*_e d$

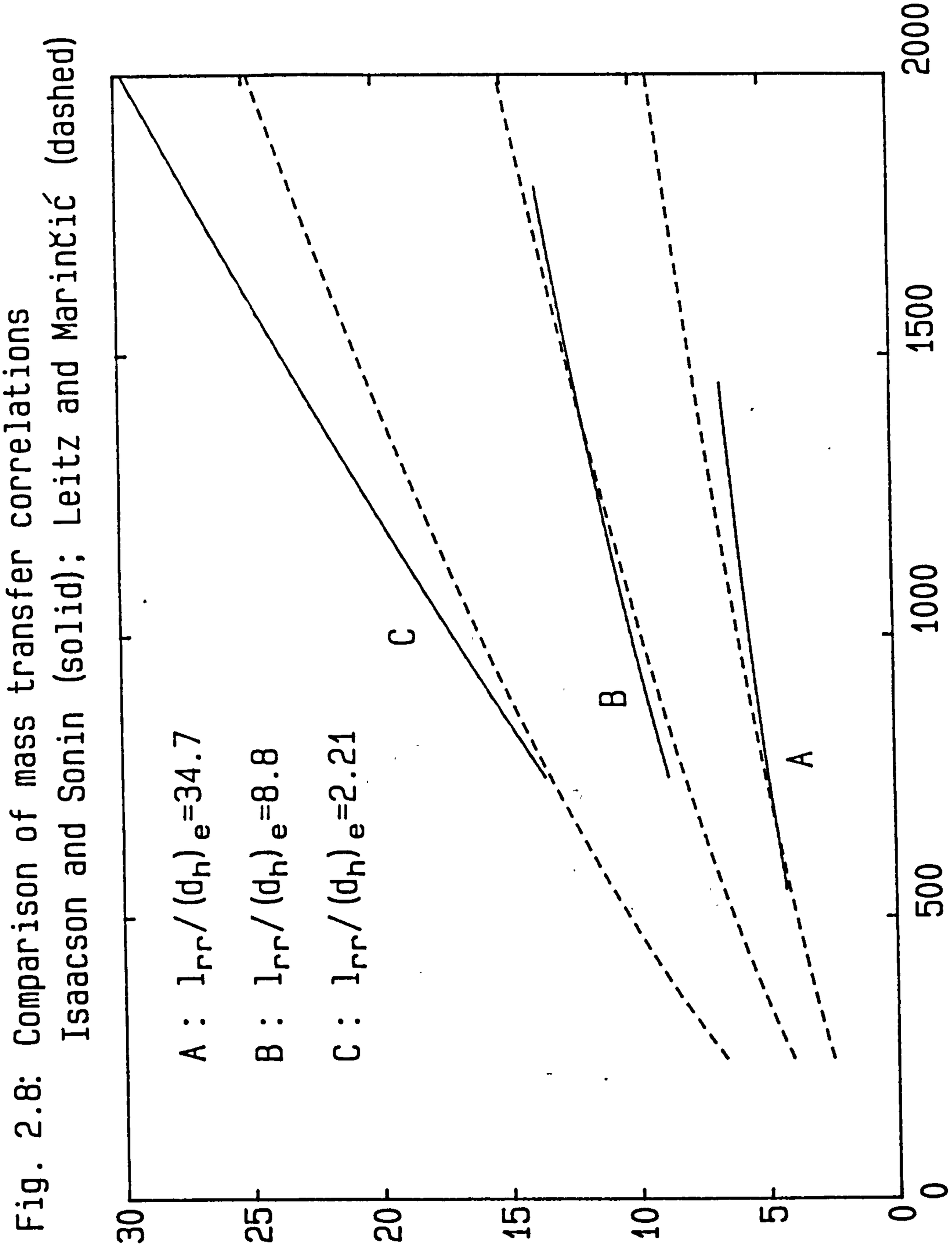

Fig. 2.8: Comparison of mass transfer correlations
Isaacson and Sonin (solid); Leitz and Marin (dashed)

A : $l_{rr}/(d_h)_e$=34.7

B : $l_{rr}/(d_h)_e$=8.8

C : $l_{rr}/(d_h)_e$=2.21

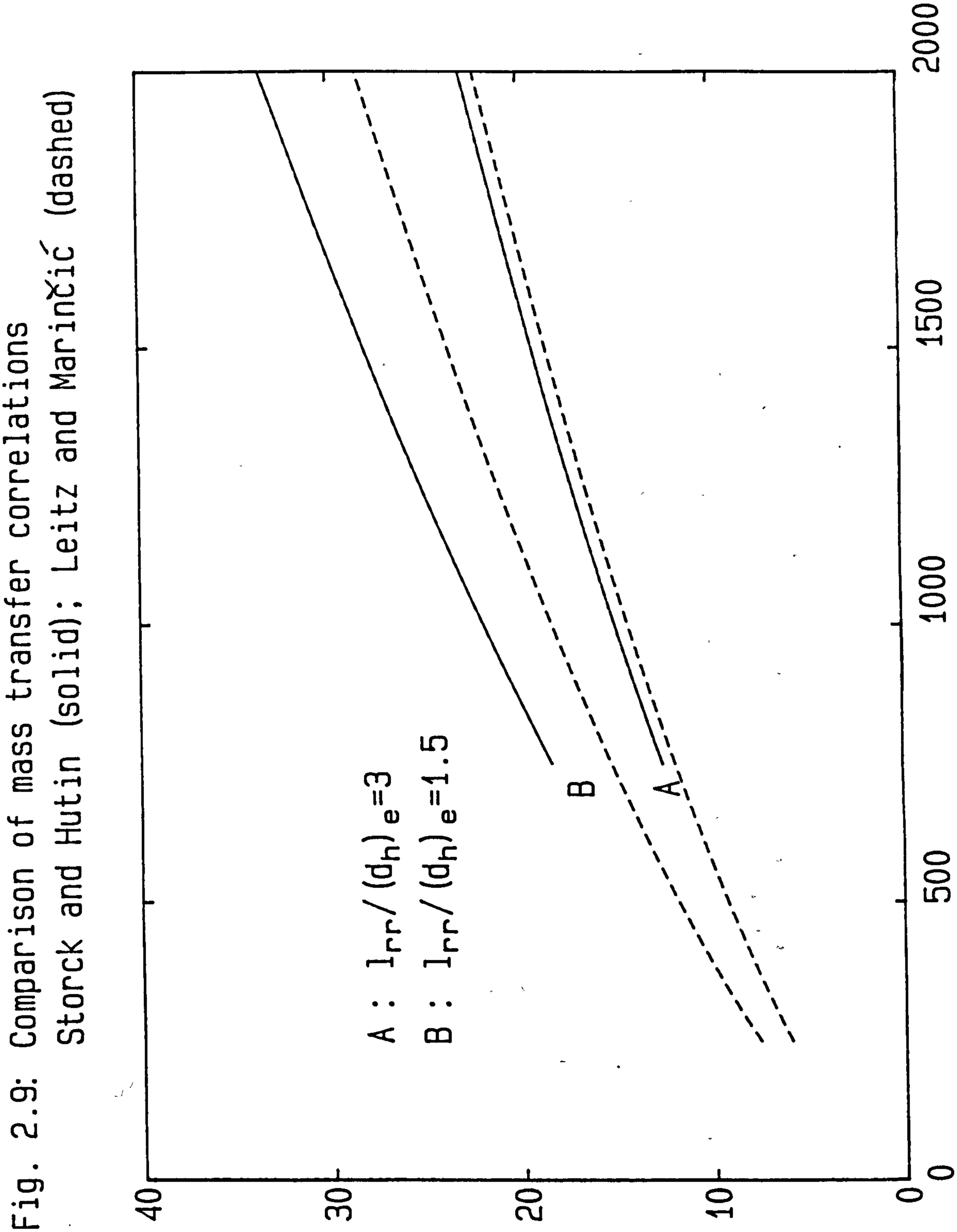

Fig. 2.9: Comparison of mass transfer correlations

Fig. 2.10: Cross-section of the geometries

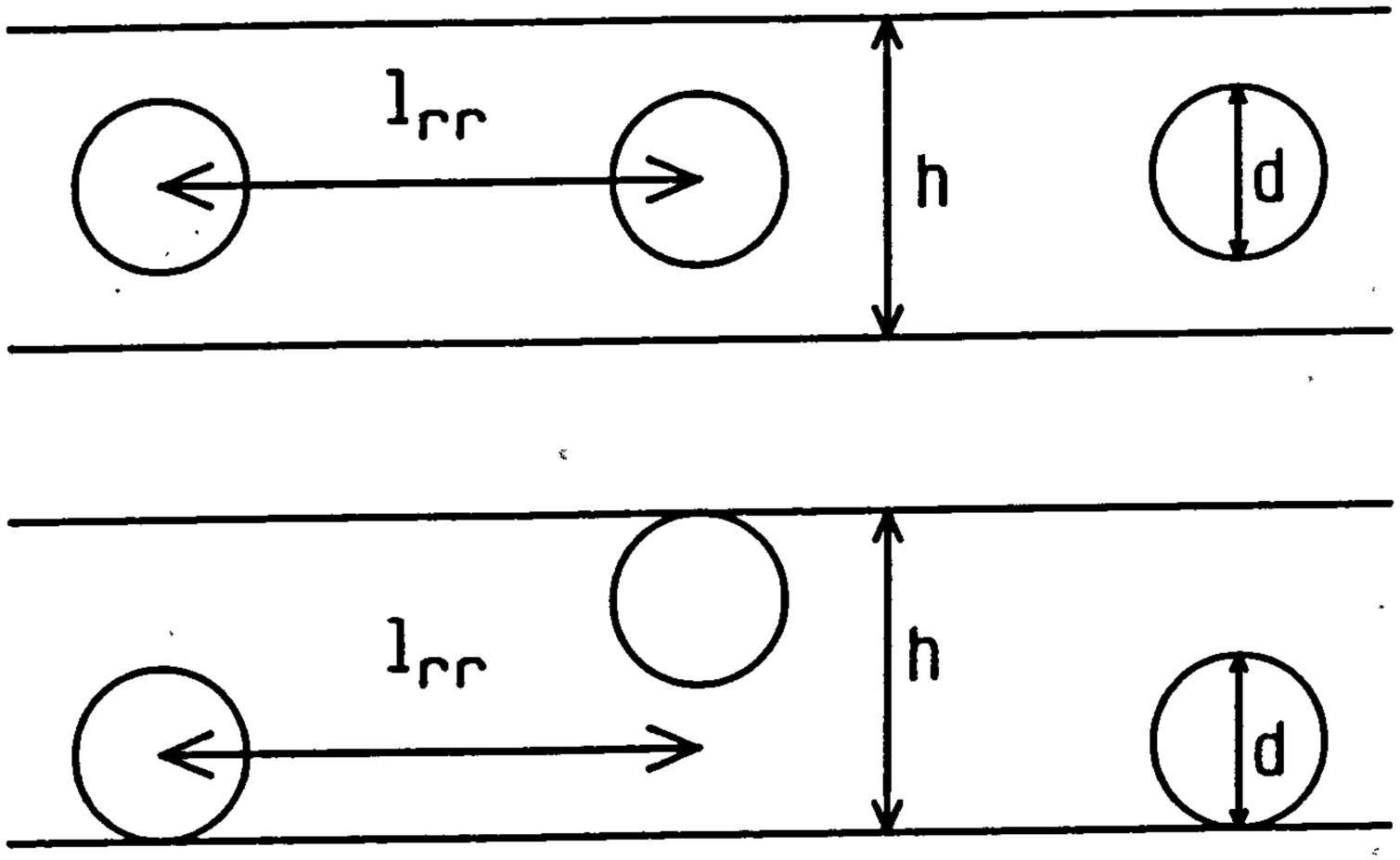

Centered rods: h = 13 mm, d = 7 mm

l_{rr} = 30, 60, 90, 120 mm

Attached staggered rods: h = 13 mm

d = 7 mm, l_{rr} = 20, 40, 60, 80, 100 mm

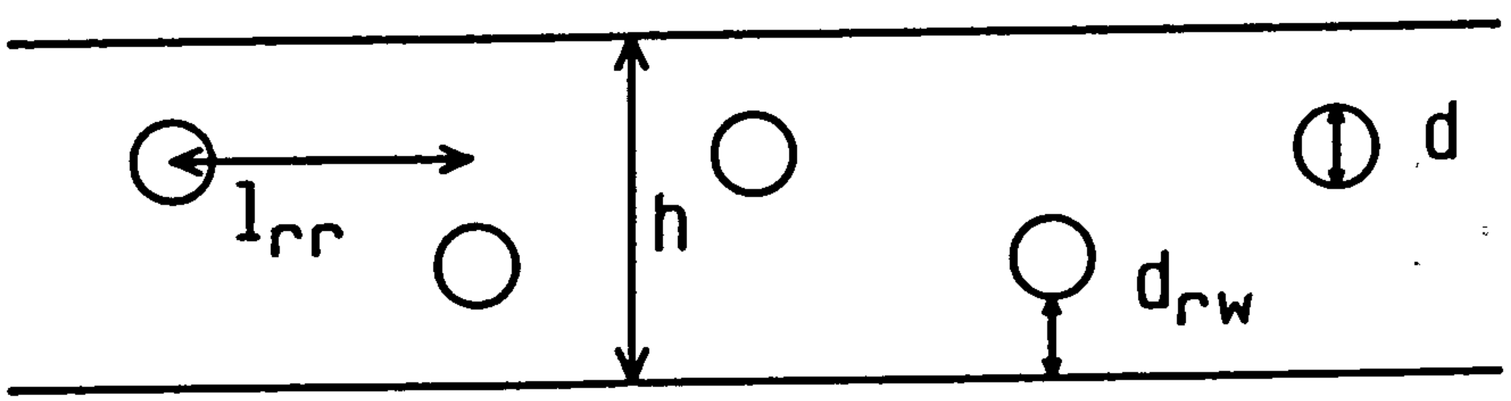

Suspended staggered rods: h = 13 mm

d = 3 mm, l_{rr} = 6, 12, 24 mm

d_{rw} = 1, 2, 3 mm

(1) MODEL FLOW CHANNEL

(2) FILAMENT LIGHT

(3) CAMERA

(4) FLOWMETER

(5) THERMOMETER

(6) STORAGE TANK

(7) CENTRIFUGAL PUMP

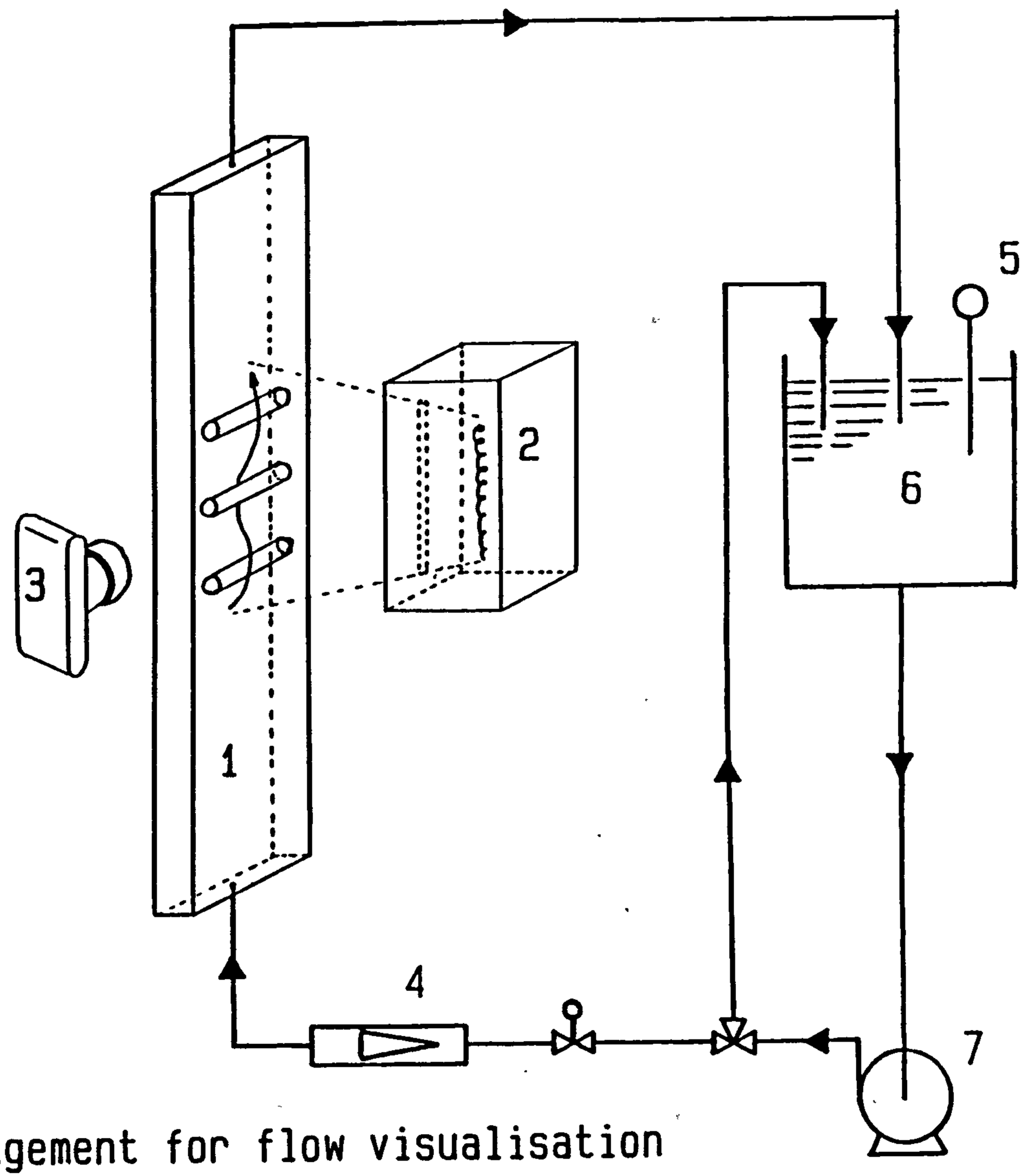

Fig. 3.1: Experimental arrangement for flow visualisation

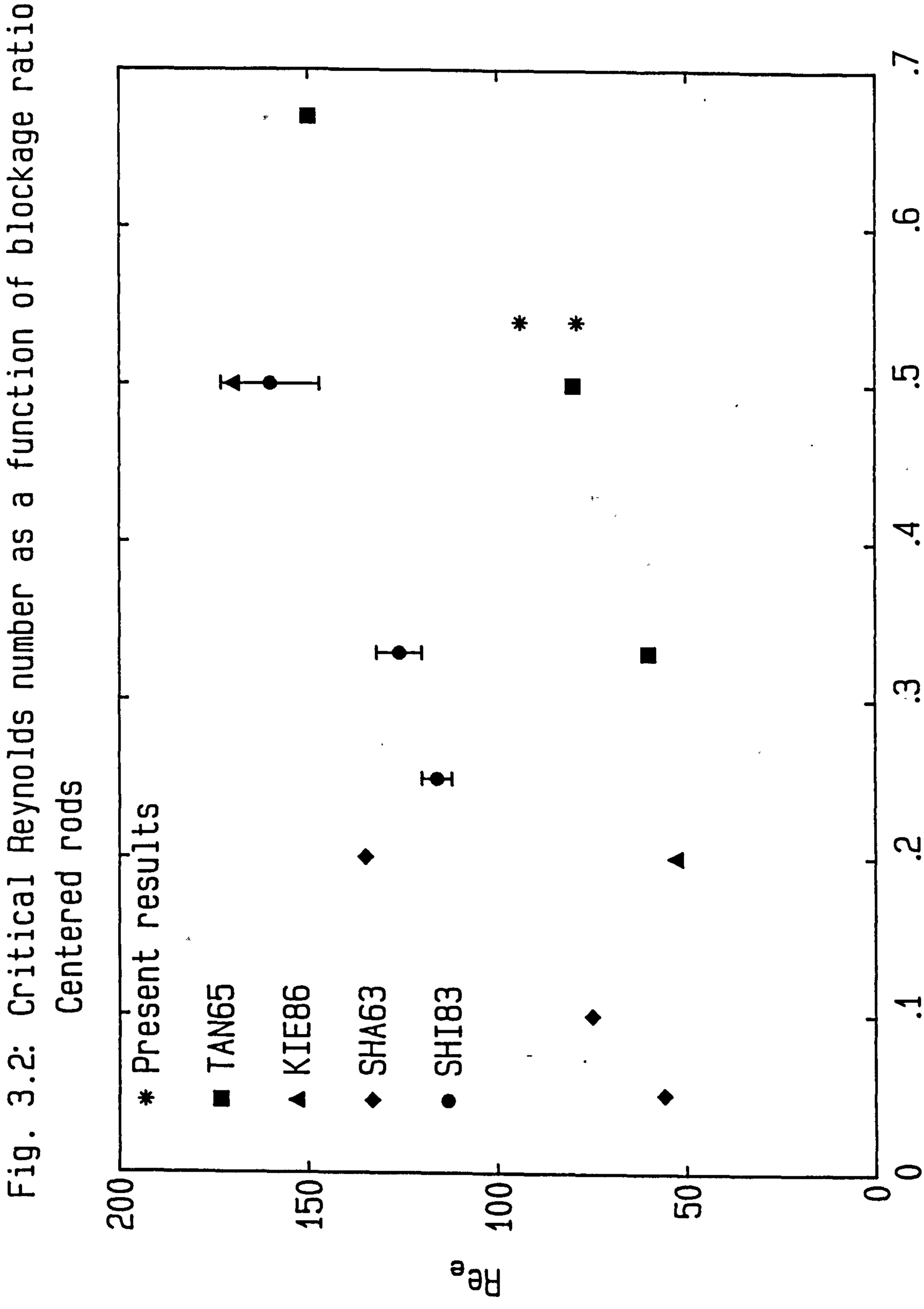
Fig. 3.2: Critical Reynolds number as a function of blockage ratio
Centered rods
* Present results
■ TAN65
▲ KIE86
◆ SHA63
● SHI83
Re_e
200
150
100
50
0
0
.1
.2
.3
.4
.5
.6
.7
Blockage ratio d/h

Fig 4.1: Dimensionless pressure gradient; Centered rods l_{rr} = 30 mm
Results from two sugar solutions of different density

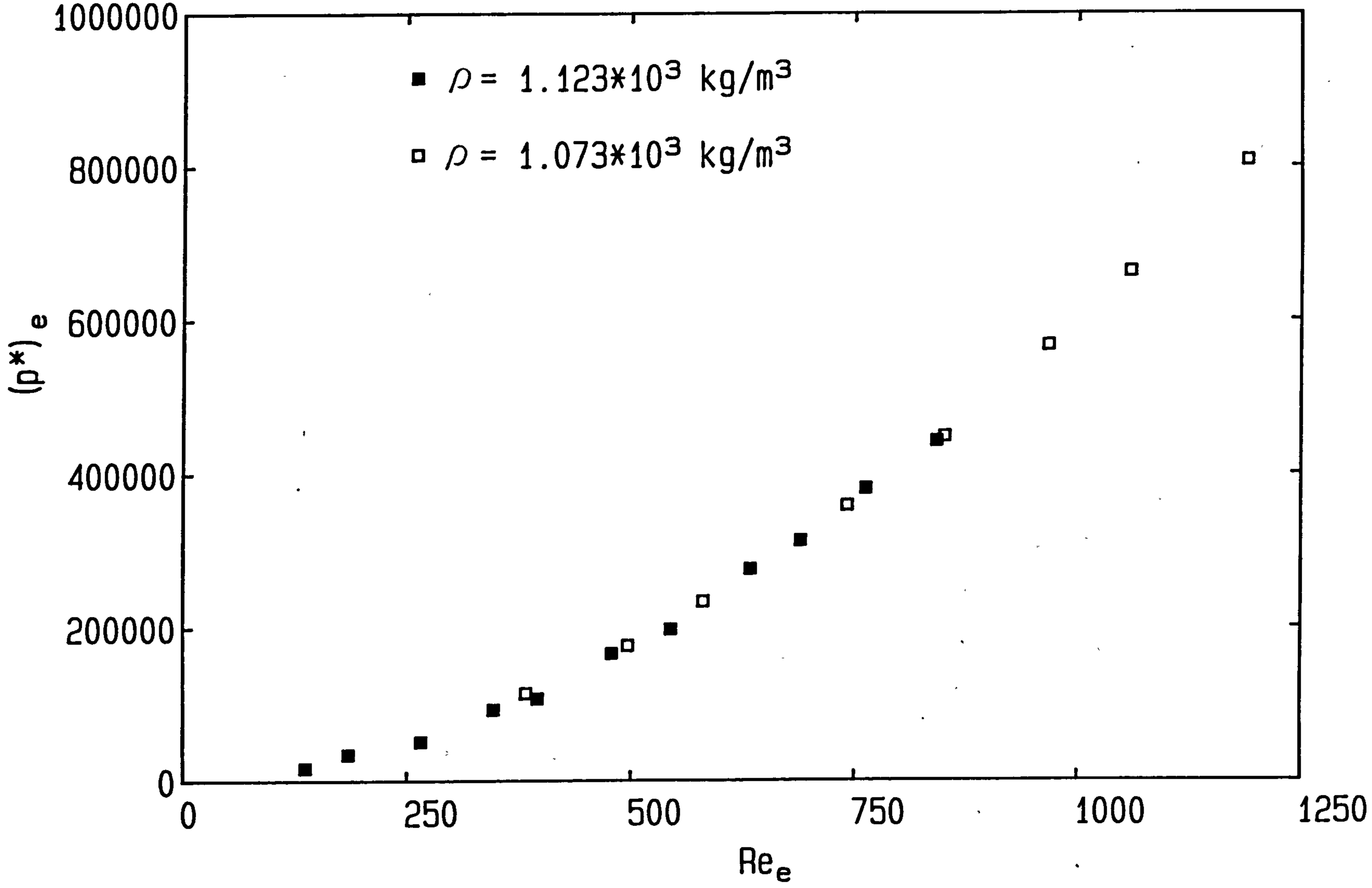

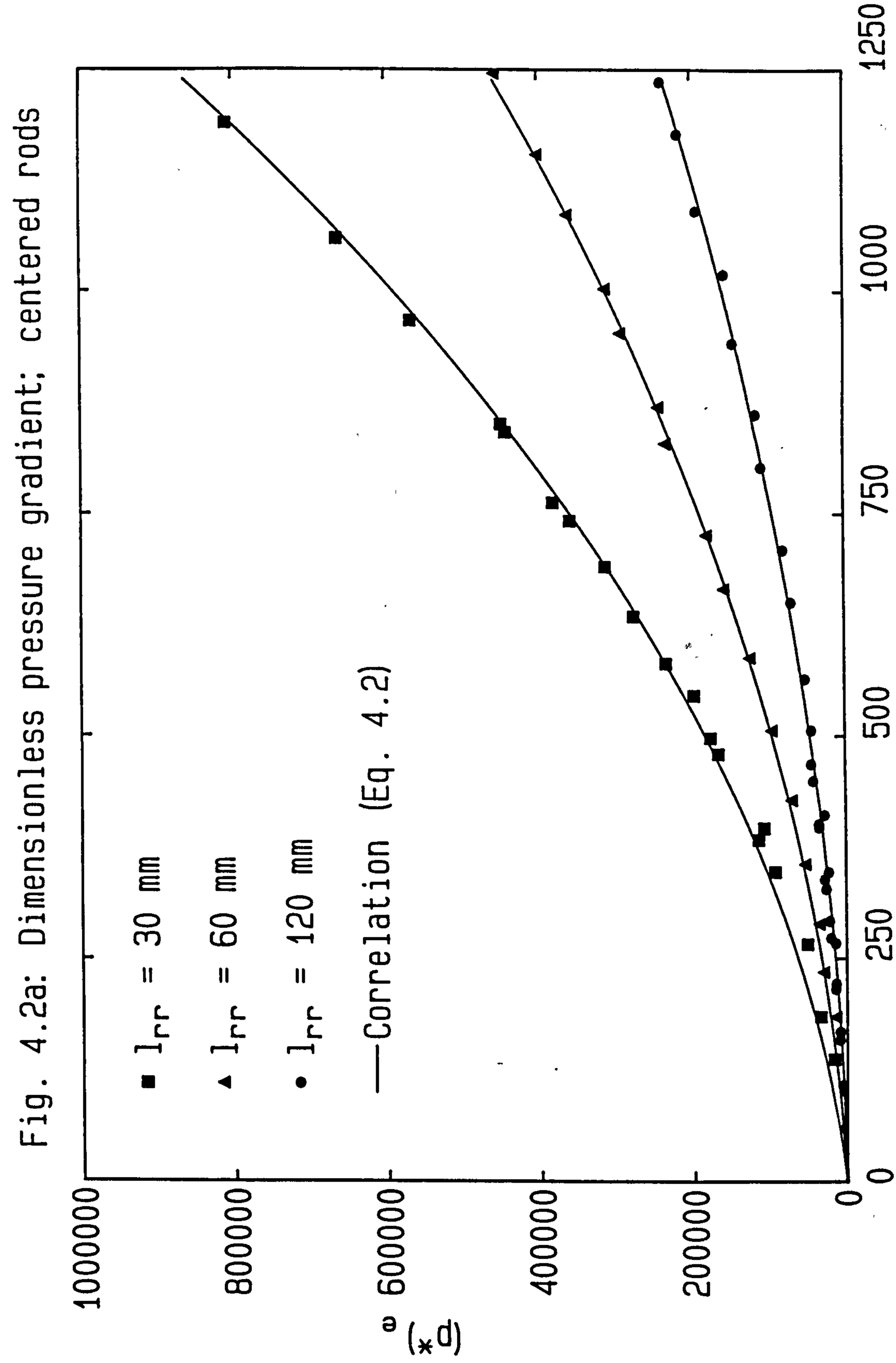

Fig. 4.2a: Dimensionless pressure gradient; centered rods

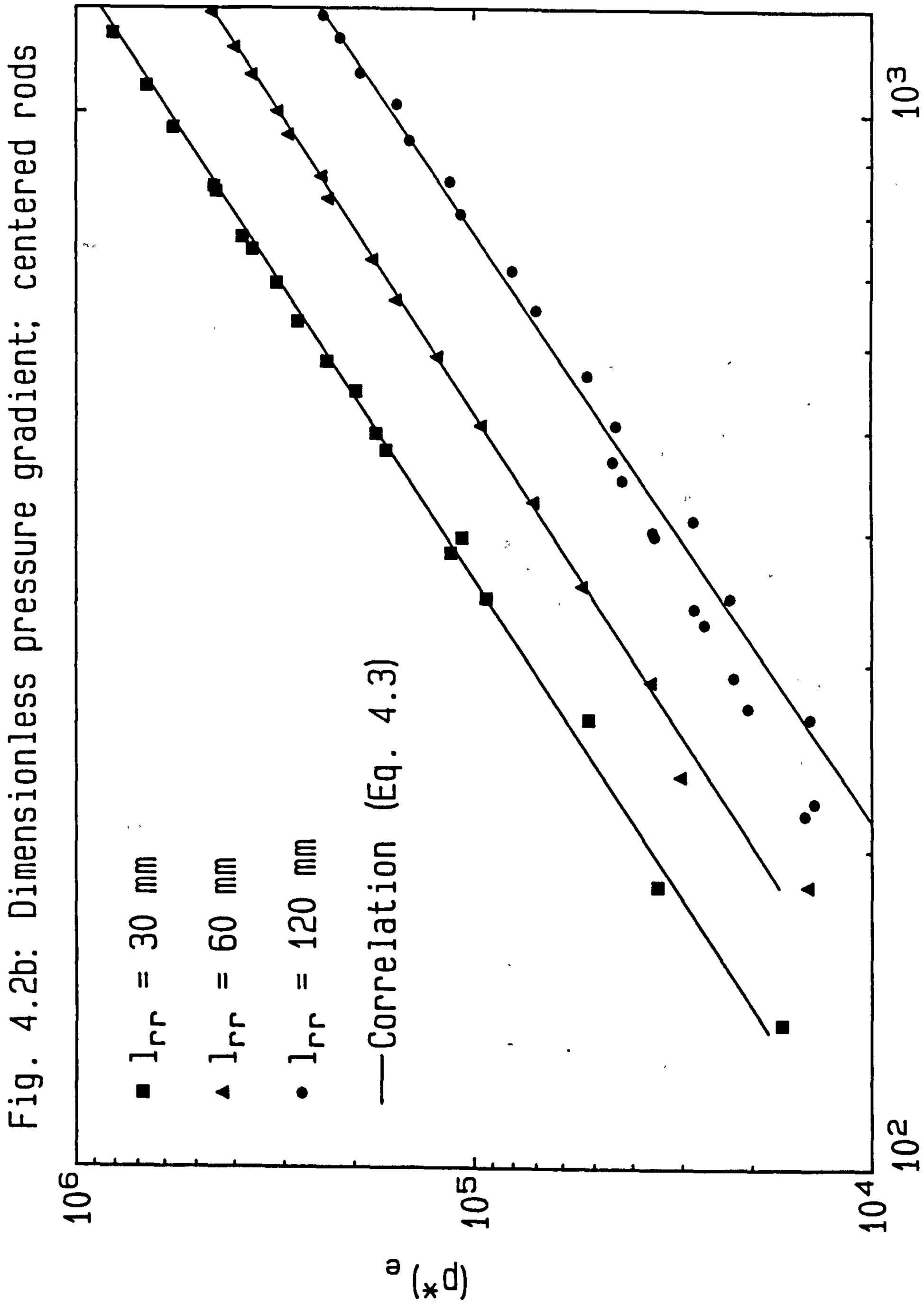
$(p^*)_a$
10^6
10^5
10^4
10^3
10^2
Re_e
l_{rr} = 30 mm
l_{rr} = 60 mm
l_{rr} = 120 mm
Correlation (Eq. 4.3)
Fig. 4.2b: Dimensionless pressure gradient; centered rods

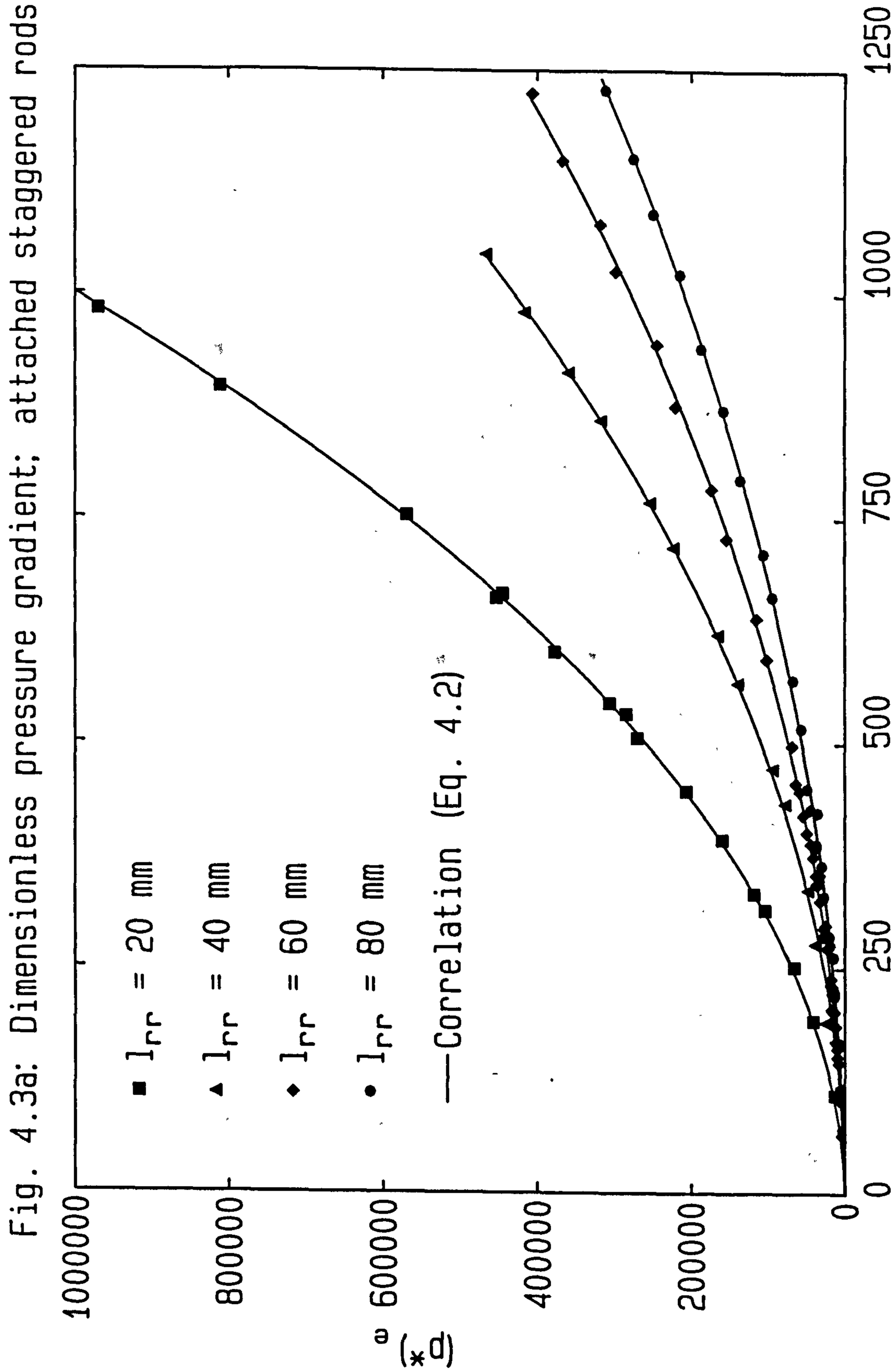
Fig. 4.3a: Dimensionless pressure gradient; attached staggered rods
■ l_{rr} = 20 mm
▲ l_{rr} = 40 mm
◆ l_{rr} = 60 mm
● l_{rr} = 80 mm
—Correlation (Eq. 4.2)
$a^{(*d)}$
1000000
800000
600000
400000
200000
0
0
250
500
750
1000
1250
Re_e

Fig. 4.3b: Dimensionless pressure gradient; attached staggered rods

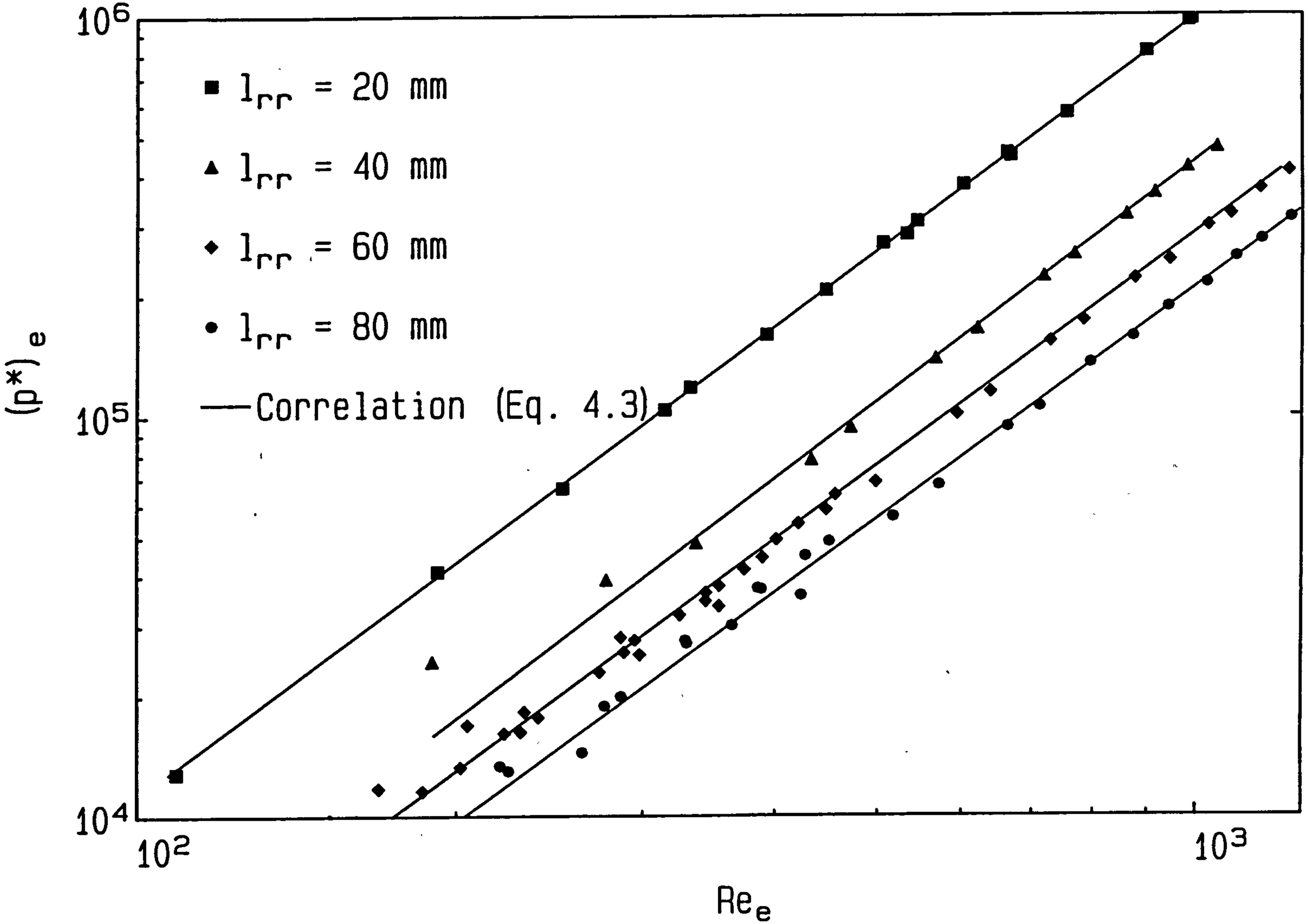

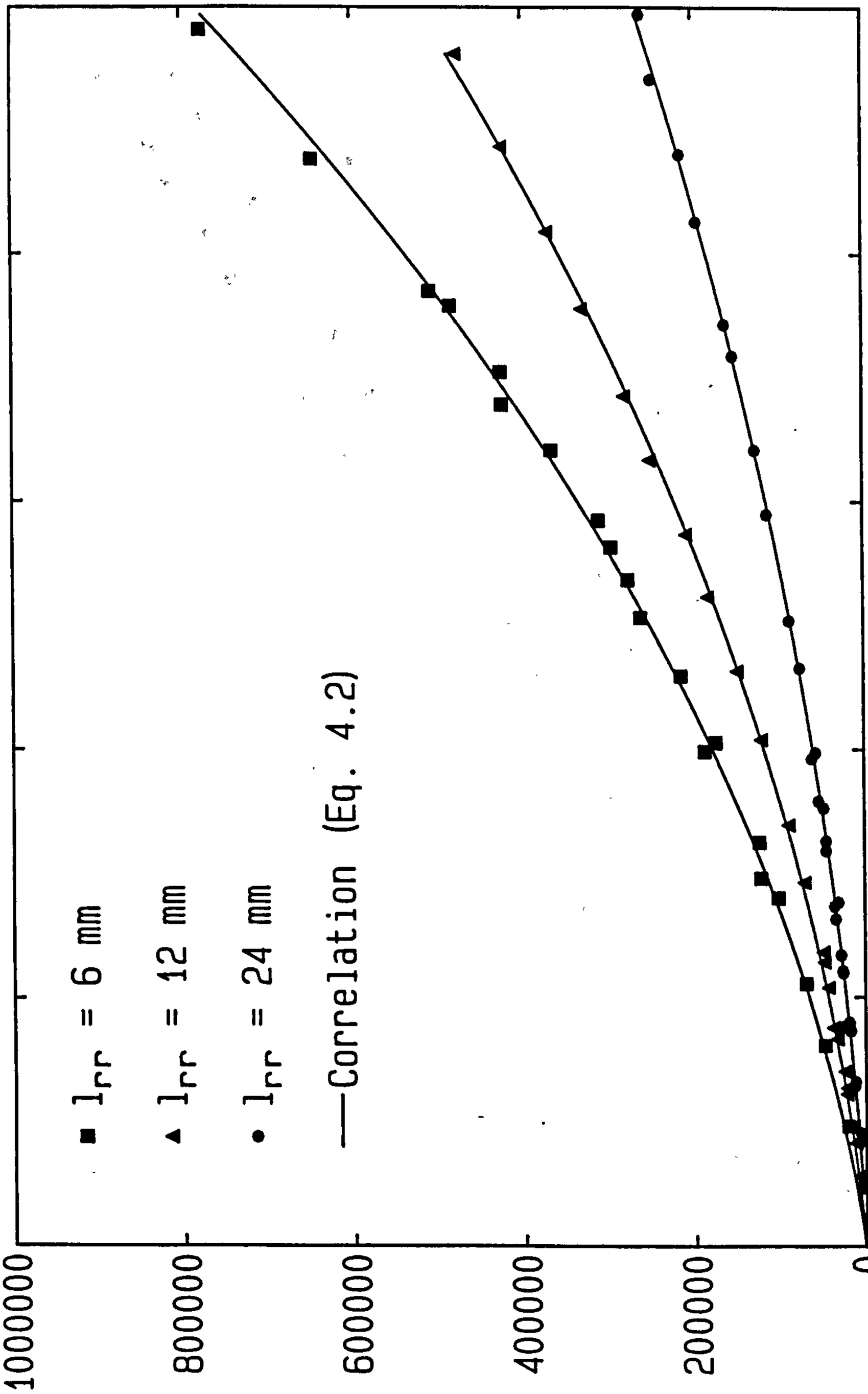
Fig. 4.4a: Dimensionless pressure gradient
Suspended staggered rods, d_{rw} = 3 mm
■ l_{rr} = 6 mm
▲ l_{rr} = 12 mm
● l_{rr} = 24 mm
—Correlation (Eq. 4.2)
$(p^*)_e$
Re_e
1000000
800000
600000
400000
200000
0
0
250
500
750
1000
1250

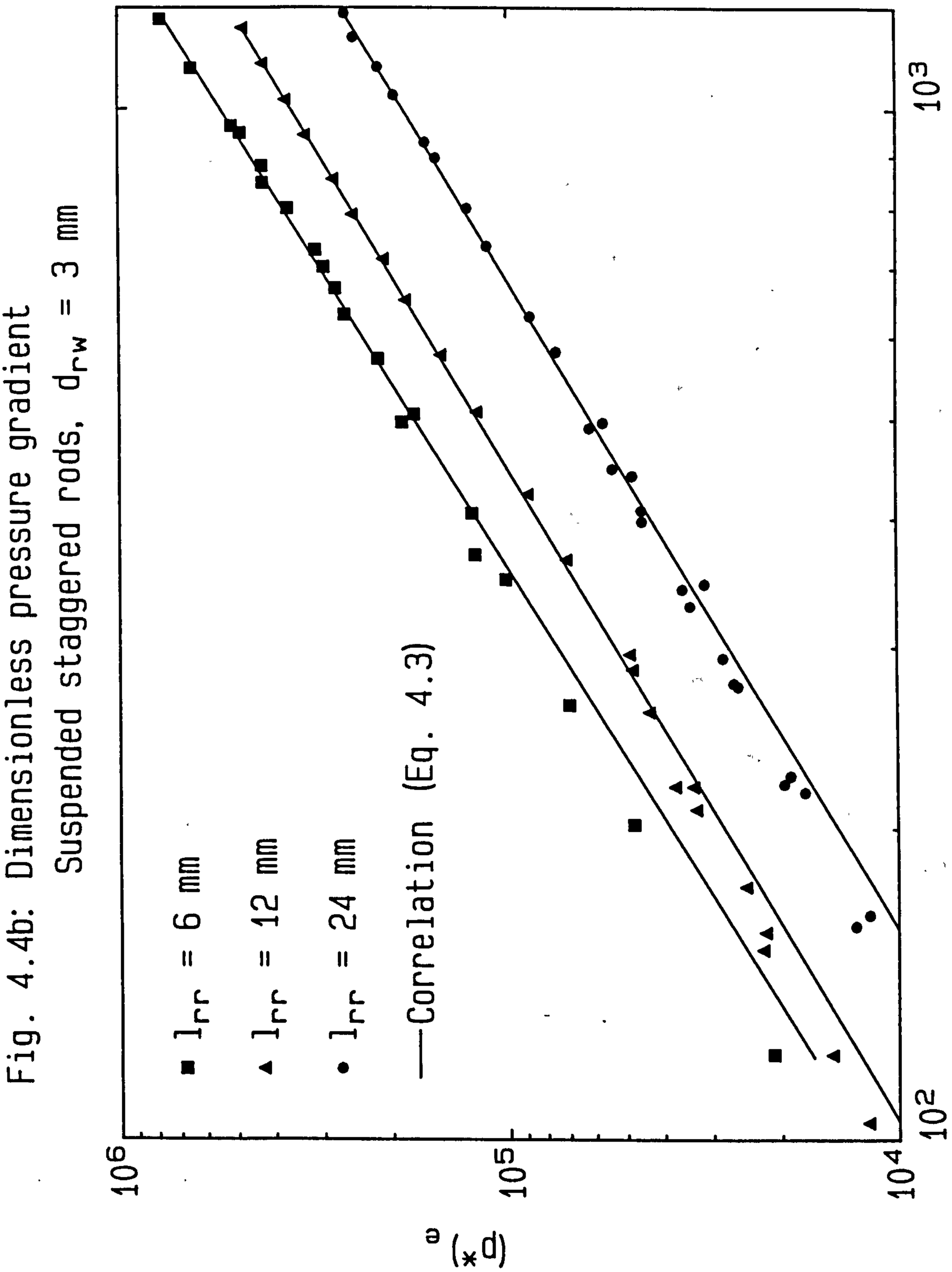
Fig. 4.4b: Dimensionless pressure gradient
Suspended staggered rods, d_{rw} = 3 mm
■ l_{rr} = 6 mm
▲ l_{rr} = 12 mm
● l_{rr} = 24 mm
—Correlation (Eq. 4.3)
$(p^*d)_e$
Re_e
10^6
10^5
10^4
10^3
10^2

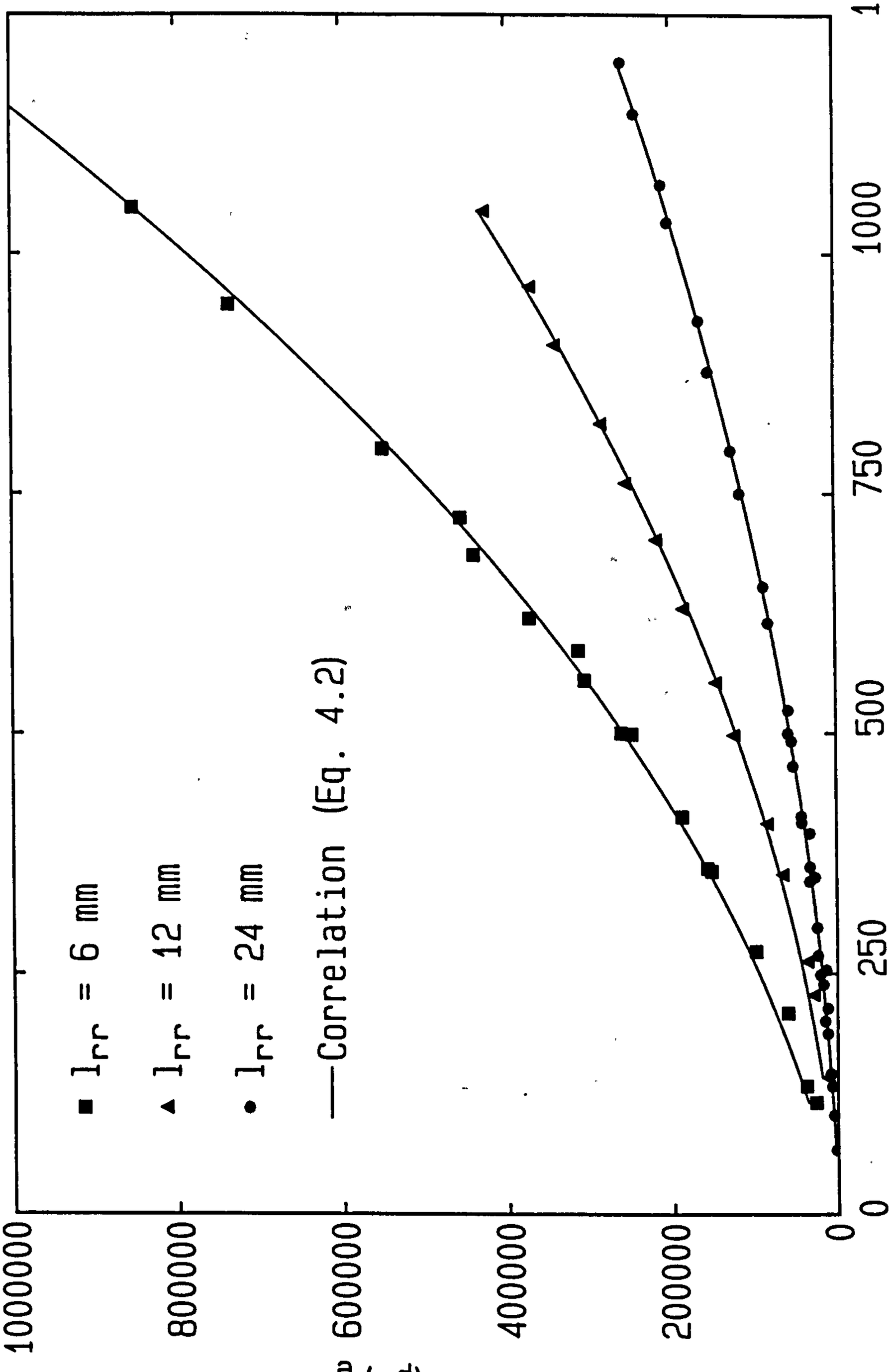

Fig. 4.5a: Dimensionless pressure gradient
Suspended staggered rods, d_{rw} = 2 mm

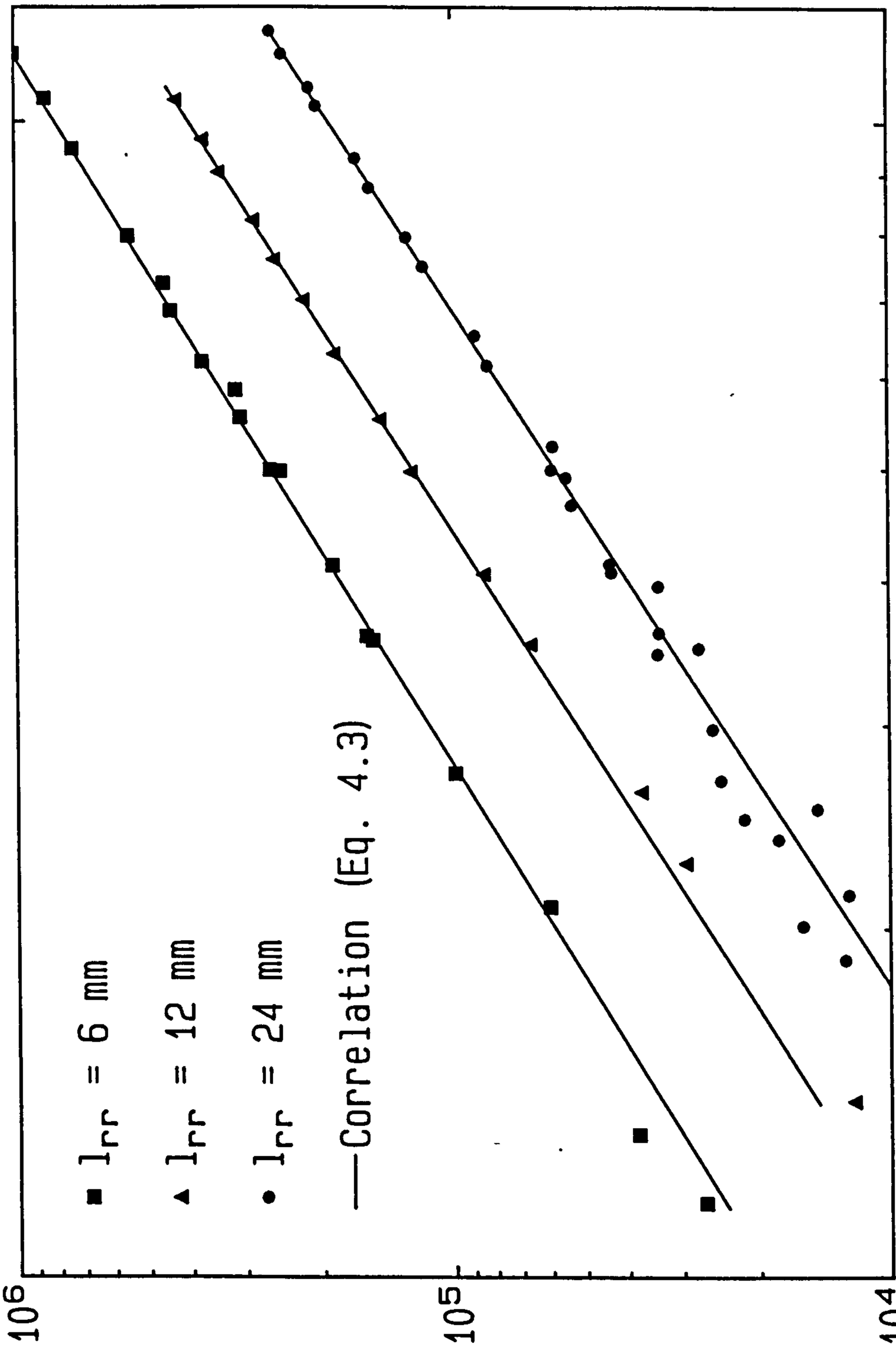
Fig. 4.5b: Dimensionless pressure gradient
Suspended staggered rods, d_{rw} = 2 mm
■ l_{rr} = 6 mm
▲ l_{rr} = 12 mm
● l_{rr} = 24 mm
—Correlation (Eq. 4.3)
$a_{(*d)}$
Re_e
10^6
10^5
10^4
10^3
10^2

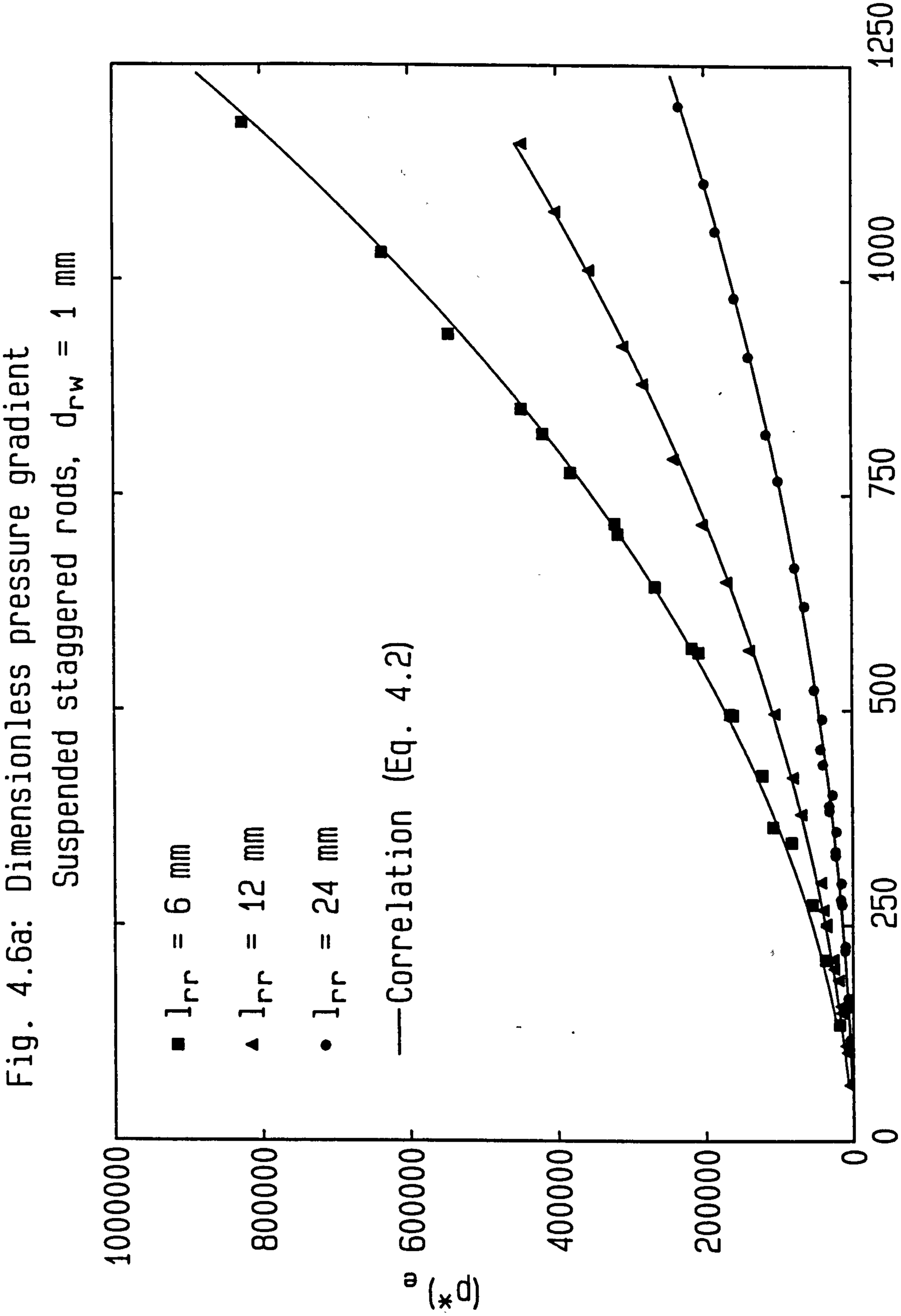

Fig. 4.6a: Dimensionless pressure gradient
Suspended staggered rods, d_{rw} = 1 mm
■ l_{rr} = 6 mm
▲ l_{rr} = 12 mm
● l_{rr} = 24 mm
—Correlation (Eq. 4.2)
$(p^*d)_a$
Re_e

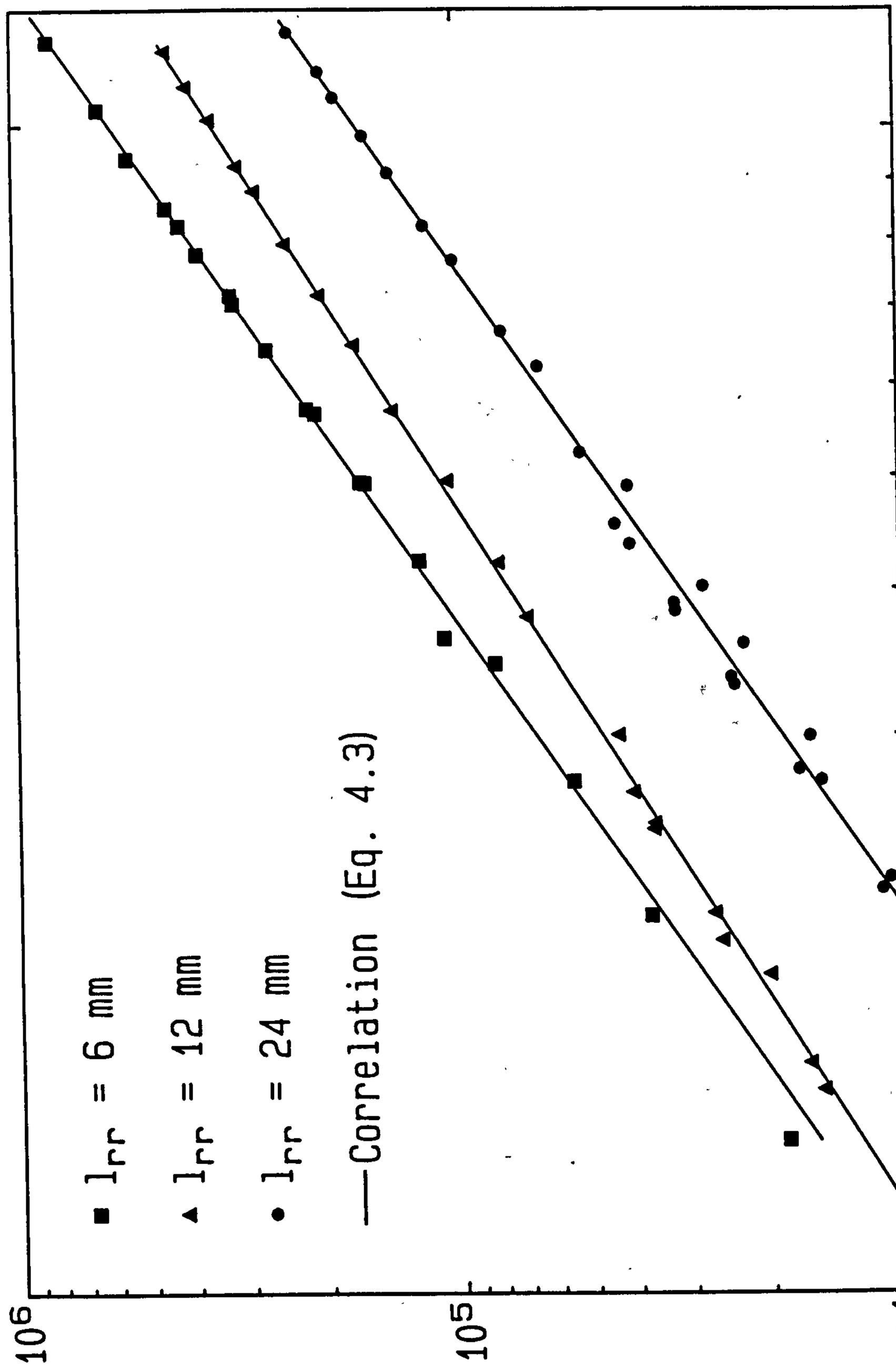

Fig. 4.6b: Dimensionless pressure gradient
Suspended staggered rods, d_{rw} = 1 mm

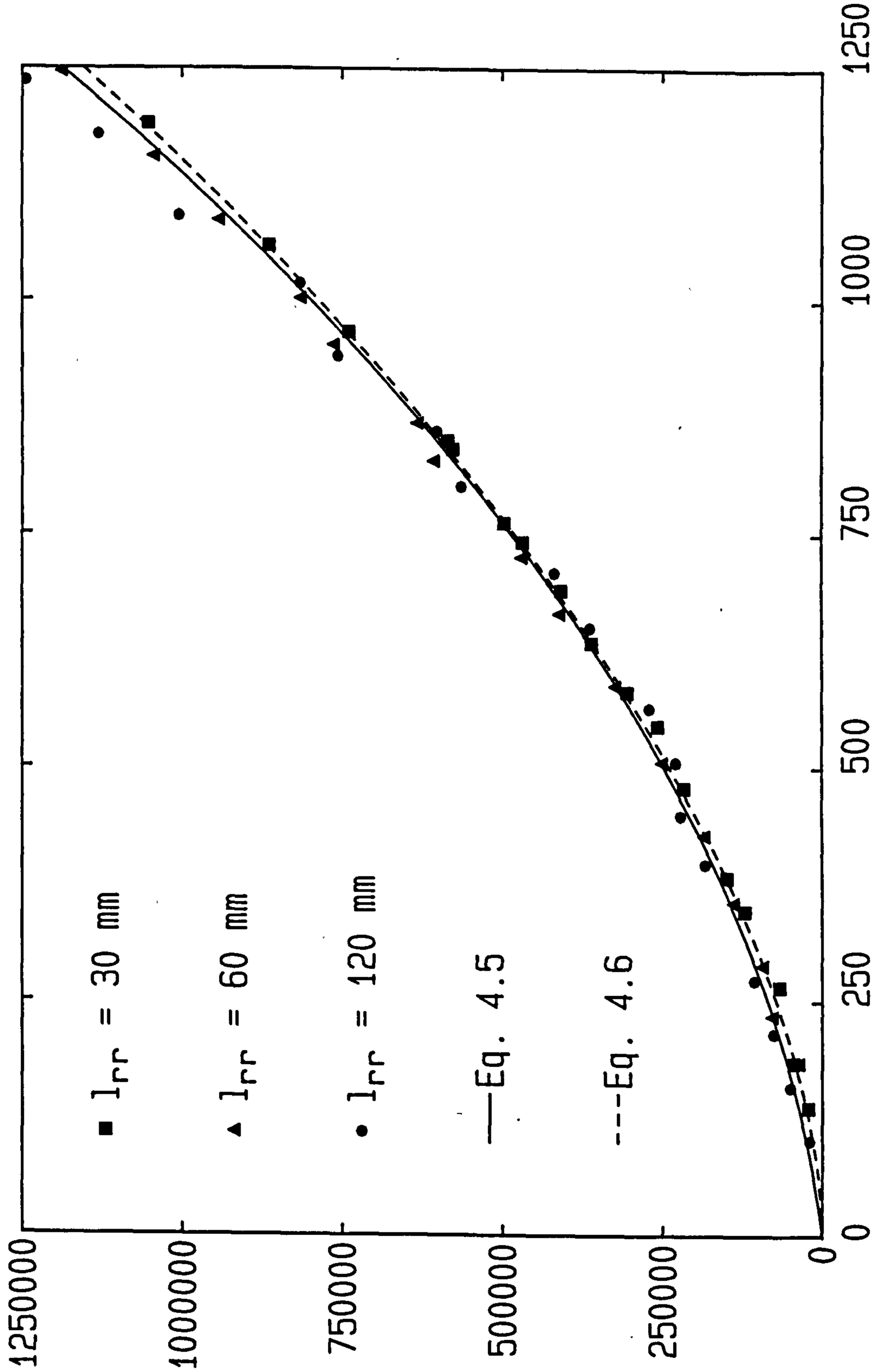

Fig. 4.7: $(p^*)_e$ $l_{rr}/(d_h)_e$ vs Re_e: Centered rods

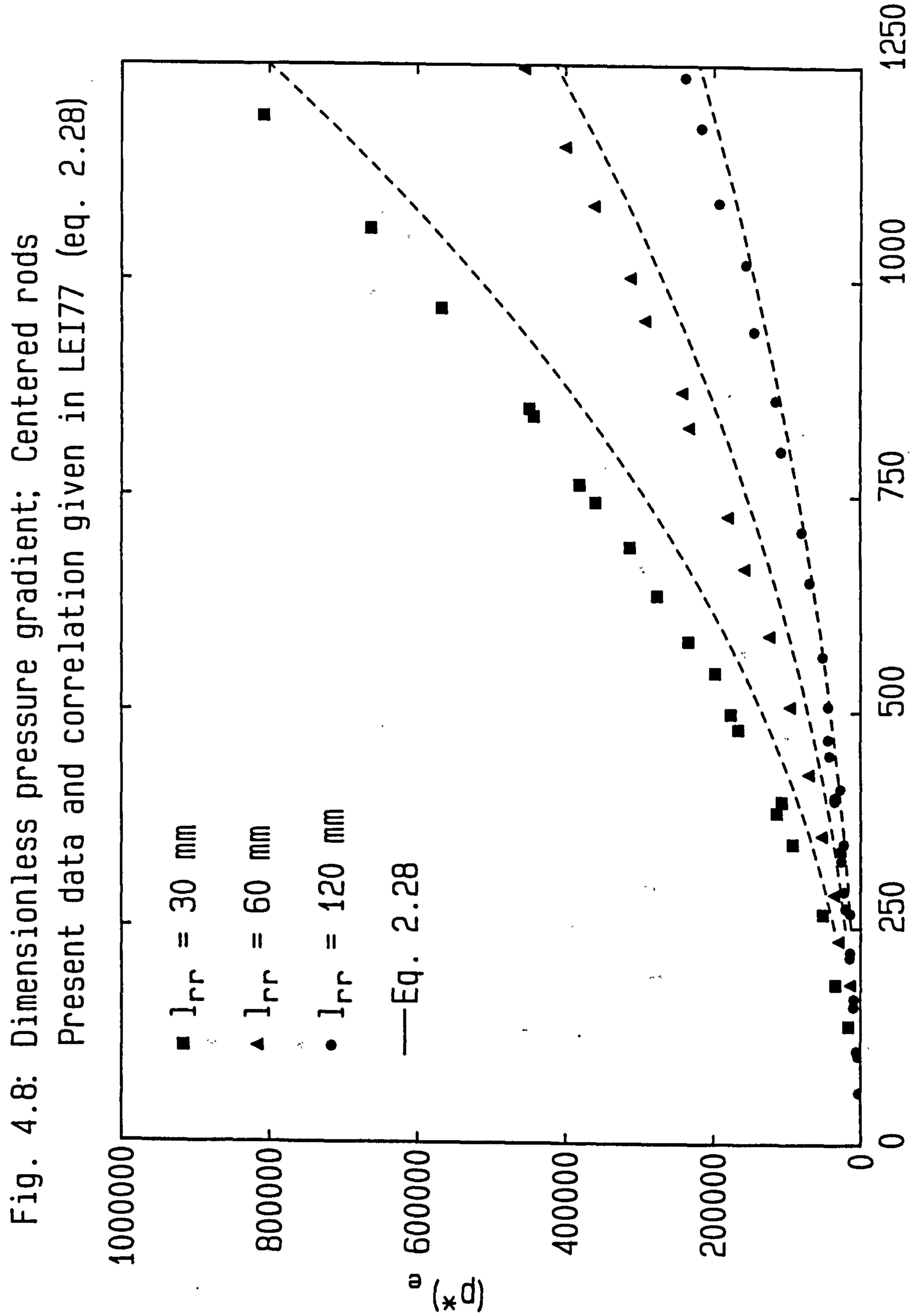

Fig. 4.8: Dimensionless pressure gradient; Centered rods
Present data and correlation given in LEI77 (eq. 2.28)

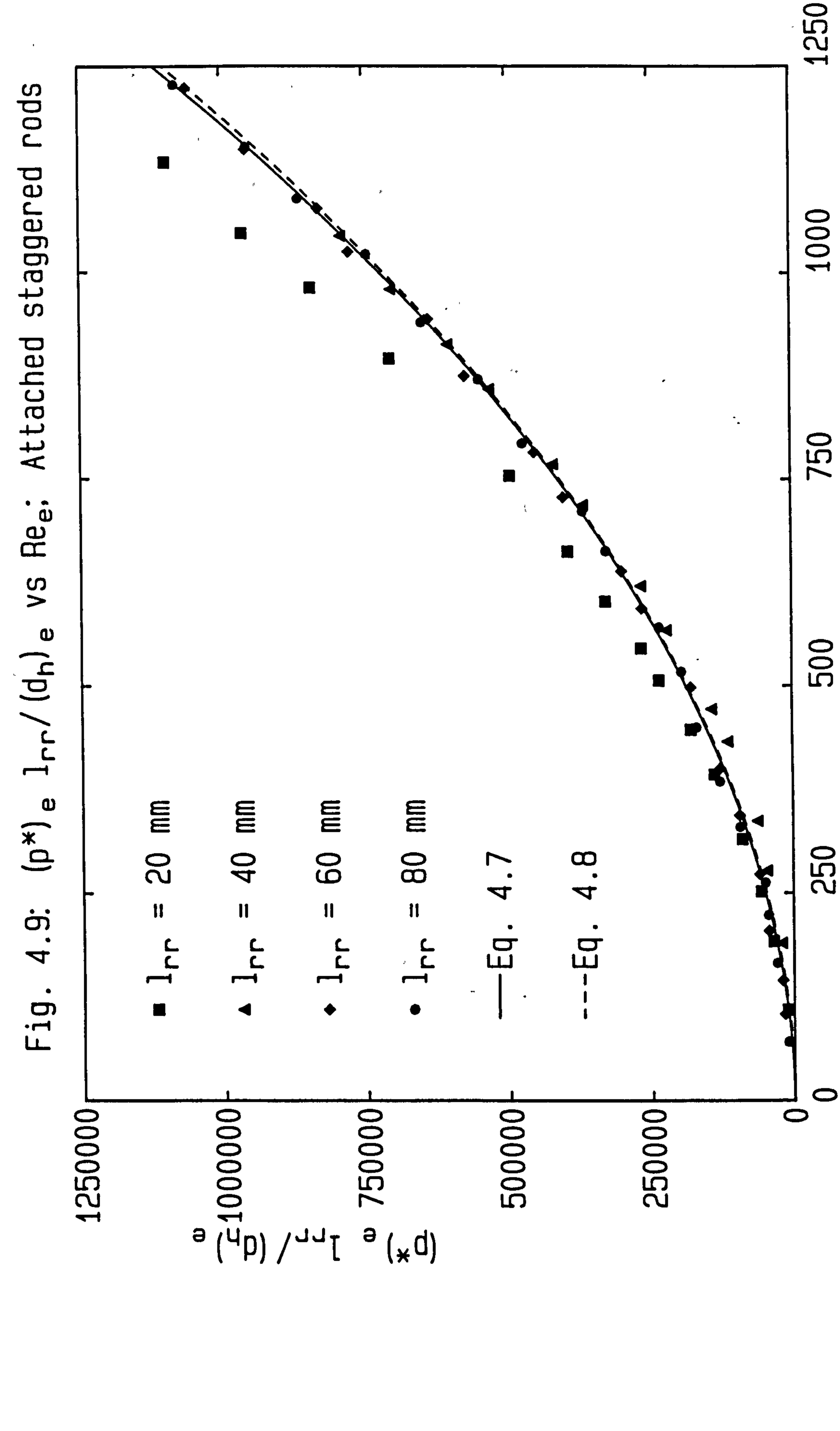

Fig. 4.9: $(p^*)_e$ $l_{rr}/(d_h)_e$ vs Re_e; Attached staggered rods

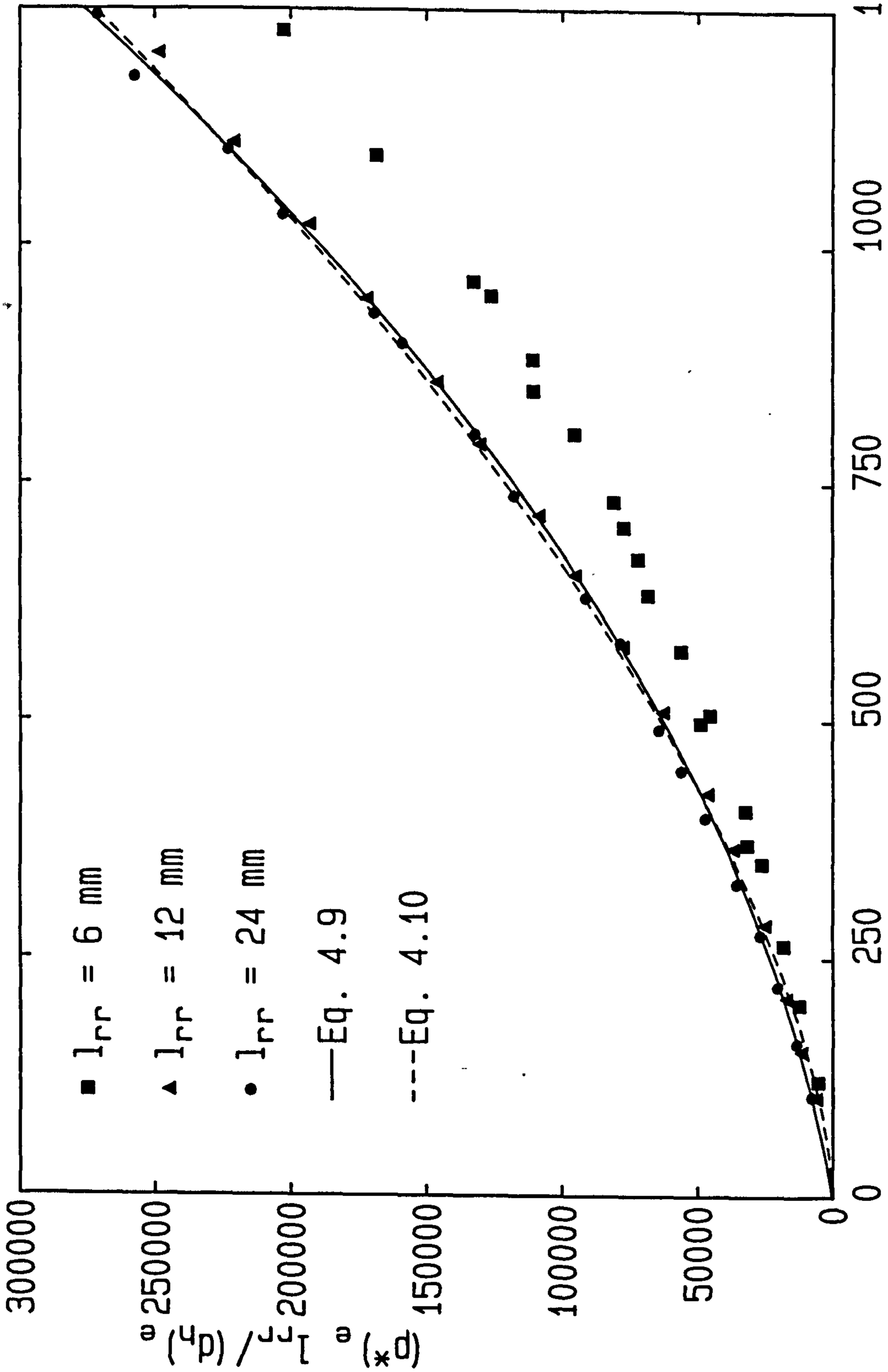

Fig. 4.10: $(p^*)_e$ $l_{rr}/(d_h)_e$ vs Re_e
Suspended staggered rods, d_{rw} = 3 mm

■ l_{rr} = 6 mm
▲ l_{rr} = 12 mm
● l_{rr} = 24 mm
—Eq. 4.9
--Eq. 4.10

Fig. 4.11: $(p^*)_e\ l_{rr}/(d_h)_e$ vs Re_e

Suspended staggered rods, d_{rw} = 2 mm

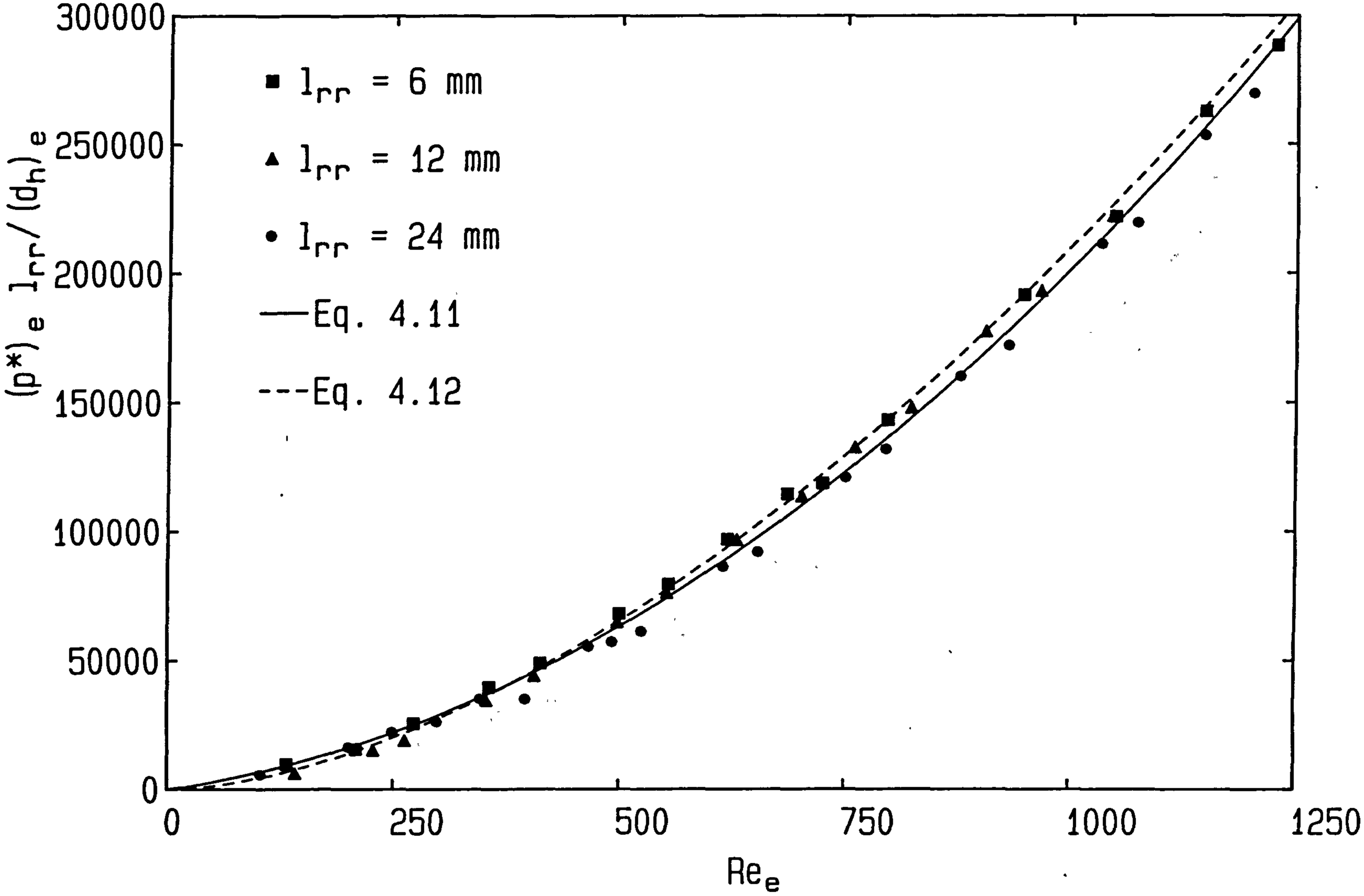

Fig. 4.12: $(p^*)_e\, l_{rr}/(d_h)_e$ vs Re_e
Suspended staggered rods, d_{rw} = 1 mm

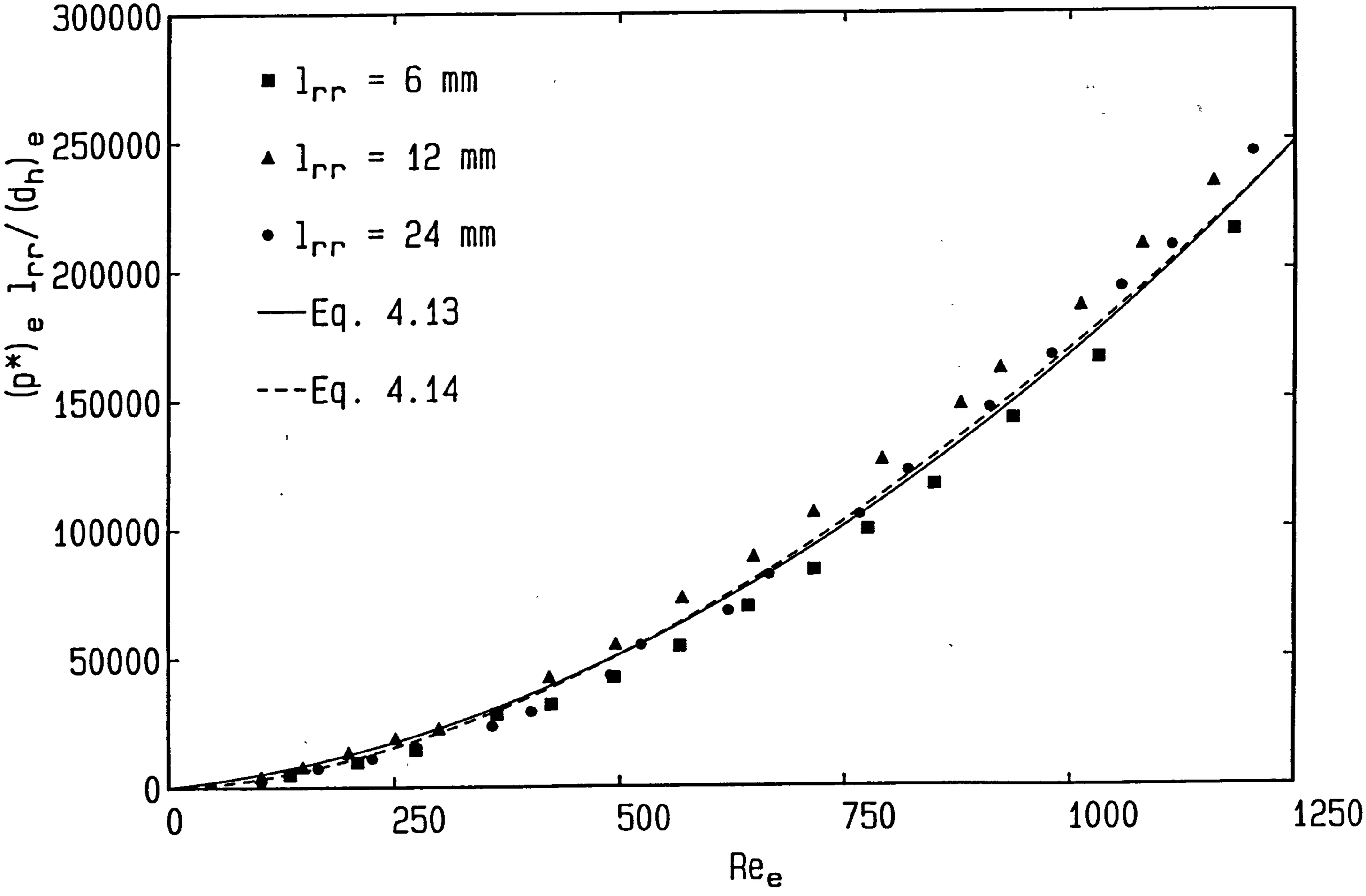

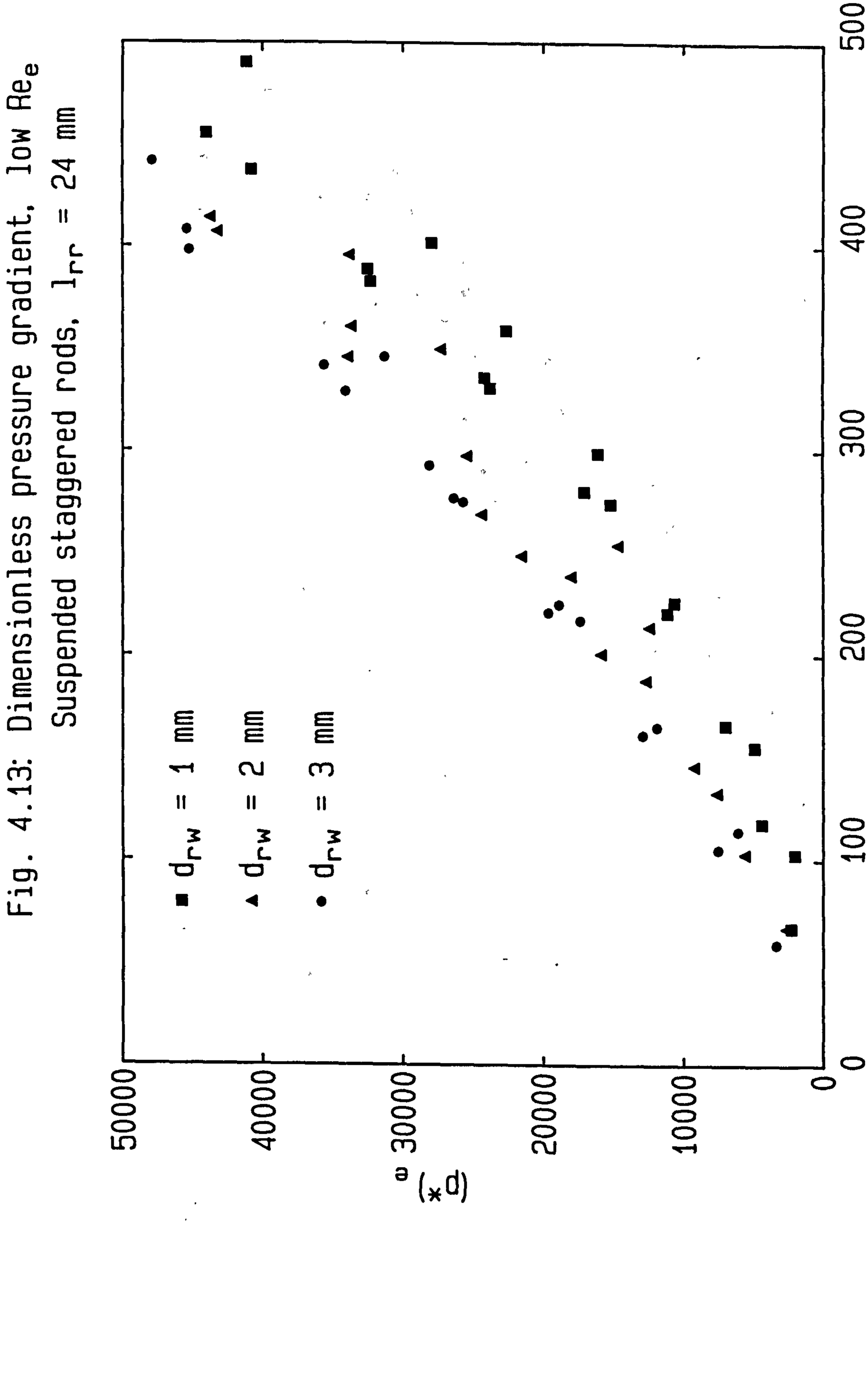

Fig. 4.13: Dimensionle
Suspended

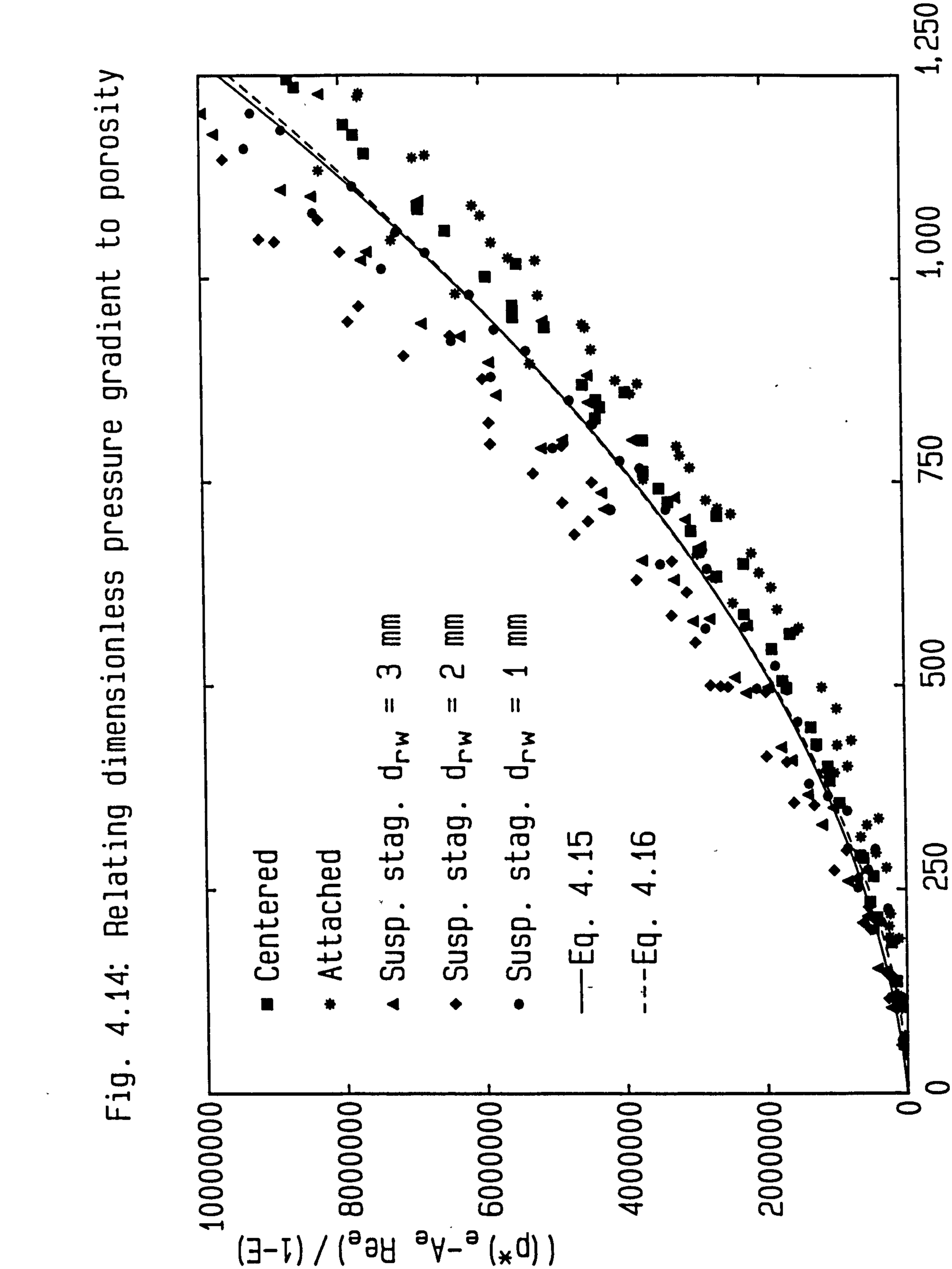
■ Centered
* Attached
▲ Susp. stag. d_{rw} = 3 mm
◆ Susp. stag. d_{rw} = 2 mm
● Susp. stag. d_{rw} = 1 mm
——Eq. 4.15
- - -Eq. 4.16
Fig. 4.14: Relating dimensionless pressure gradient to porosity
$(p^*)\, e^{-A_e\, Re_e} / (1-\varepsilon)$
Re_e
0
250
500
750
1,000
1,250
2000000
4000000
6000000
8000000
10000000

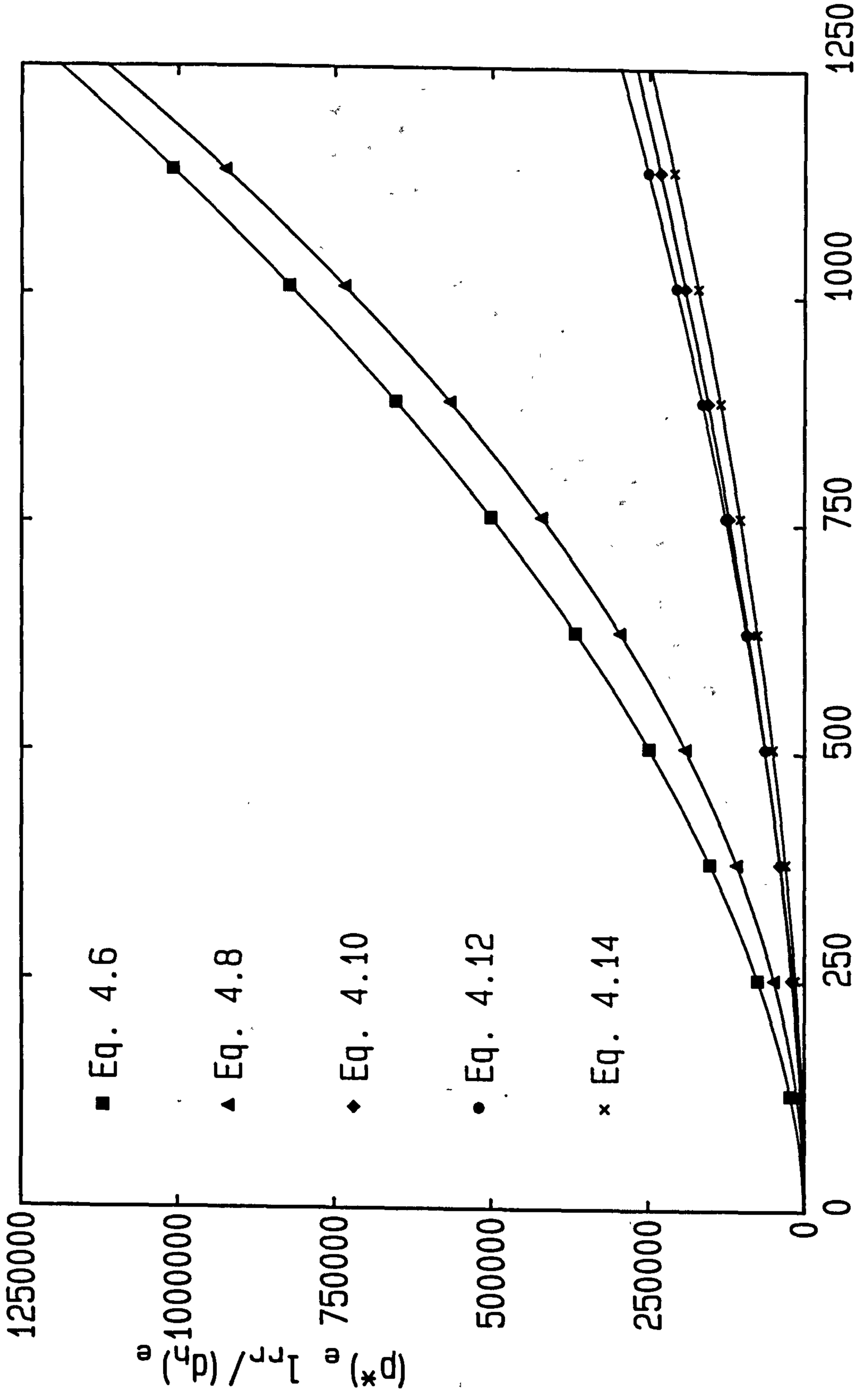

Fig. 4.15: Comparison of the dimensionless pressure gradient correlations

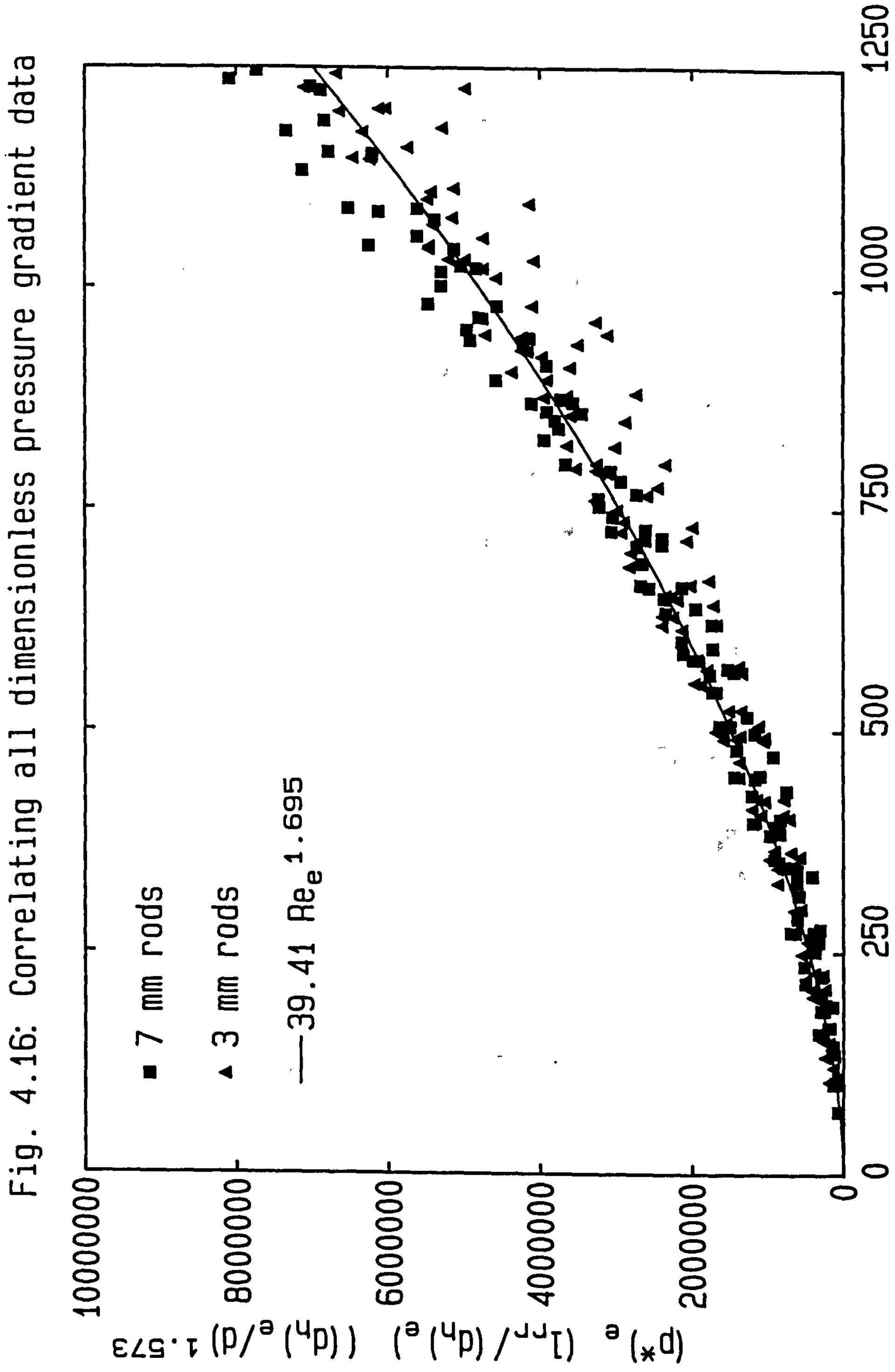
Fig. 4.16: Correlating all dimensionless pressure gradient data
■ 7 mm rods
▲ 3 mm rods
—39.41 $Re_e^{1.695}$
$(p^*)_e$ $(1_{rr}/(d_h)_e)$ $((d_h)_e/d)$ 1.573
10000000
8000000
6000000
4000000
2000000
0
0
250
500
750
1000
1250
Re_e

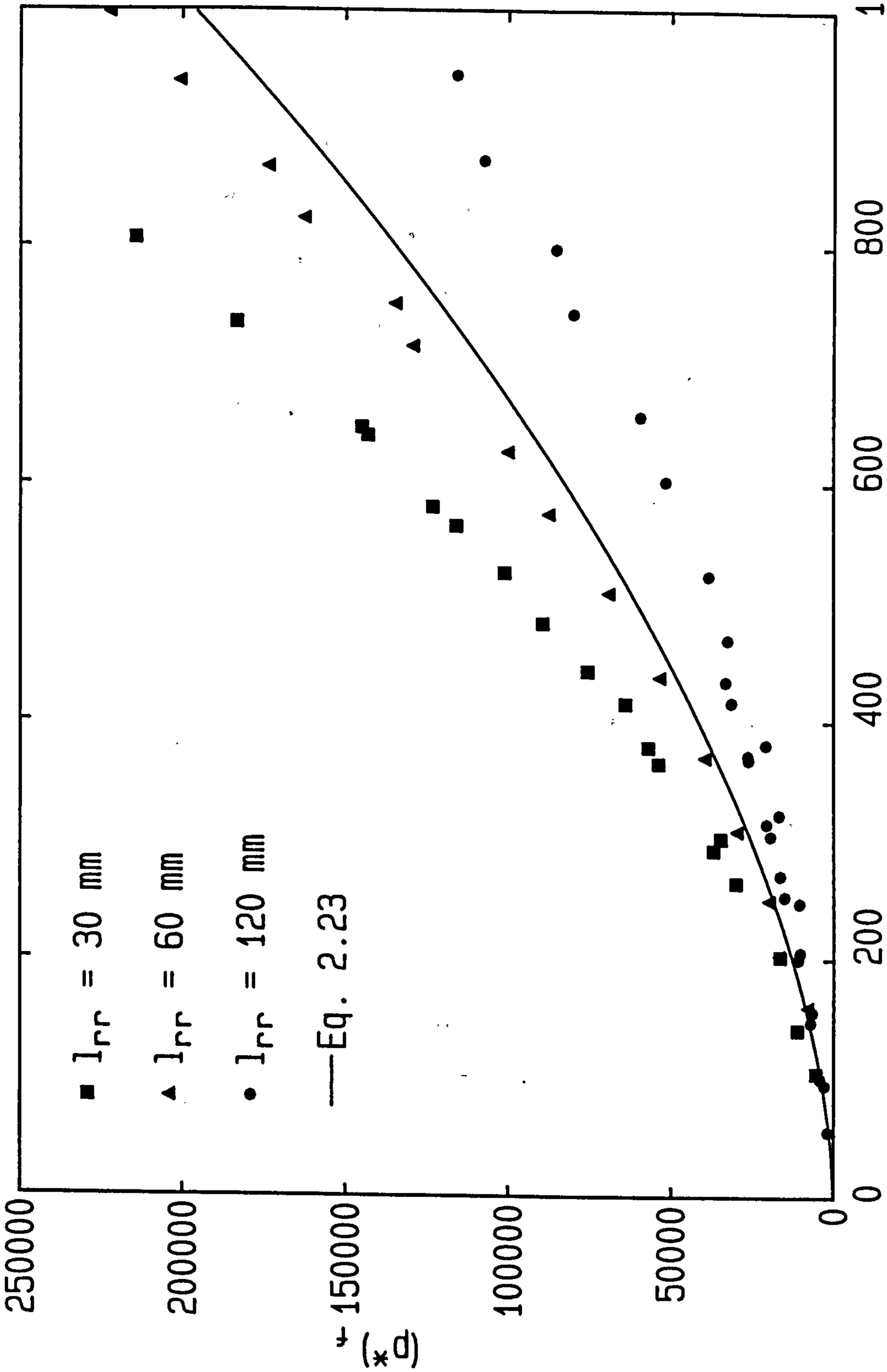

Fig. 4.17: Dimensionless pressure gradient; Centered rods
'Filled channel' parameters

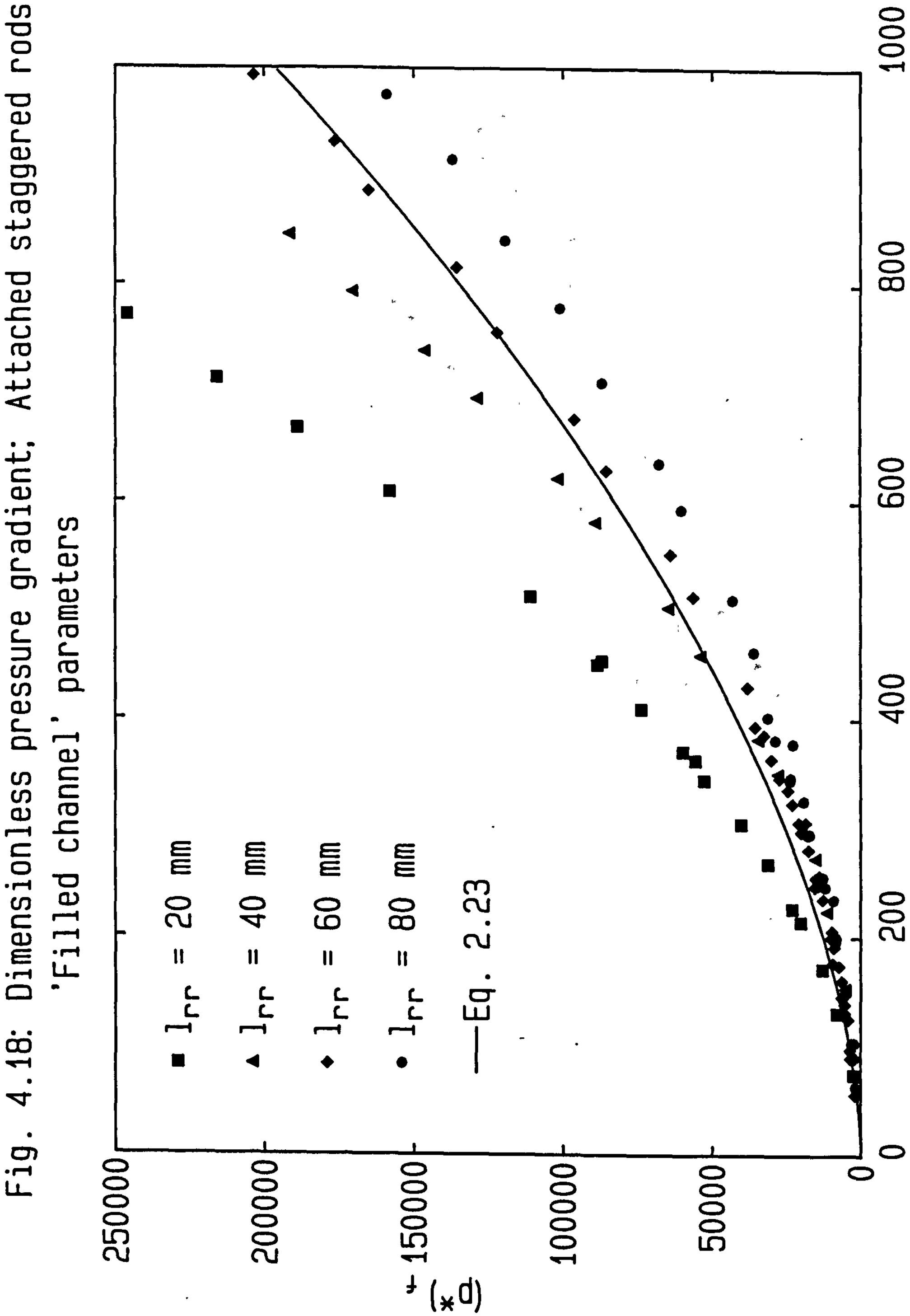

Fig. 4.18: Dimensionless pressure gradient; Attached staggered rods 'Filled channel' parameters

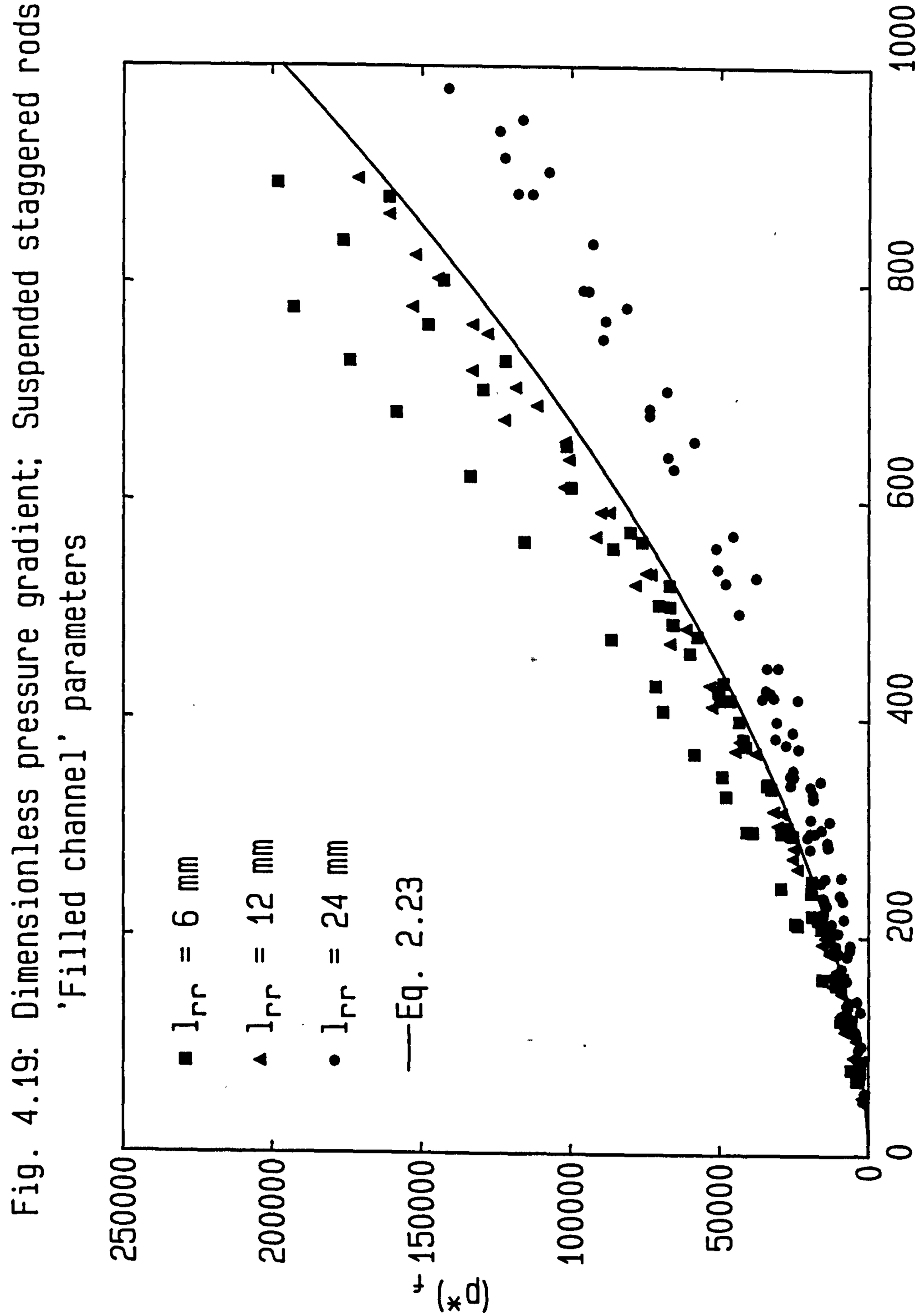

Fig. 4.19: Dimensionless pressure gradient; Suspended staggered rods 'Filled channel' parameters

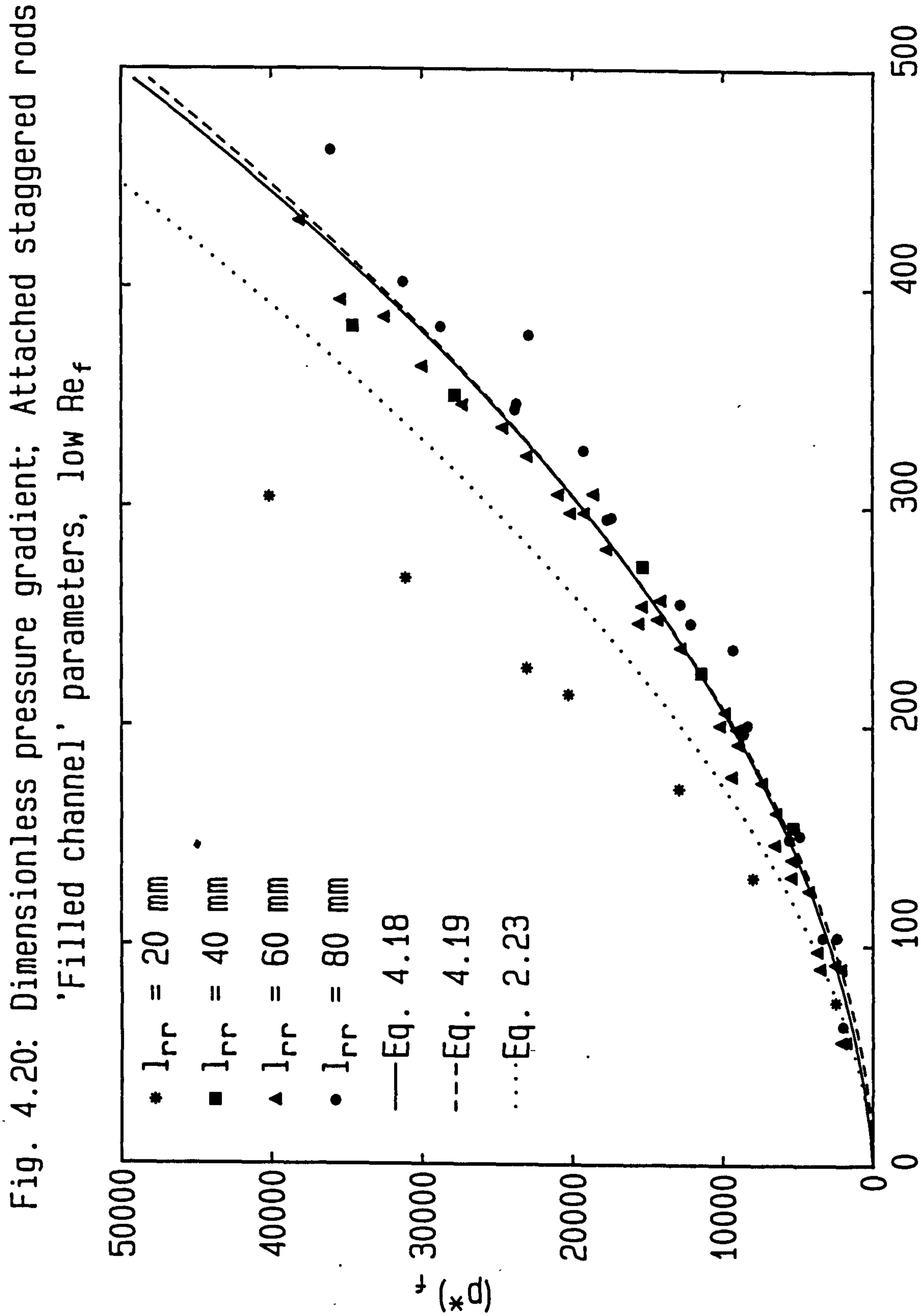

Fig. 4.20: Dimensionless pressure gradient; Attached s
'Filled channel' parameters, low Re_f

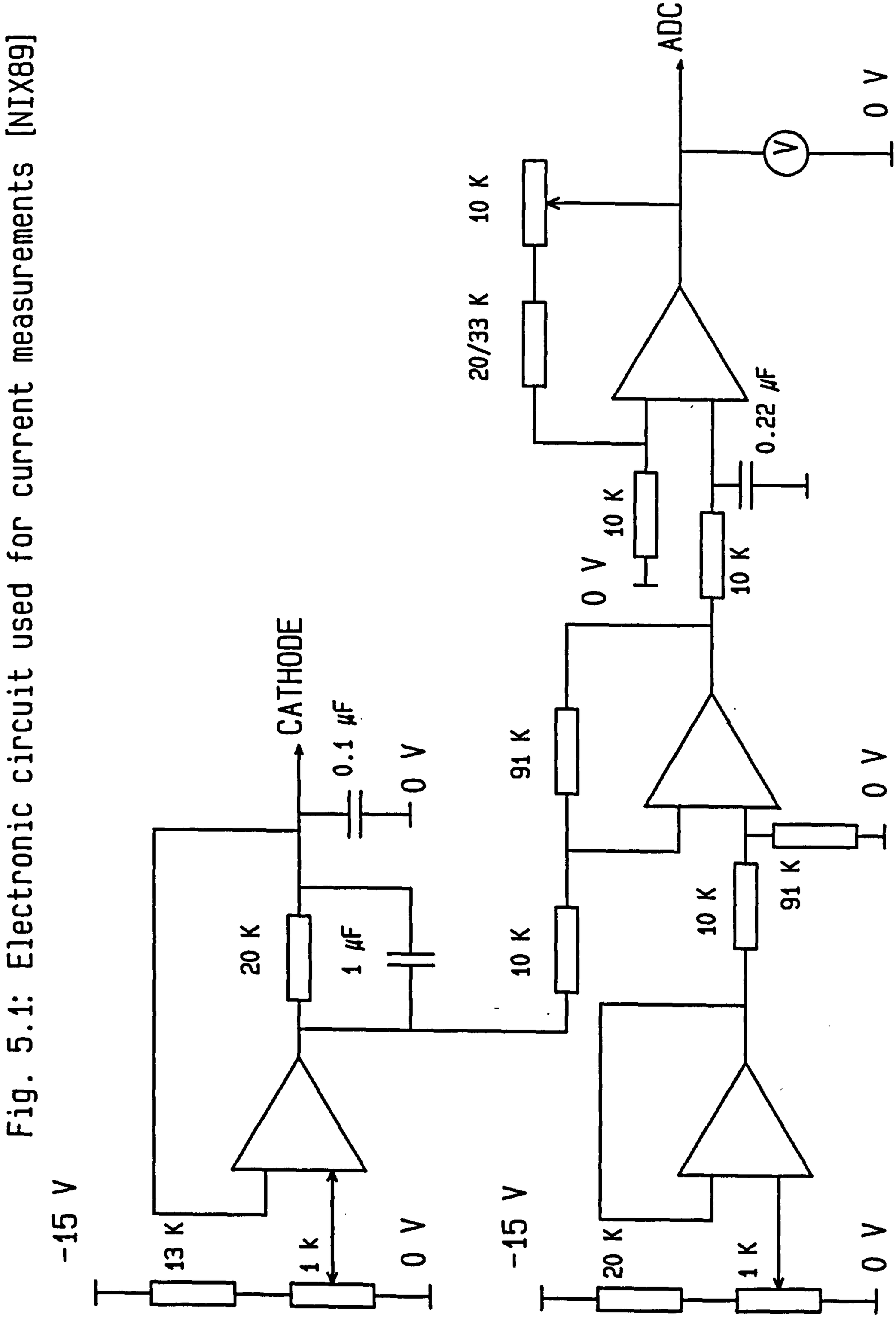

Fig. 5.1: Electronic circuit used for current measurements [NIX89]

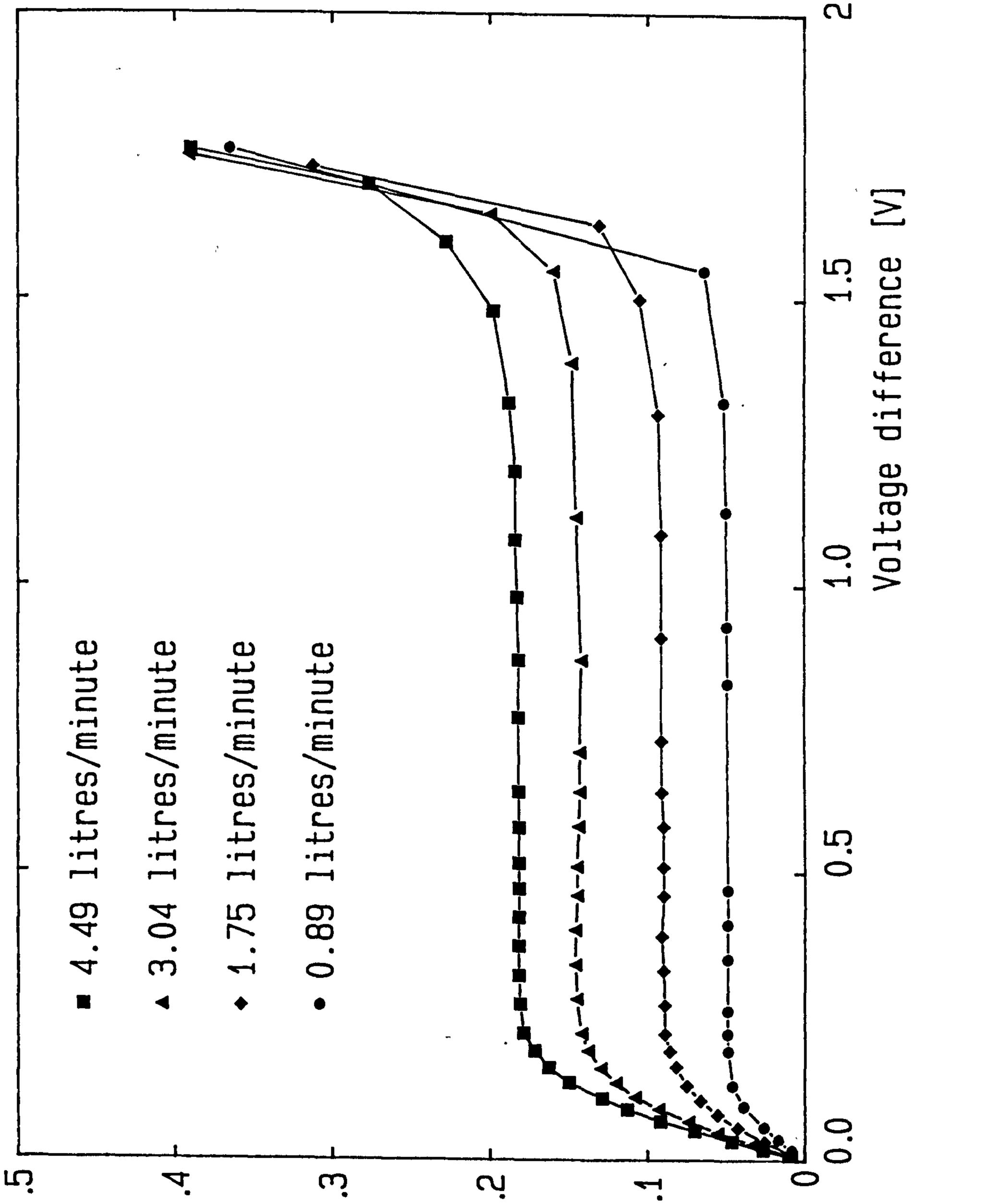

Fig. 5.2: Polarisation curves at different flow rates
Centered rods, l_{rr} = 30 mm, large electrode

Fig. 5.3: Spectrophotometer calibration curve, λ = 420 nm

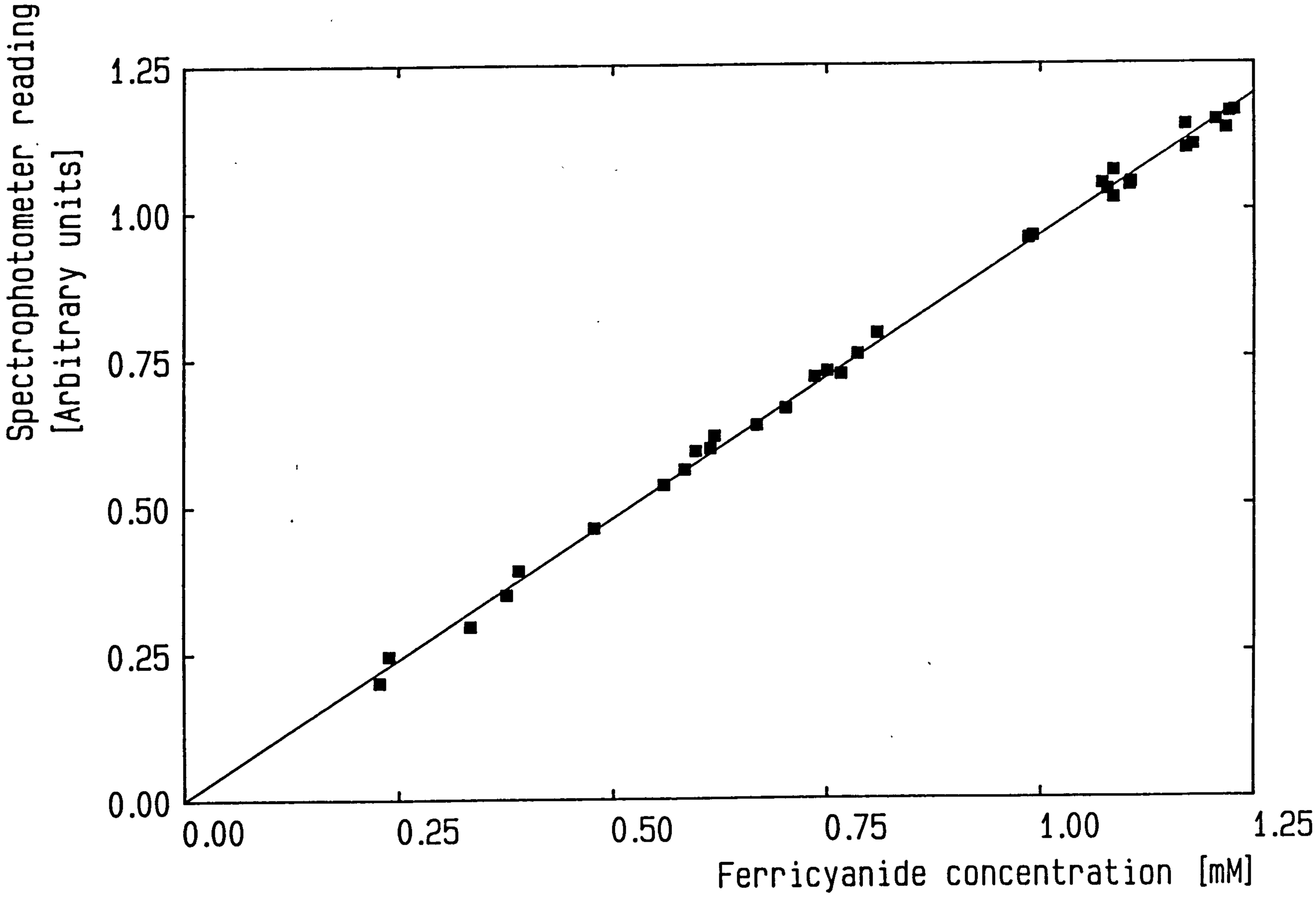

Fig. 5.4: Day-to-day variation in ferricyanide concentration

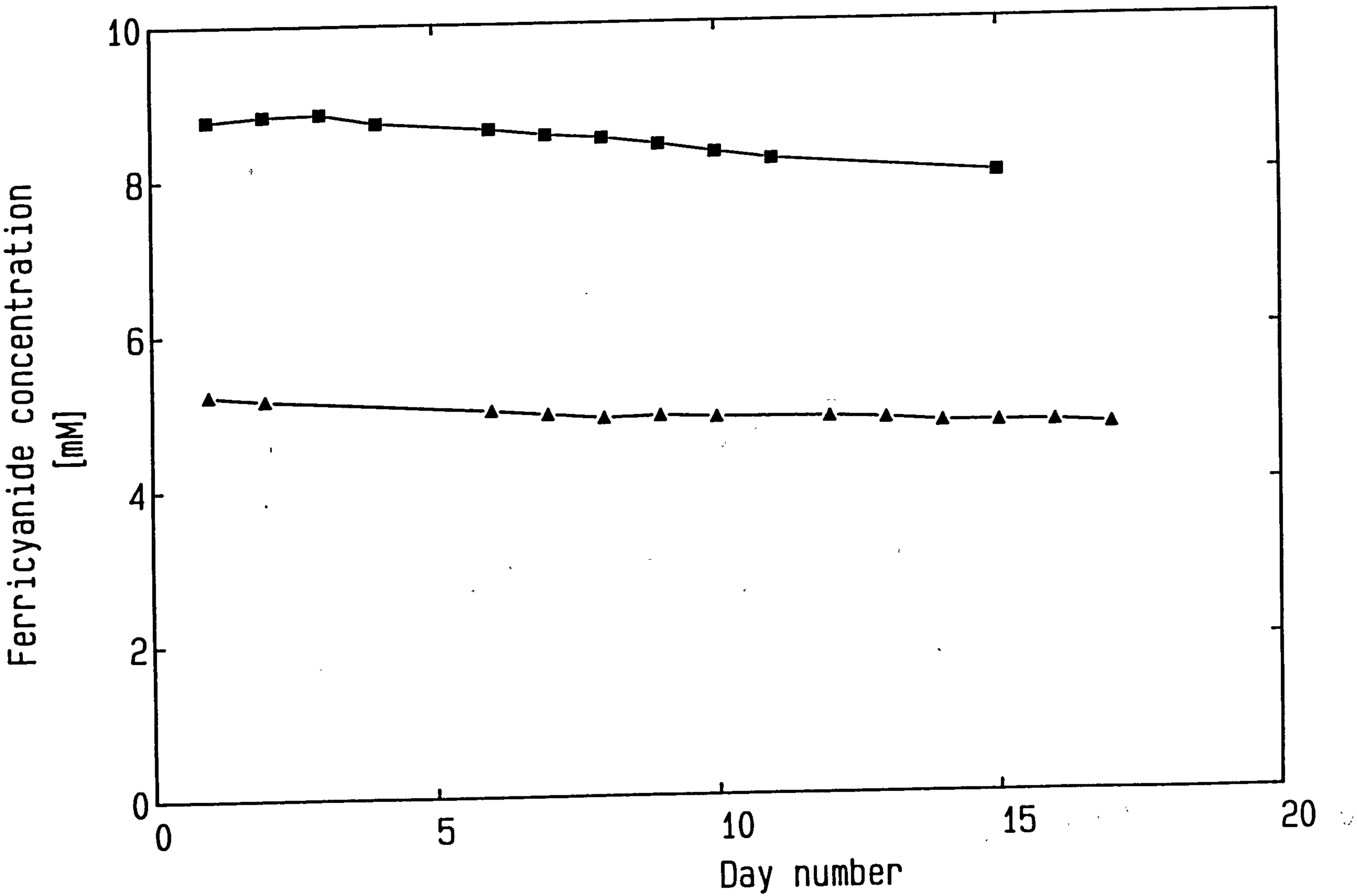

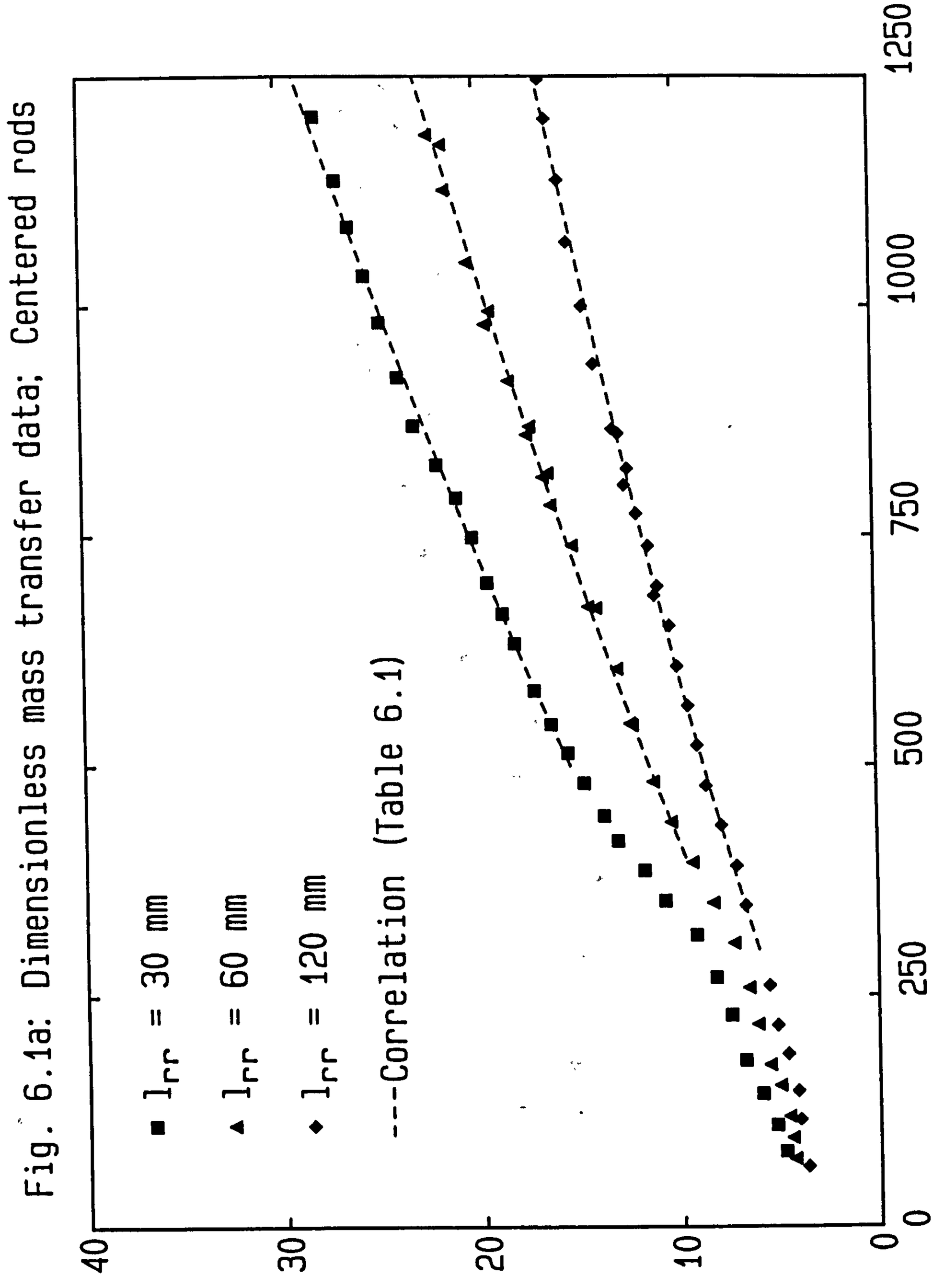
Fig. 6.1a: Dimensionless mass transfer data; Centered rods
■ l_{rr} = 30 mm
▲ l_{rr} = 60 mm
◆ l_{rr} = 120 mm
---Correlation (Table 6.1)
$Sh_e/Sc^{1/3}$
Re_e
0
250
500
750
1000
1250
10
20
30
40

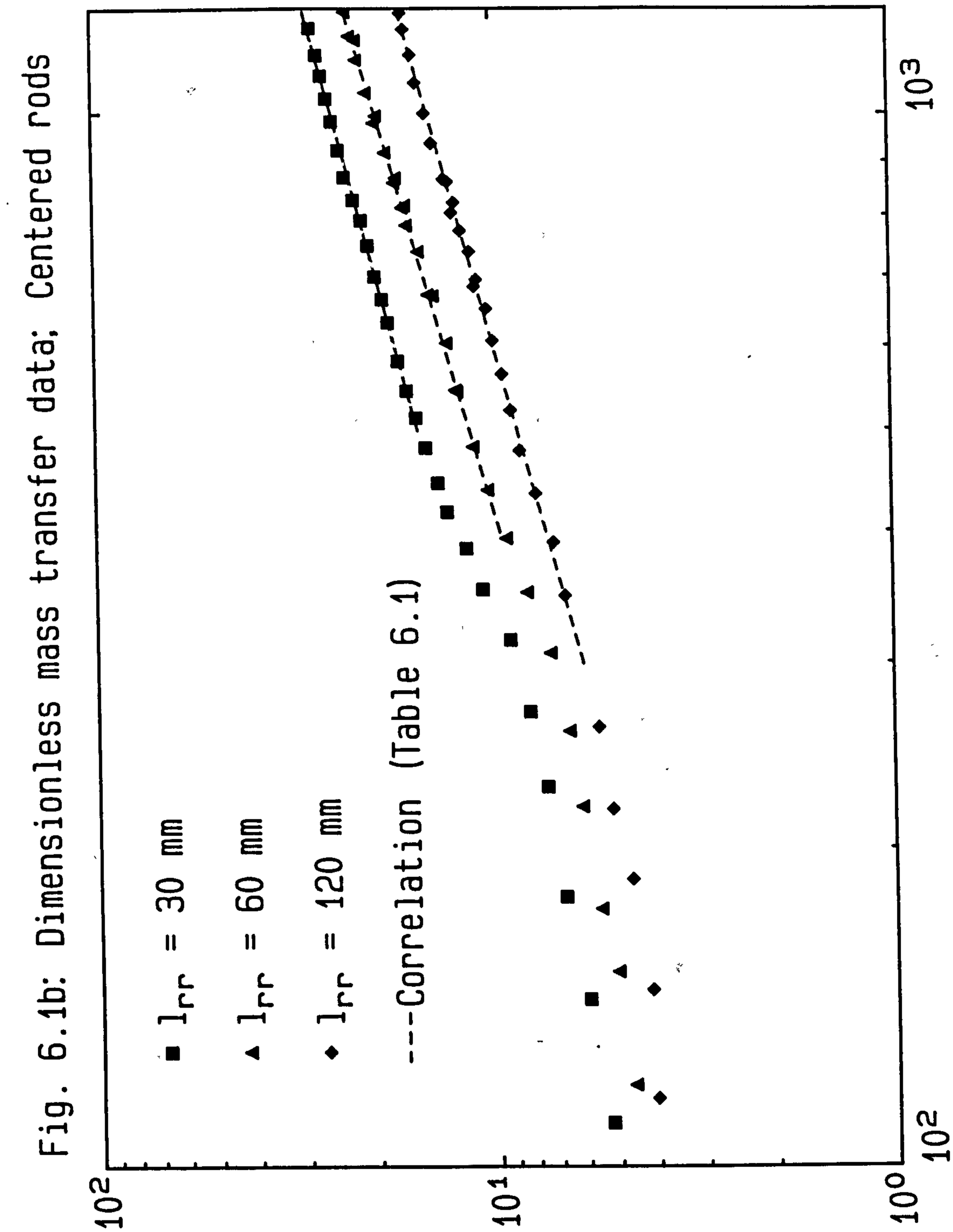
Fig. 6.1b: Dimensionless mass transfer data; Centered rods
■ l_{rr} = 30 mm
▲ l_{rr} = 60 mm
◆ l_{rr} = 120 mm
---Correlation (Table 6.1)
$Sh_e/Sc^{1/3}$
Re_e
10^2
10^1
10^0
10^3
10^2

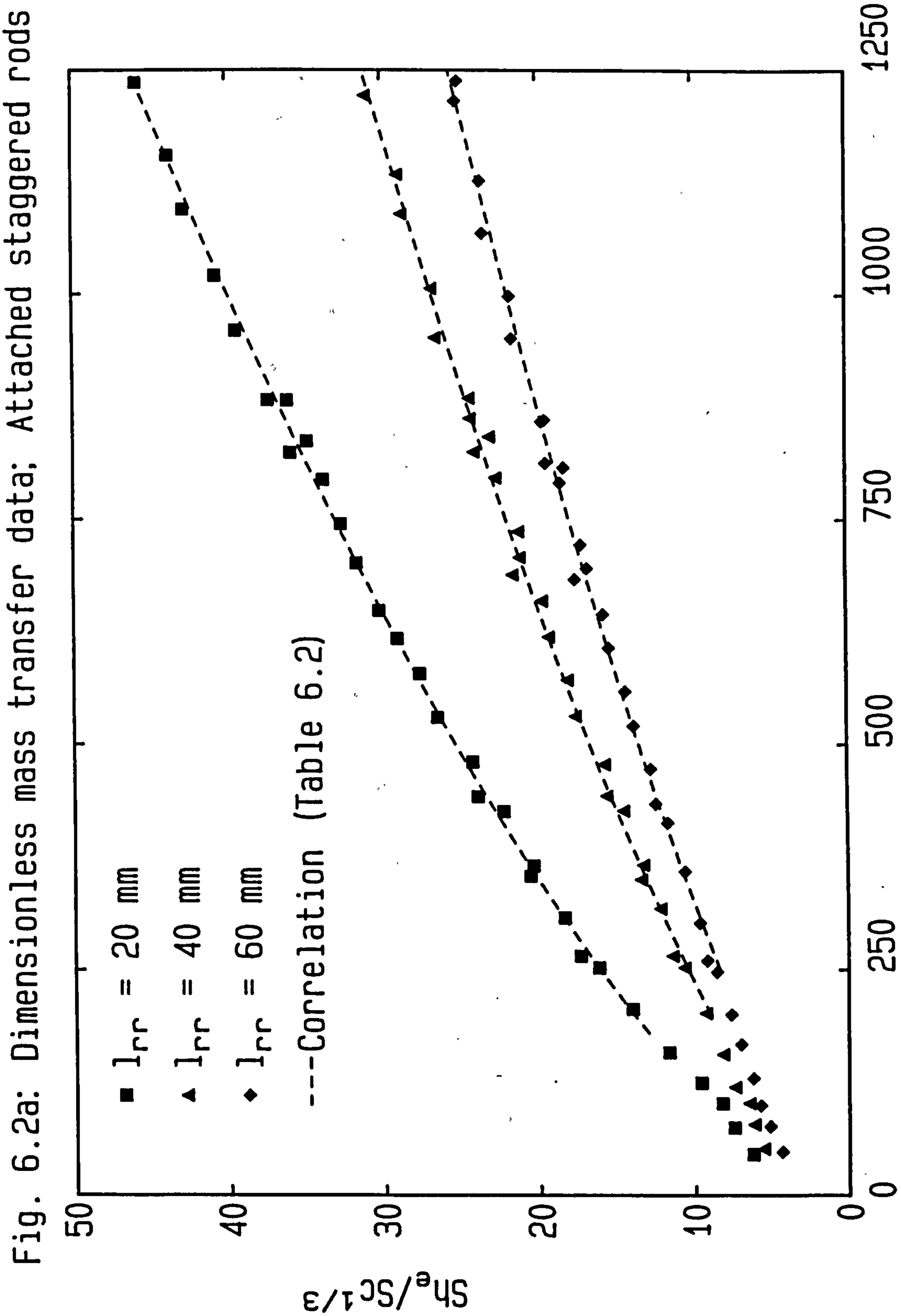
Fig. 6.2a: Dimensionless mass transfer data; Attached staggered rods
■ l_{rr} = 20 mm
▲ l_{rr} = 40 mm
◆ l_{rr} = 60 mm
---Correlation (Table 6.2)
$Sh_e/Sc^{1/3}$
Re_e
0
10
20
30
40
50
250
500
750
1000
1250

Fig. 6.2b: Dimensionless mass transfer data; Attached staggered rods

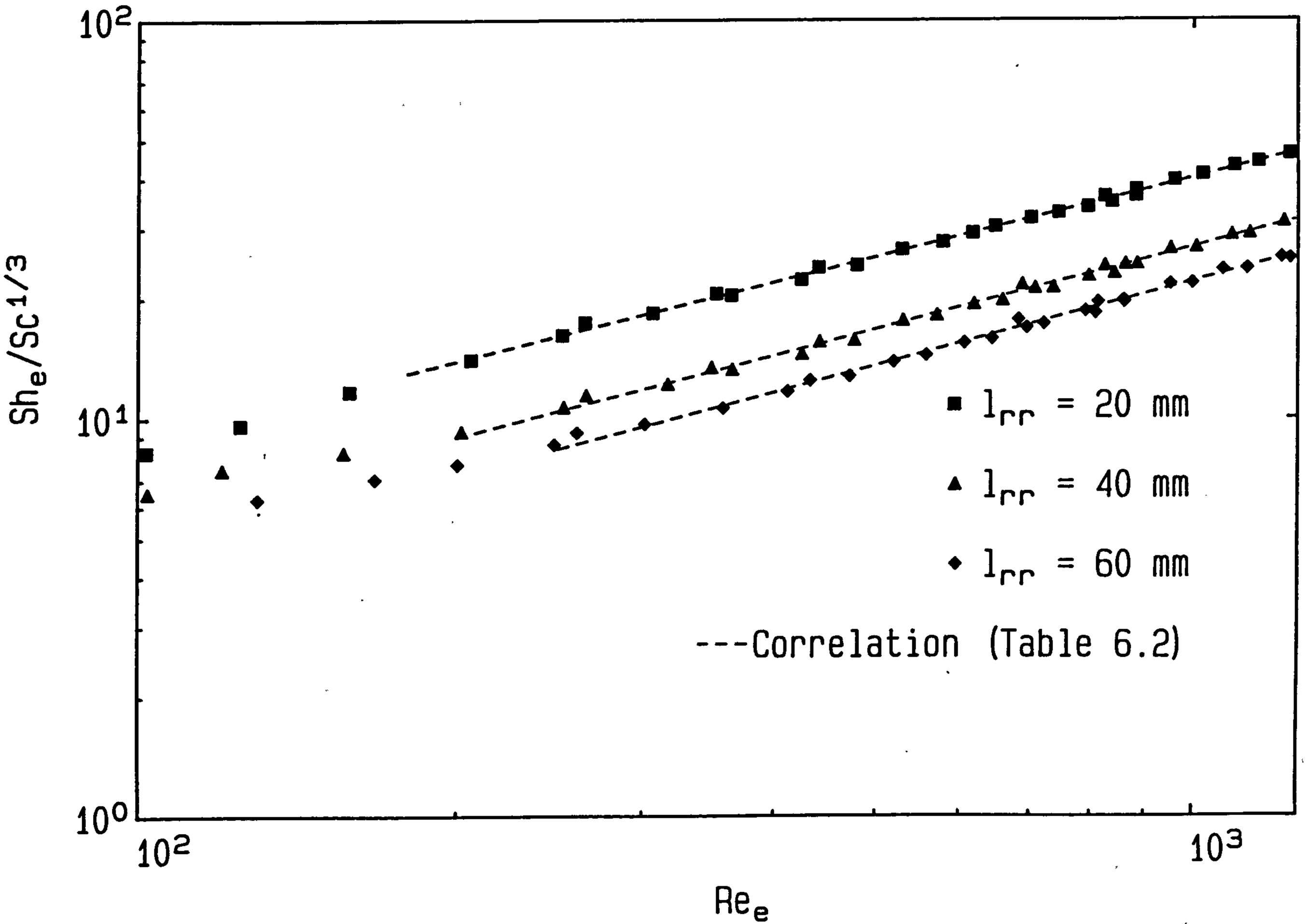

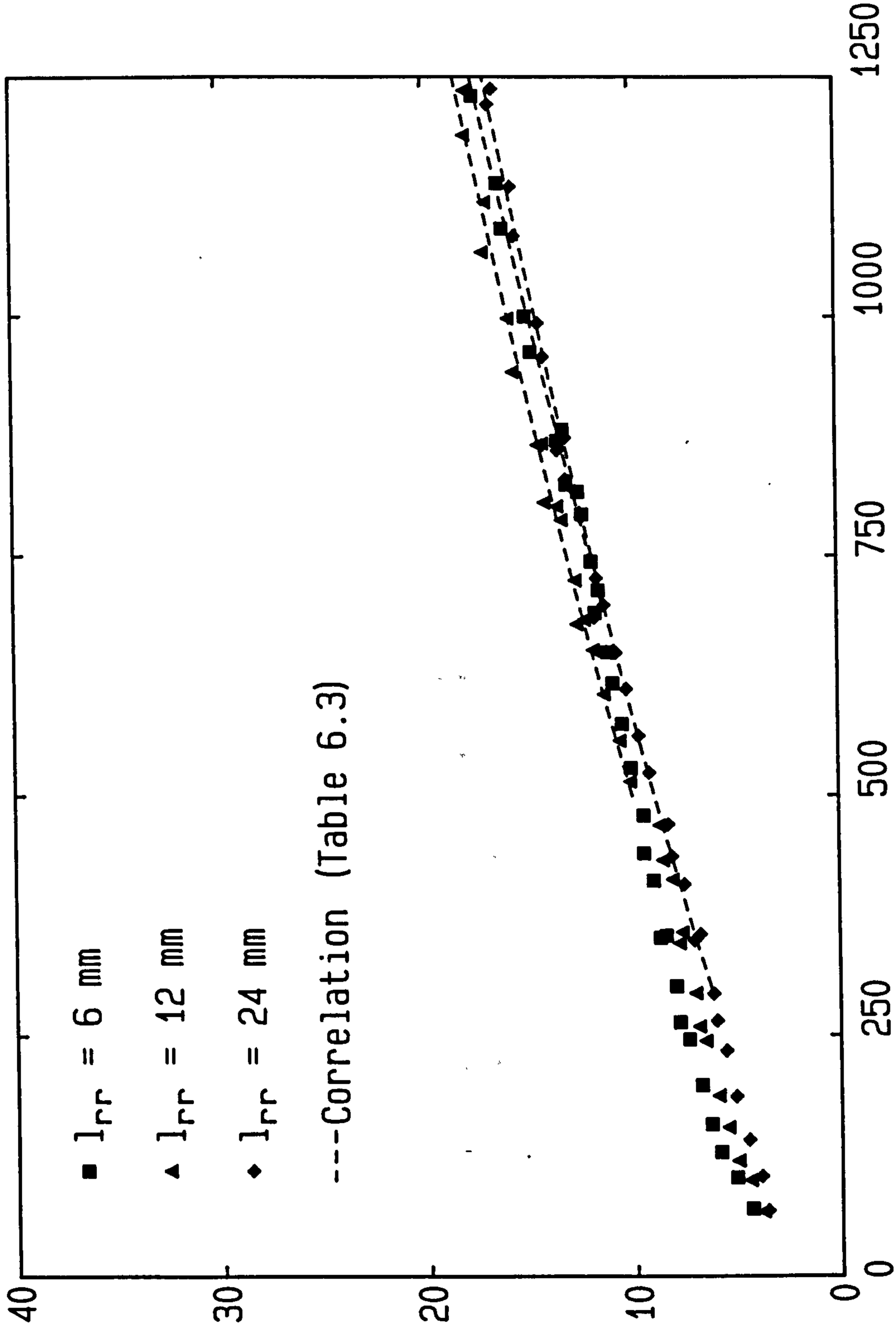
Fig. 6.3a: Dimensionless mass transfer data
Suspended staggered rods, d_{rw} = 3 mm
■ l_{rr} = 6 mm
▲ l_{rr} = 12 mm
◆ l_{rr} = 24 mm
---Correlation (Table 6.3)
$Sh_e/Sc^{1/3}$
Re_e
0
250
500
750
1000
1250
0
10
20
30
40

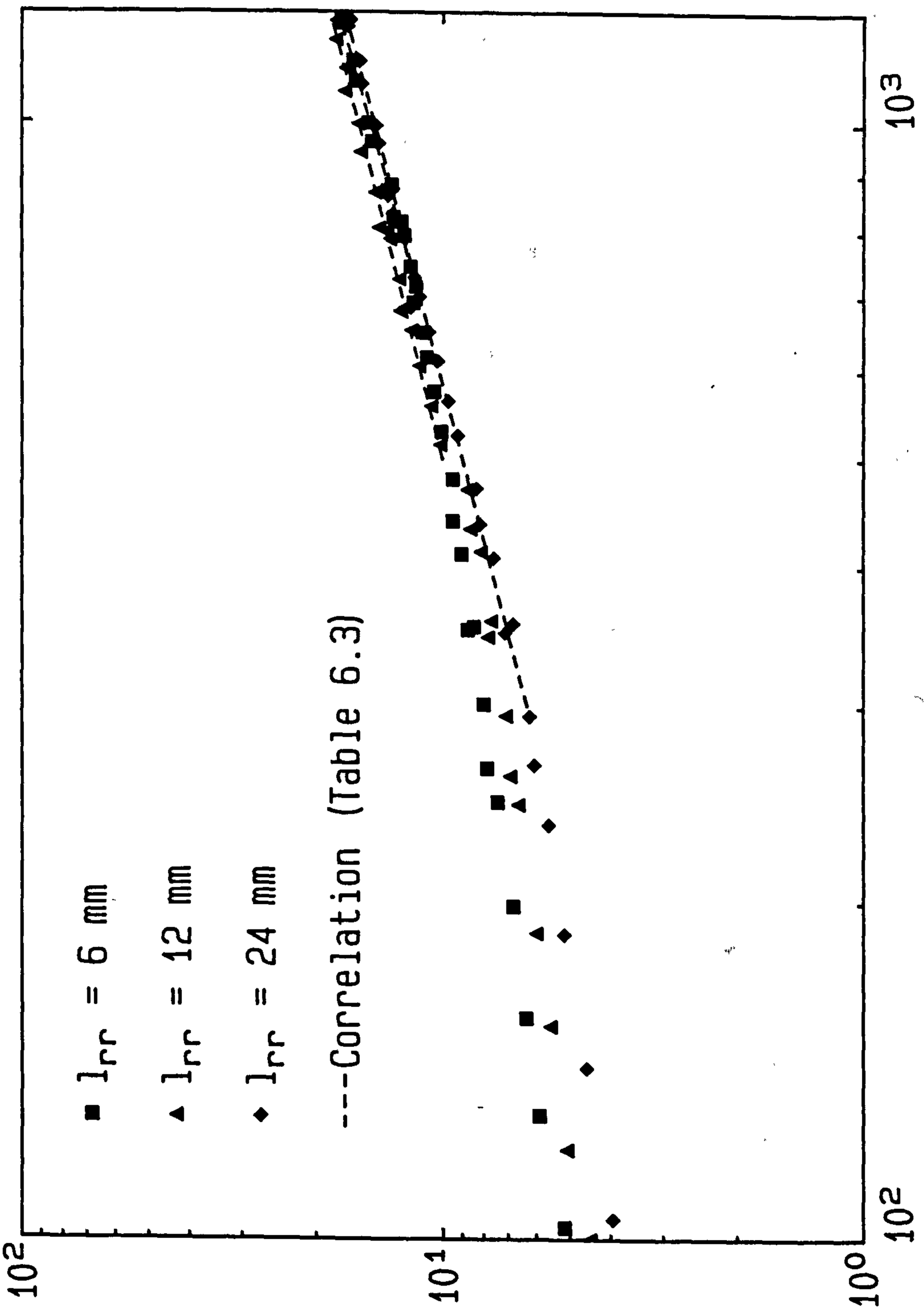
Fig. 6.3b: Dimensionless mass tranfer data for
Suspended staggered rods, d_{rw} = 3 mm
■ l_{rr} = 6 mm
▲ l_{rr} = 12 mm
◆ l_{rr} = 24 mm
---Correlation (Table 6.3)
$Sh_e/Sc^{1/3}$
Re_e
10^2
10^1
10^0
10^2
103

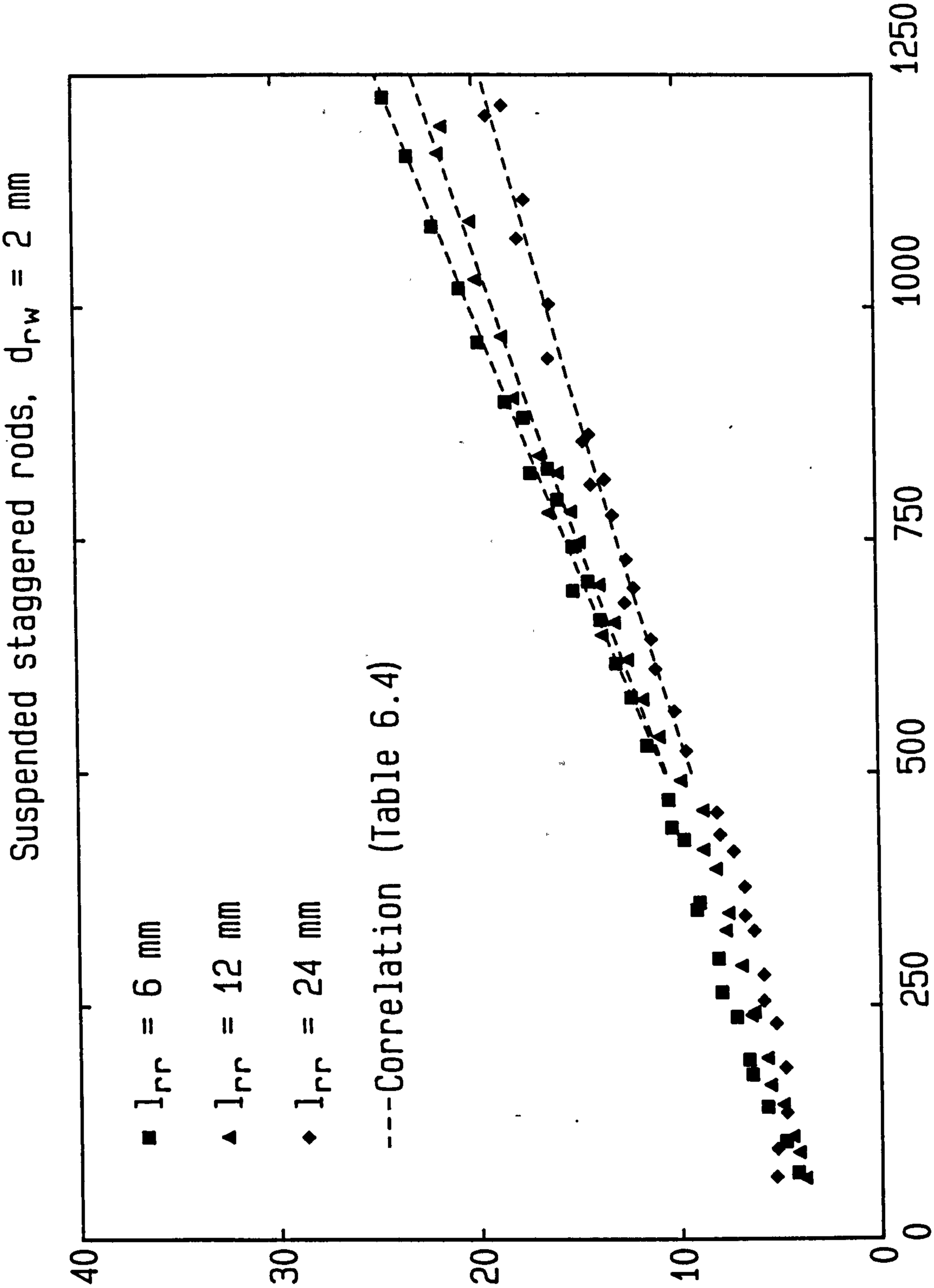

Fig. 6.4a: Dimensionless mass transfer data
Suspended staggered rods, d_{rw} = 2 mm

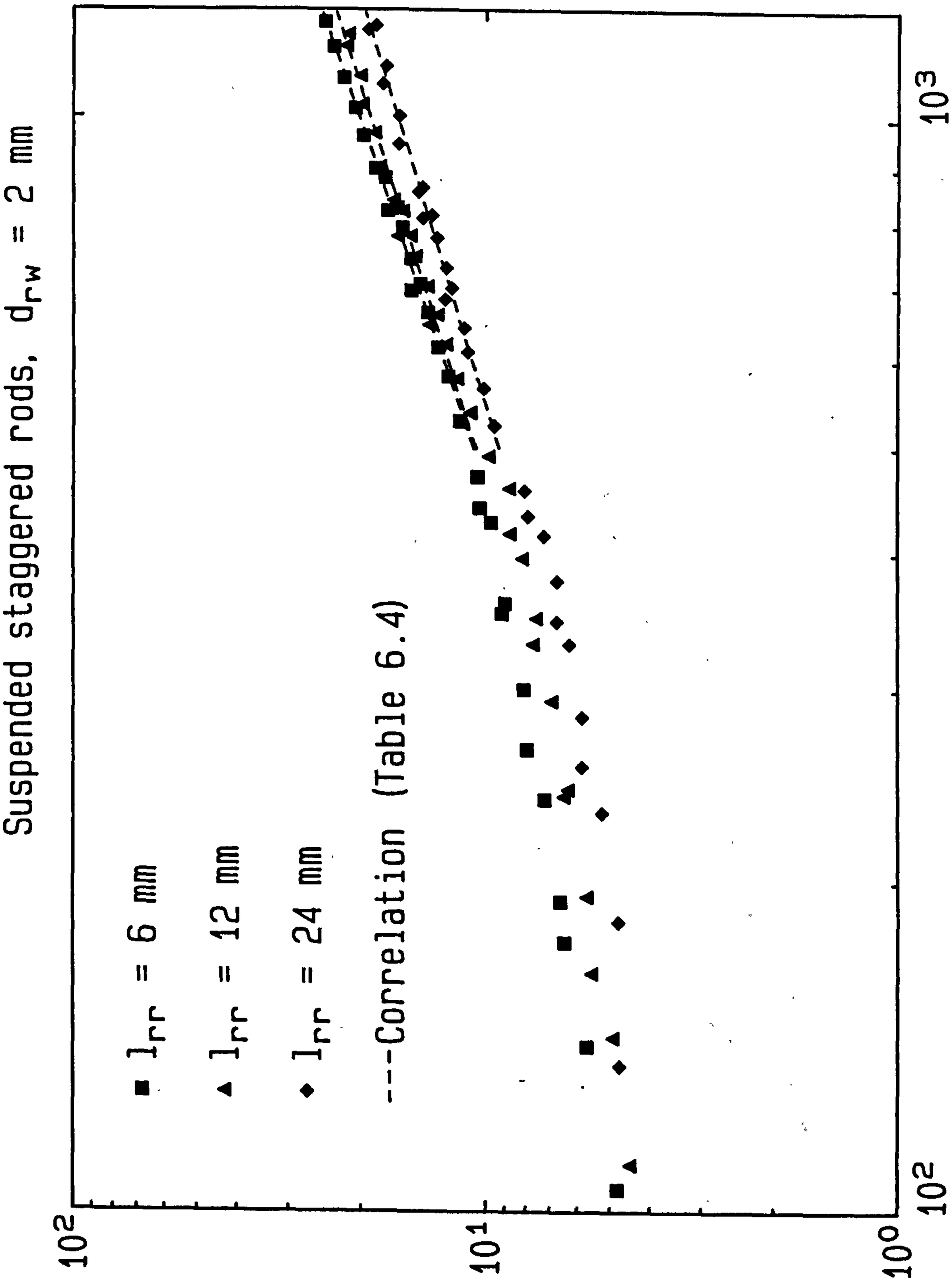

Fig. 6.4b: Dimensionless mass transfer data
Suspended staggered rods, d_{rw} = 2 mm

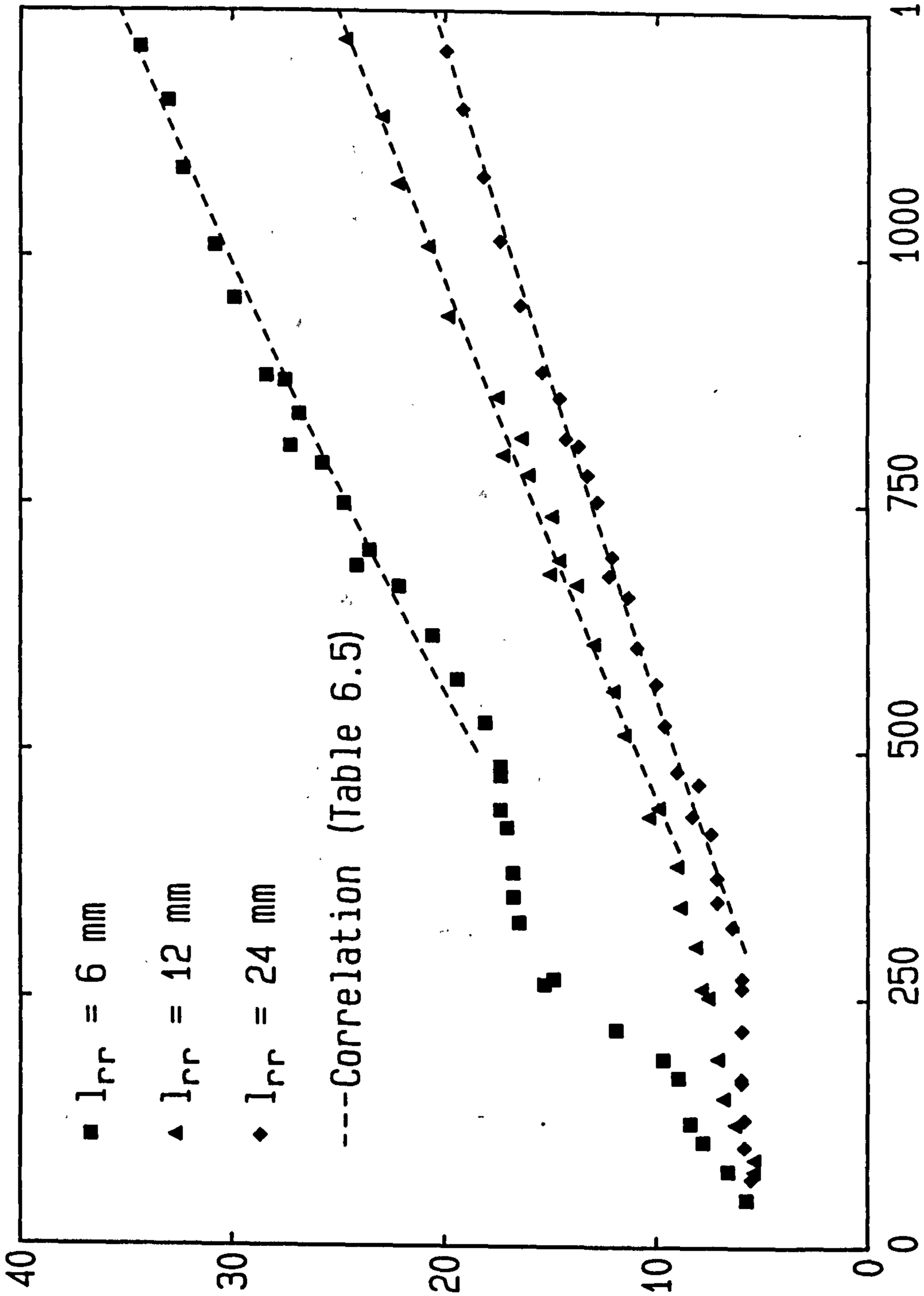

Fig. 6.5a: Dimensionless mass transfer data for Suspended staggered rods, d_{rw} = 1 mm

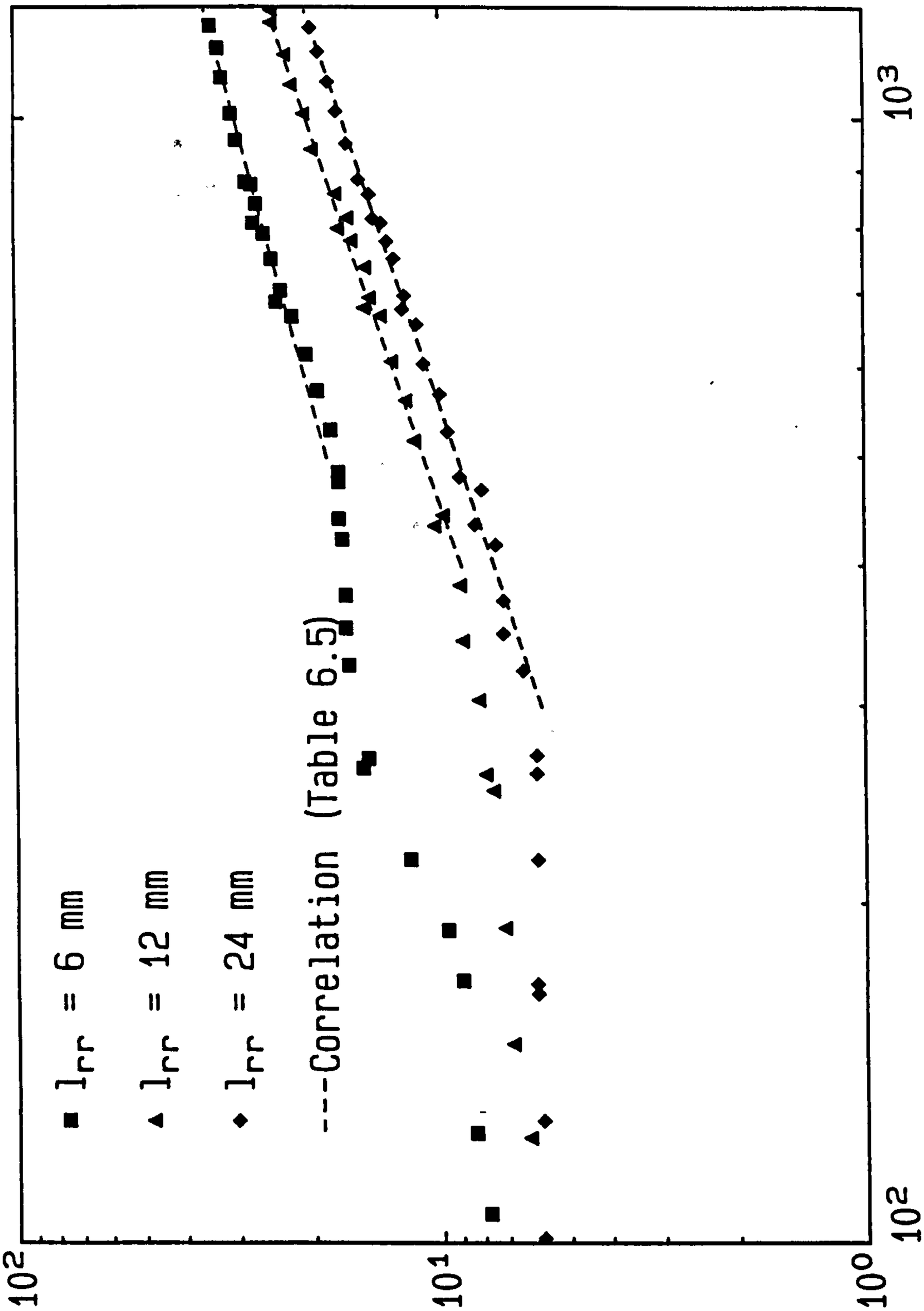

Fig. 6.5b: Dimensionless mass transfer data
Suspended staggered rods, d_{rw} = 1 mm

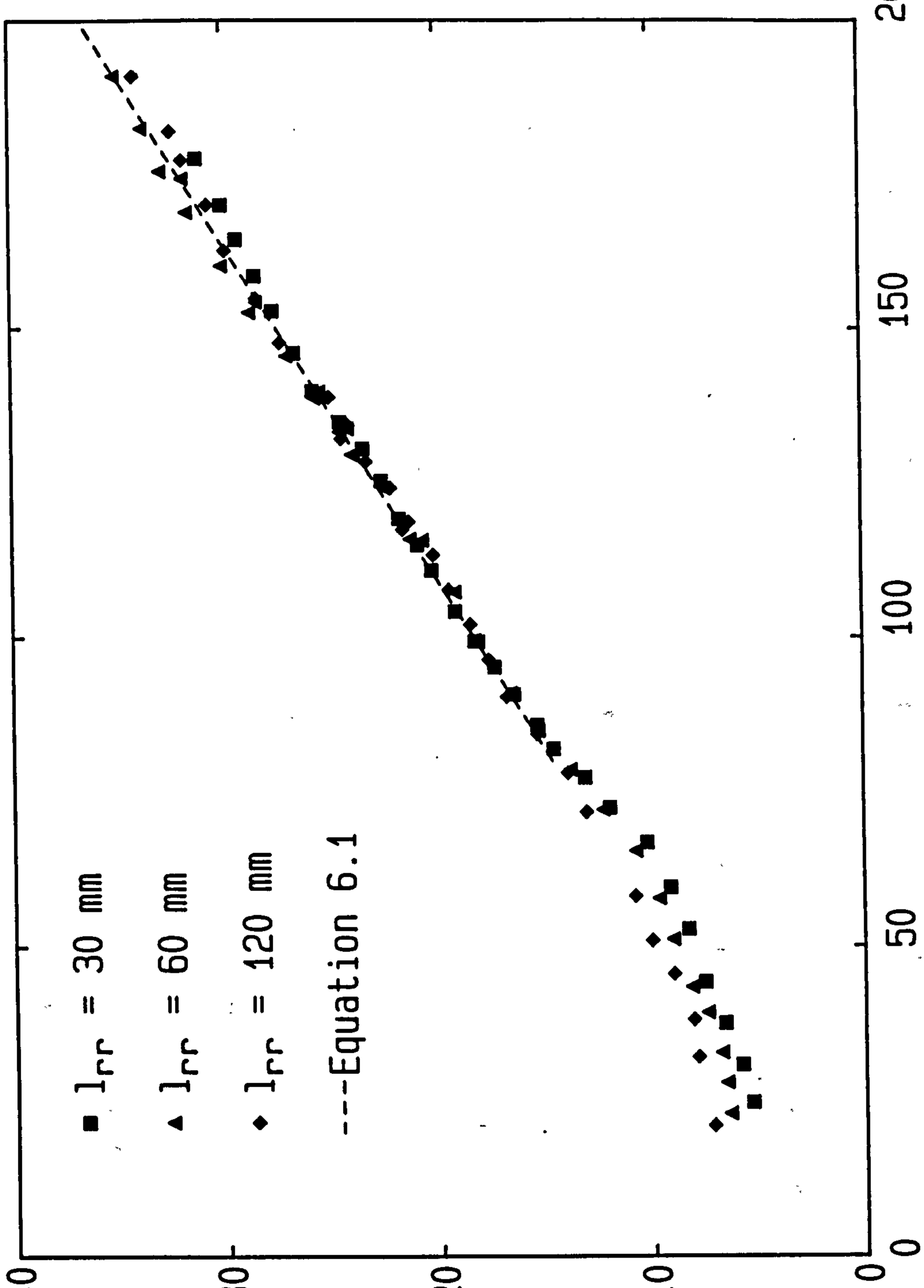

Fig. 6.6: Correlating mass transfer data for centered rods

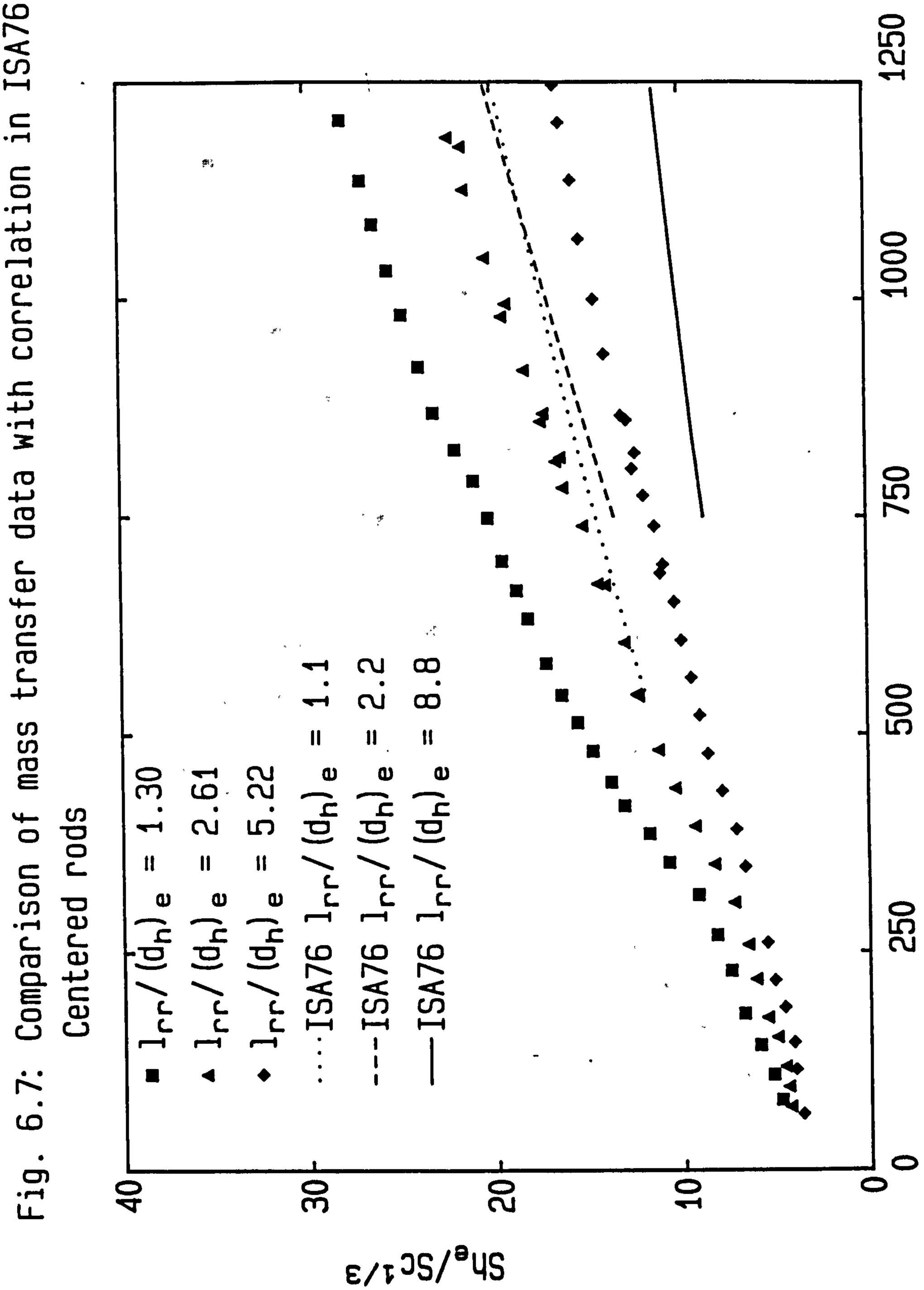

Fig. 6.7: Comparison of mass transfer data with correlation in ISA76

Fig. 6.8: Comparison of mass transfer data with correlation in FOC83
Attached staggered rods

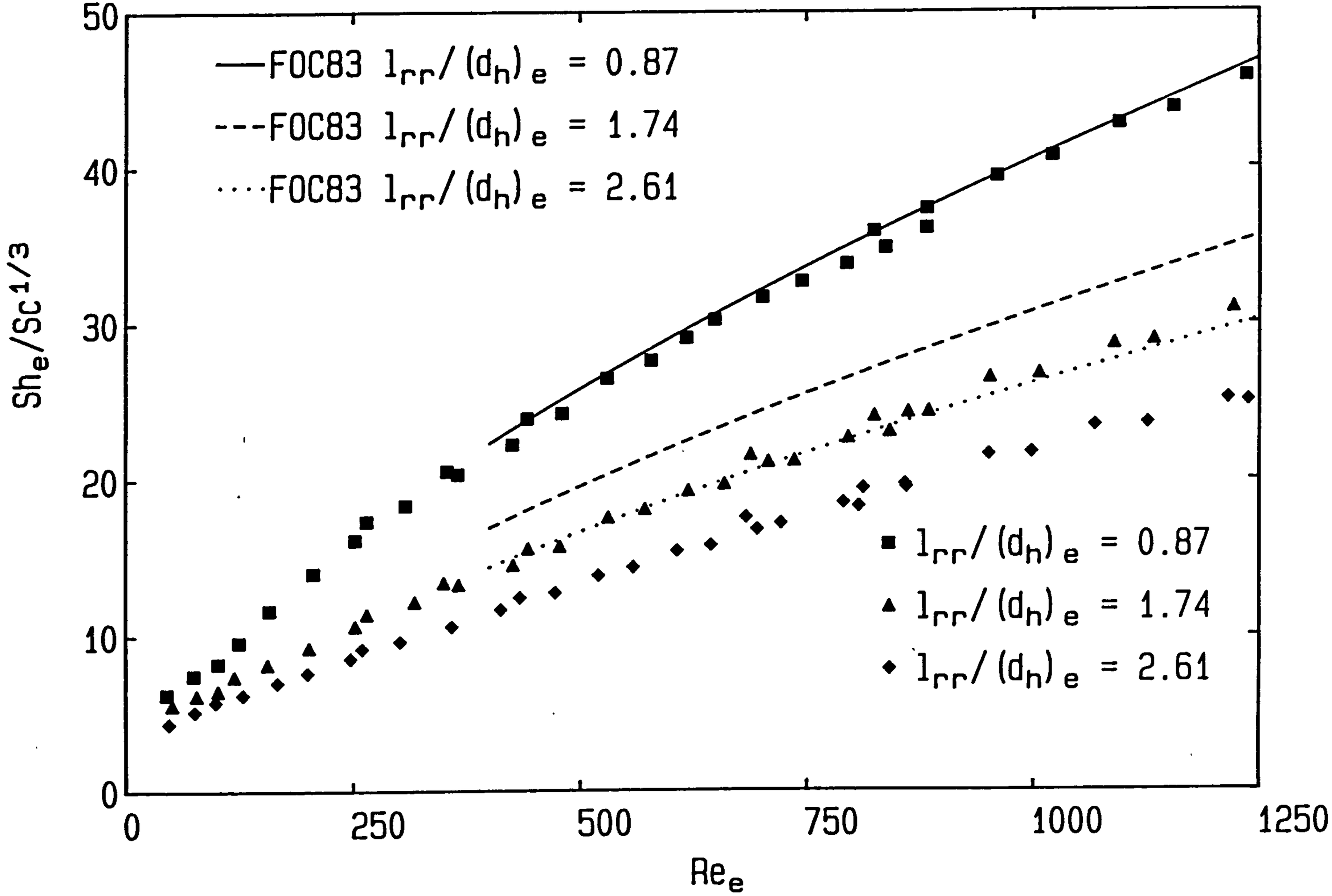

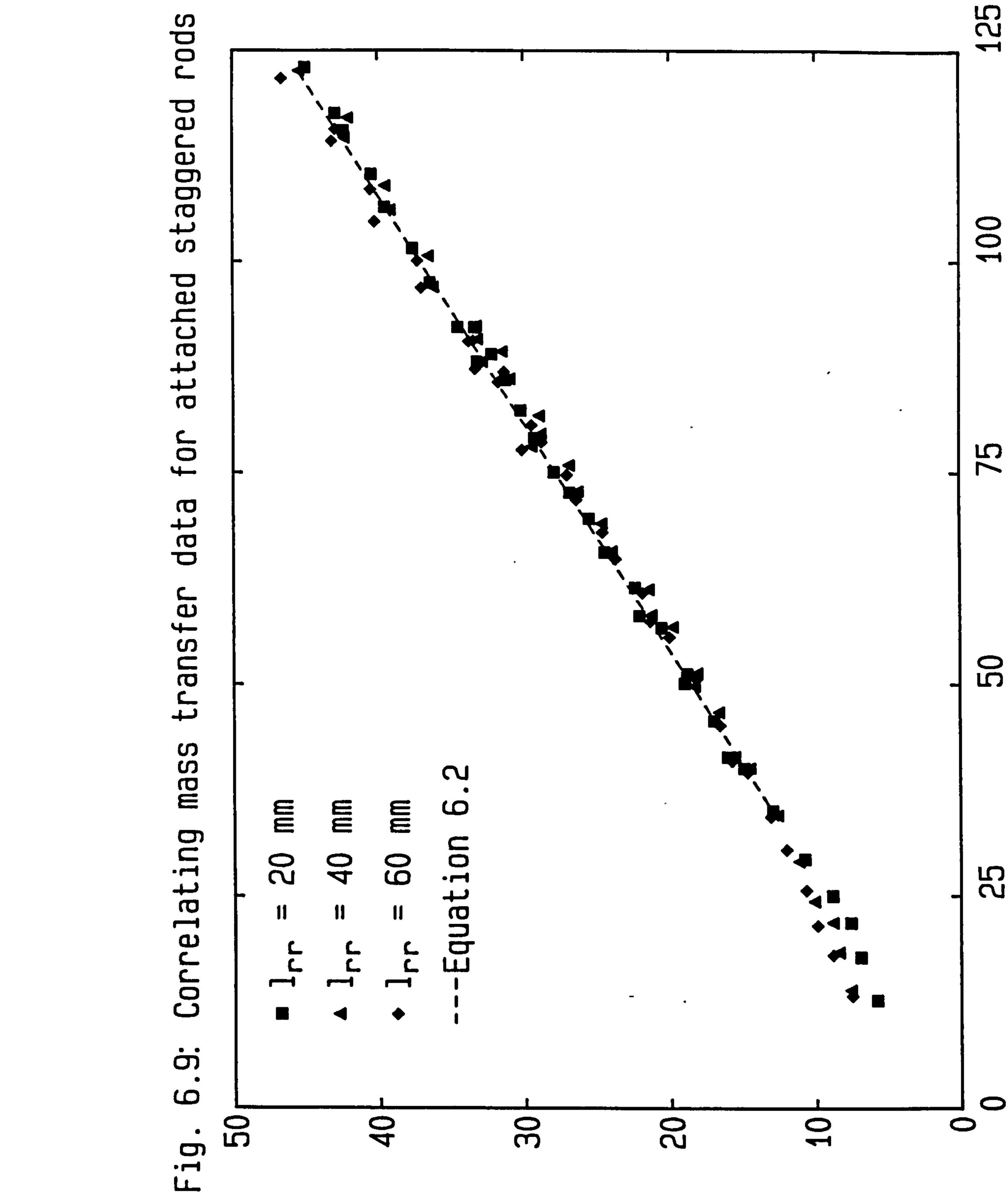
Fig. 6.9: Correlating mass transfer data for attached staggered rods
■ l_{rr} = 20 mm
▲ l_{rr} = 40 mm
◆ l_{rr} = 60 mm
---Equation 6.2
$(Sh_e/Sc^{1/3})$ $(l_{rr}/(d_h)_e)^{0.563}$
0
25
50
75
100
125
$(Re_e)^{0.667}$
0
10
20
30
40
50

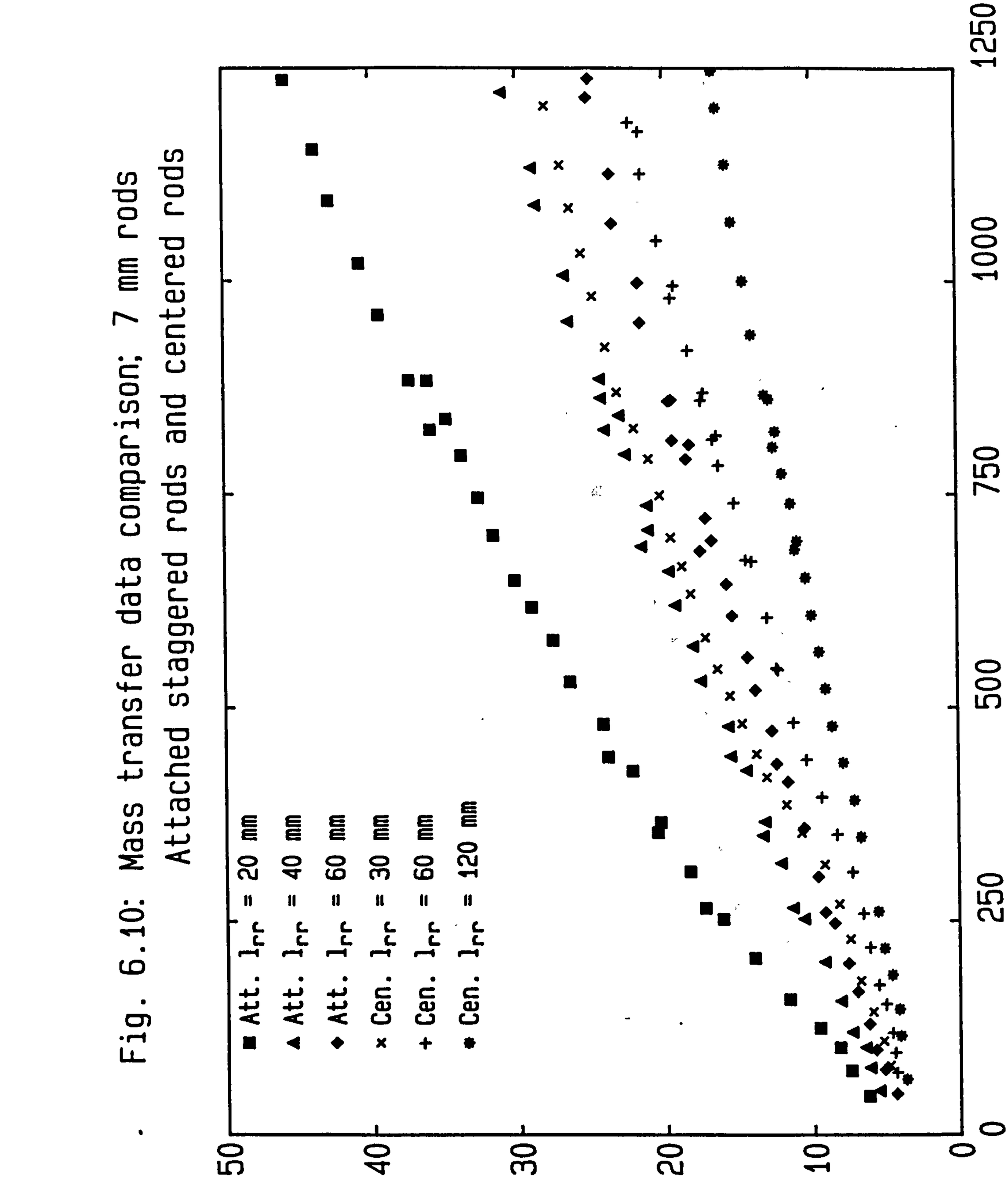
Fig. 6.10: Mass transfer data comparison; 7 mm rods
Attached staggered rods and centered rods
■ Att. l_{rr} = 20 mm
▲ Att. l_{rr} = 40 mm
◆ Att. l_{rr} = 60 mm
× Cen. l_{rr} = 30 mm
+ Cen. l_{rr} = 60 mm
✱ Cen. l_{rr} = 120 mm
$Sh_e/Sc^{1/3}$
Re_e
0
250
500
750
1000
1250
10
20
30
40
50

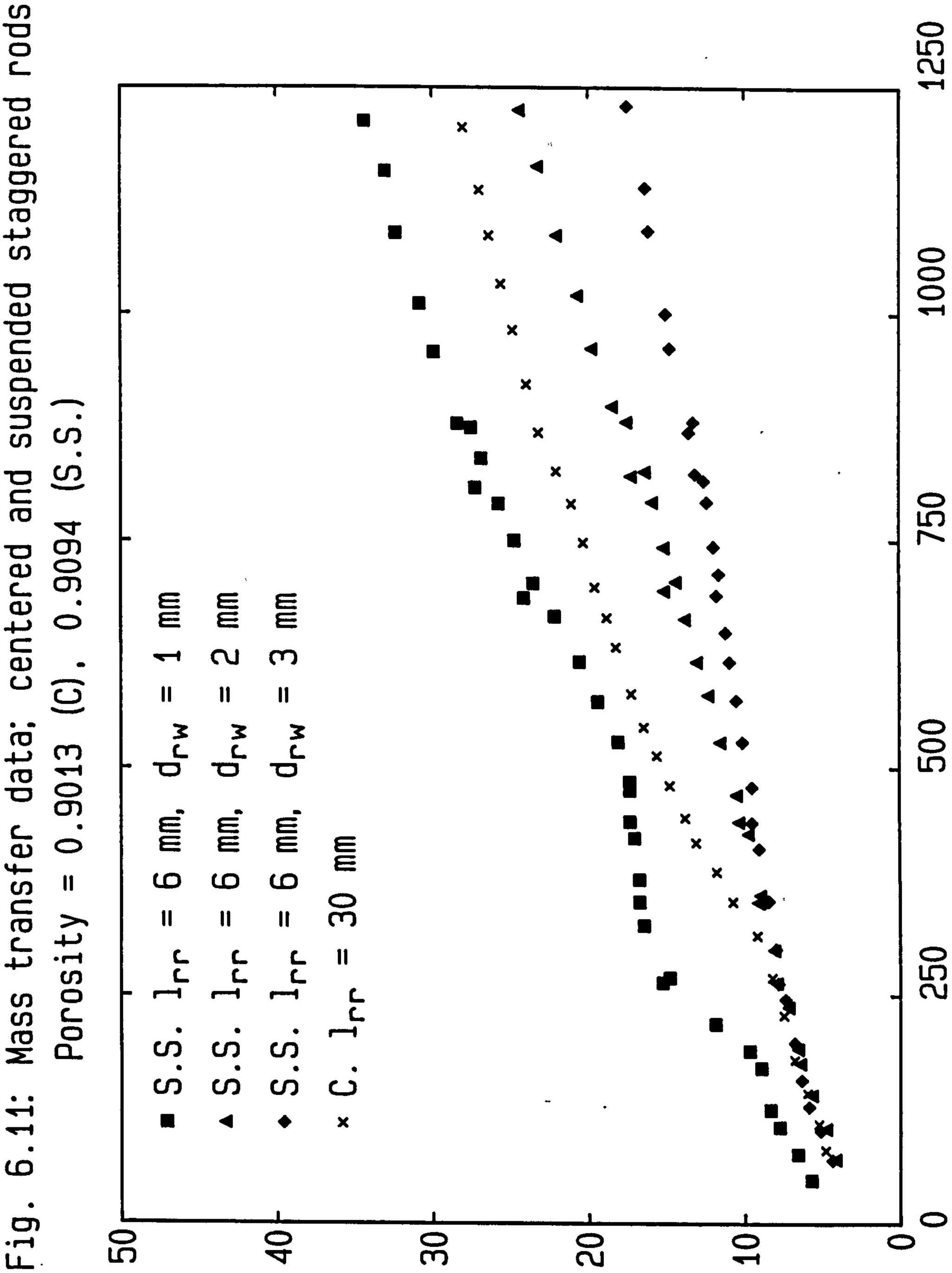

Fig. 6.11: Mass transfer data; ce

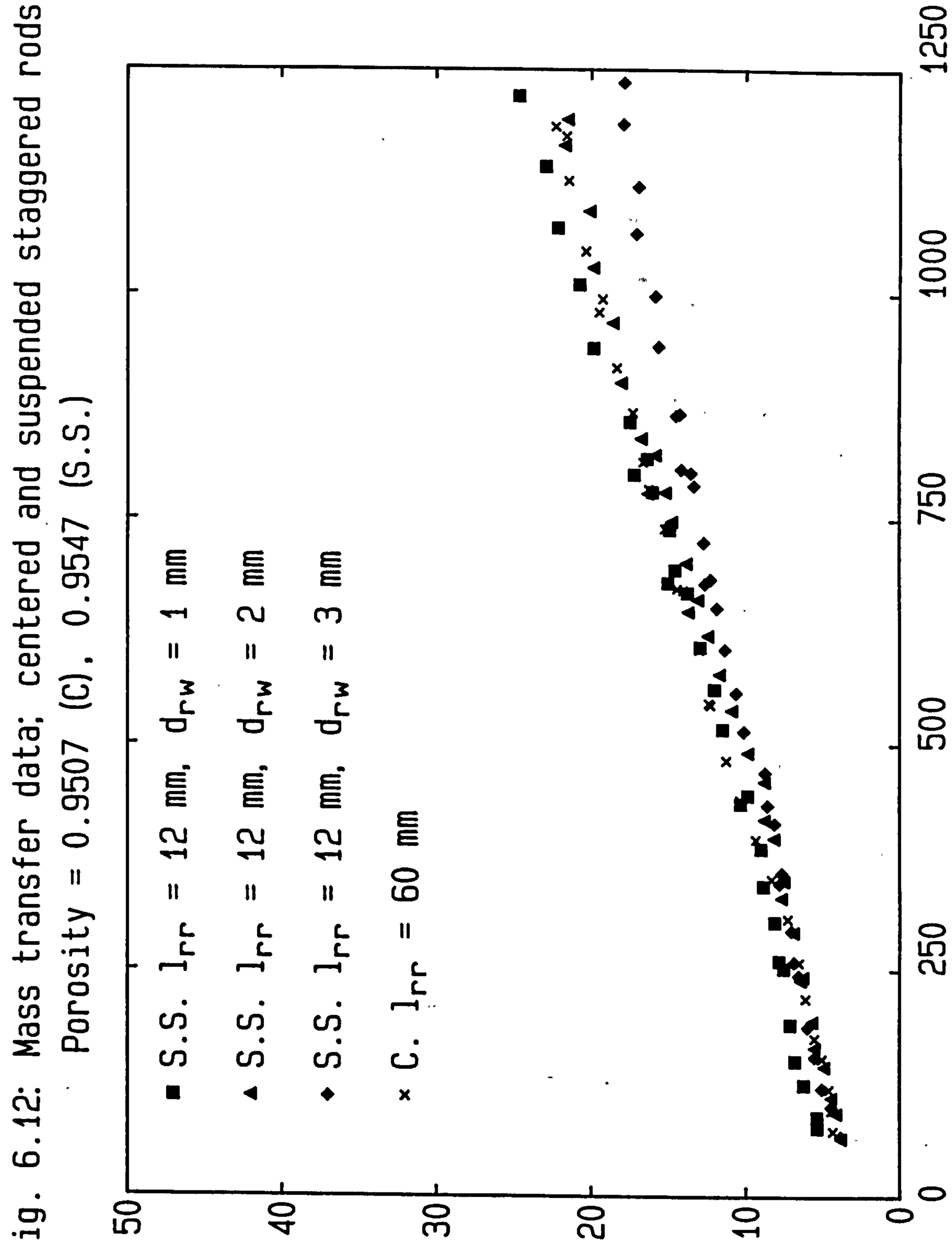

Fig. 6.12: Mass transfer data; centered and suspended staggered rods
Porosity = 0.9507 (C). 0.9547 (S.S.)

Fig. 6.13: Mass transfer data; centered and suspended staggered rods
Porosity = 0.9753 (C), 0.9773 (S.S.)

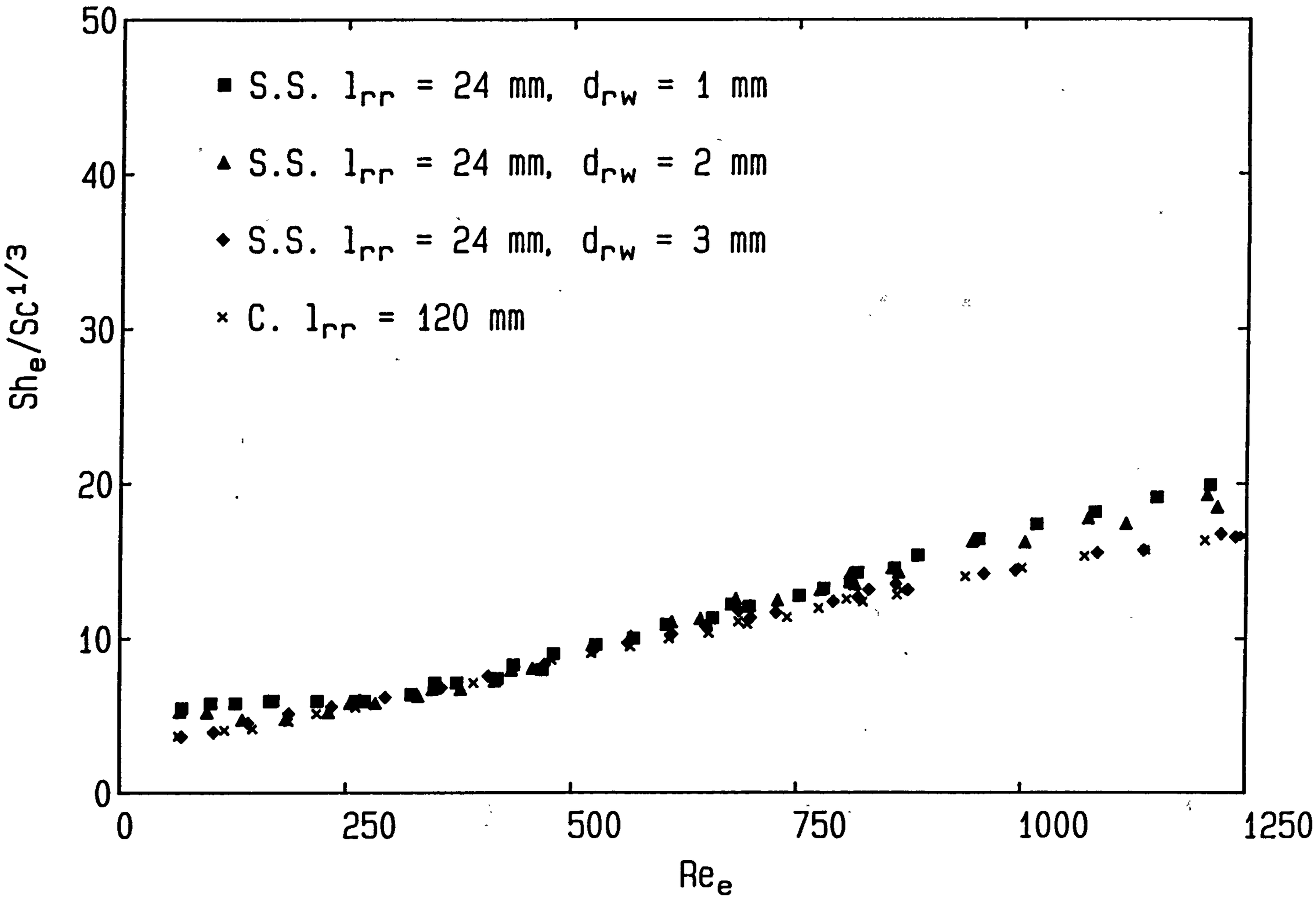

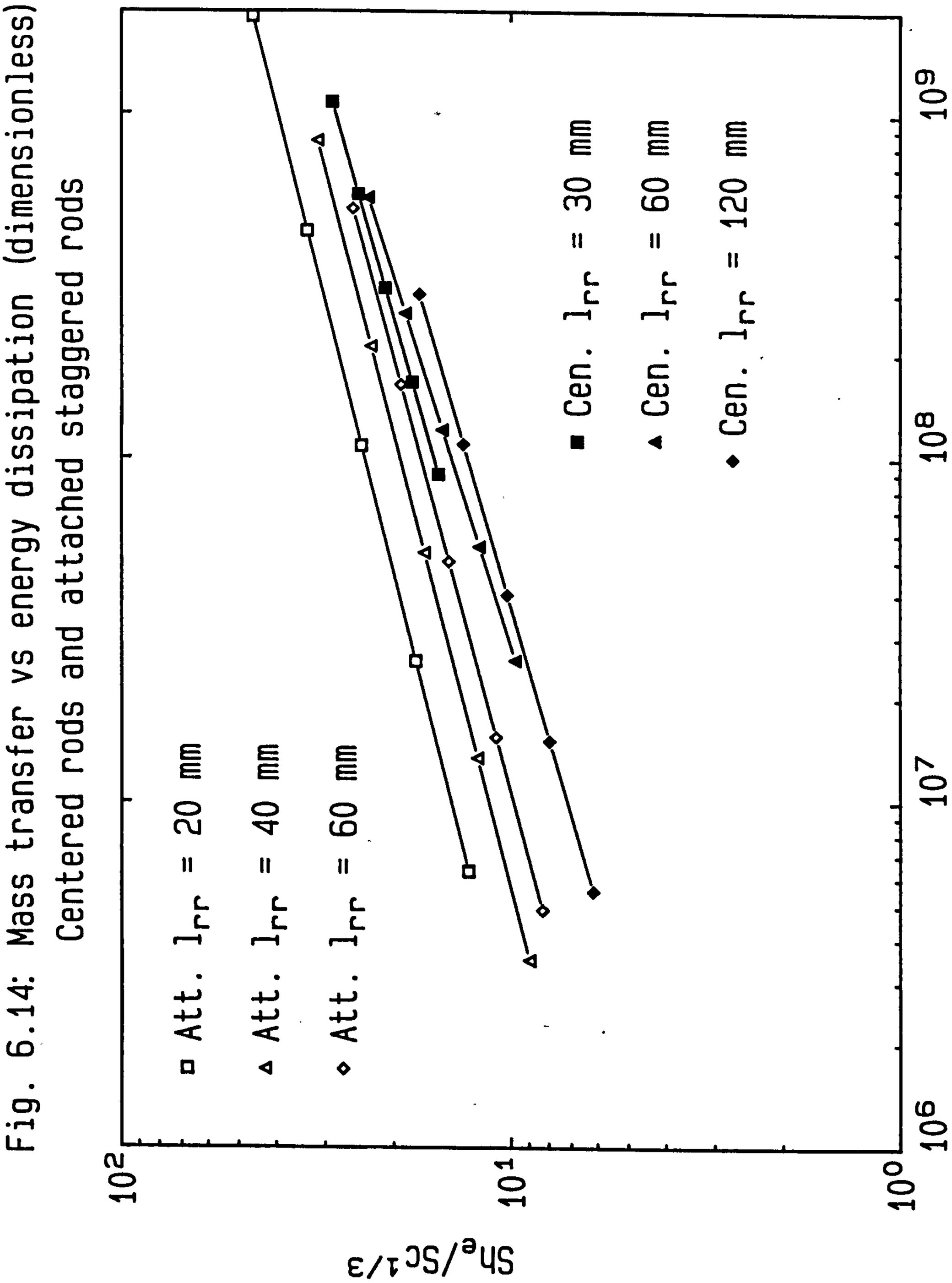

Fig. 6.14: Mass transfer vs energy dissipation (dimensionless)
Centered rods and attached staggered rods

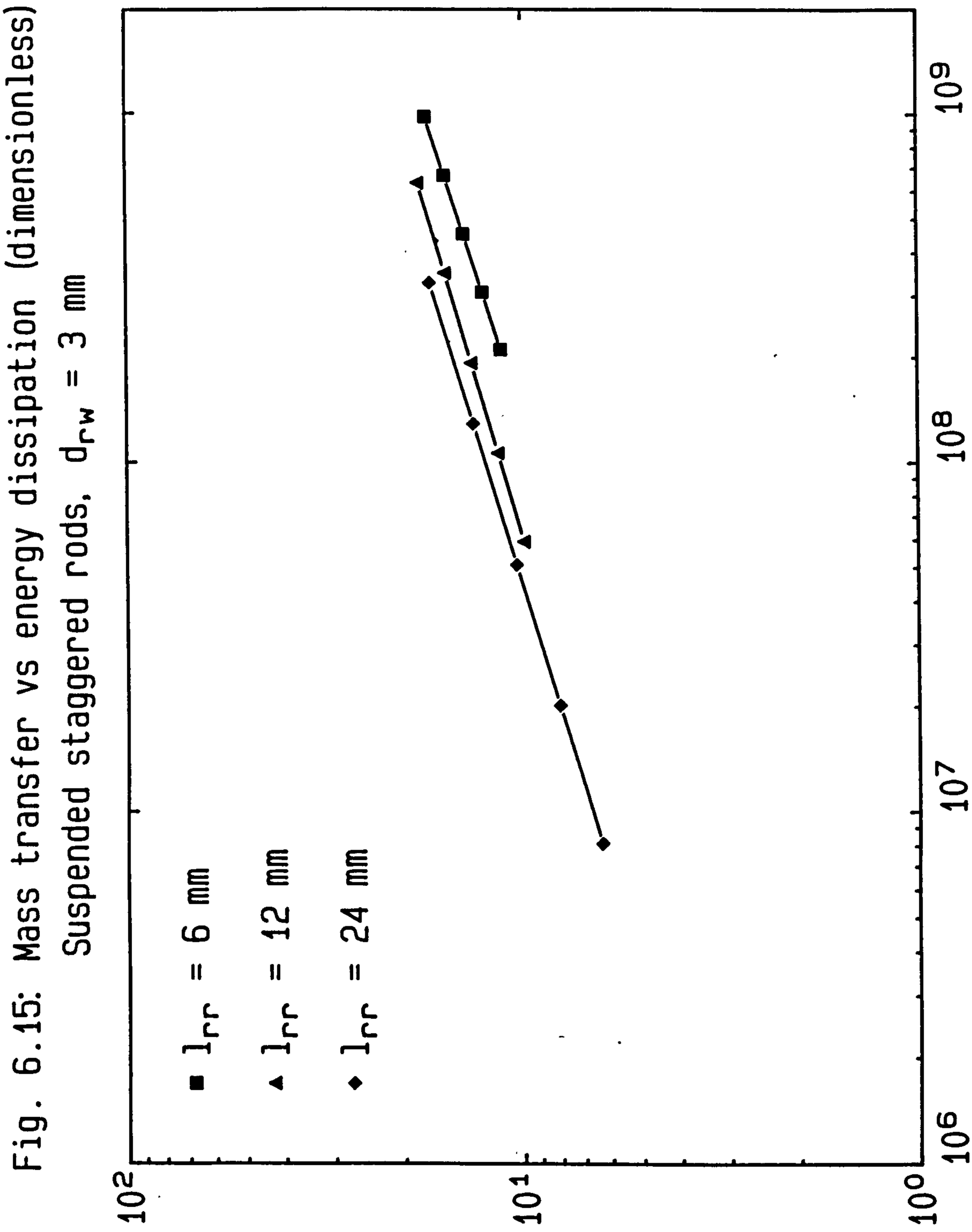
Fig. 6.15: Mass transfer vs energy dissipation (dimensionless)
Suspended staggered rods, d_{rw} = 3 mm
■ l_{rr} = 6 mm
▲ l_{rr} = 12 mm
◆ l_{rr} = 24 mm
$Sh_e/Sc^{1/3}$
Po
10^2
10^1
10^0
10^9
10^8
10^7
10^6

Fig. 6.16: Mass transfer vs energy dissipation (dimensionless)
Suspended staggered rods, d_{rw} = 2 mm

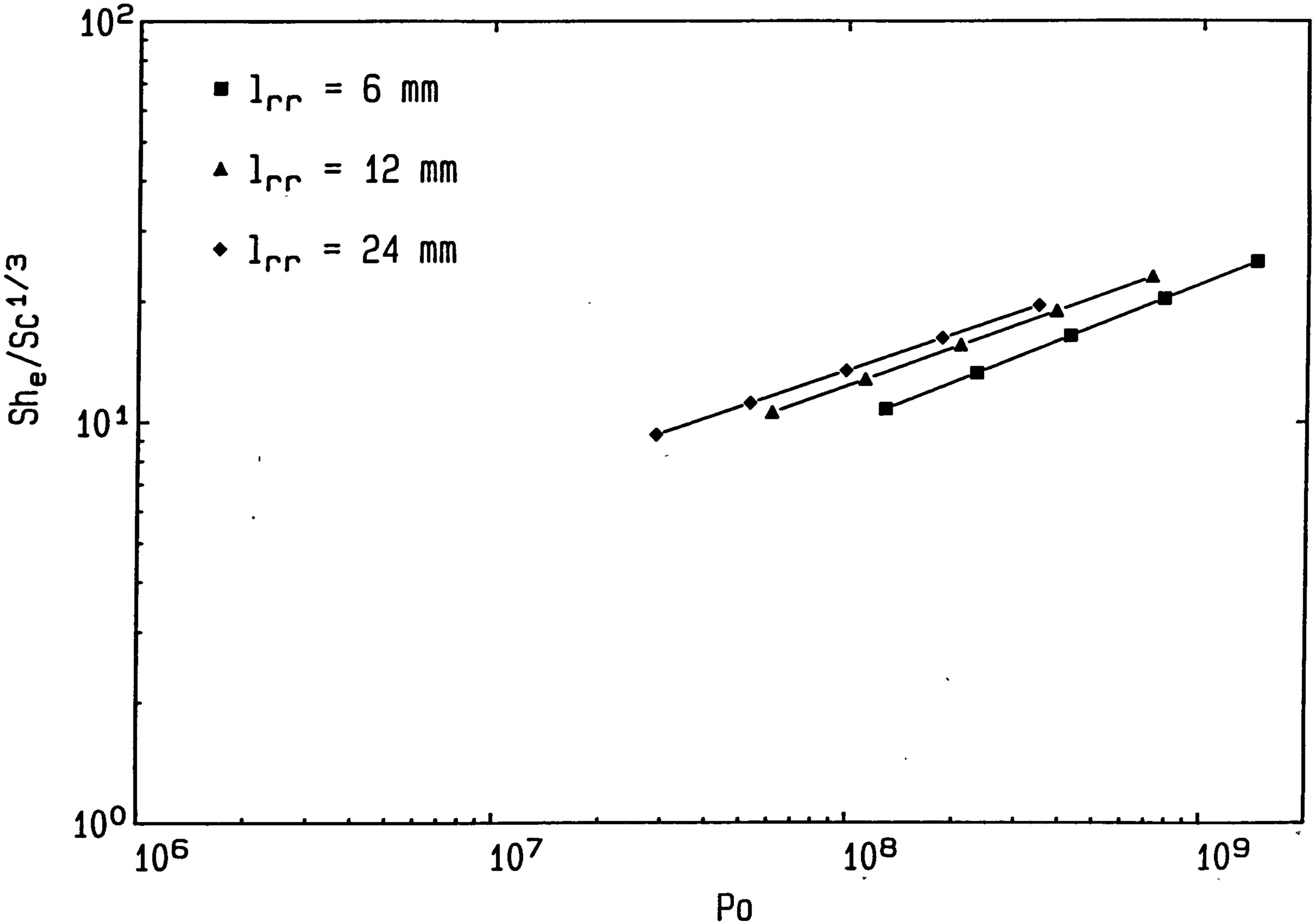

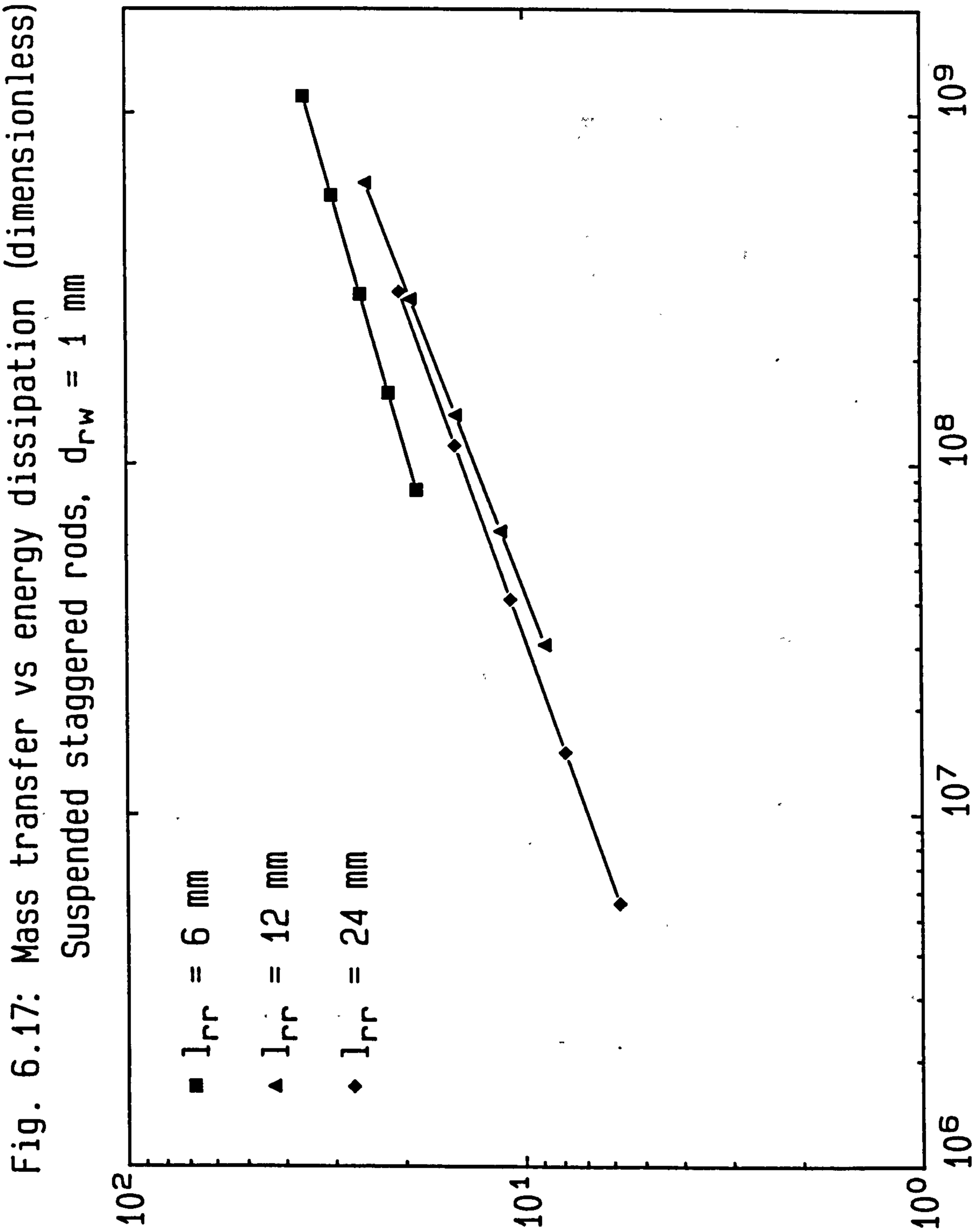

Fig. 6.17: Mass transfer vs energy dissipation (dimensionless)
Suspended staggered rods, d_{rw} = 1 mm

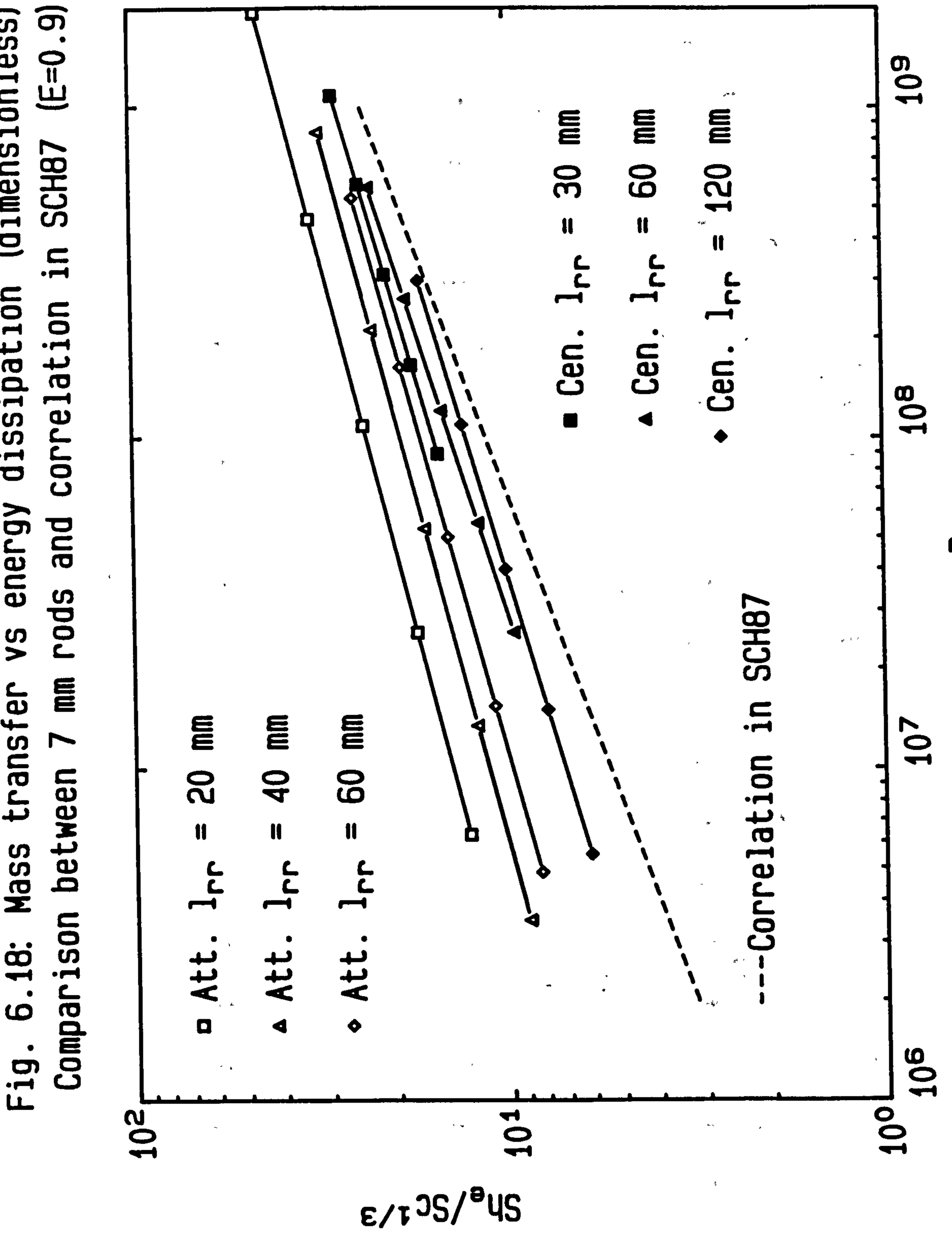
Fig. 6.18: Mass transfer vs energy dissipation (dimensionless)
Comparison between 7 mm rods and correlation in SCH87 (E=0.9)
Sh_e/Sc^1/3
Po
10^2
10^1
10^0
10^8
10^7
10^6
10^9
□ Att. l_rr = 20 mm
△ Att. l_rr = 40 mm
◇ Att. l_rr = 60 mm
■ Cen. l_rr = 30 mm
▲ Cen. l_rr = 60 mm
◆ Cen. l_rr = 120 mm
---Correlation in SCH87

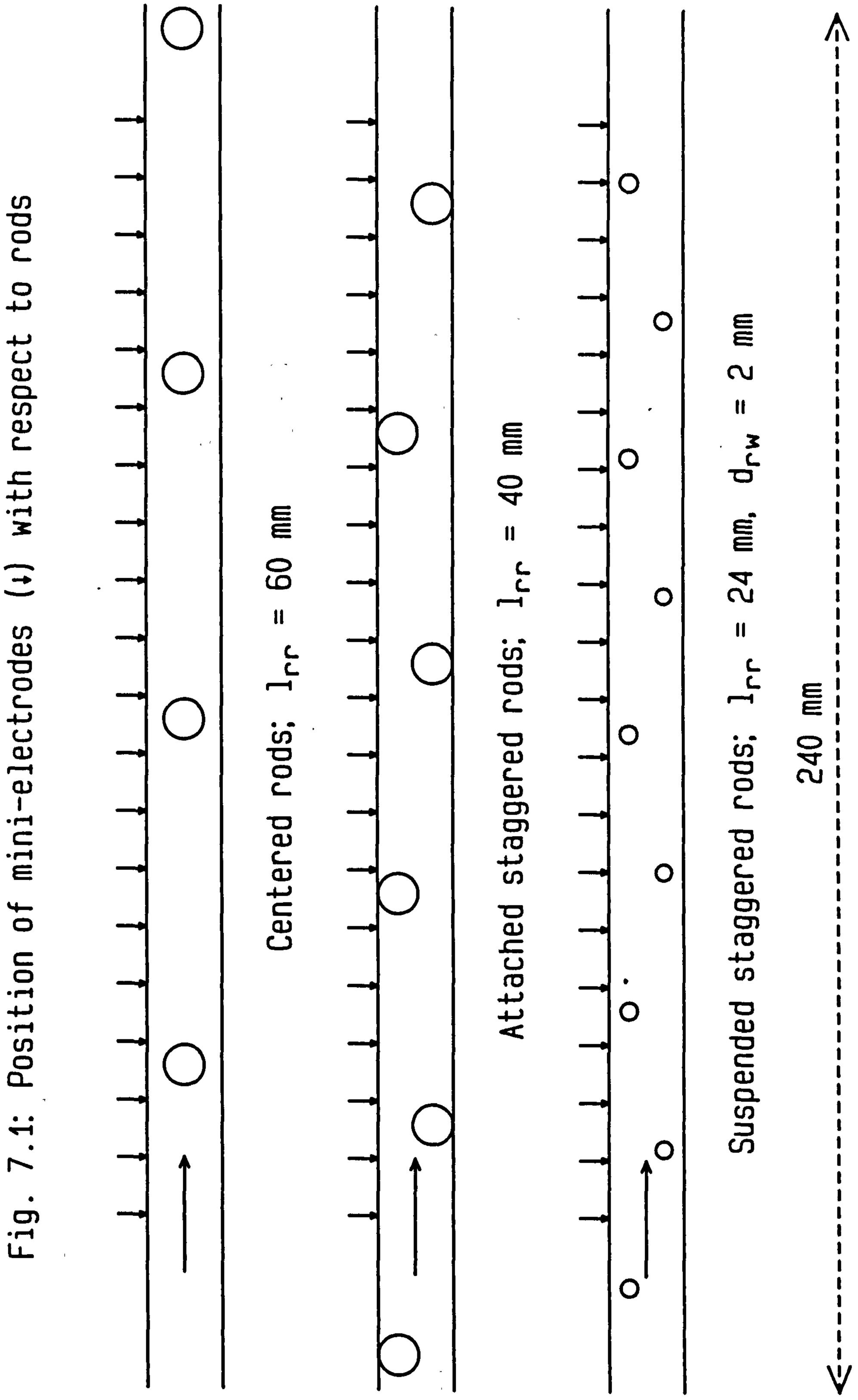
Position of mini-electrodes (↓) with respect to rods
Centered rods; l_{rr} = 60 mm
Attached staggered rods; l_{rr} = 40 mm
Suspended staggered rods; l_{rr} = 24 mm, d_{rw} = 2 mm
240 mm

Fig. 7.1: P

Fig. 7.1/ctd.

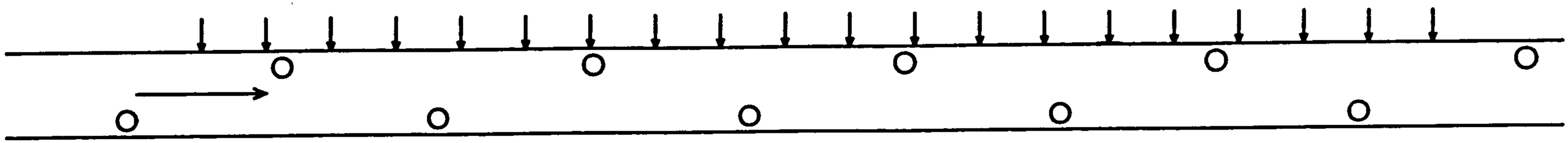

Suspended staggered rods; l_{rr} = 24 mm, d_{rw} = 1 mm

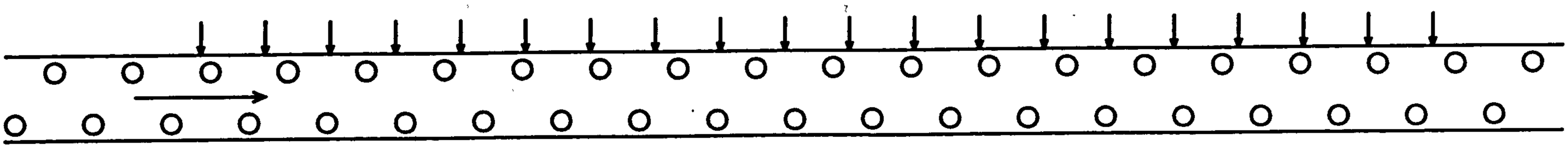

Suspended staggered rods; l_{rr} = 6 mm, d_{rw} = 1 mm

240 mm

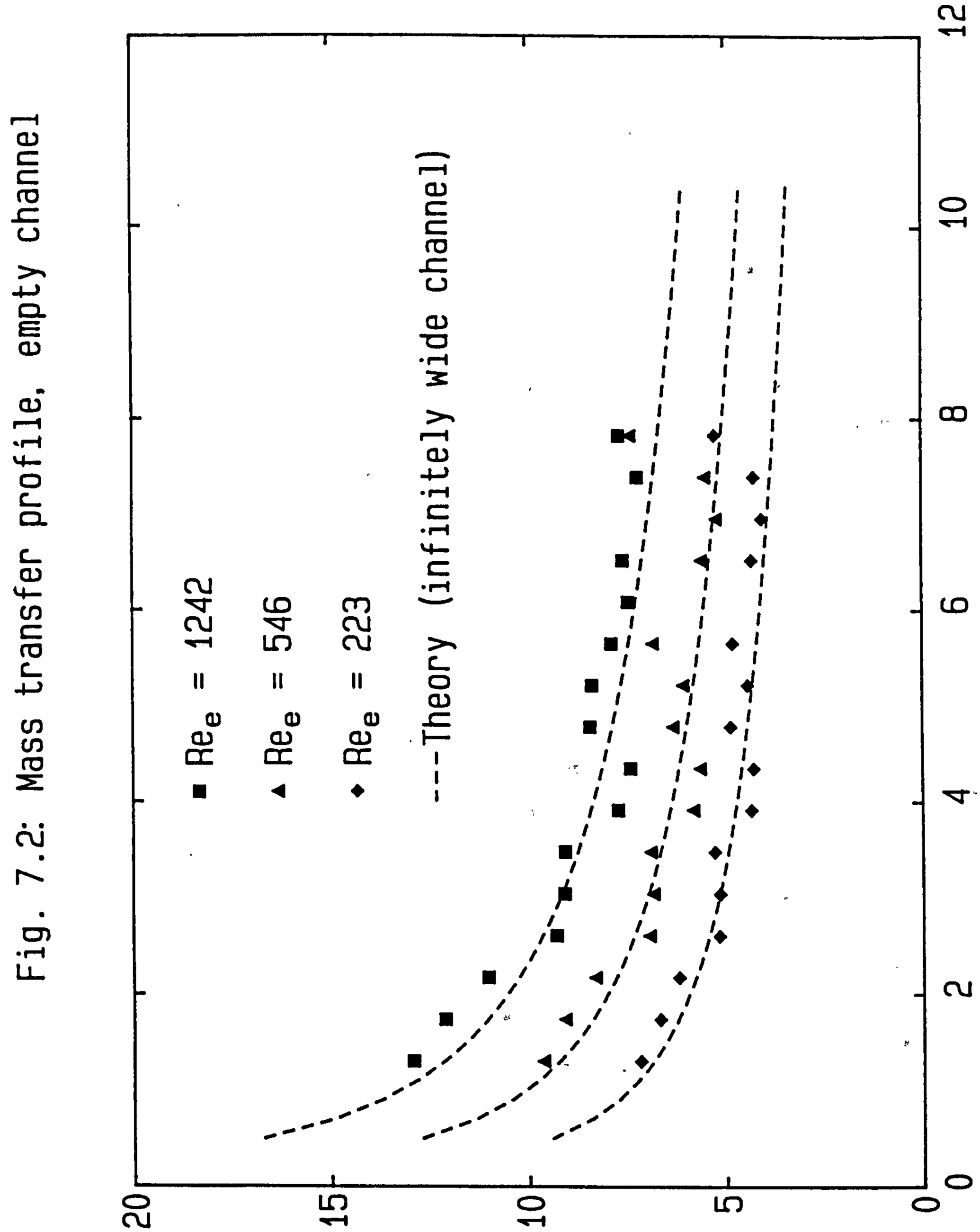

Fig. 7.2: Mass transfer profile, empty channel

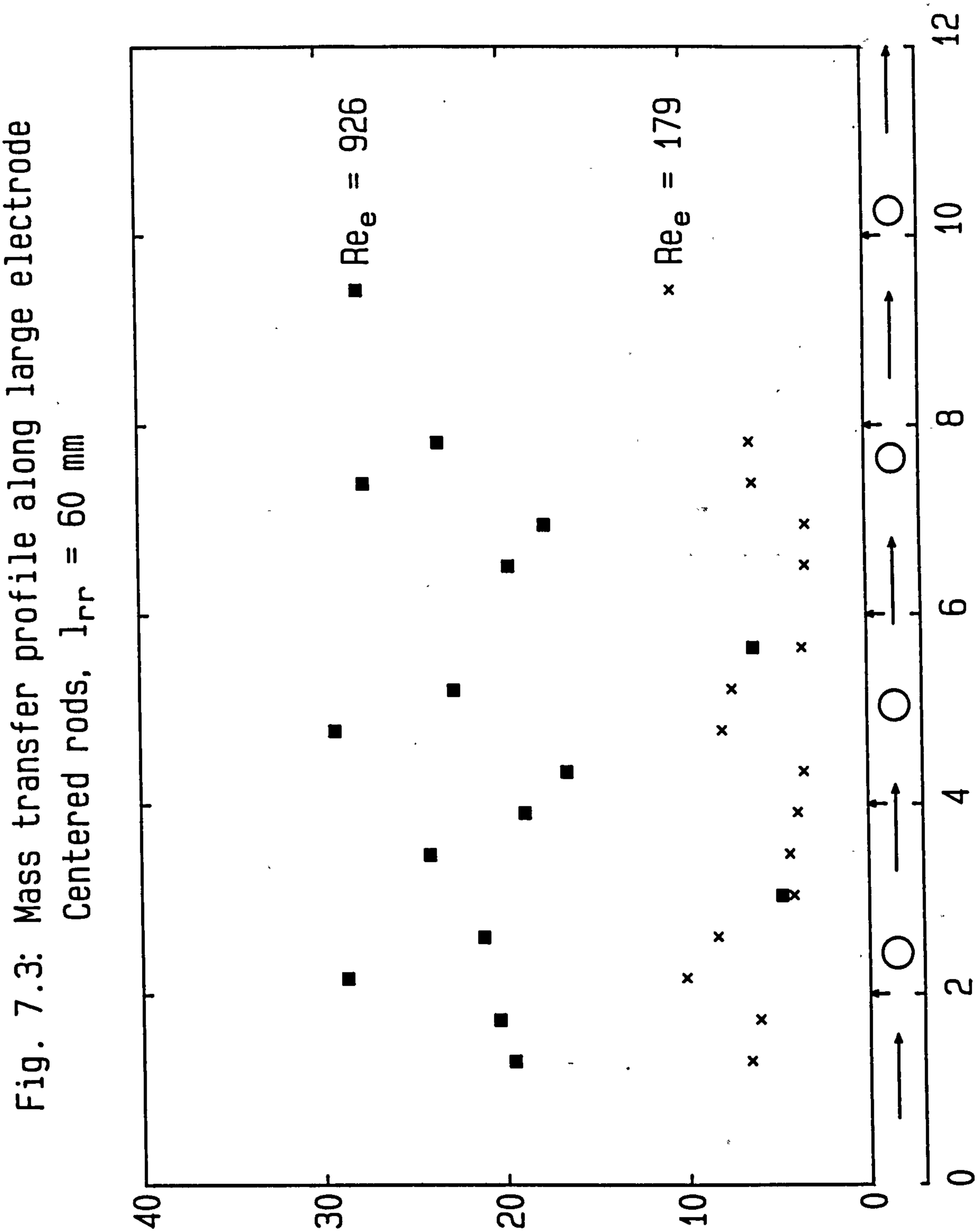

Fig. 7.3: Mass transfer profile along large electrode
Centered rods, l_{rr} = 60 mm

Fig. 7.4: Mass transfer between rods (mini-electrodes)

Centered rods, l_{rr} = 60 mm

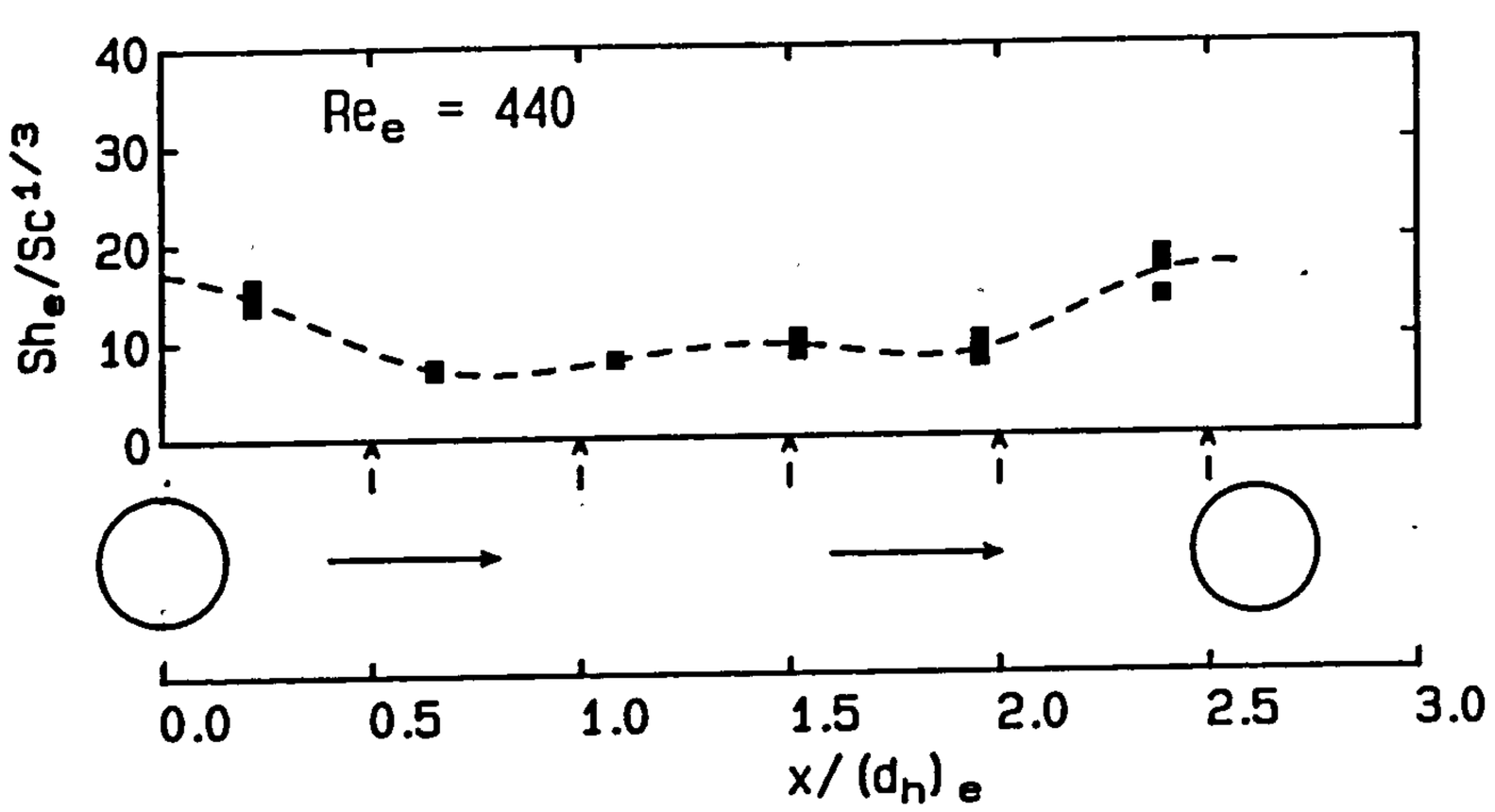

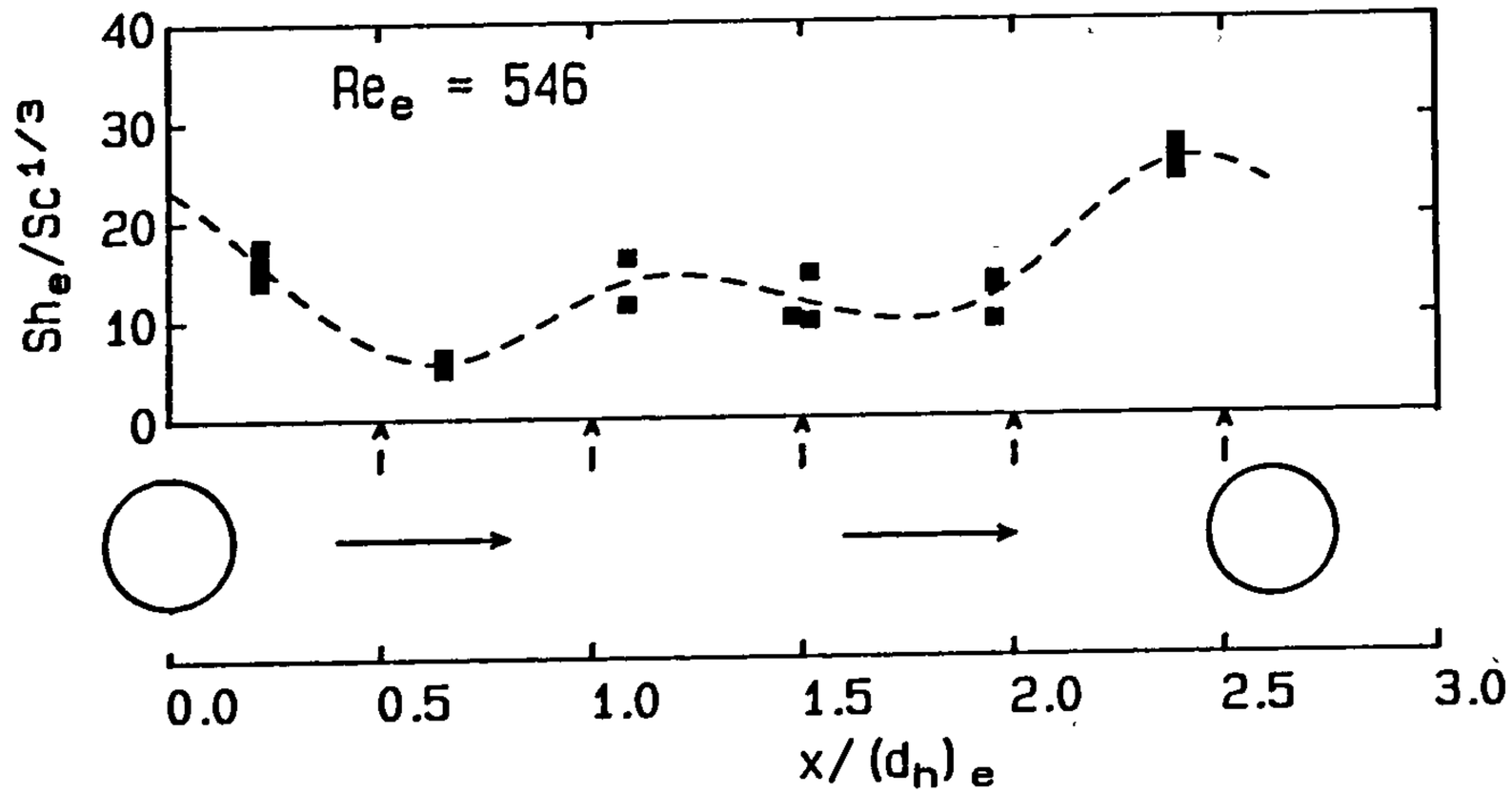

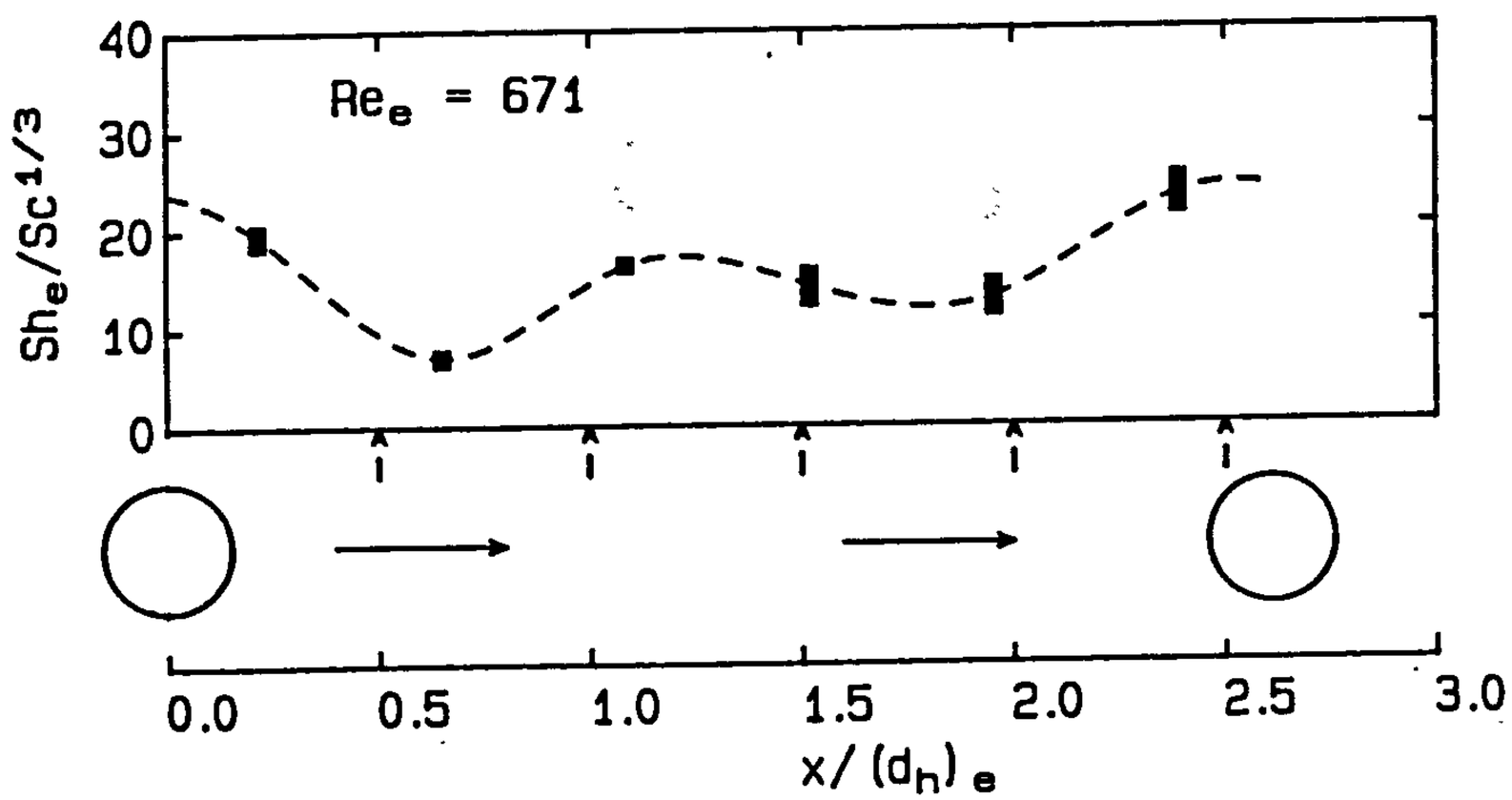

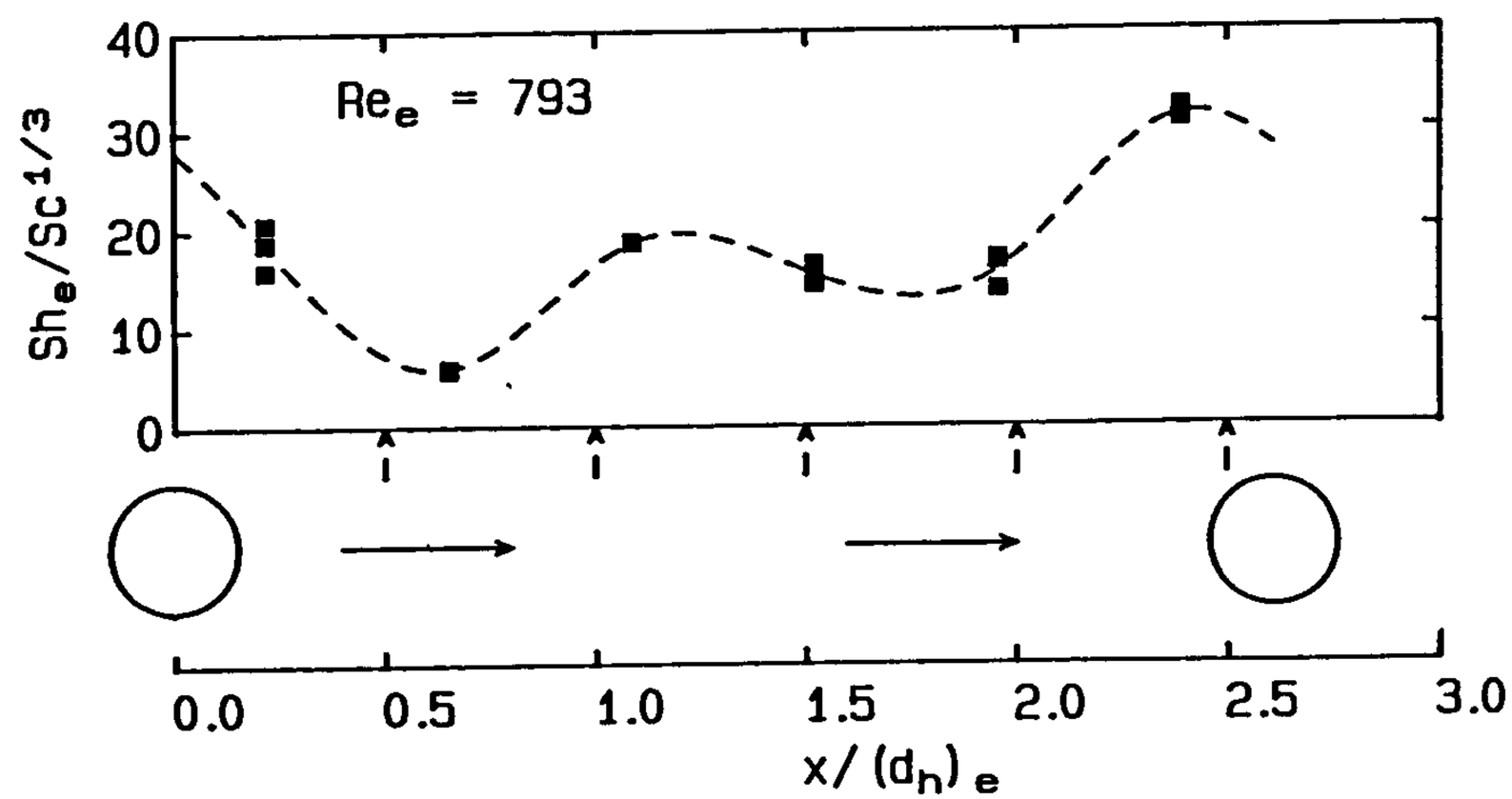

Fig. 7.4/ctd.

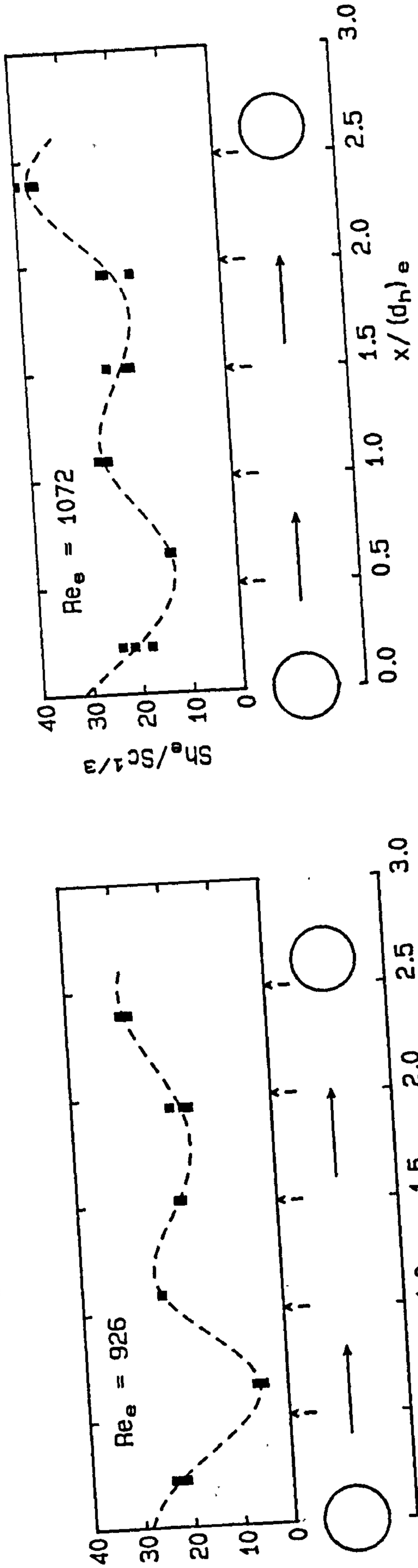
Re_e = 1072
Re_e = 926
Re_e = 1228
Sh_e/Sc^1/3
x/(d_h)_e
0
10
20
30
40
0.0
0.5
1.0
1.5
2.0
2.5
3.0

Fig. 7.5: Mass transfer between two rods (dual electrode)
Centered rods, l_{rr} = 60 mm

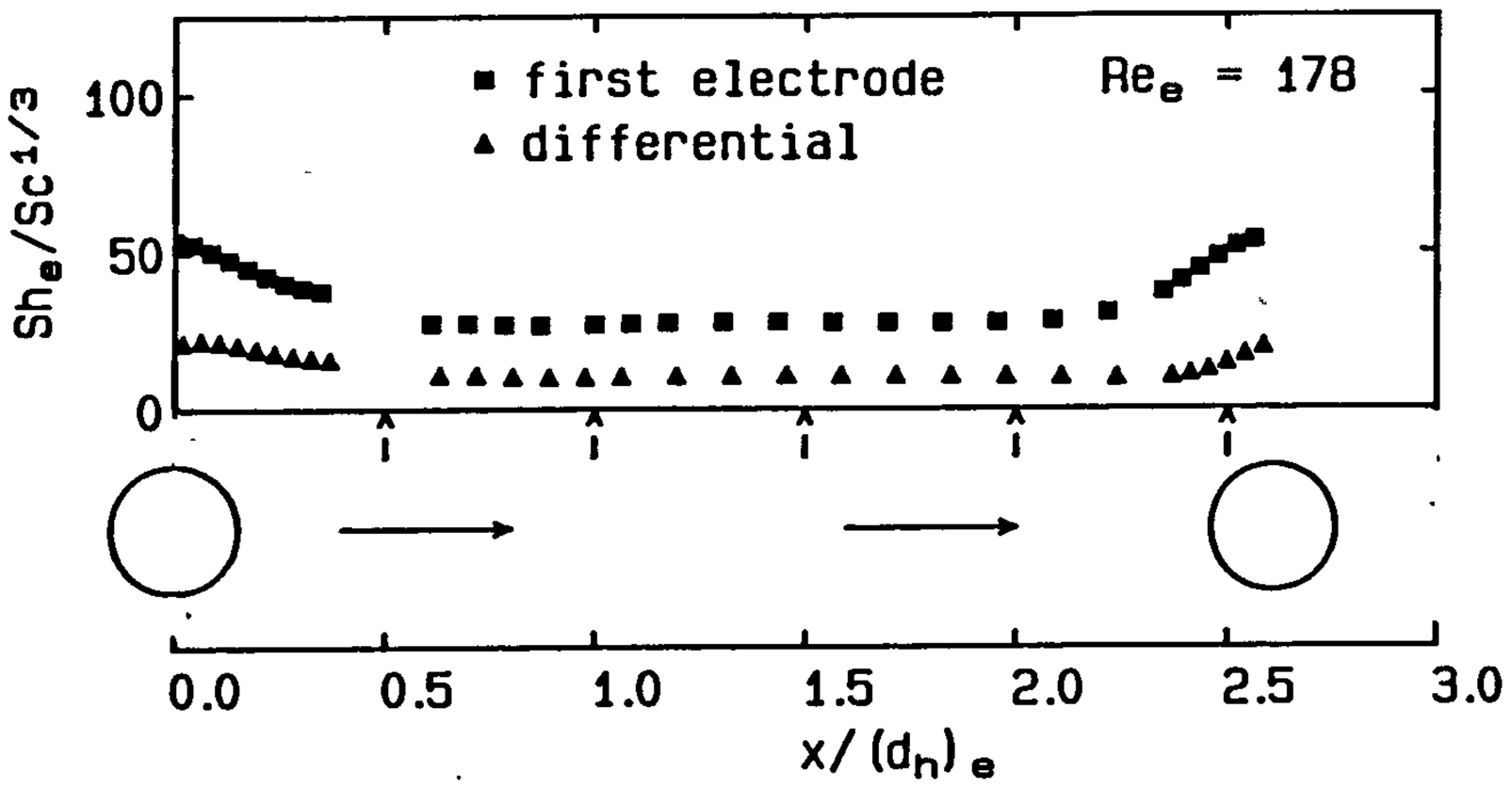

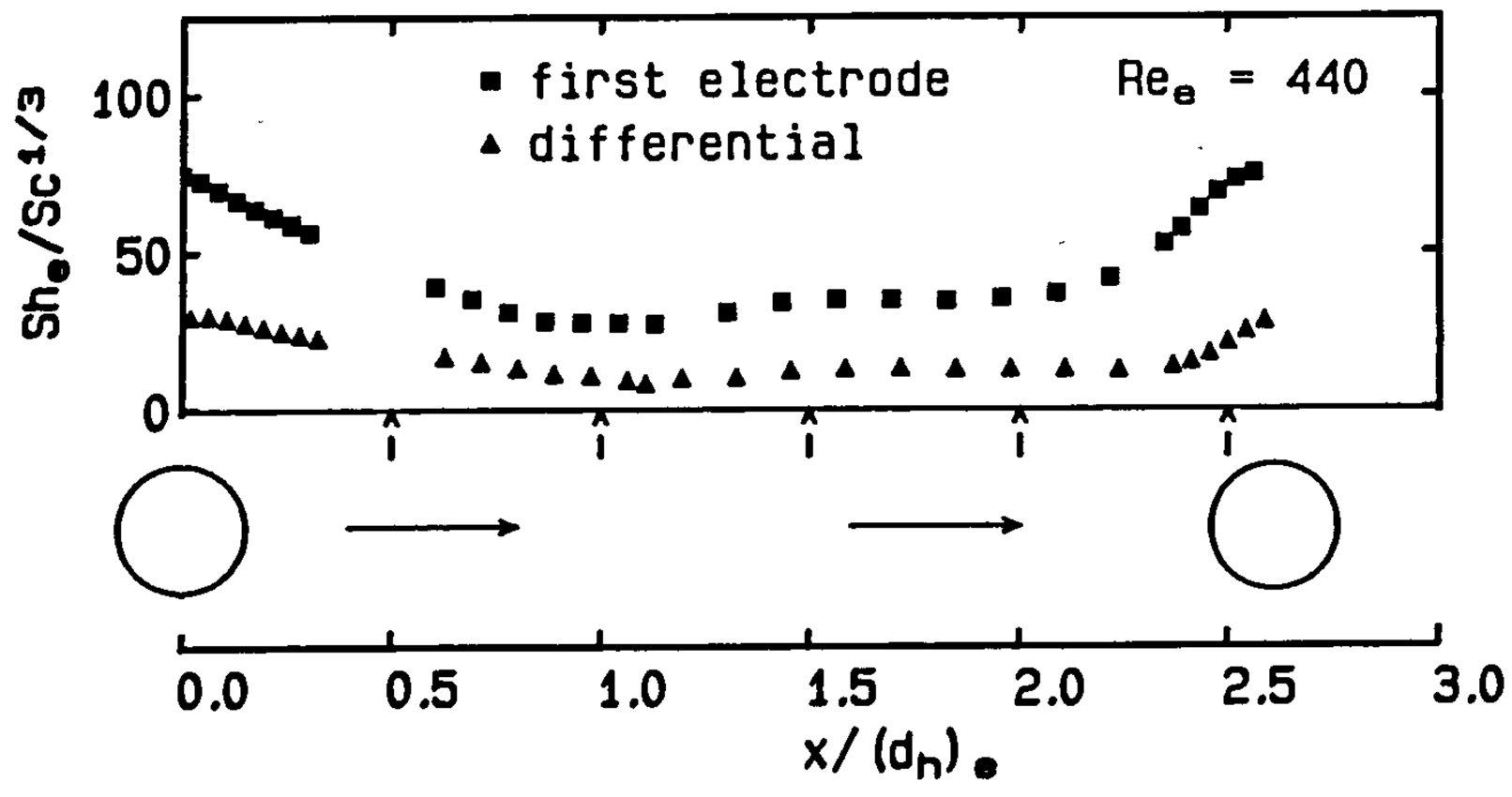

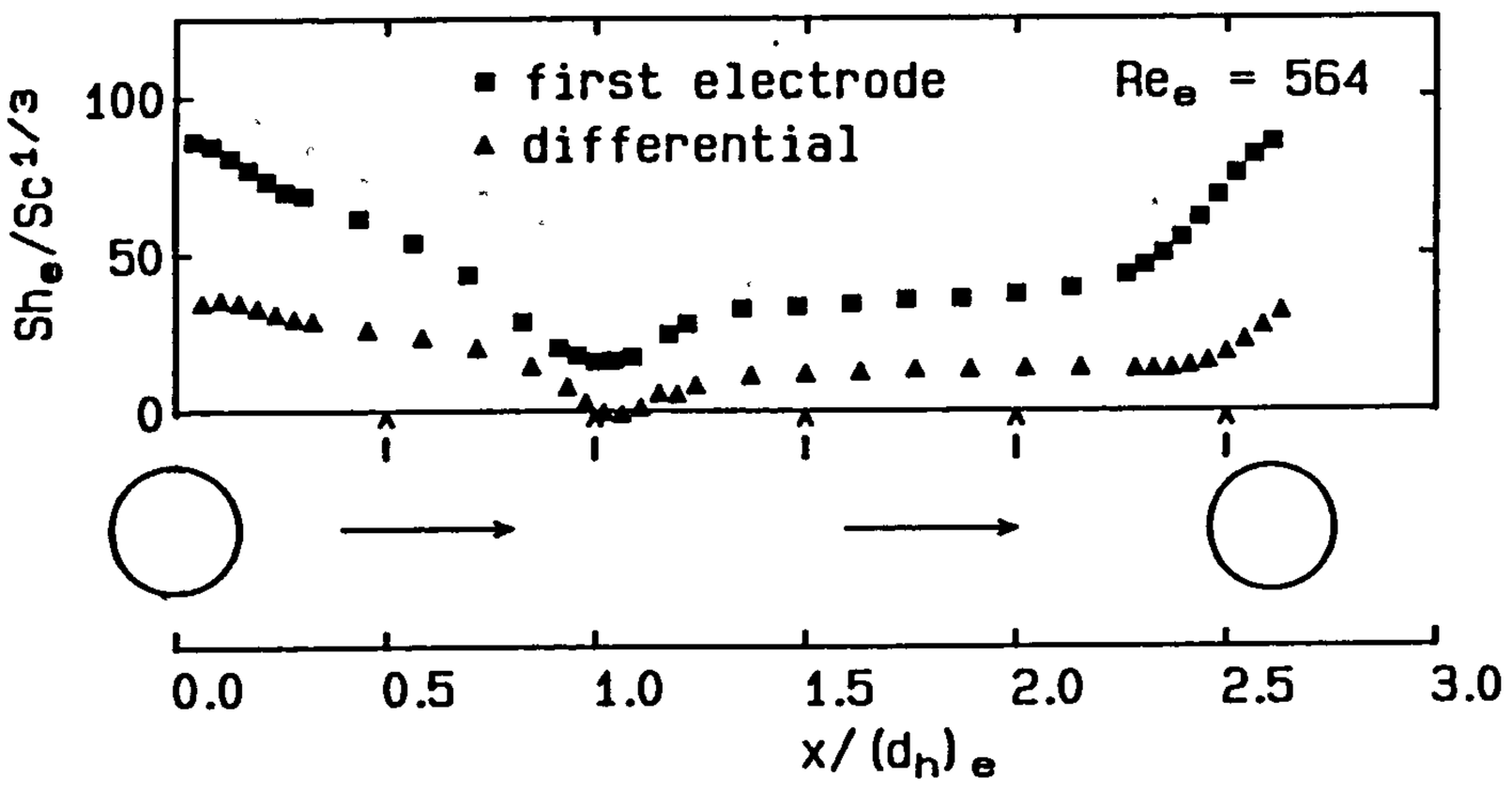

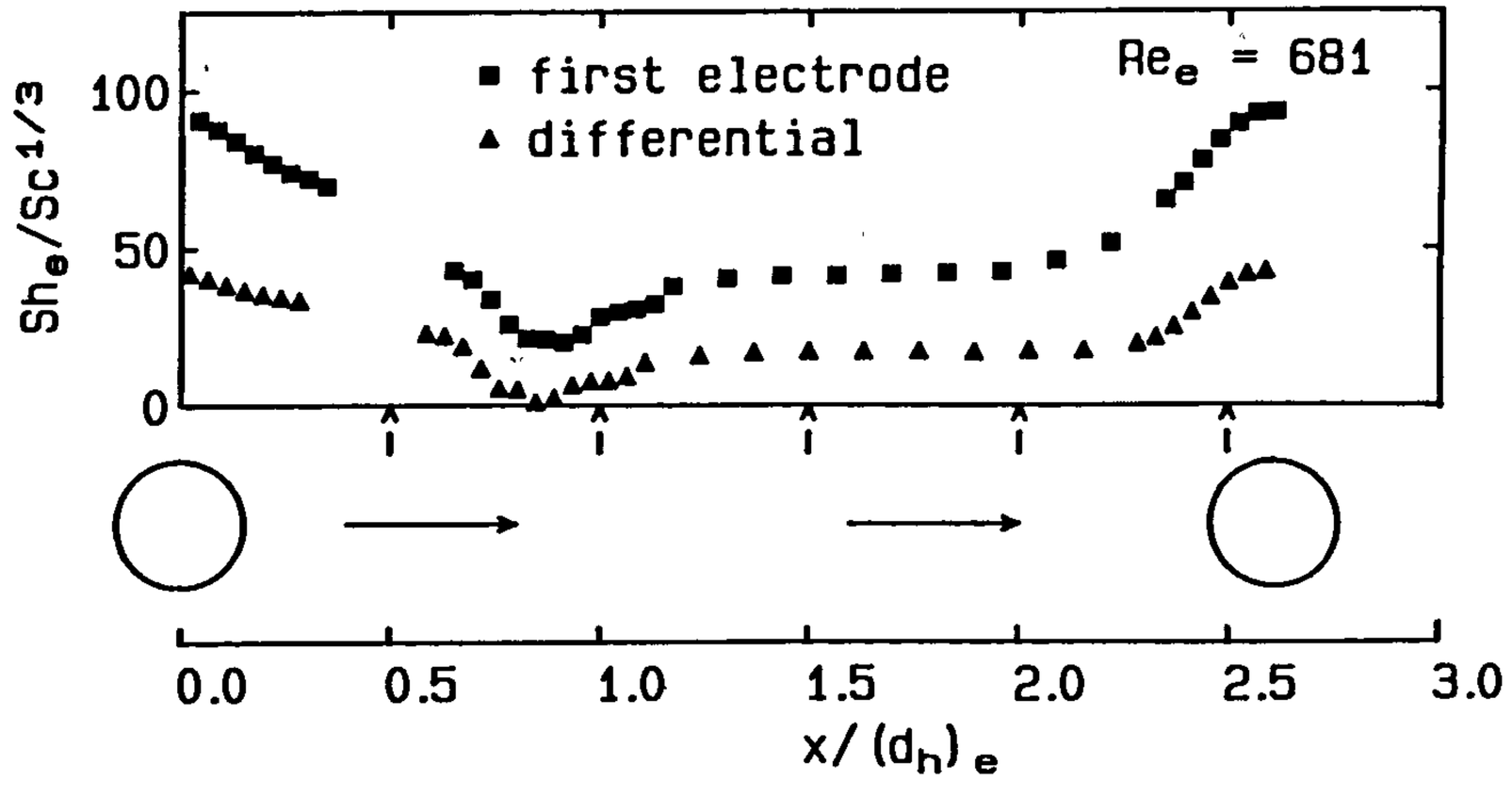

Fig. 7.5/ctd.

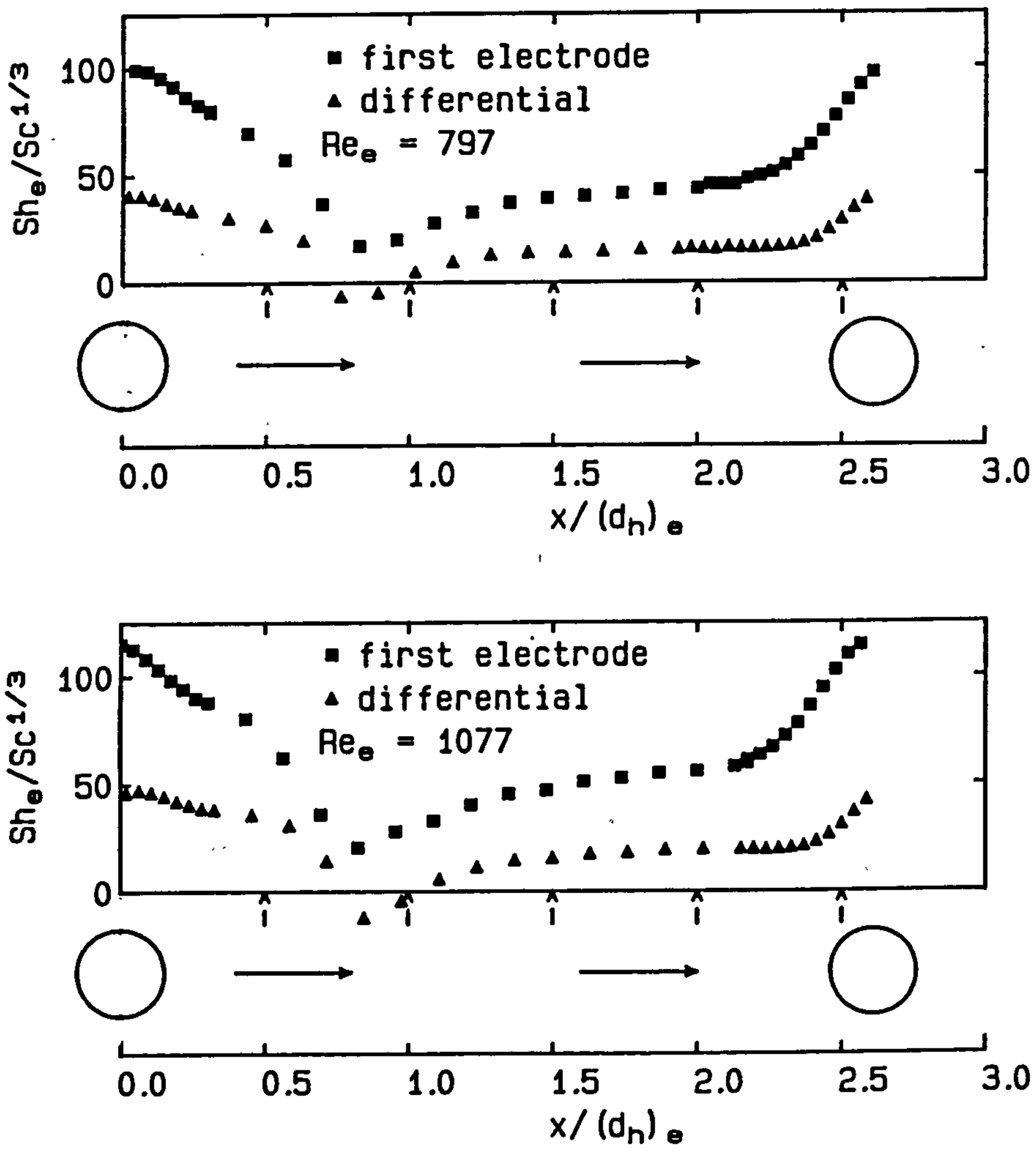
first electrode
differential
Re_e = 797
Sh_e/Sc^1/3
100
50
0
0.0
0.5
1.0
1.5
2.0
2.5
3.0
x/(d_h)_e

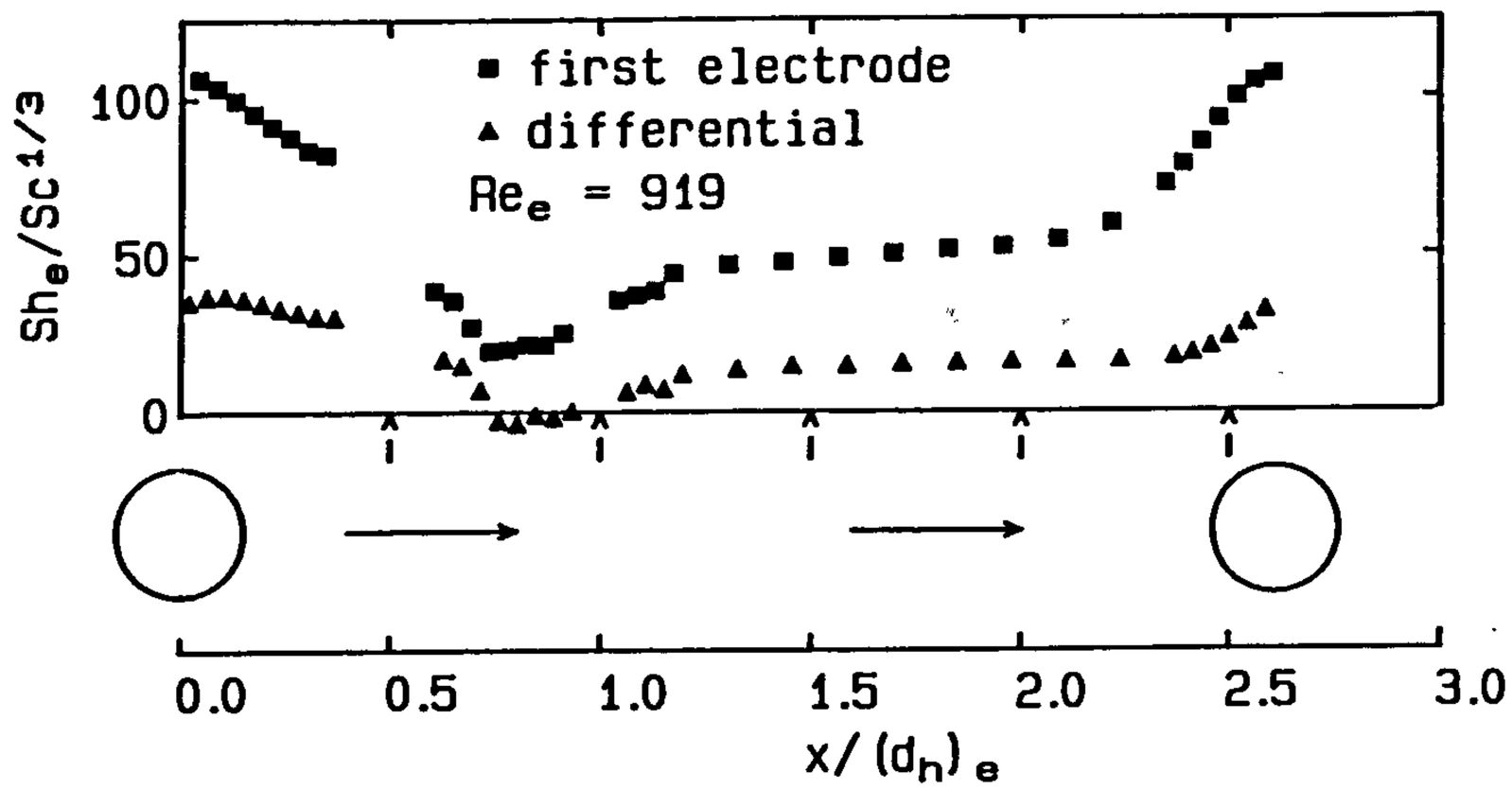
first electrode
differential
Re_e = 919
Sh_e/Sc^1/3
100
50
0
0.0
0.5
1.0
1.5
2.0
2.5
3.0
x/(d_h)_e

first electrode
differential
Re_e = 1077
Sh_e/Sc^1/3
100
50
0
0.0
0.5
1.0
1.5
2.0
2.5
3.0
x/(d_h)_e

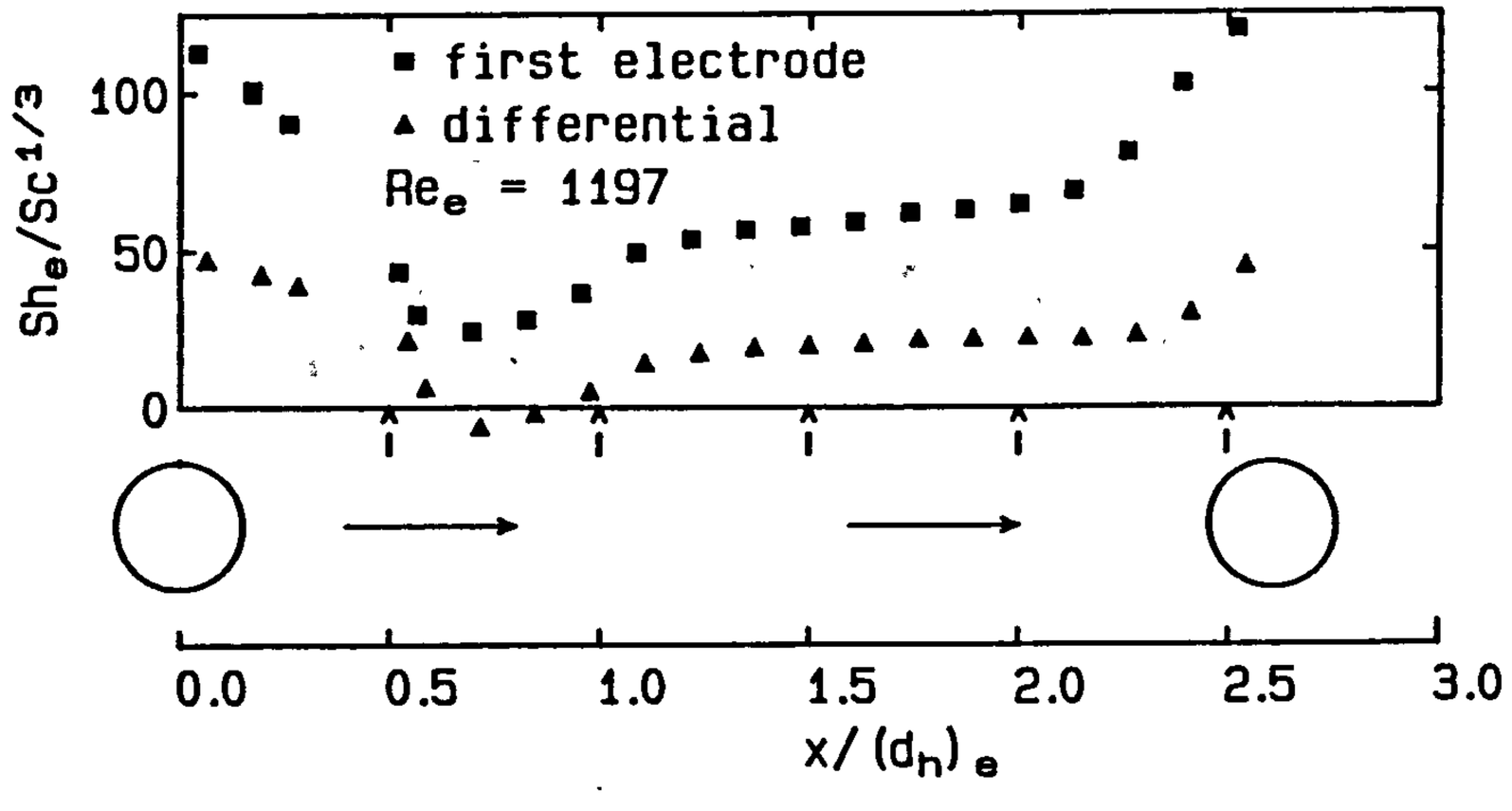
first electrode
differential
Re_e = 1197
Sh_e/Sc^1/3
100
50
0
0.0
0.5
1.0
1.5
2.0
2.5
3.0
x/(d_h)_e

Fig. 7.6: Mass transfer standard deviation (first electrode)
Centered rods, l_{rr} = 60 mm

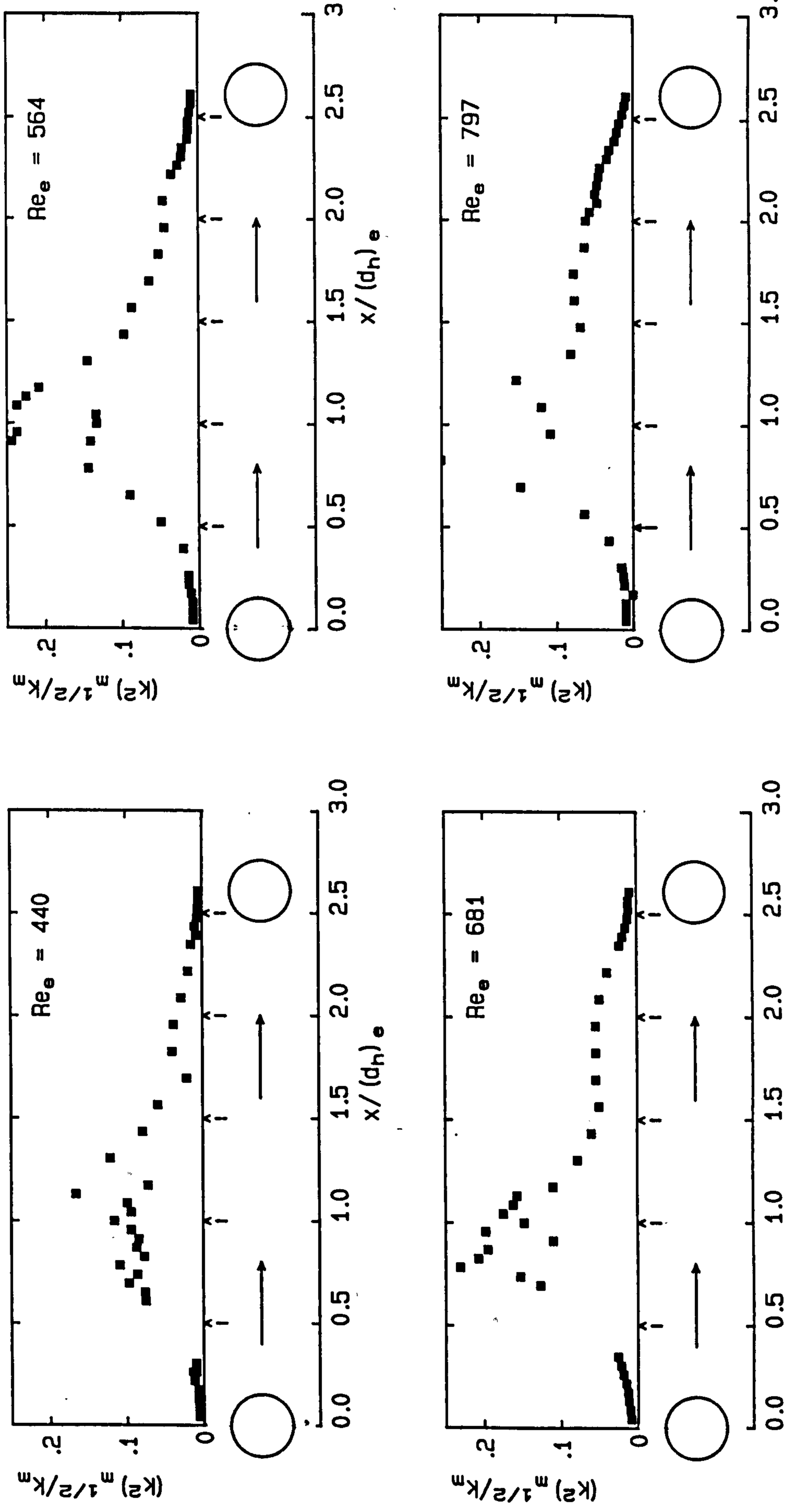

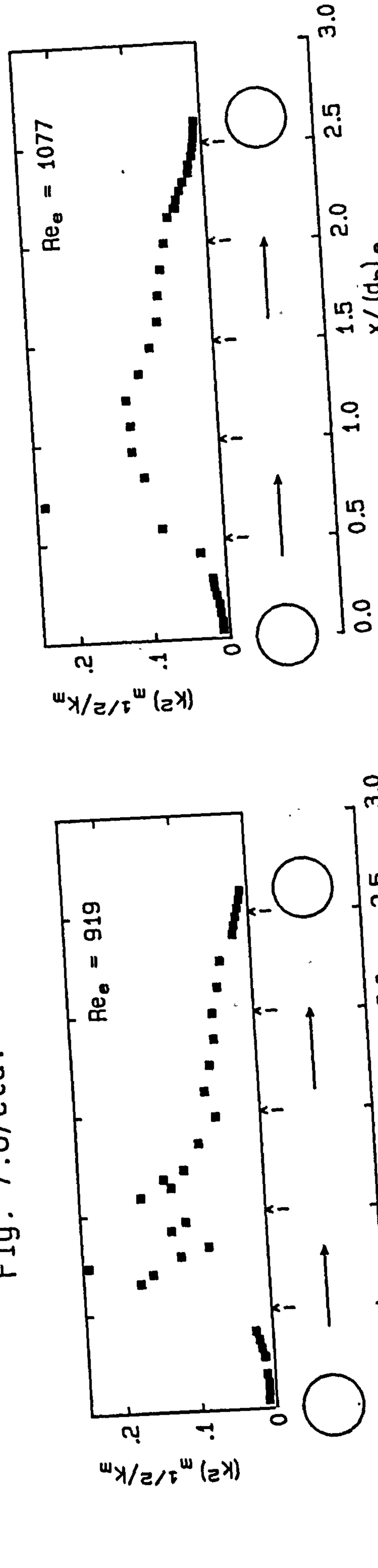

Fig. 7.6/ctd.

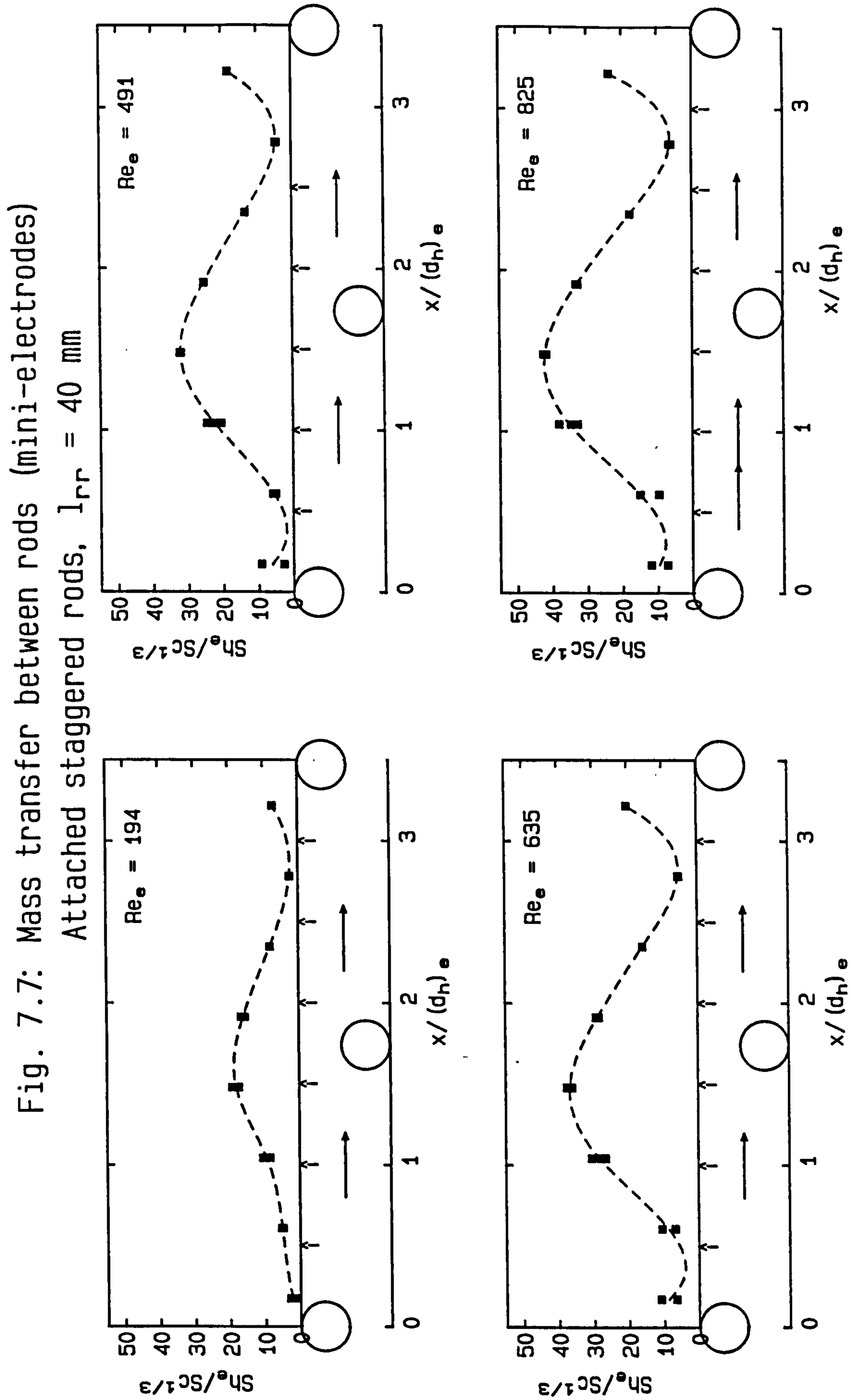

Fig. 7.7: Mass transfer between rods (mini-electrodes)
Attached staggered rods, l_{rr} = 40 mm

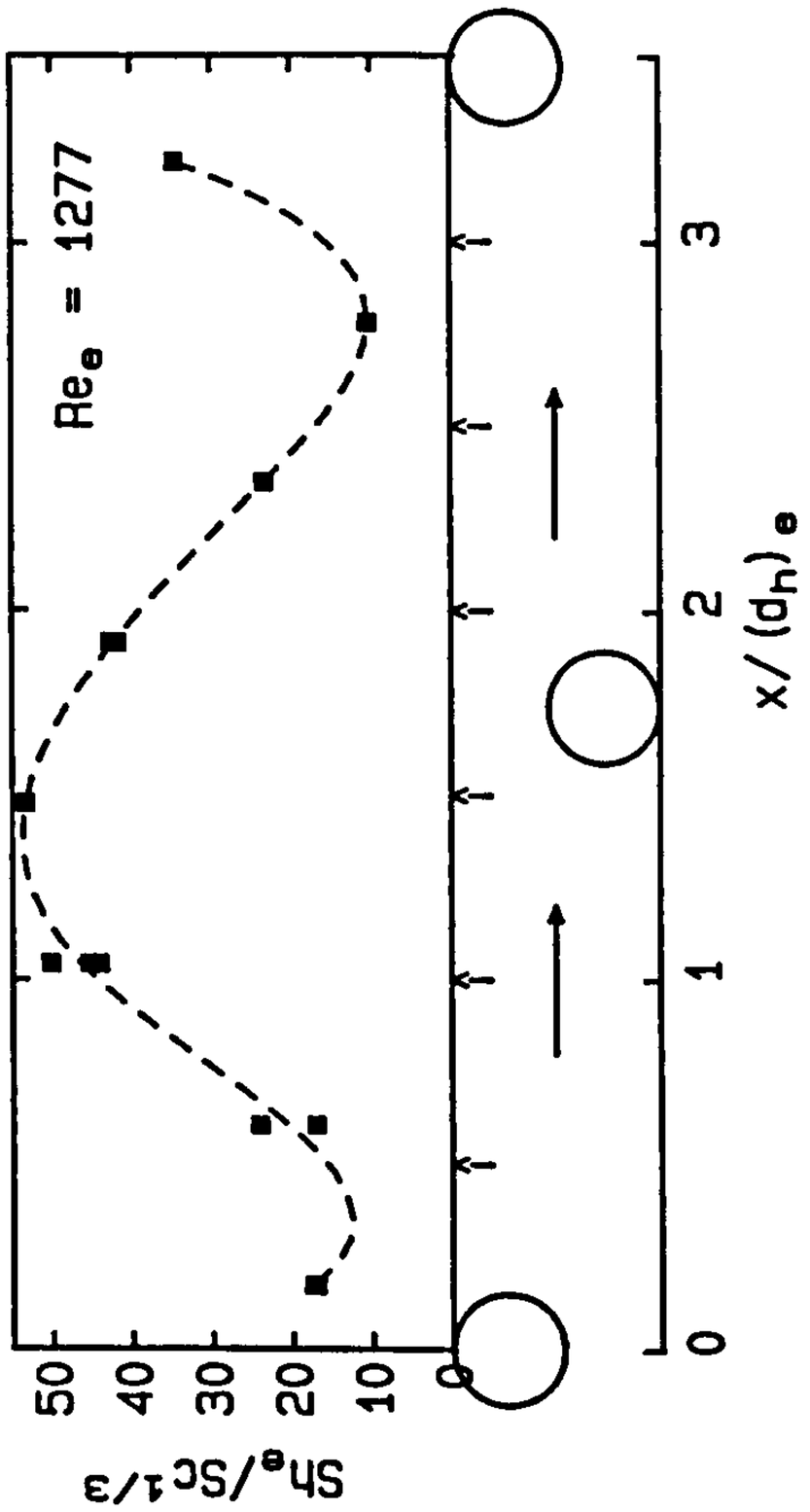
Re_e = 1277
$Sh_e/Sc^{1/3}$
50
40
30
20
10
0
$x/(d_h)_e$
3
2
1
0

Fig. 7.7/ctd.

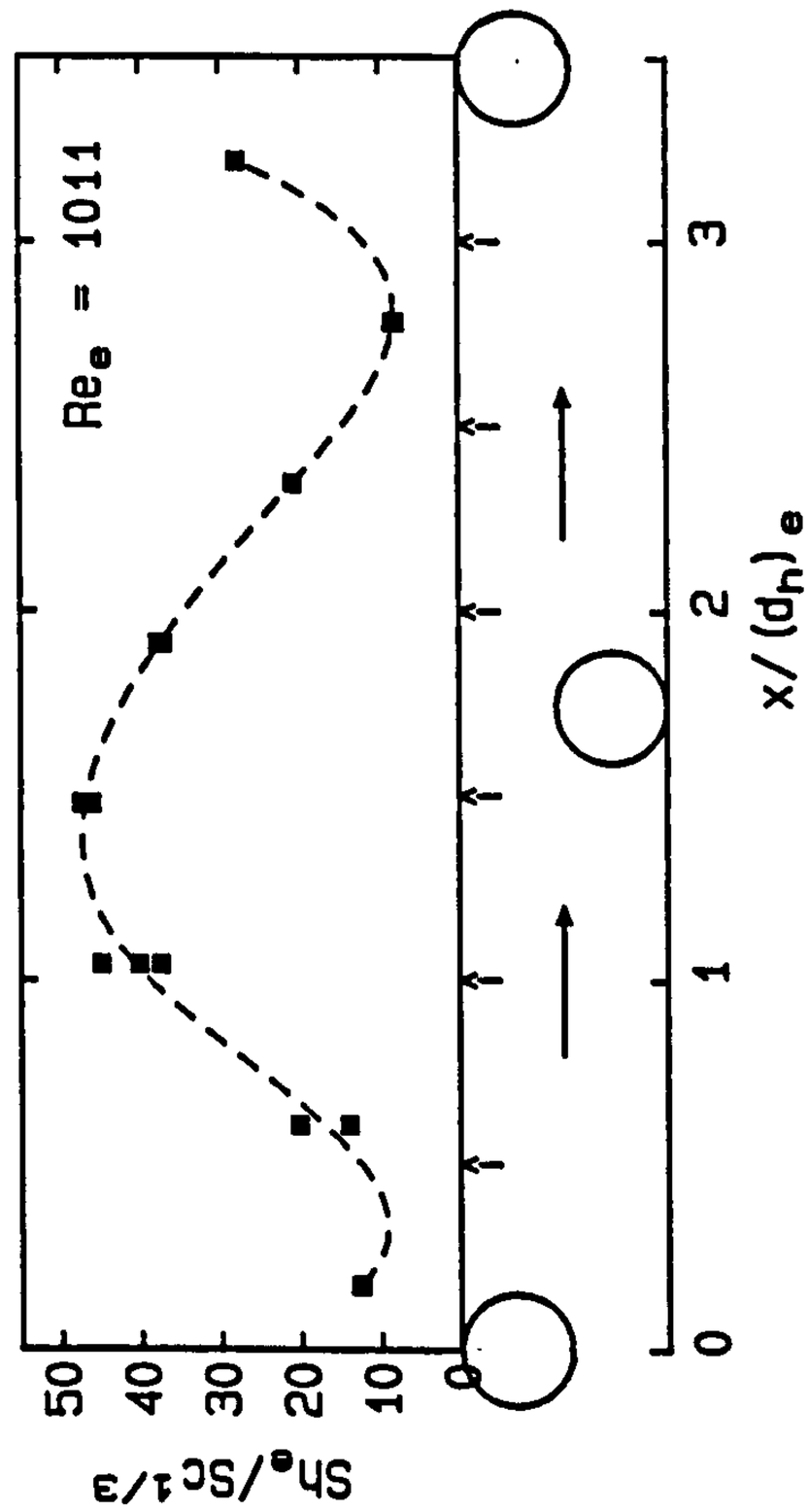
Re_e = 1011
$Sh_e/Sc^{1/3}$
50
40
30
20
10
0
$x/(d_h)_e$
3
2
1
0

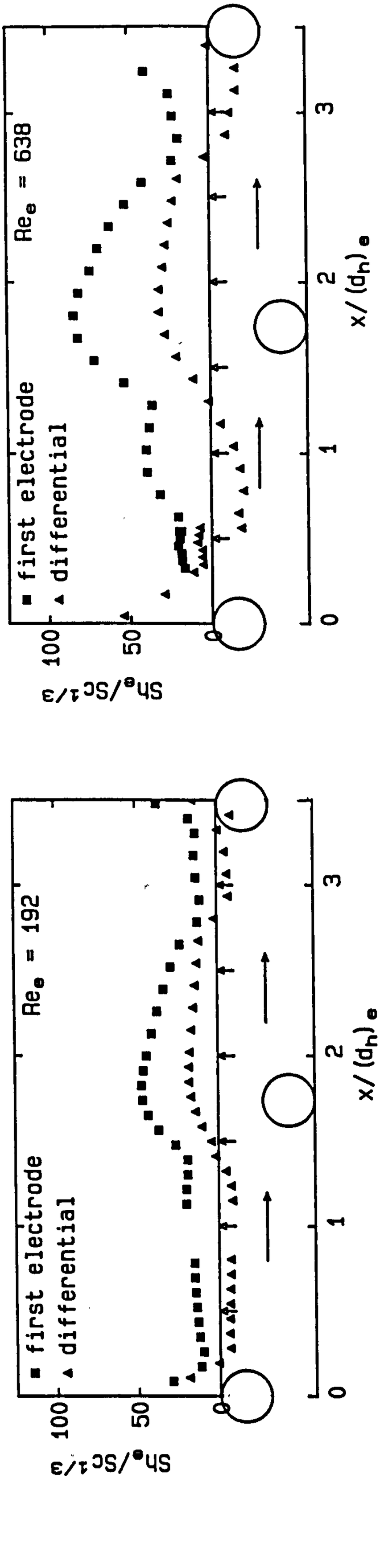

Fig. 7.8: Mass transfer between rods (dual electrode)
Attached staggered rods, l_{rr} = 40 mm

Fig. 7.9: Mass transfer standard deviation (first electrode)
Attached staggered rods, l_{rr} = 40 mm

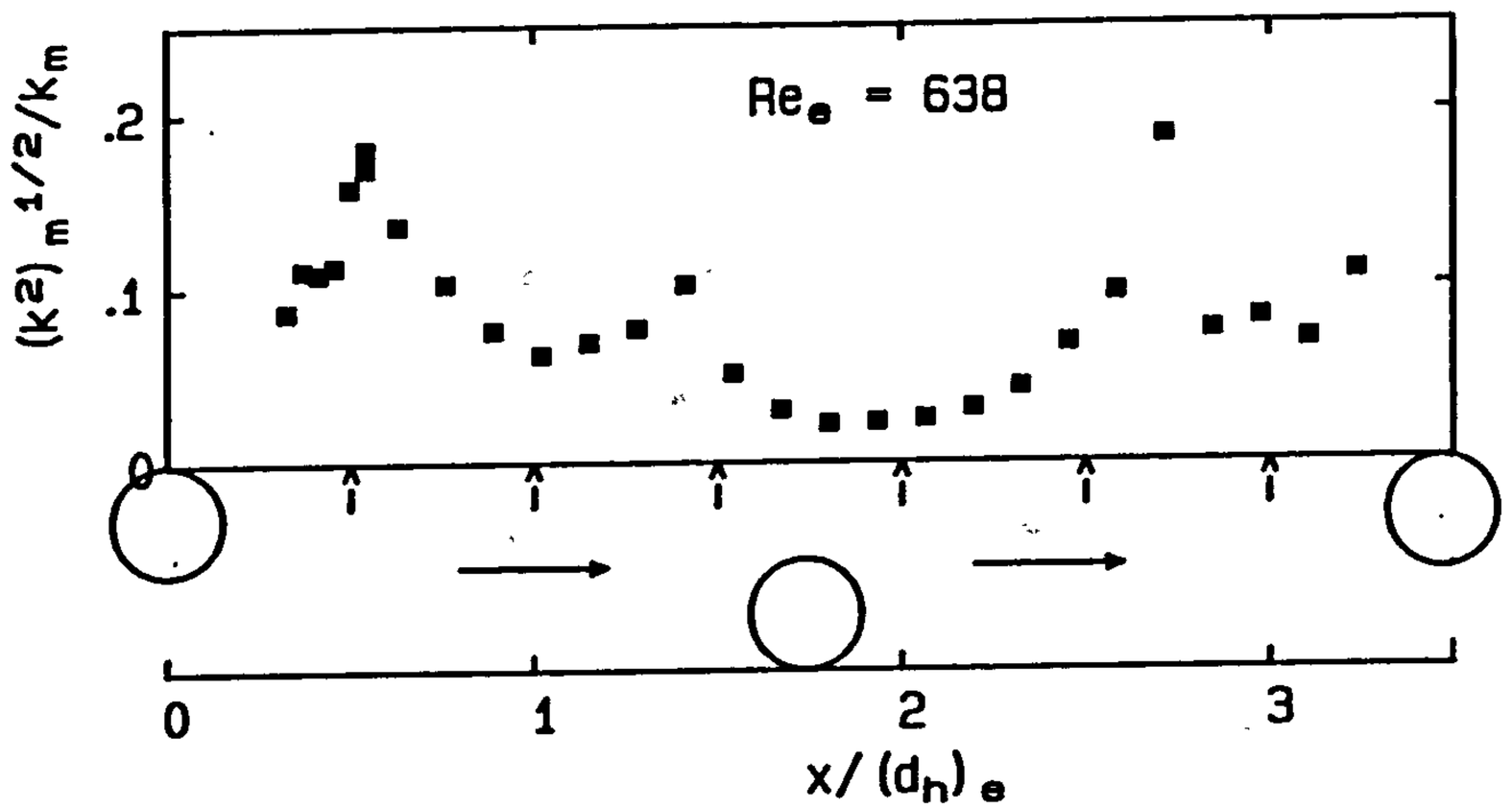

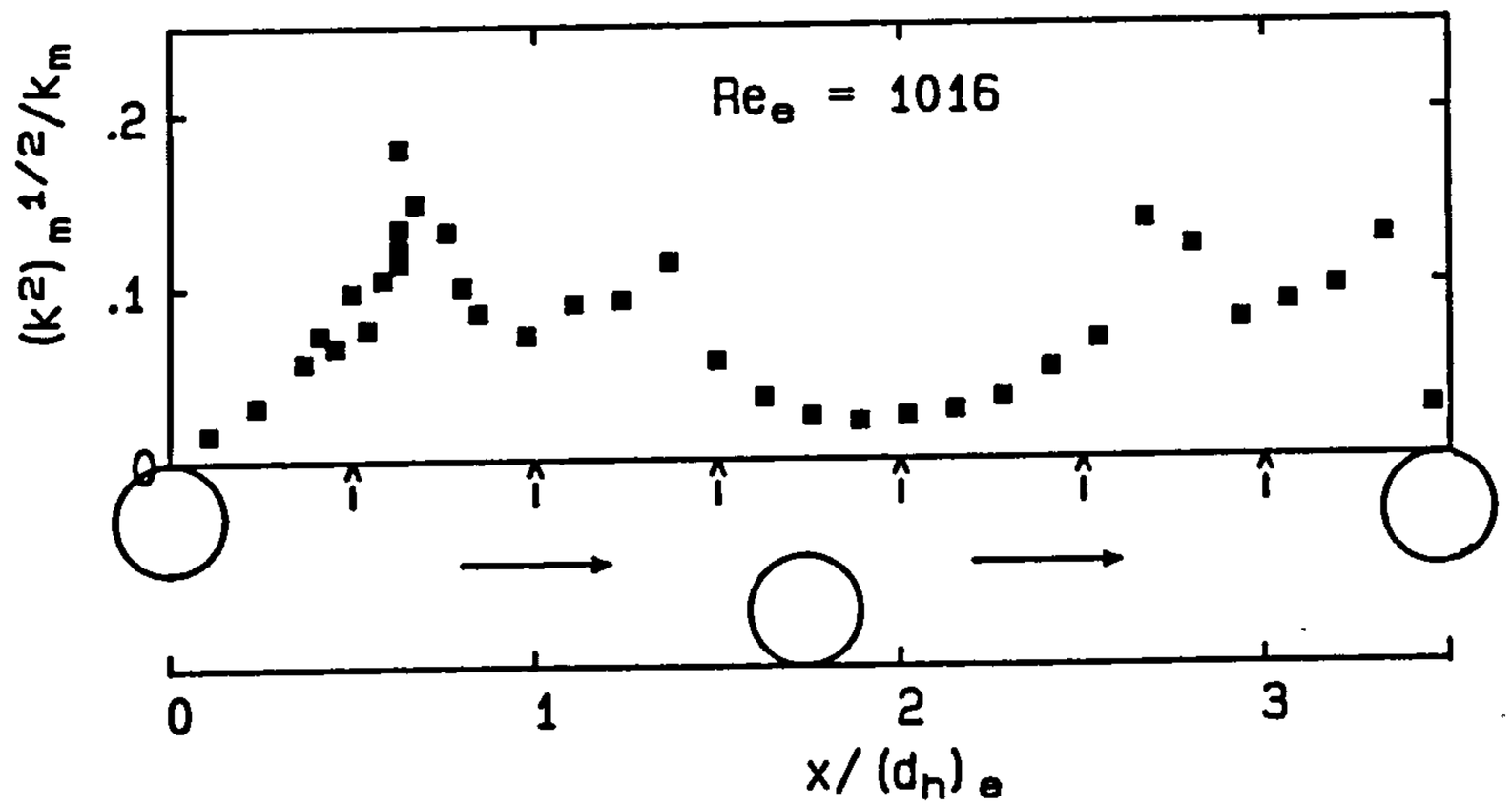

Fig. 7.10: Mass transfer between rods (mini-electrodes)
Suspended staggered rods, l_{rr} = 24 mm, d_{rw} = 2 mm

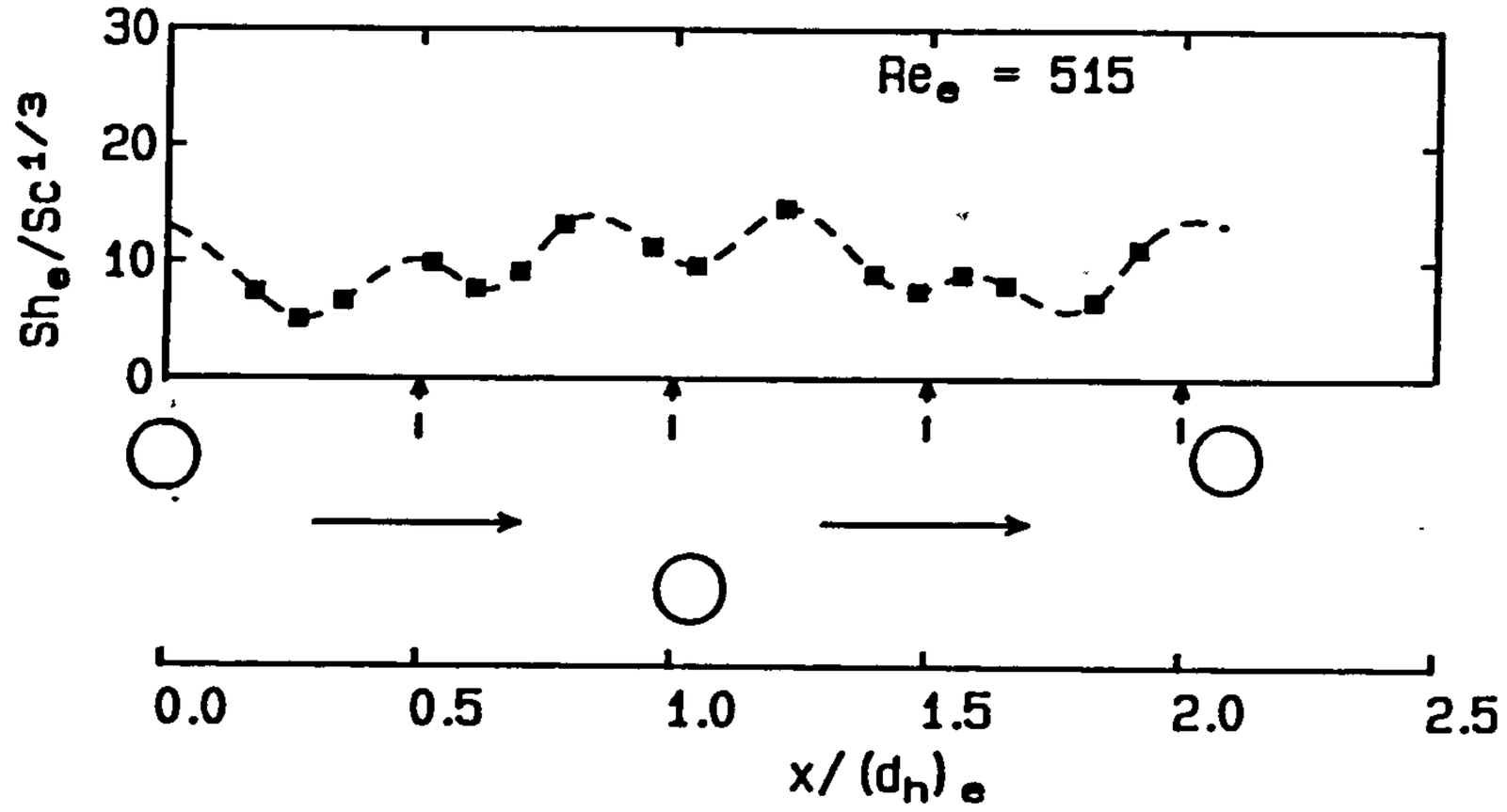

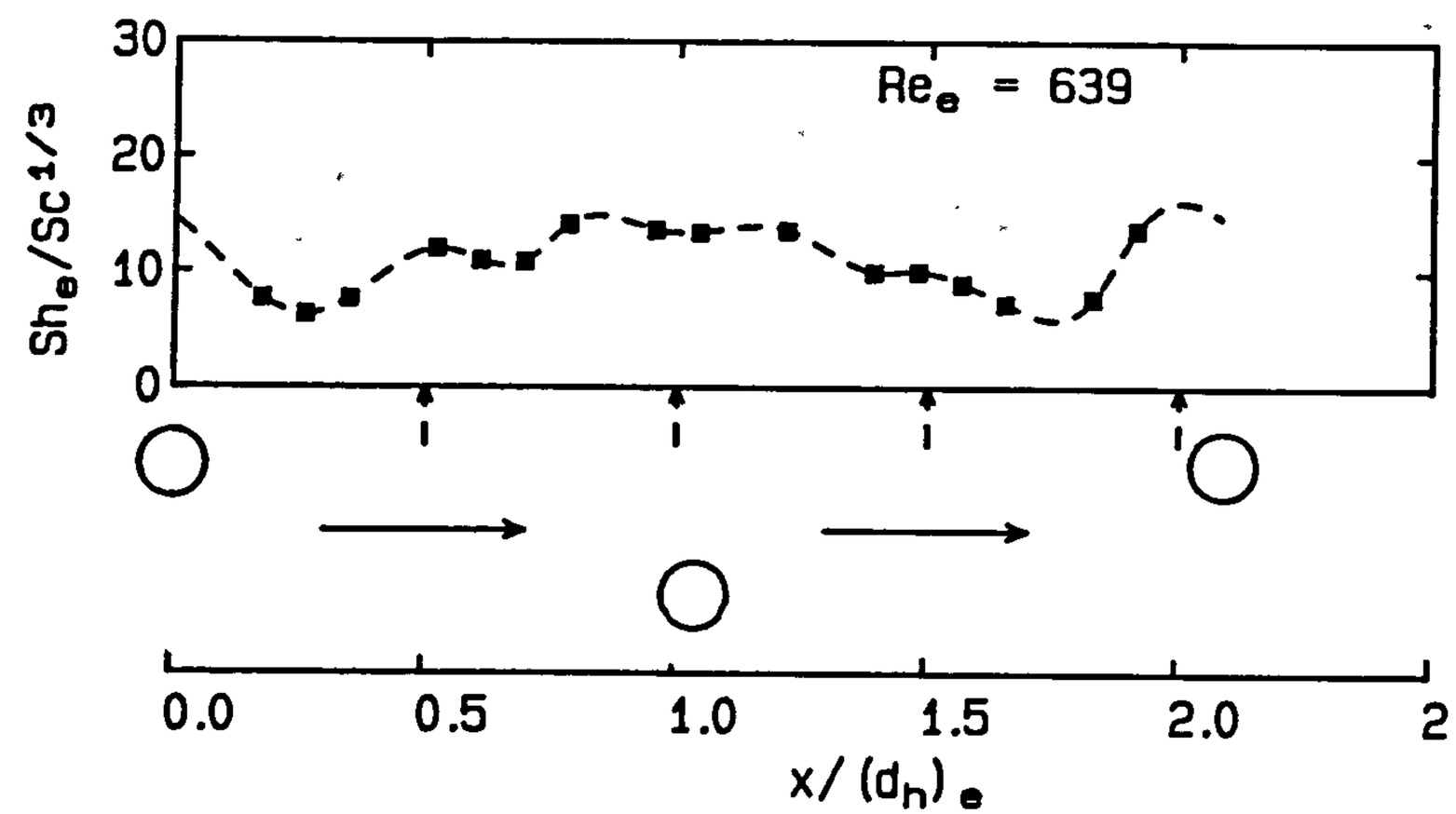

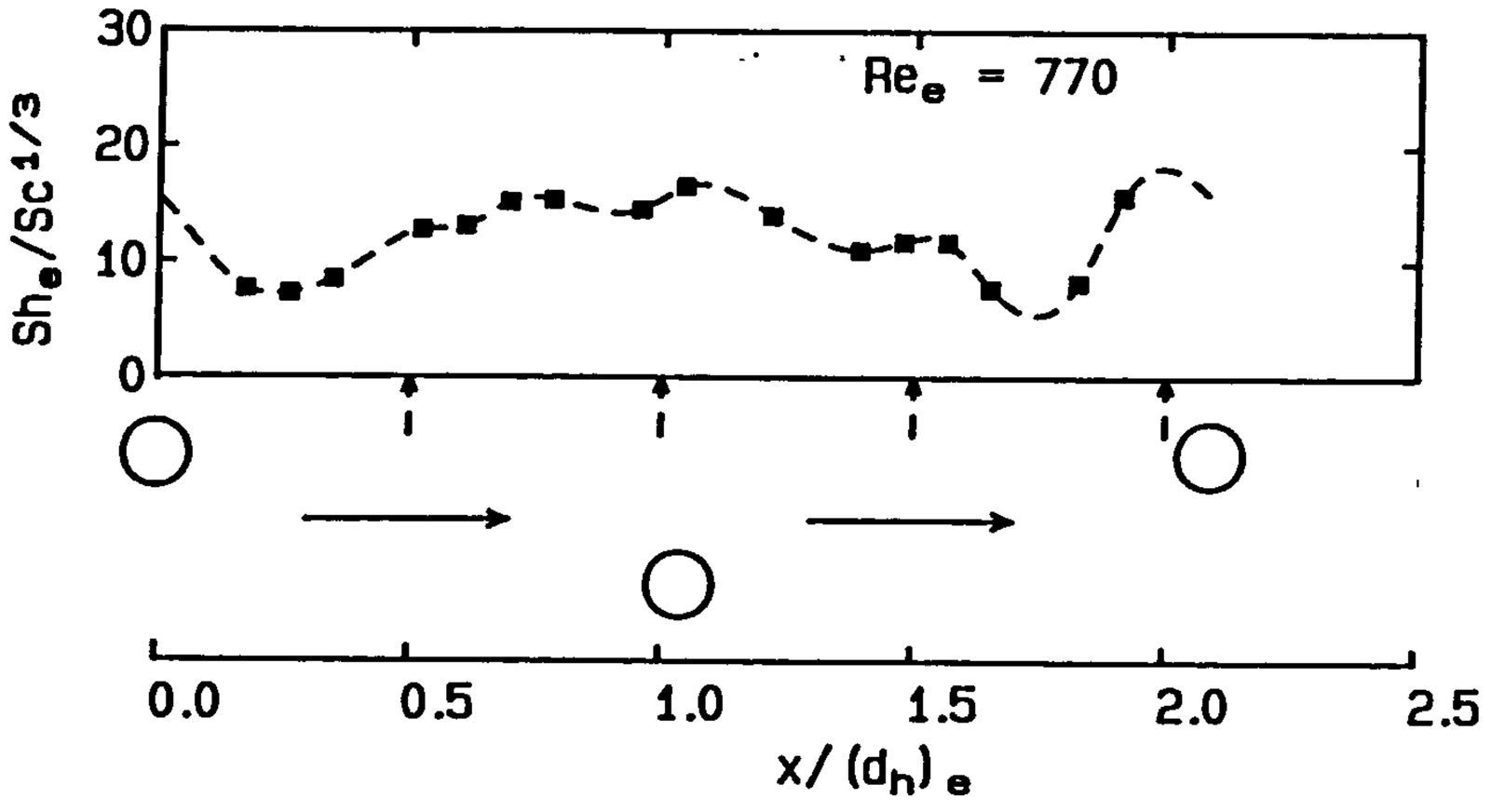

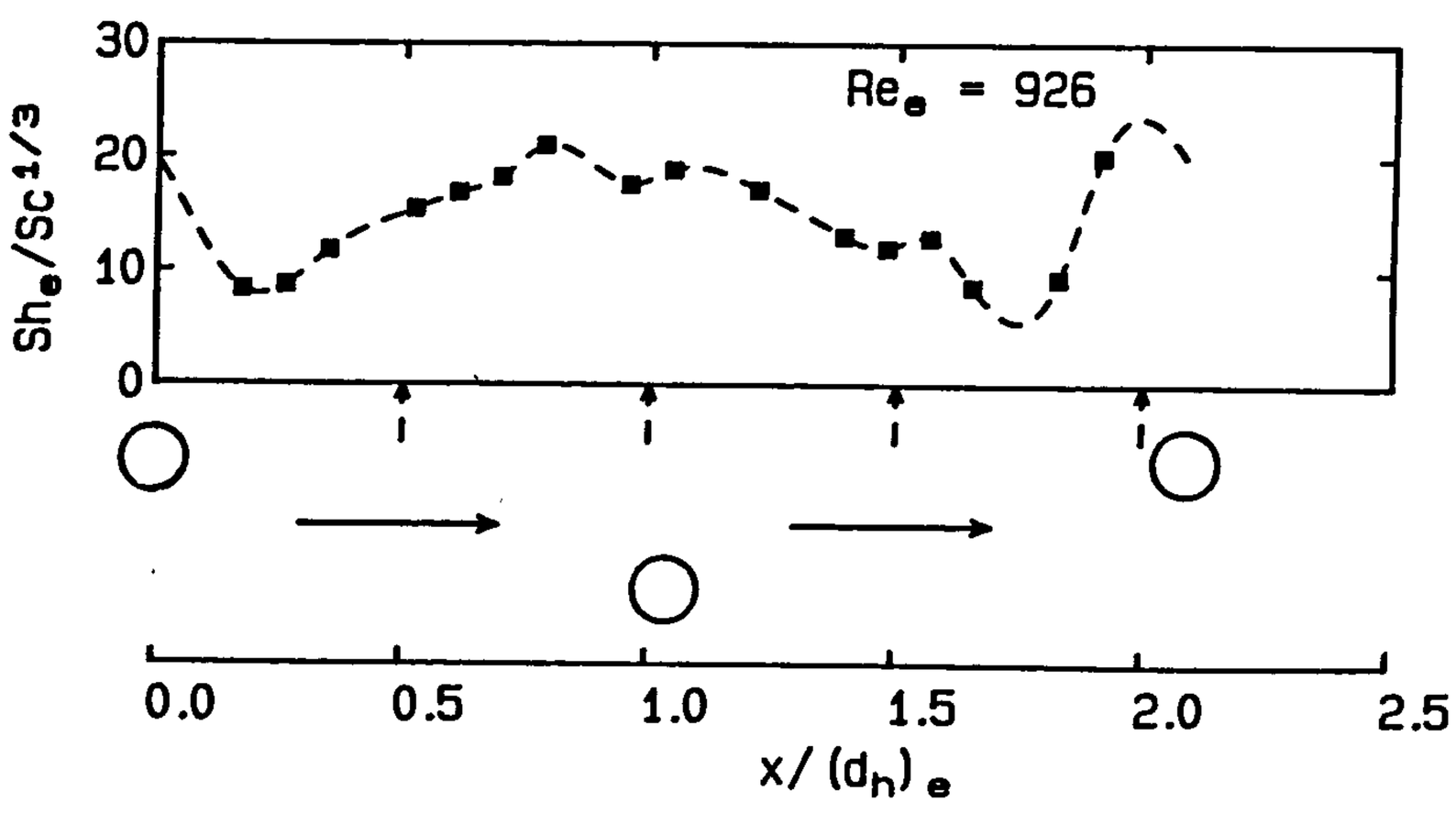

Fig. 7.10/ctd.

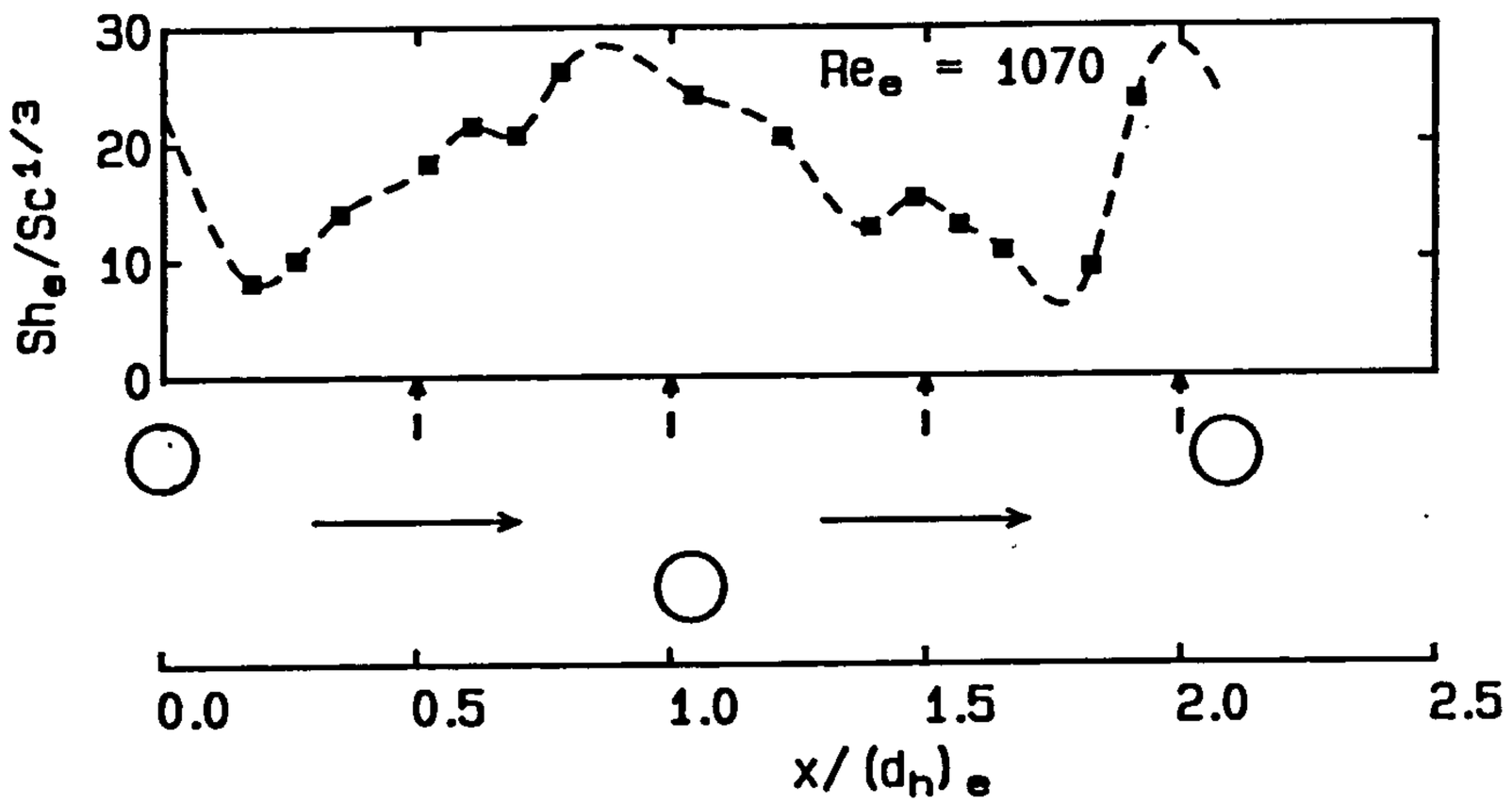
Re_e = 1070
$Sh_e/Sc^{1/3}$
30
20
10
0
0.0
0.5
1.0
1.5
2.0
2.5
$x/(d_h)_e$

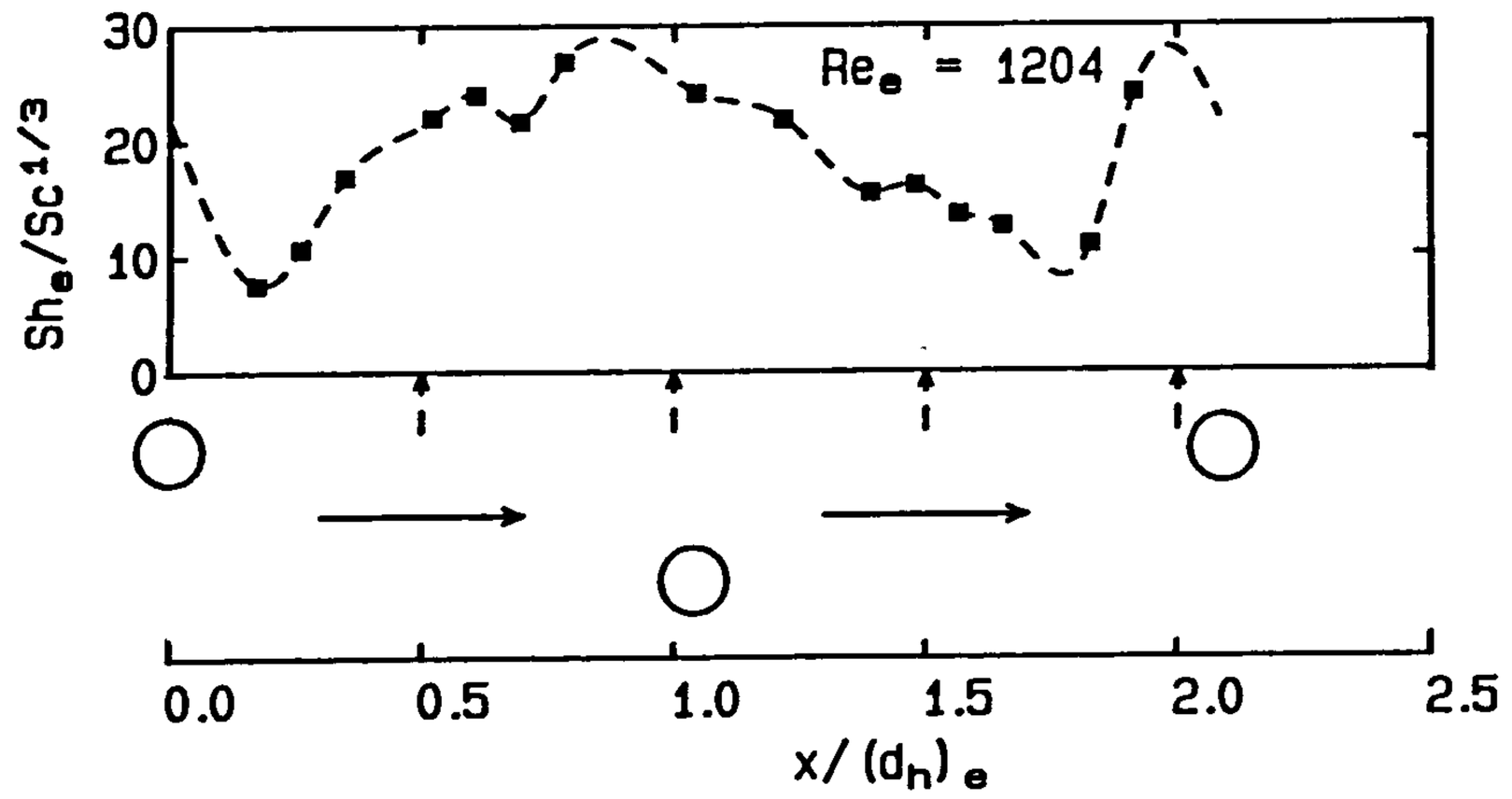
Re_e = 1204
$Sh_e/Sc^{1/3}$
30
20
10
0
0.0
0.5
1.0
1.5
2.0
2.5
$x/(d_h)_e$

Fig. 7.11: Mass transfer between rods (dual electrode)
Suspended staggered rods, l_{rr} = 24 mm, d_{rw} = 2 mm

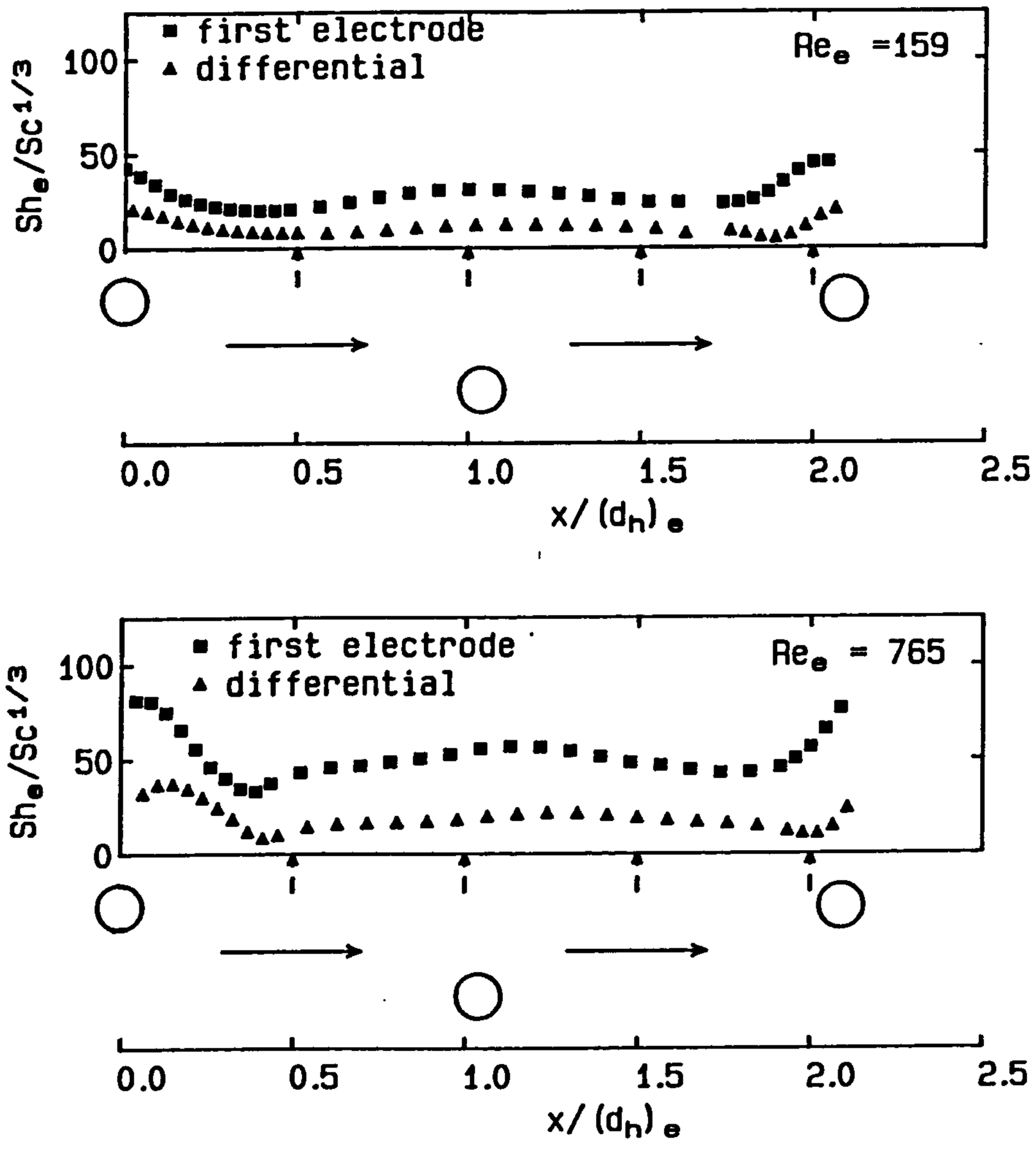

Fig. 7.11/ctd.

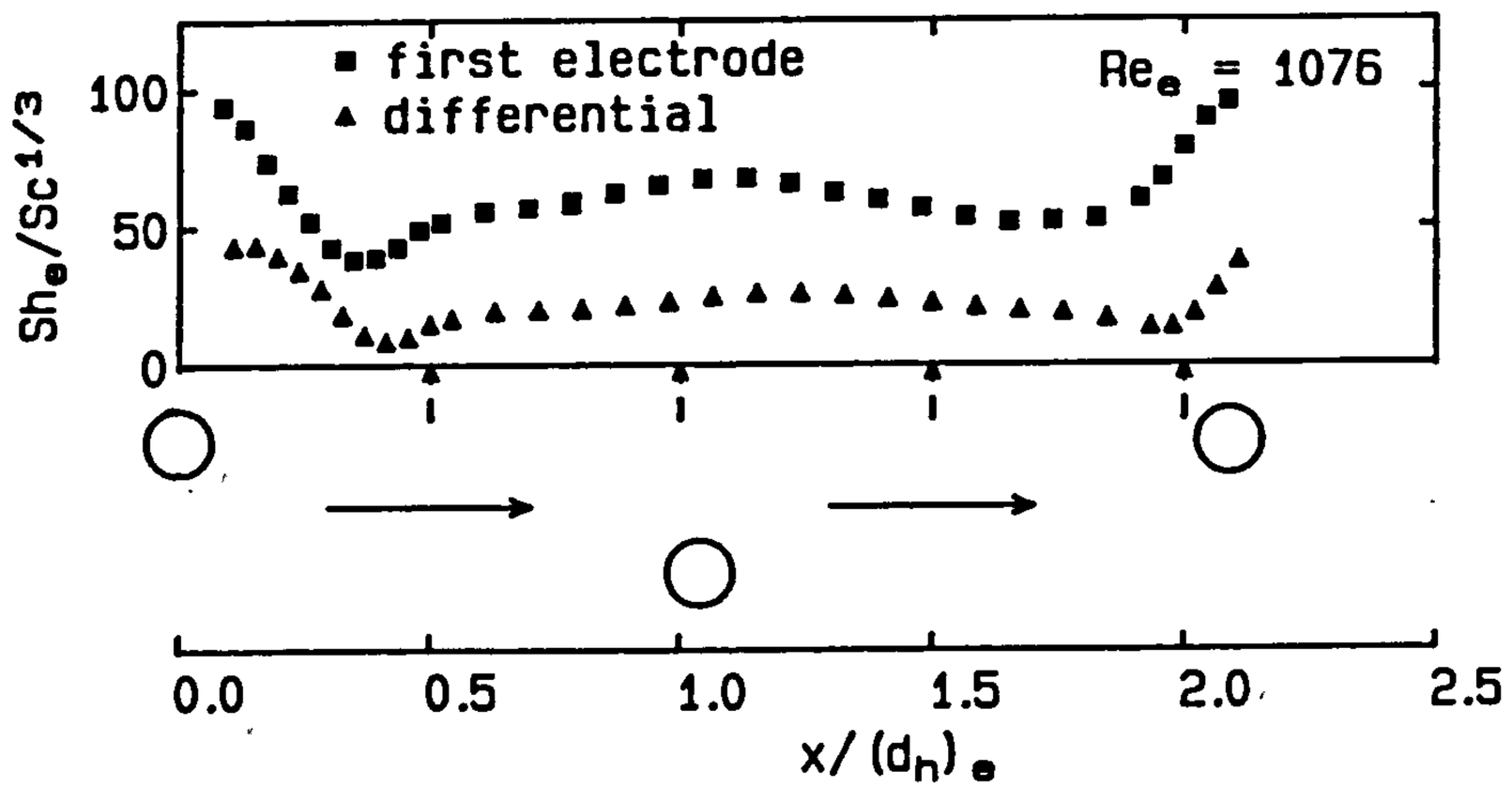
first electrode
differential
Re_e = 1076
Sh_e/Sc^1/3
100
50
0
0.0
0.5
1.0
1.5
2.0
2.5
x/(d_h)_e

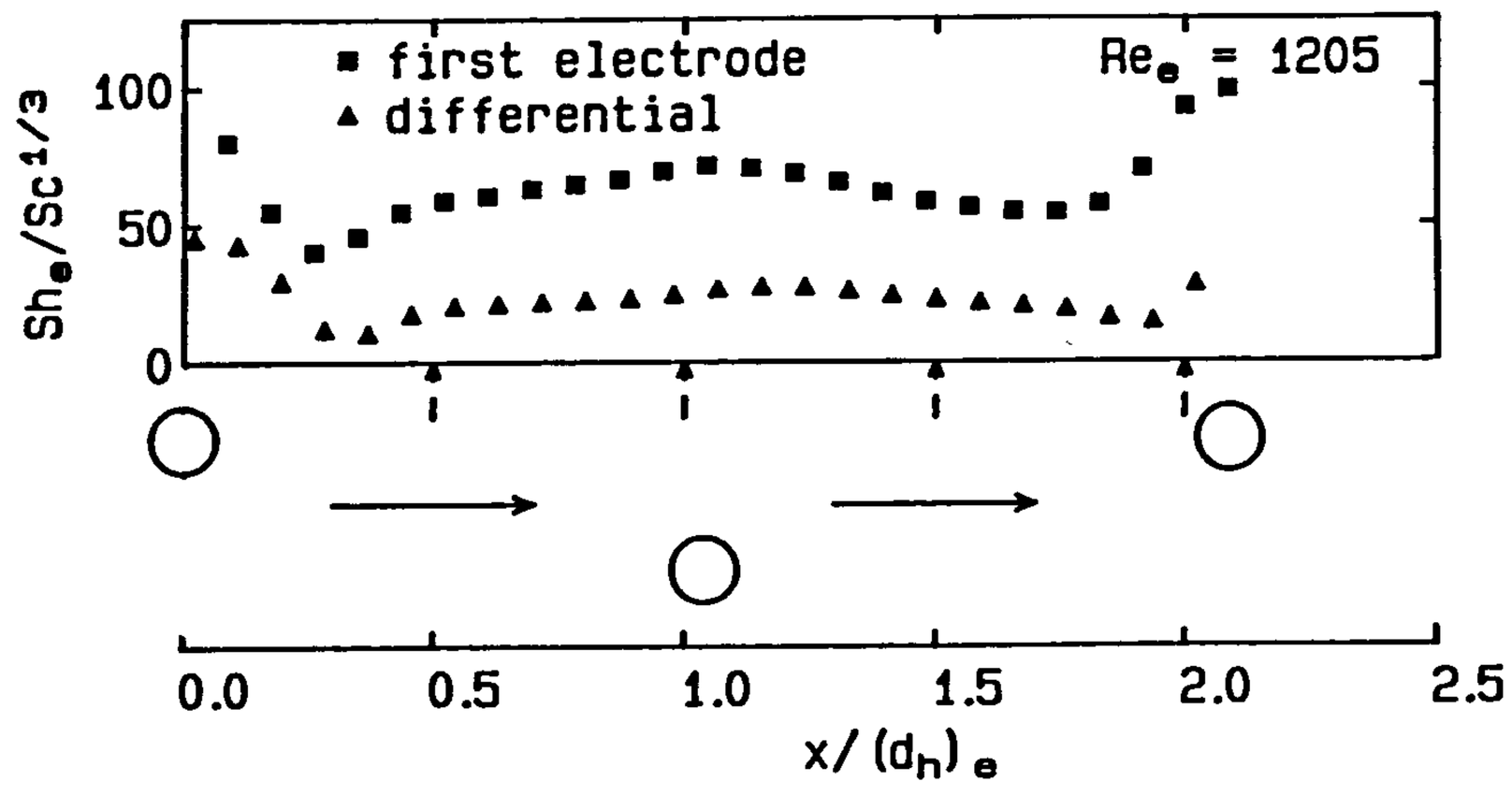
first electrode
differential
Re_e = 1205
Sh_e/Sc^1/3
100
50
0
0.0
0.5
1.0
1.5
2.0
2.5
x/(d_h)_e

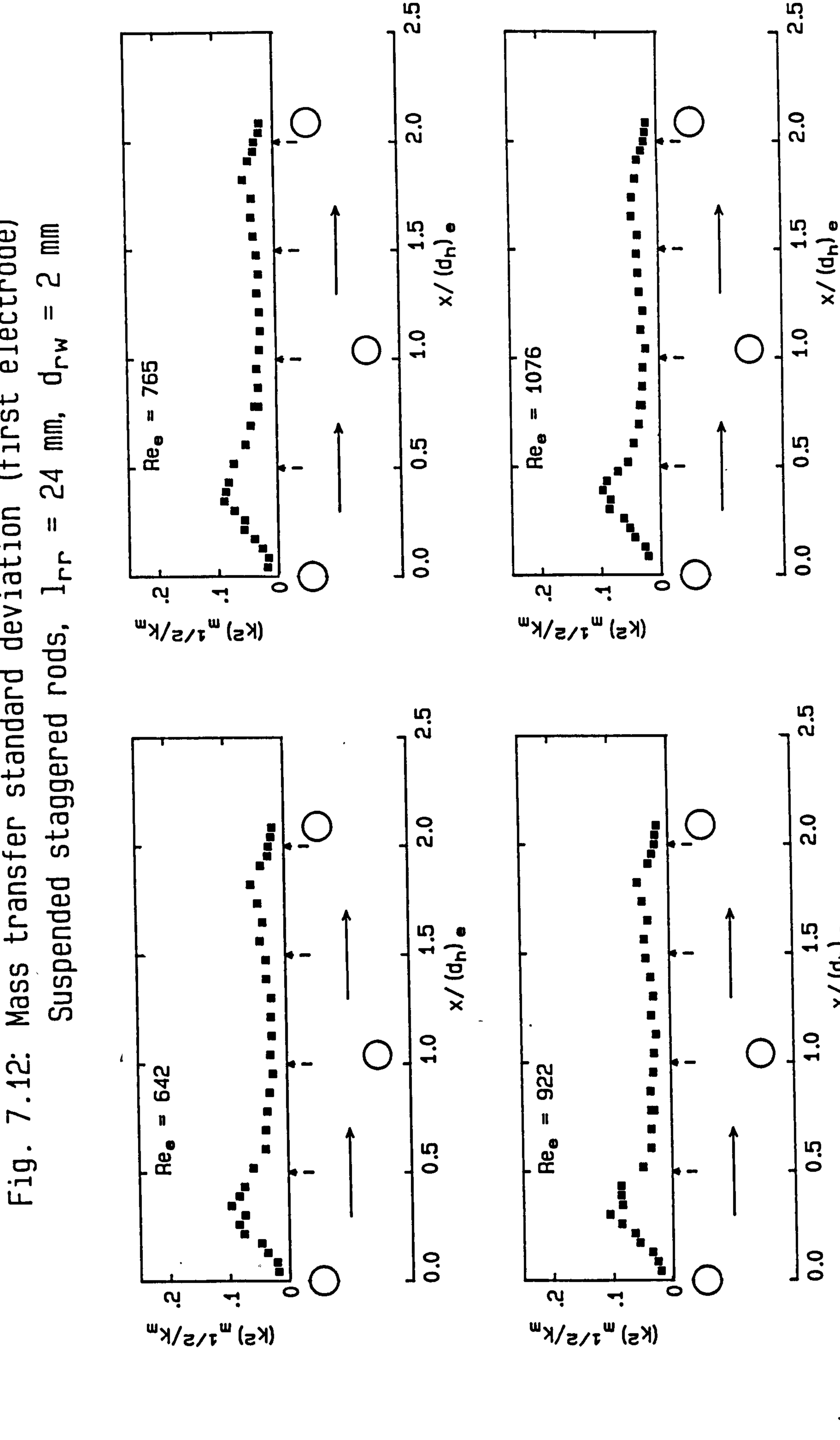

Fig. 7.12: Mass transfer standard deviation (first electrode)
Suspended staggered rods, l_{rr} = 24 mm, d_{rw} = 2 mm

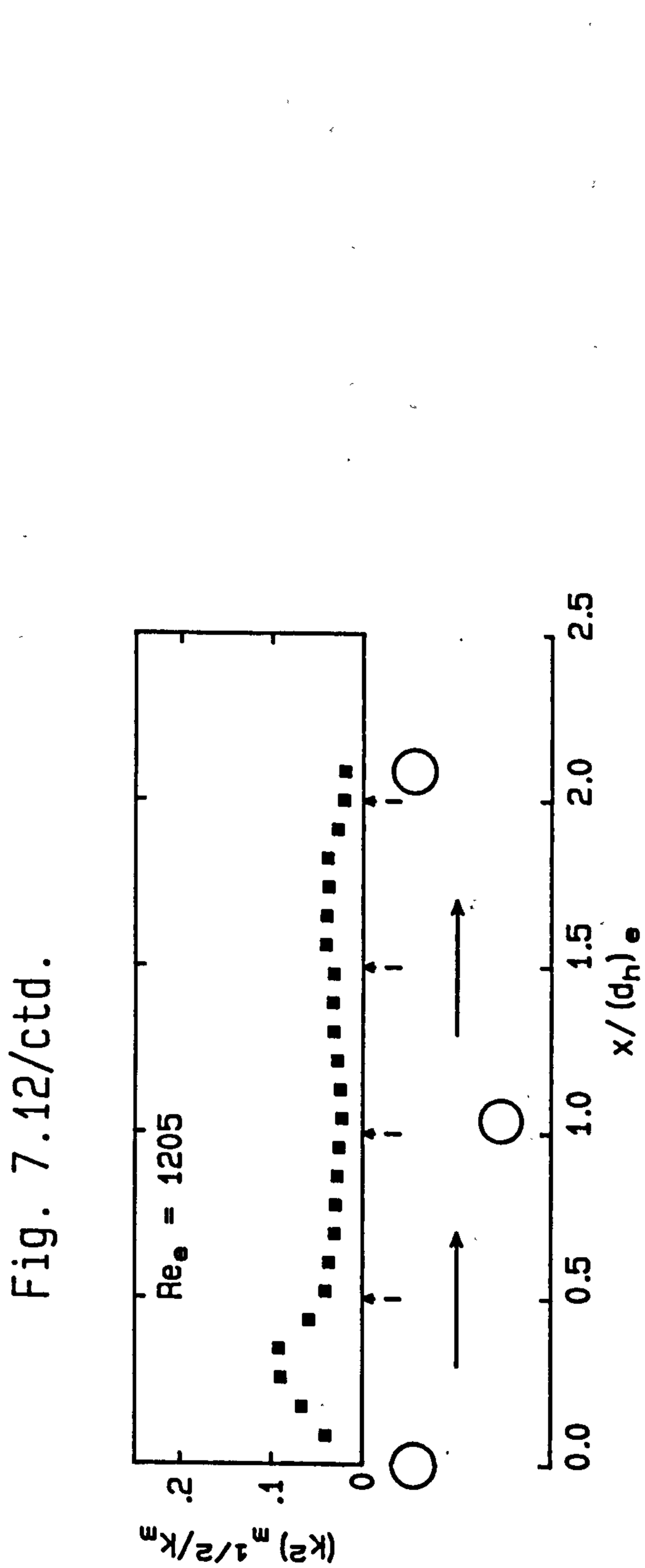

Fig. 7.12/ctd.

Fig. 7.13: Mass transfer between rods (mini-electrodes)
Suspended staggered rods, l_{rr} = 24 mm, d_{rw} = 1 mm

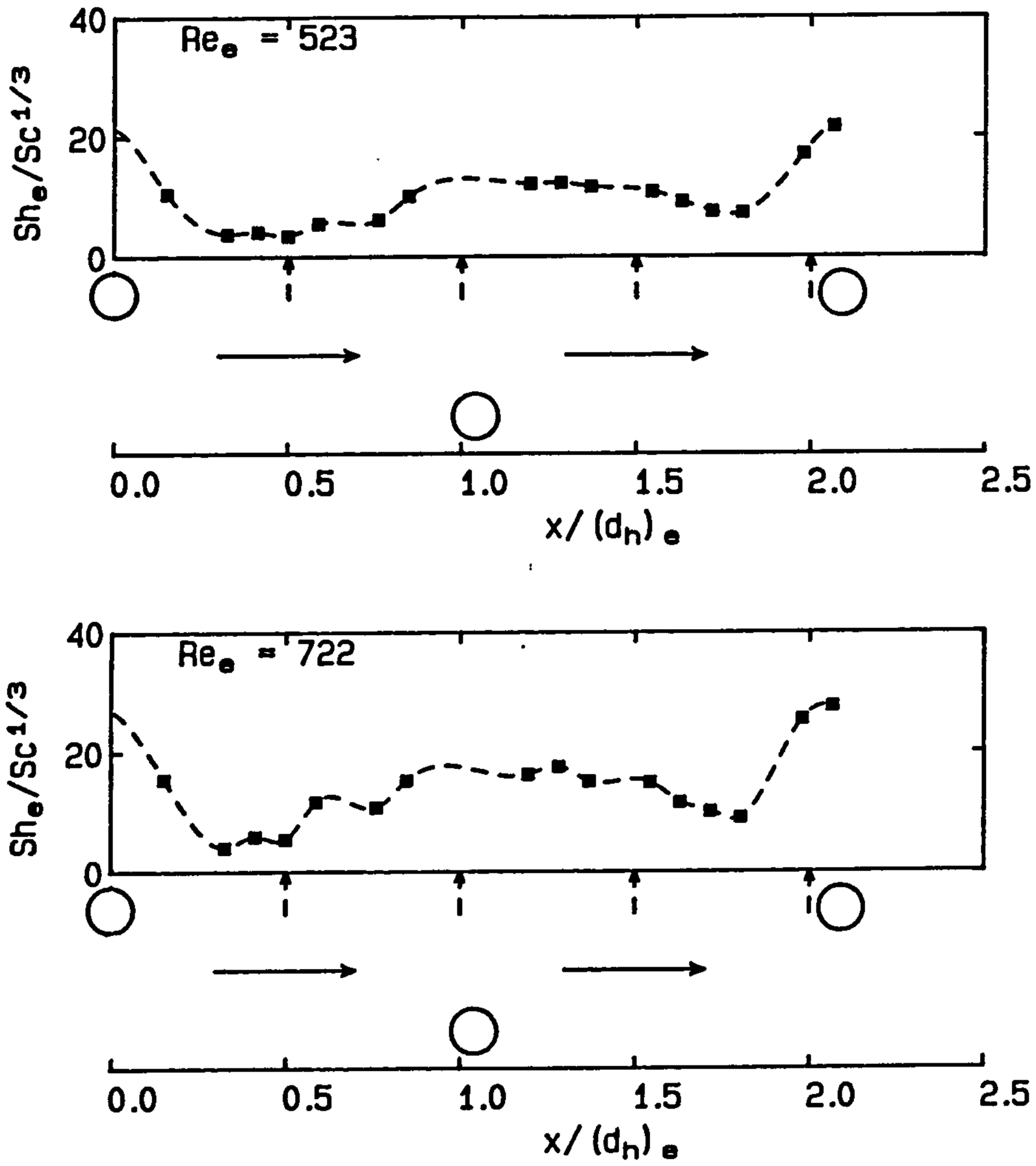

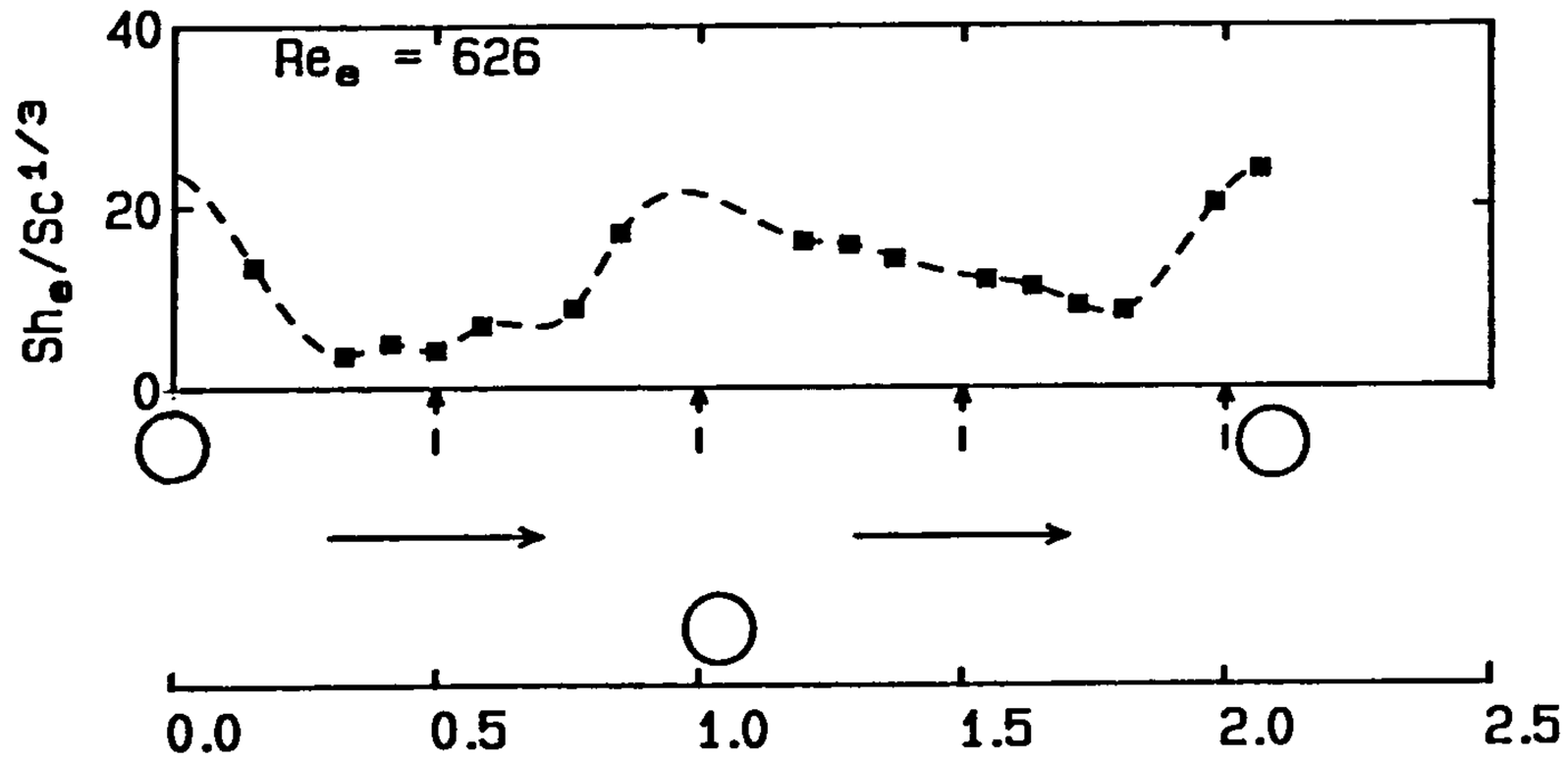

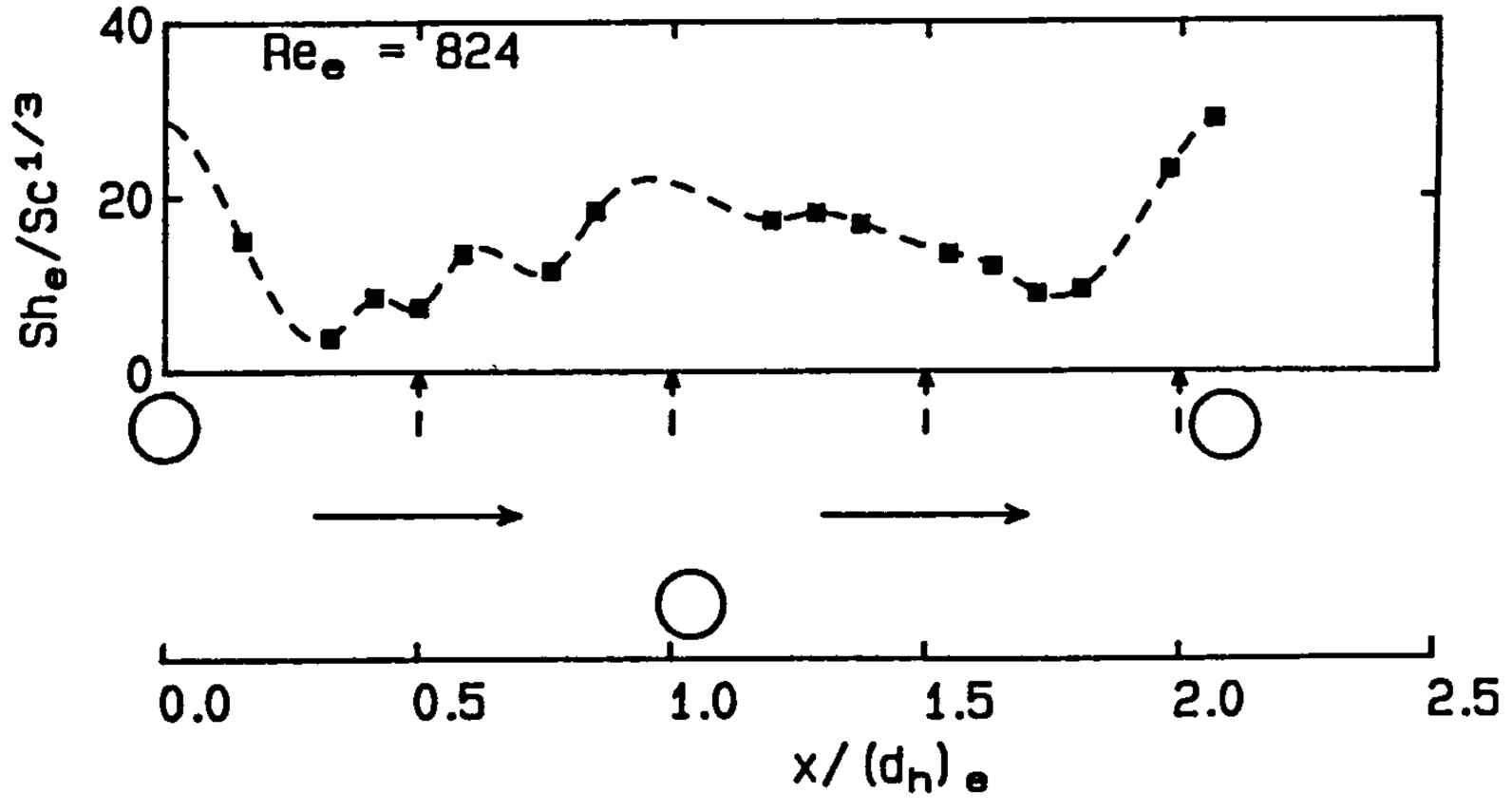

Fig. 7.13/ctd.

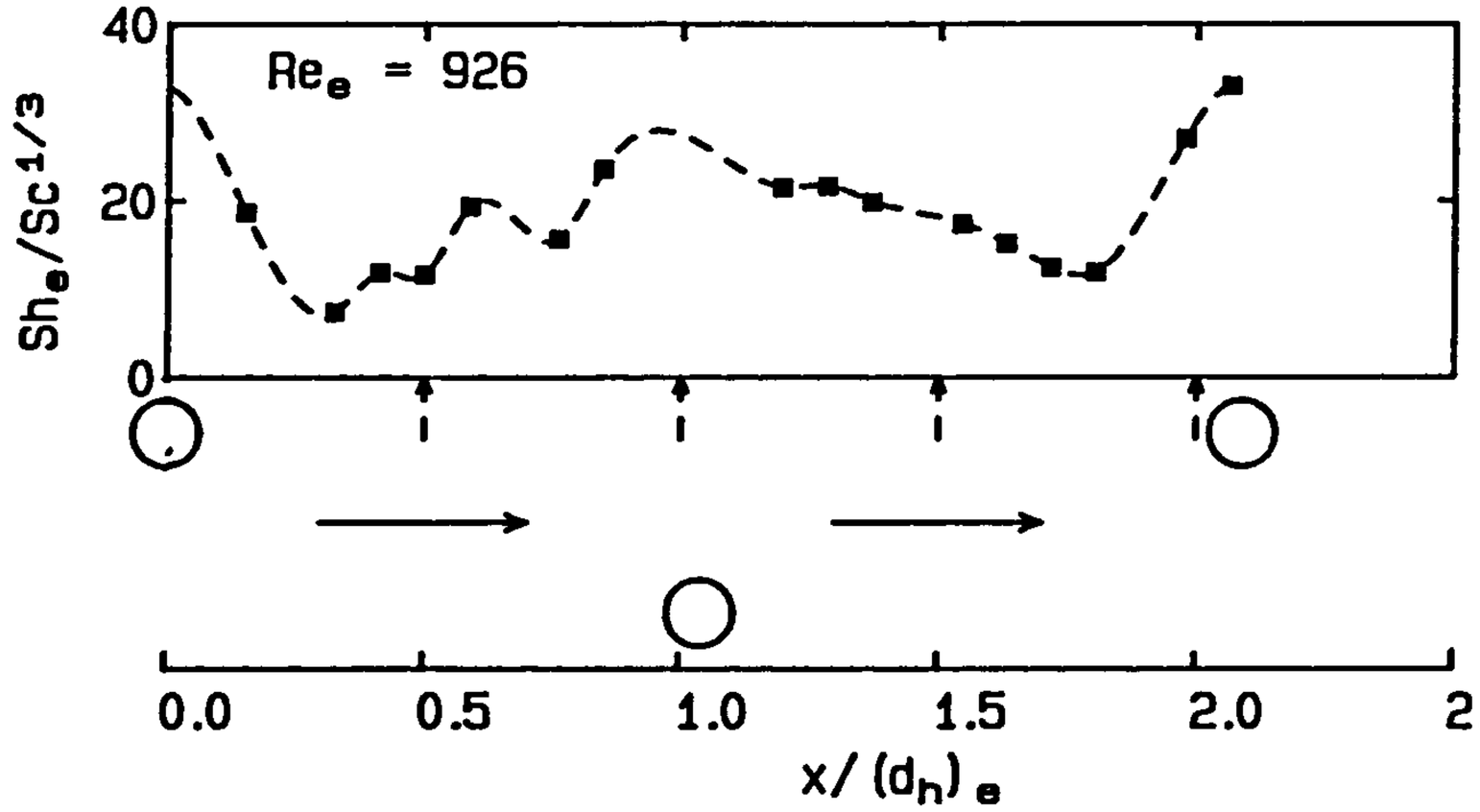
Re$_e$ = 926
Sh$_e$/Sc$^{1/3}$
40
20
0
0.0
0.5
1.0
1.5
2.0
2.5
x/ (d$_h$) $_e$

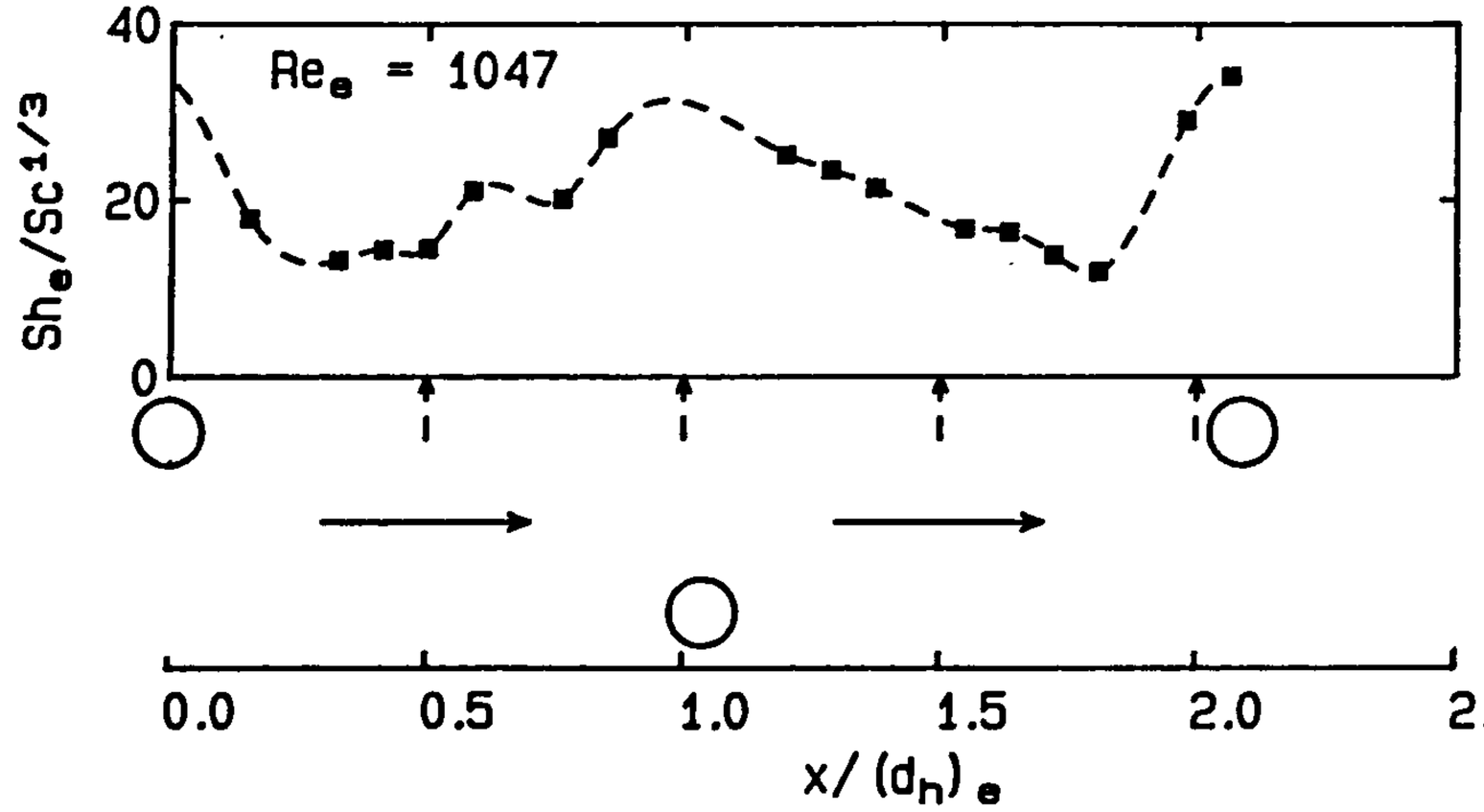
Re$_e$ = 1047
Sh$_e$/Sc$^{1/3}$
40
20
0
0.0
0.5
1.0
1.5
2.0
2.5
x/ (d$_h$) $_e$

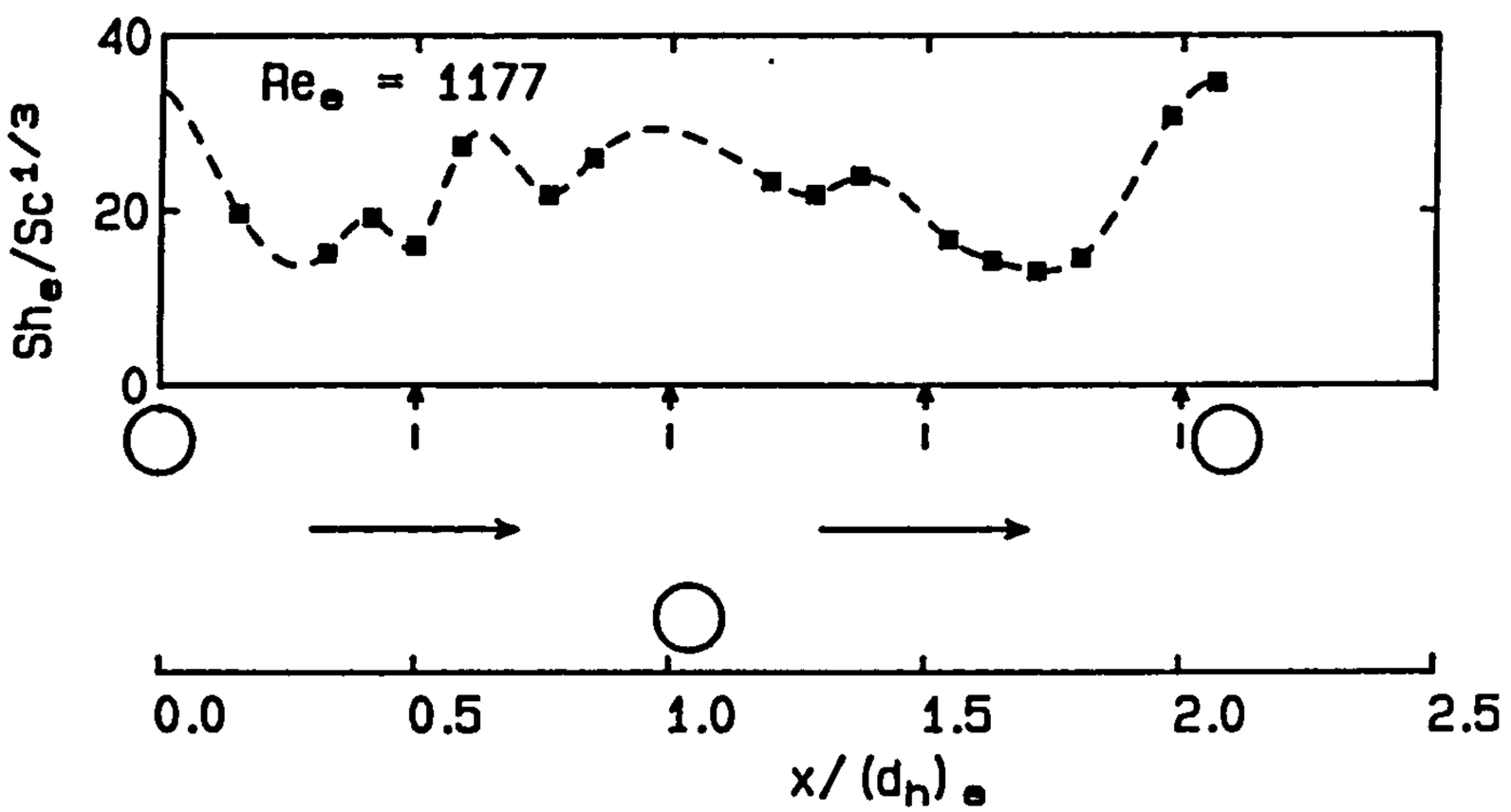
Re$_e$ = 1177
Sh$_e$/Sc$^{1/3}$
40
20
0
0.0
0.5
1.0
1.5
2.0
2.5
x/ (d$_h$) $_e$

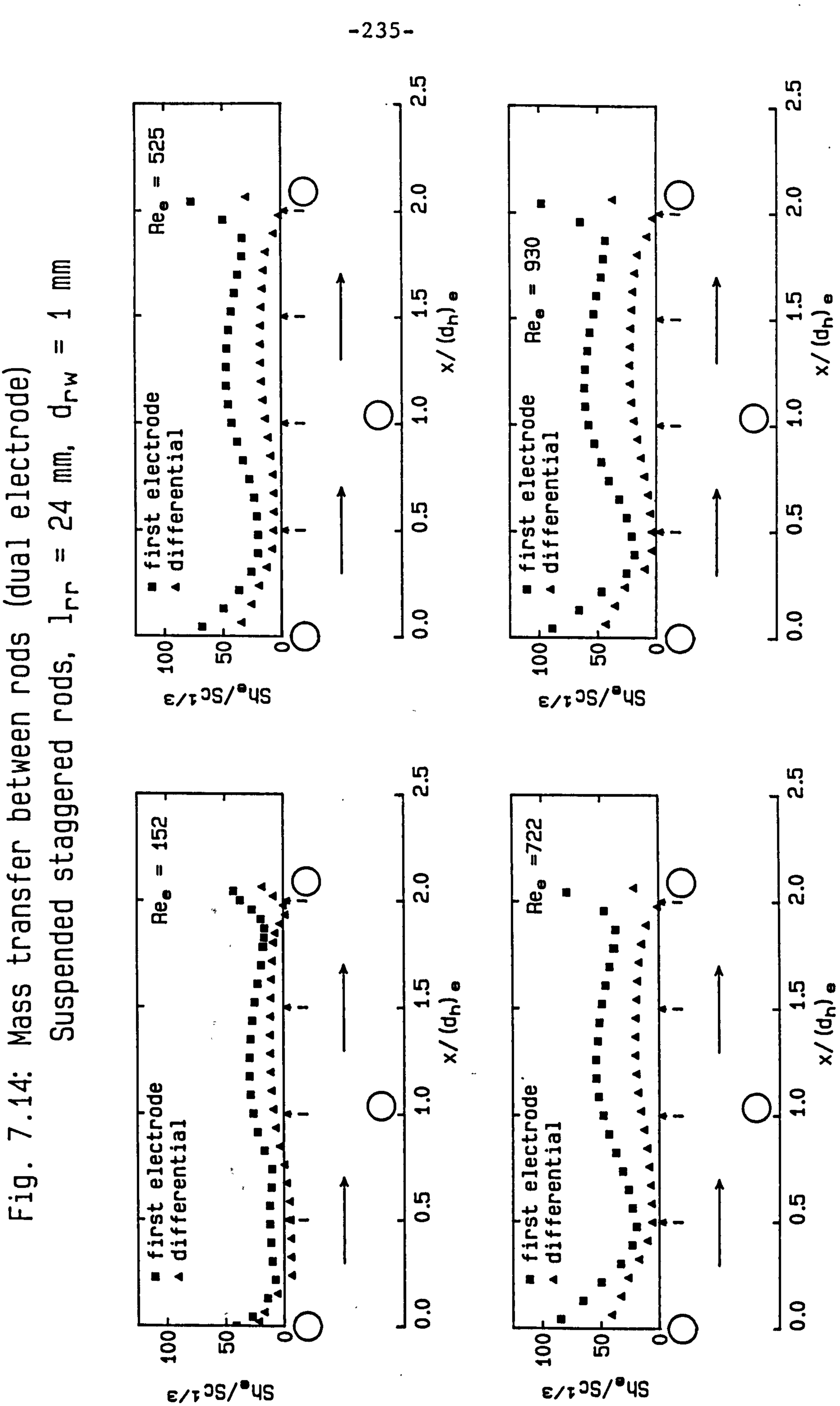

Fig. 7.14: Mass transfer between rods (dual electrode)
Suspended staggered rods, l_{rr} = 24 mm, d_{rw} = 1 mm

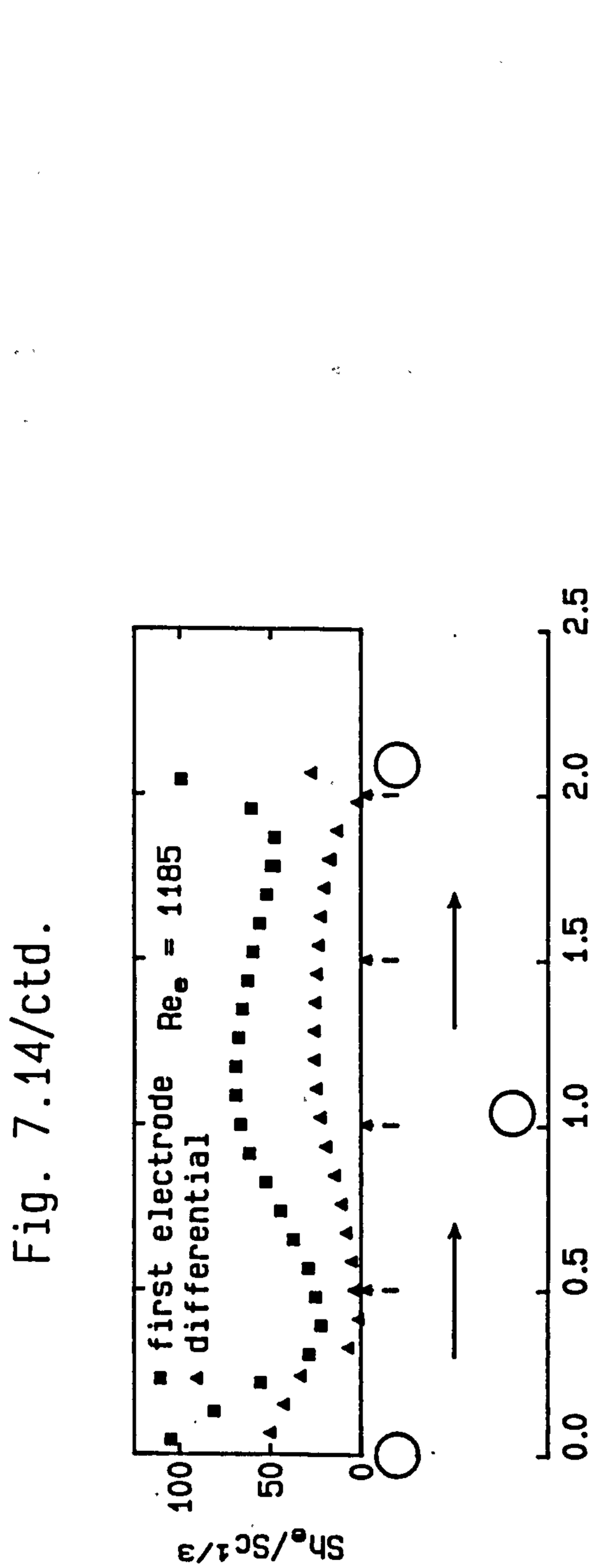
first electrode Re$_e$ = 1185
differential
100
50
0
Sh$_e$/Sc$^{1/3}$
1.0
1.5
2.0
2.5
x/(d$_h$)$_e$
0.0
0.5

Fig. 7.14/ctd.

Fig. 7.15: Mass transfer standard deviation (first electrode)
Suspended staggered rods, l_{rr} = 24 mm, d_{rw} = 1 mm

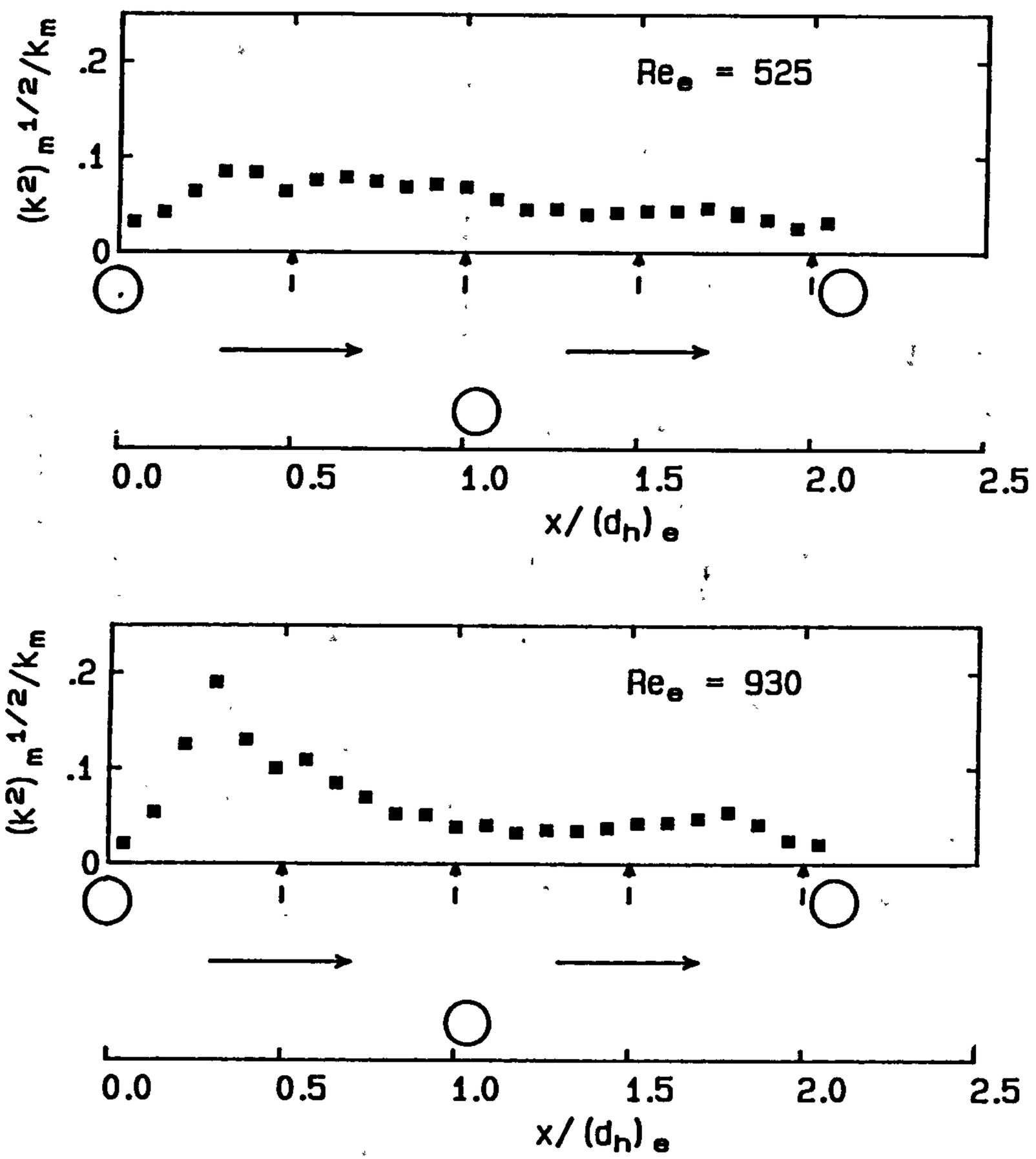

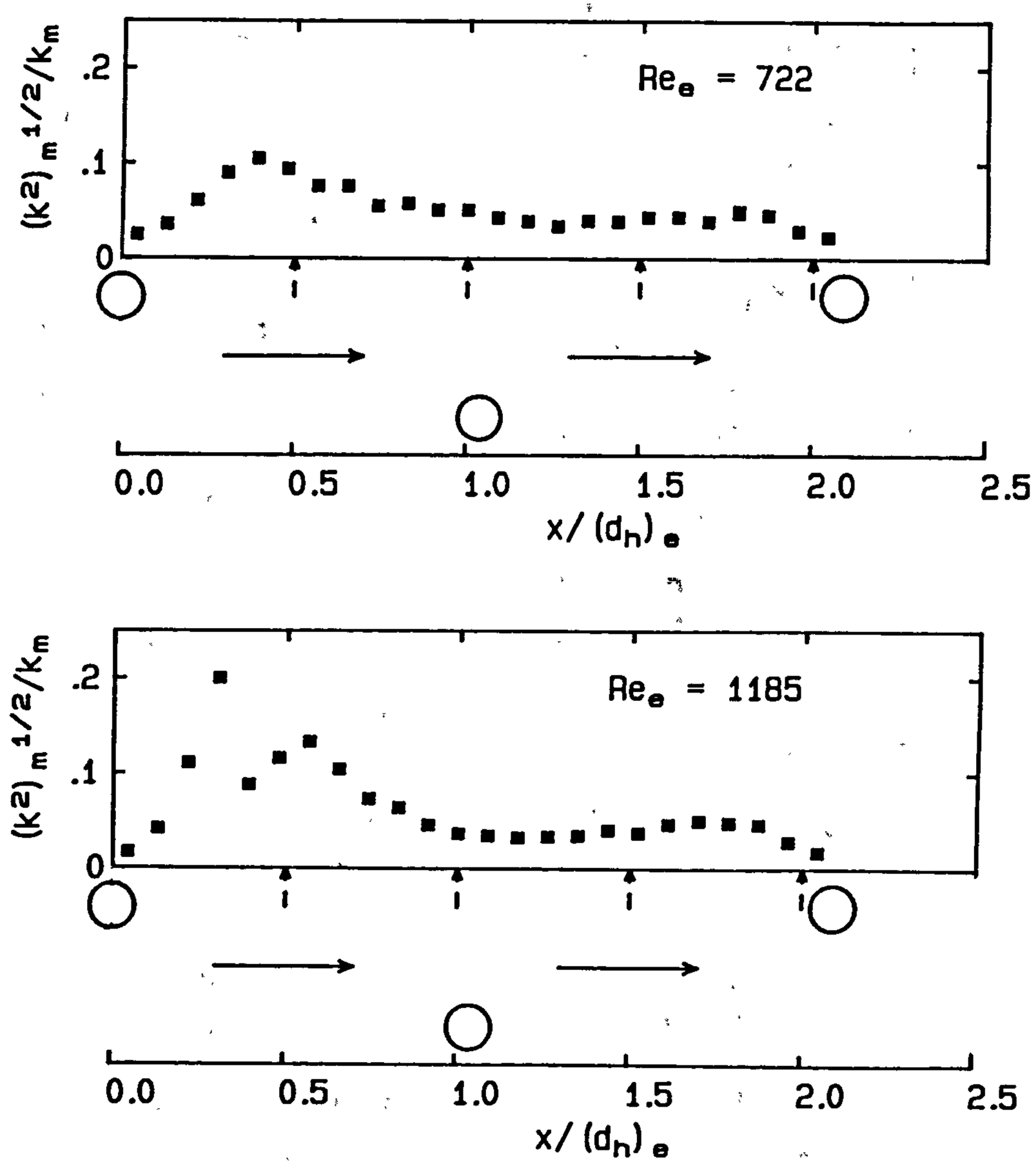

Fig. 7.16: Mass transfer between rods (mini-electrodes)
Suspended staggered rods, l_{rr} = 6 mm, d_{rw} = 1 mm

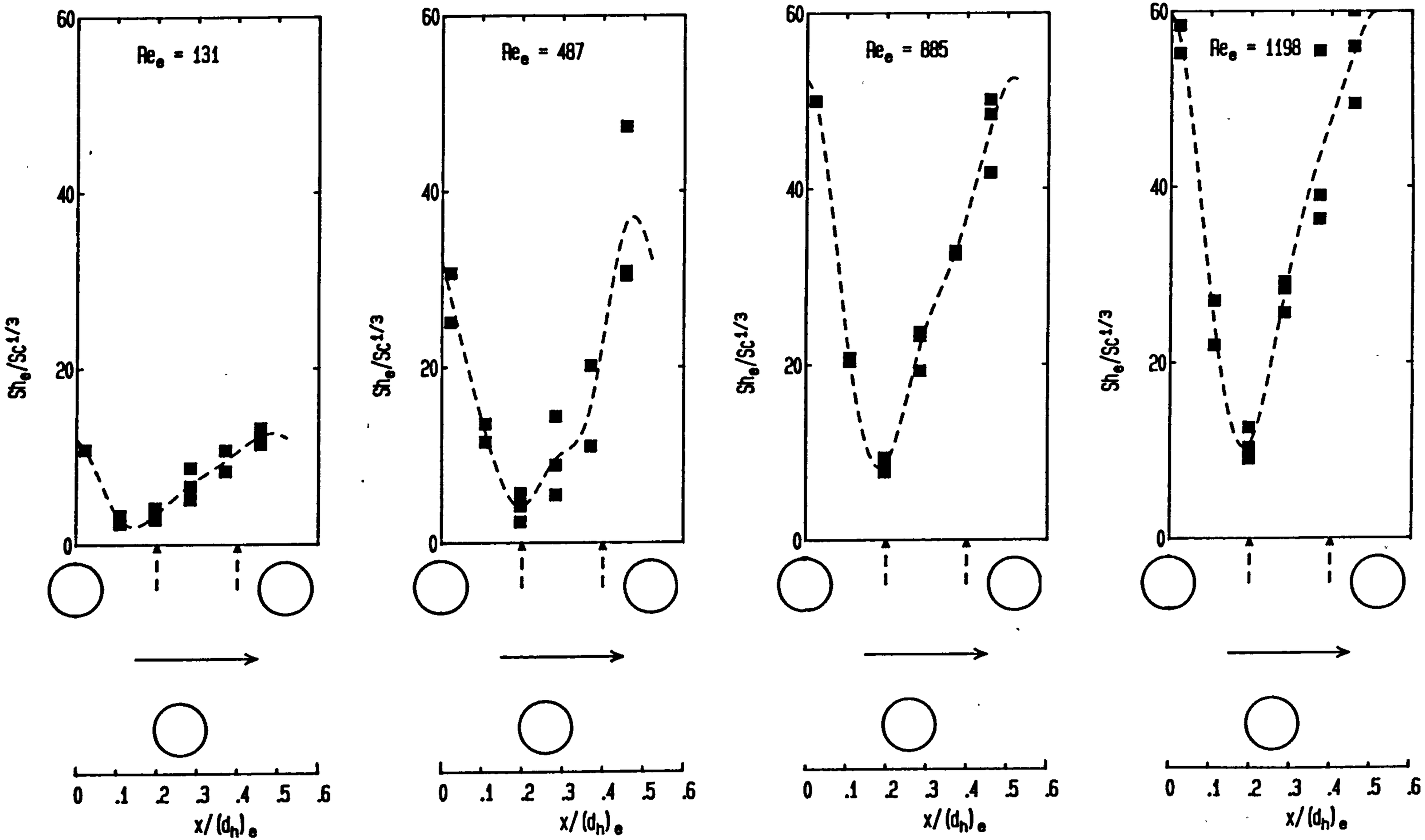

Fig. 7.17: Mass transfer fluctuations, Centered rods, l_{rr} = 60 mm

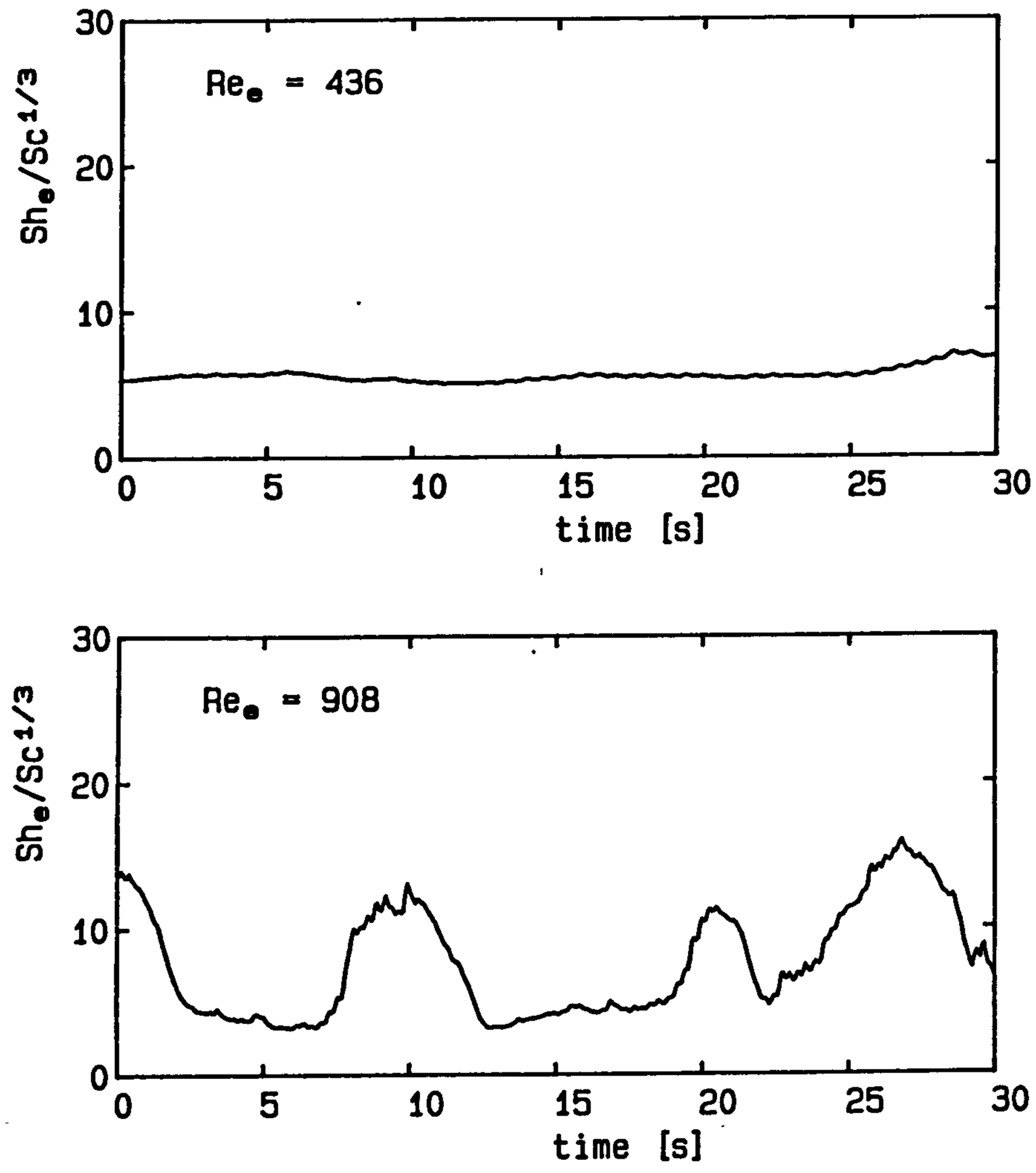

Fig. 7.18: Mass transfer fluctuations
Attached staggered rods, l_{rr} = 40 mm

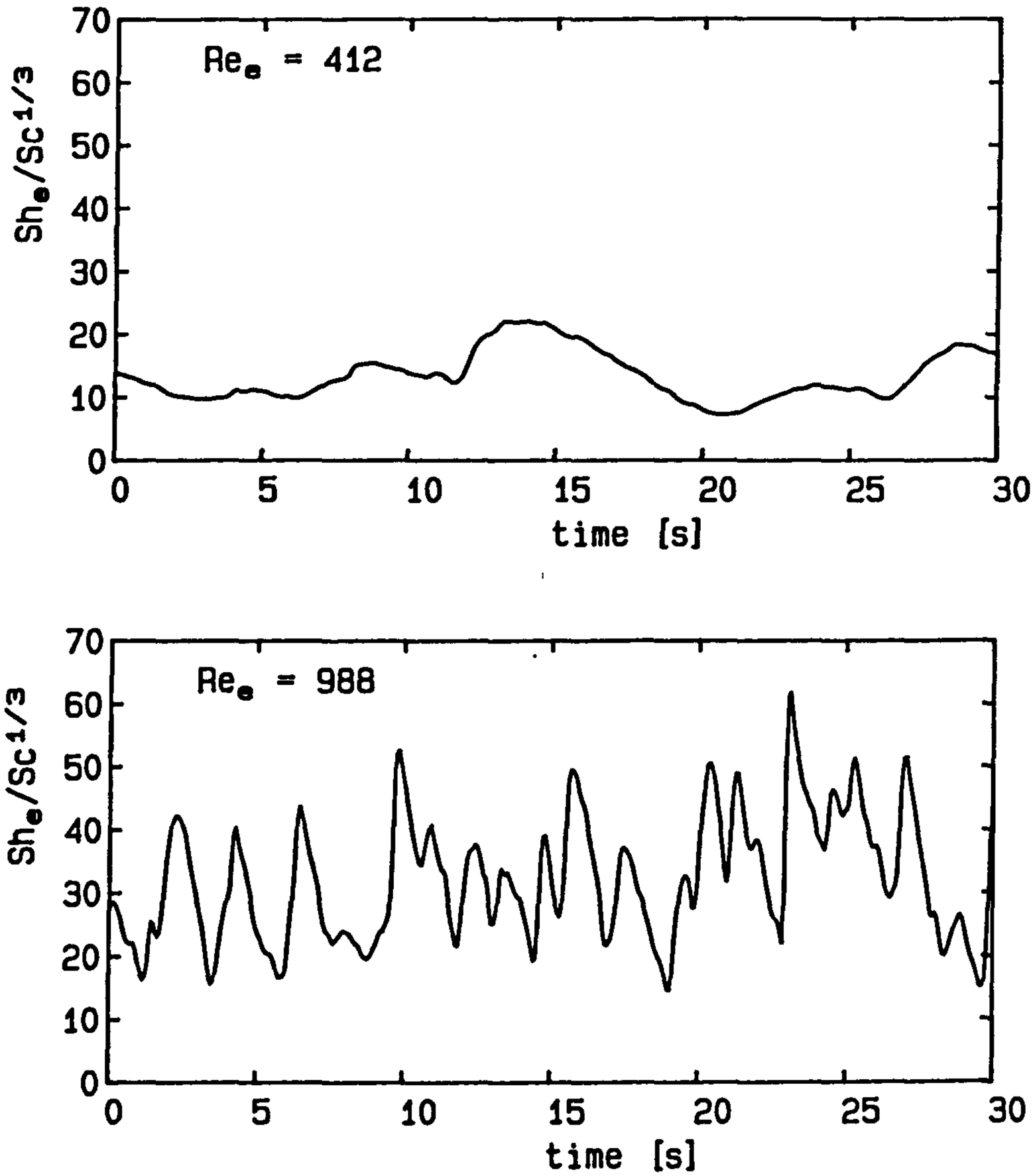

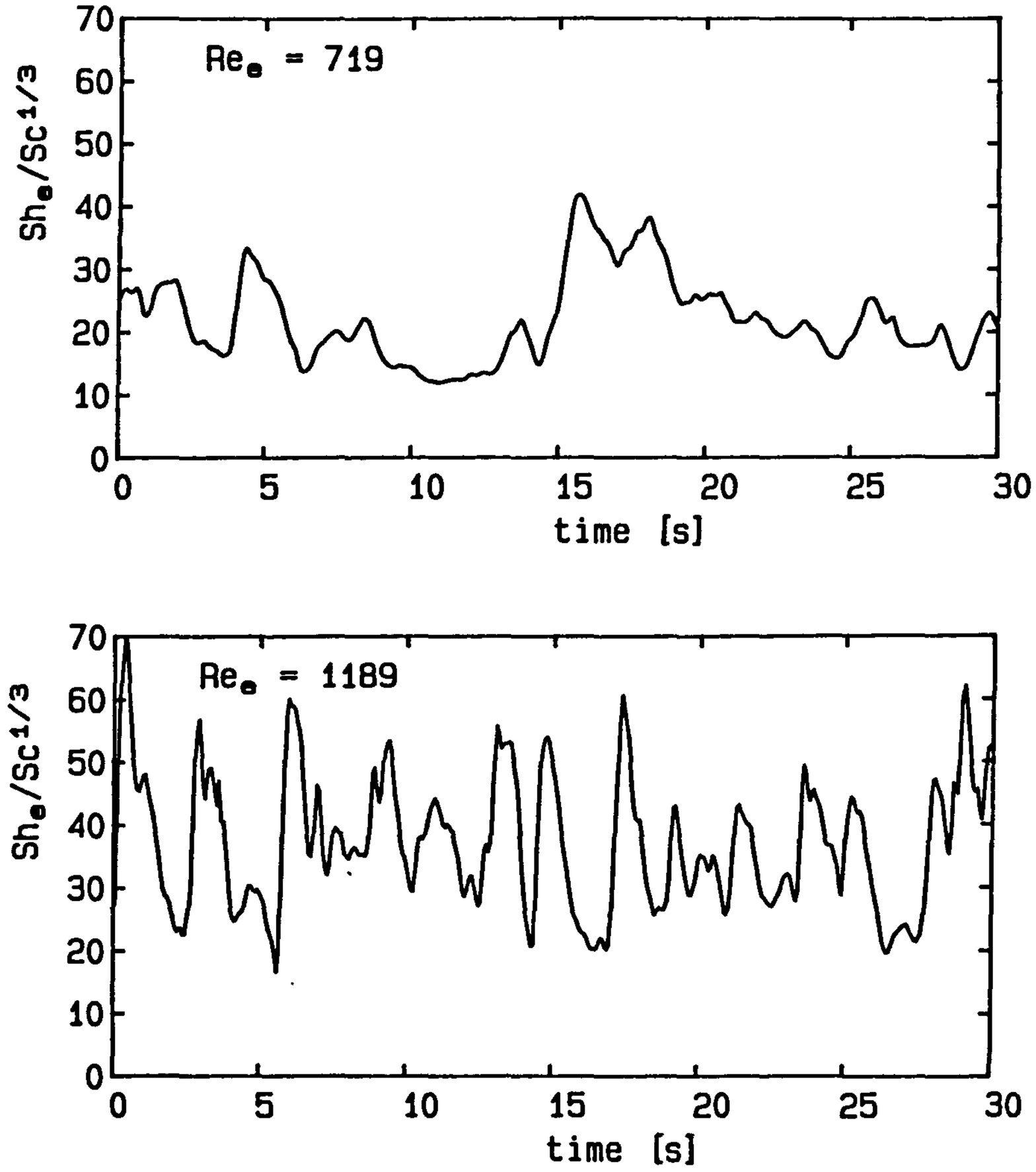

Fig. 7.19: Mass transfer fluctuations
Suspended staggered rods, l_{rr} = 24 mm, d_{rw} = 2 mm

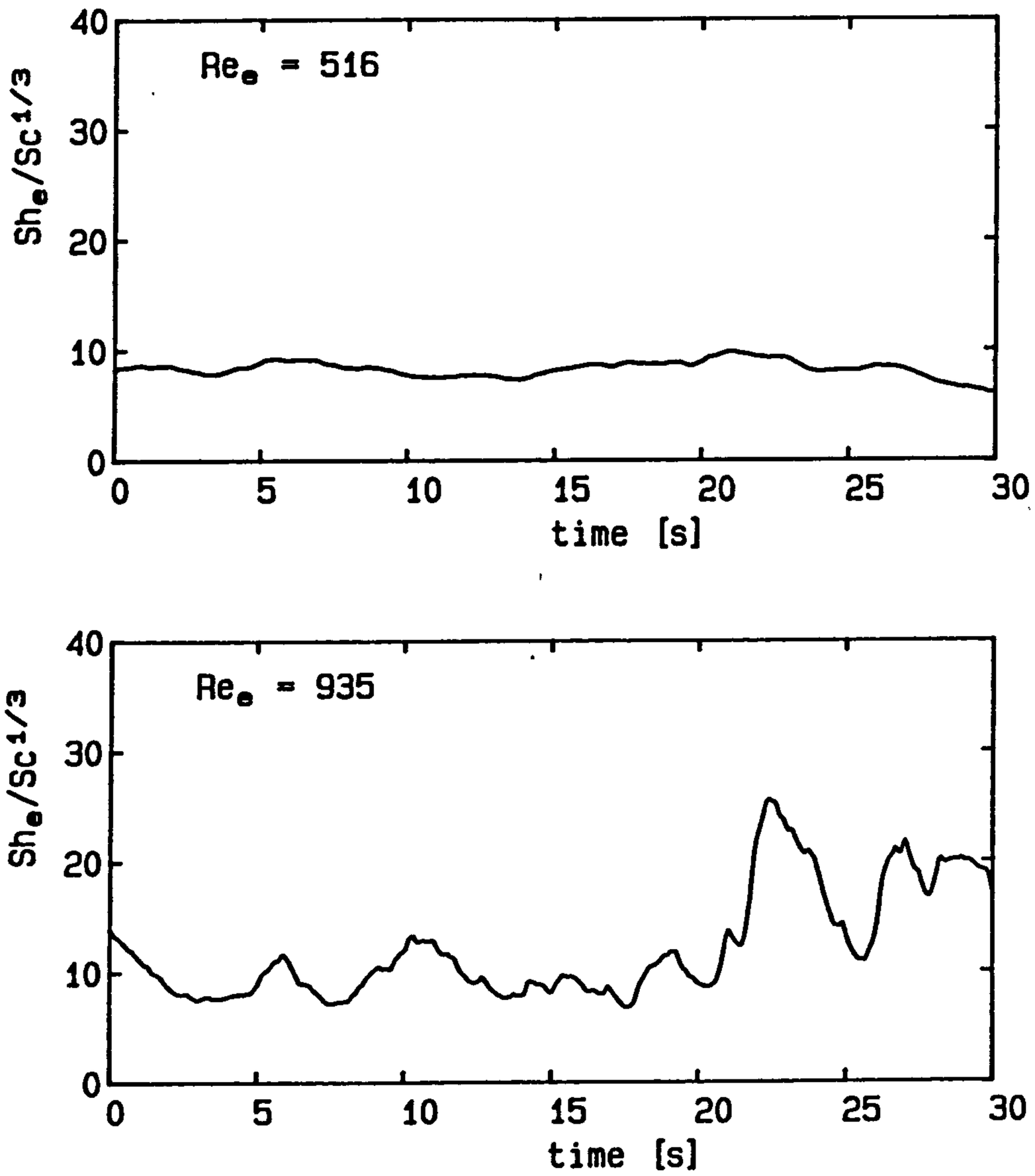

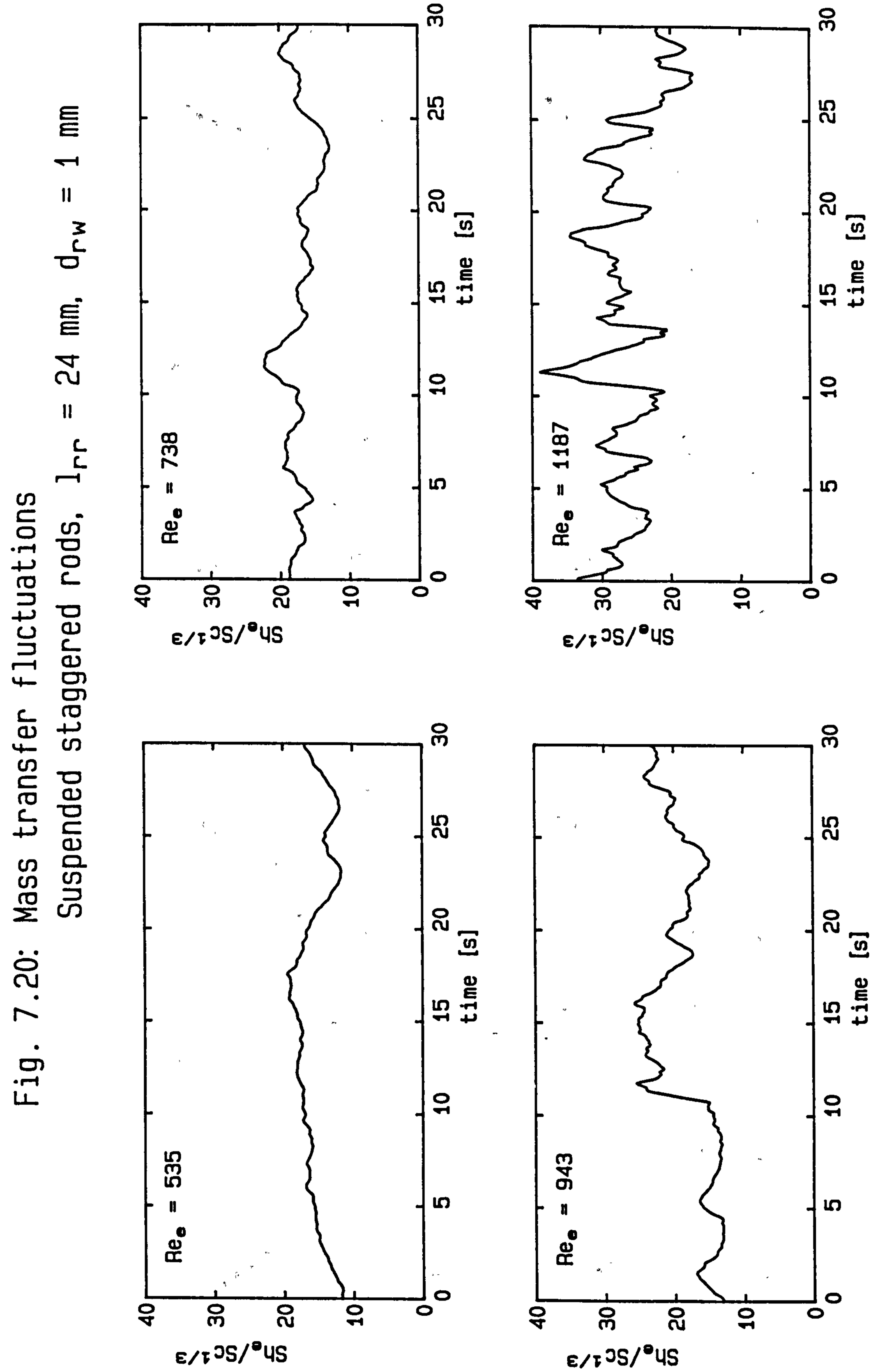

Fig. 7.20: Mass transfer fluctuations
Suspended staggered rods, l_{rr} = 24 mm, d_{rw} = 1 mm

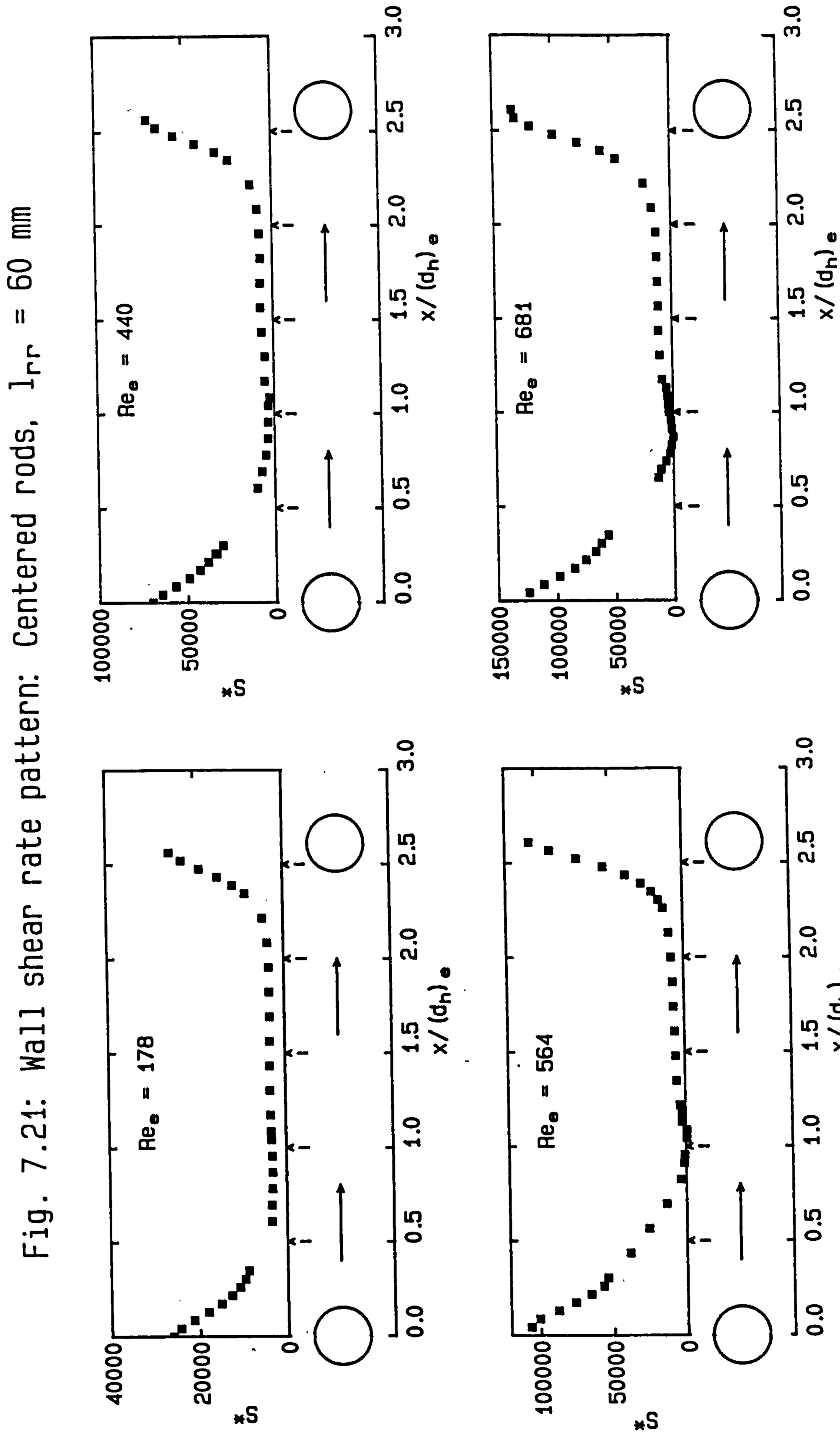

Fig. 7.21: Wall shear rate pattern: Centered rods, l_{rr} = 60 mm

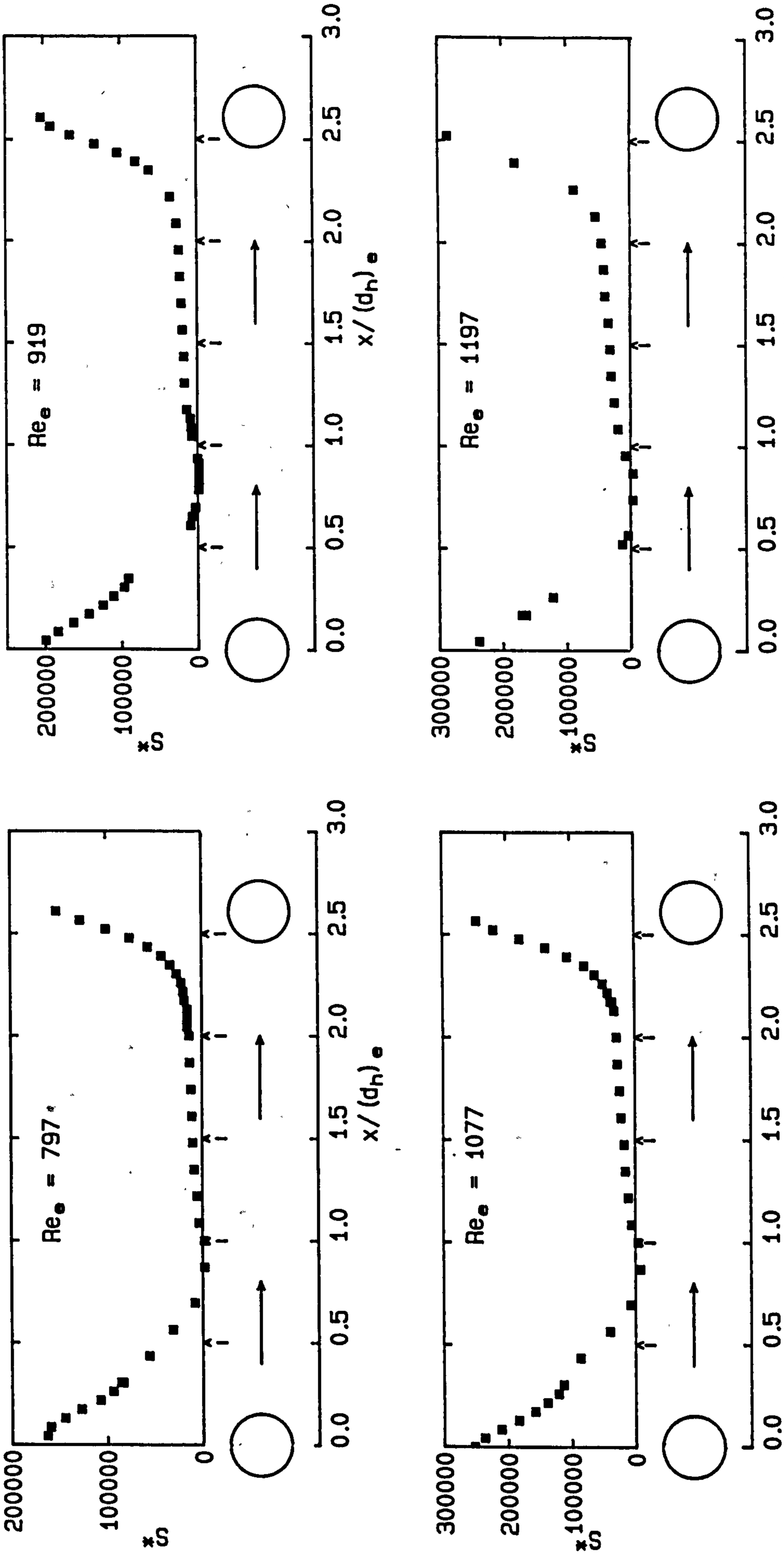
Re_e = 919
Re_e = 1197
Re_e = 797
Re_e = 1077
x/(d_h)_e
*S
0.0
0.5
1.0
1.5
2.0
2.5
3.0
0
100000
200000
300000

Fig. 7.21/ctd.

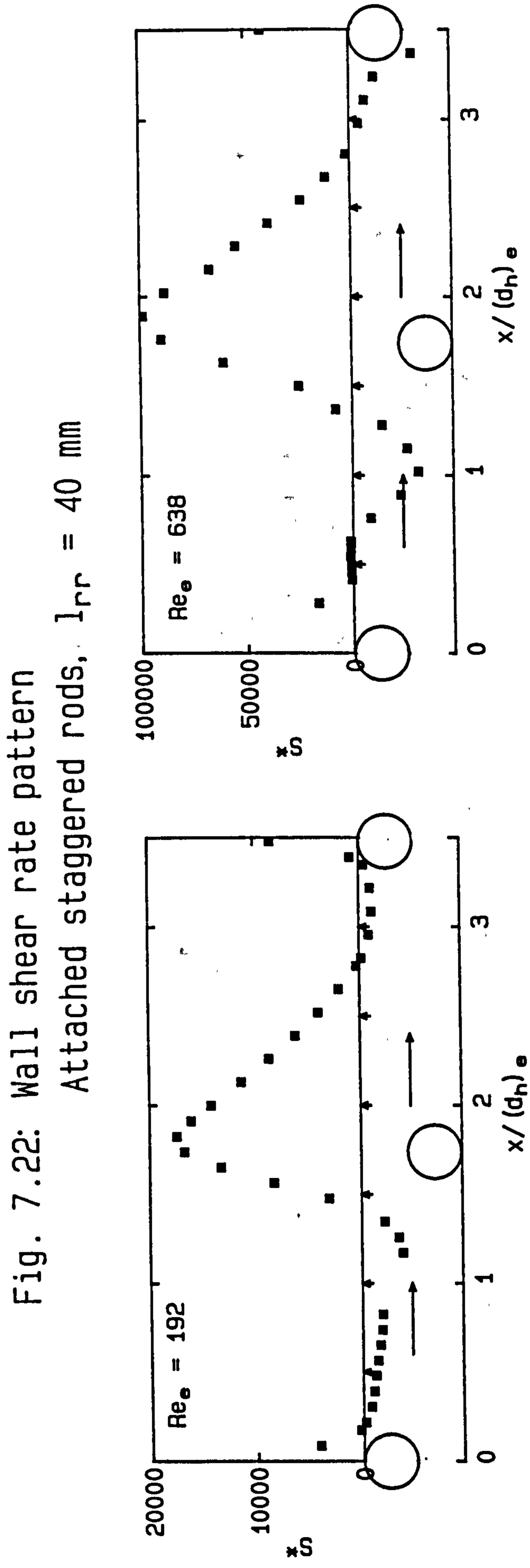

Fig. 7.22: Wall shear rate pattern
Attached staggered rods, l_{rr} = 40 mm

Fig. 7.23: Wall shear rate pattern

Suspended staggered rods, l_{rr} = 24 mm, d_{rw} = 2 mm

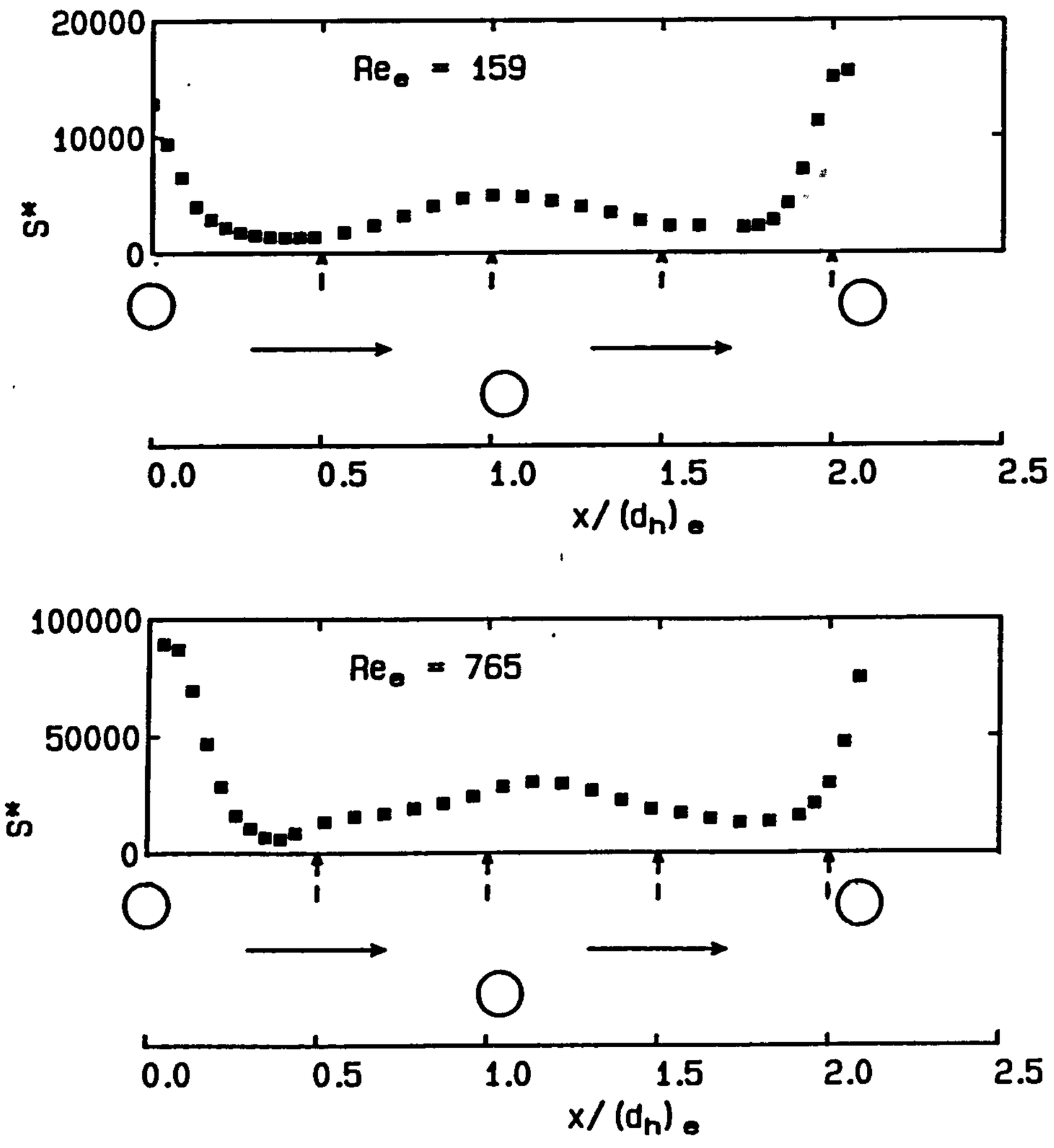

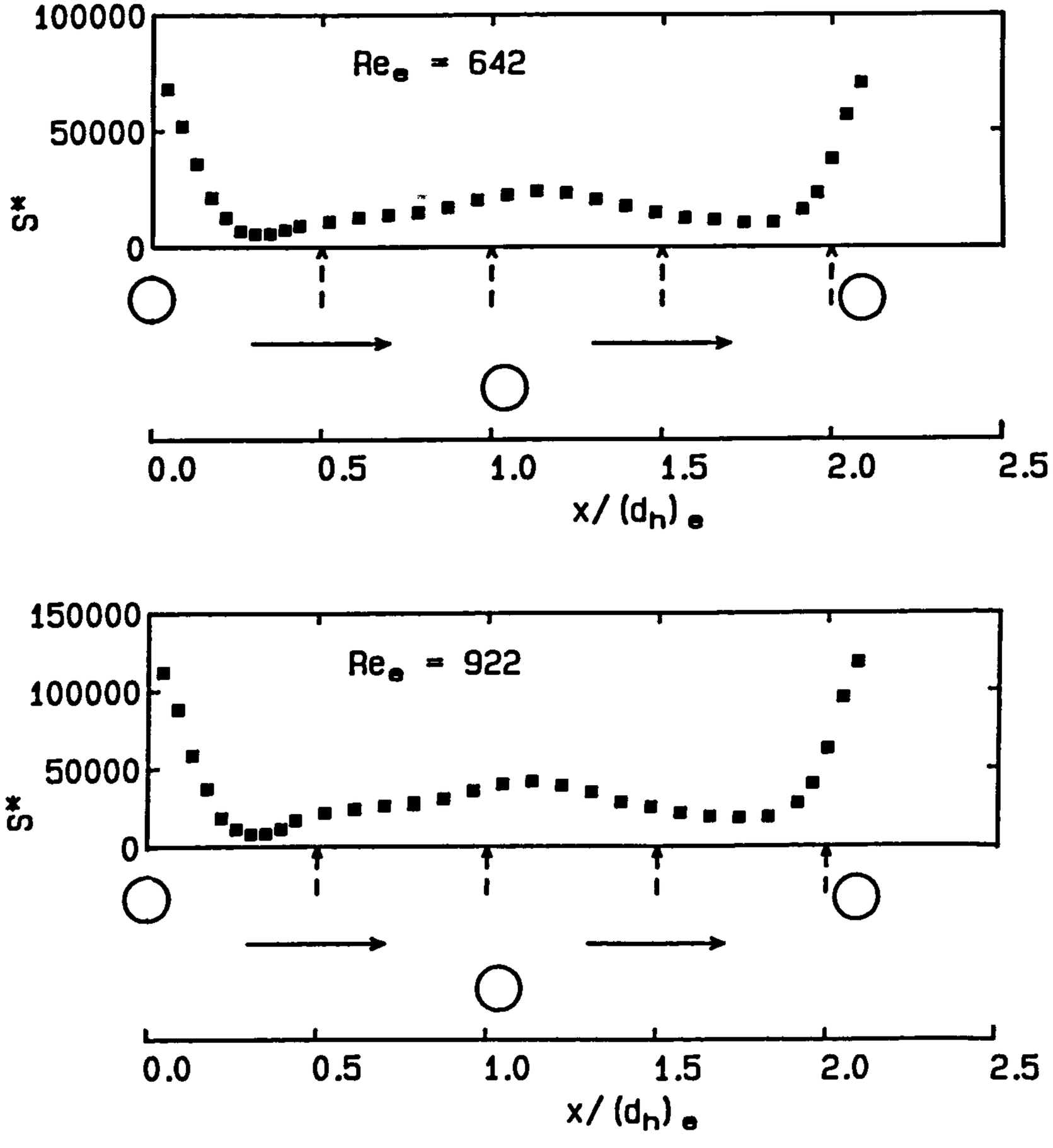

Fig. 7.23/ctd.

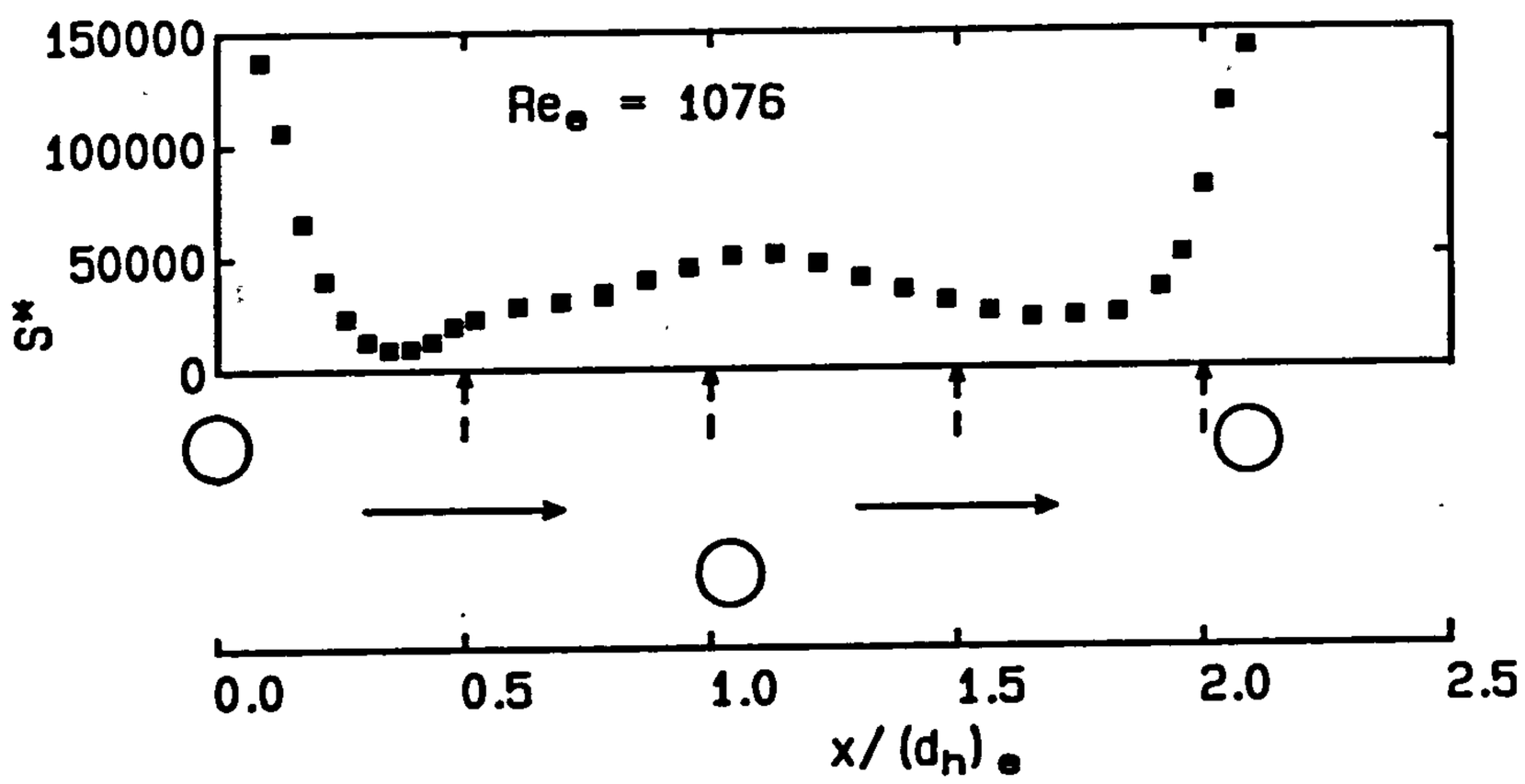
150000
100000
50000
0
S*
Re$_e$ = 1076
0.0
0.5
1.0
1.5
2.0
2.5
x/ (d$_h$)$_e$

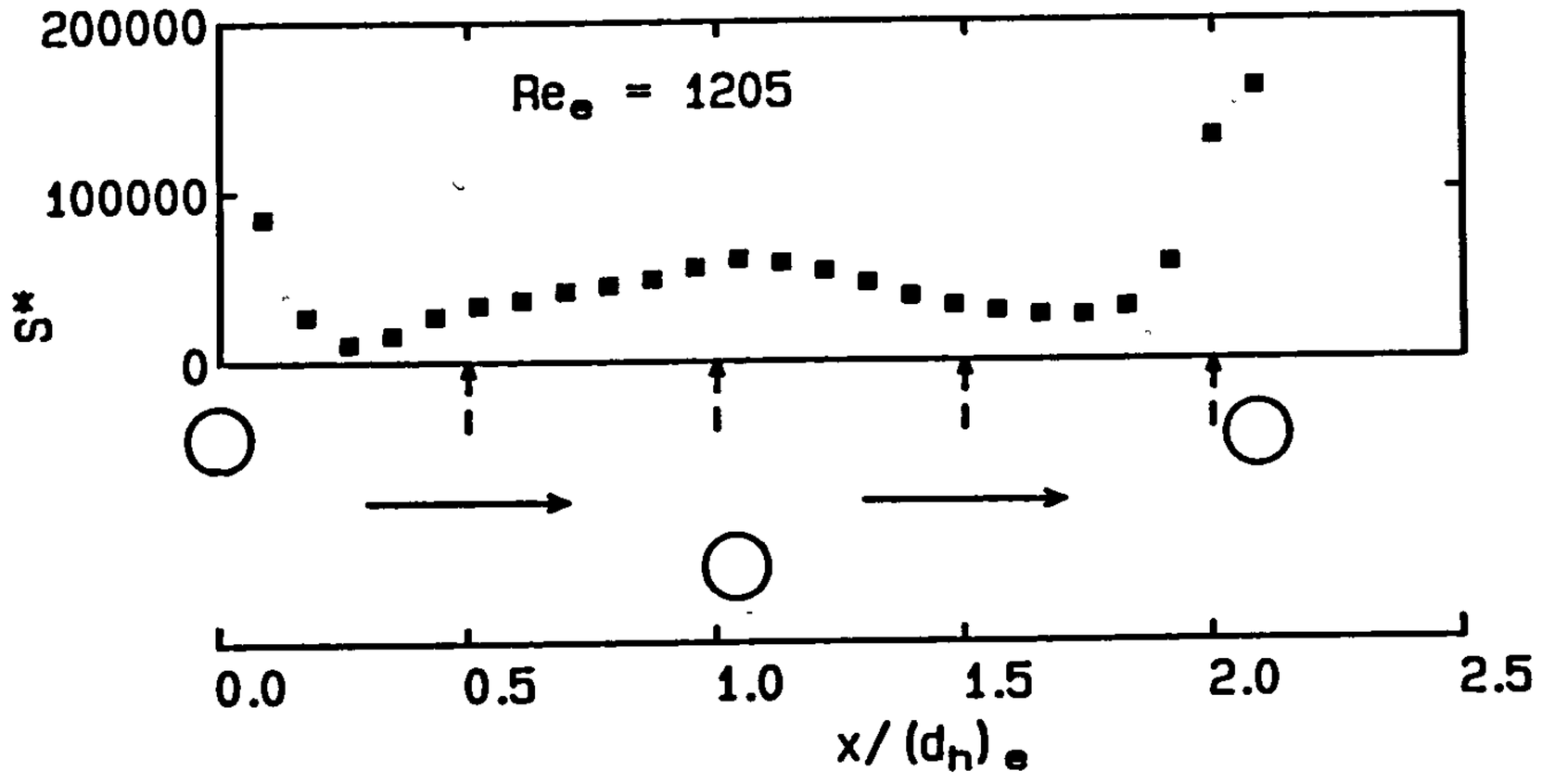
200000
100000
0
S*
Re$_e$ = 1205
0.0
0.5
1.0
1.5
2.0
2.5
x/ (d$_h$)$_e$

Fig. 7.24: Wall shear rate pattern
Suspended staggered rods, l_{rr} = 24 mm, d_{rw} = 1 mm

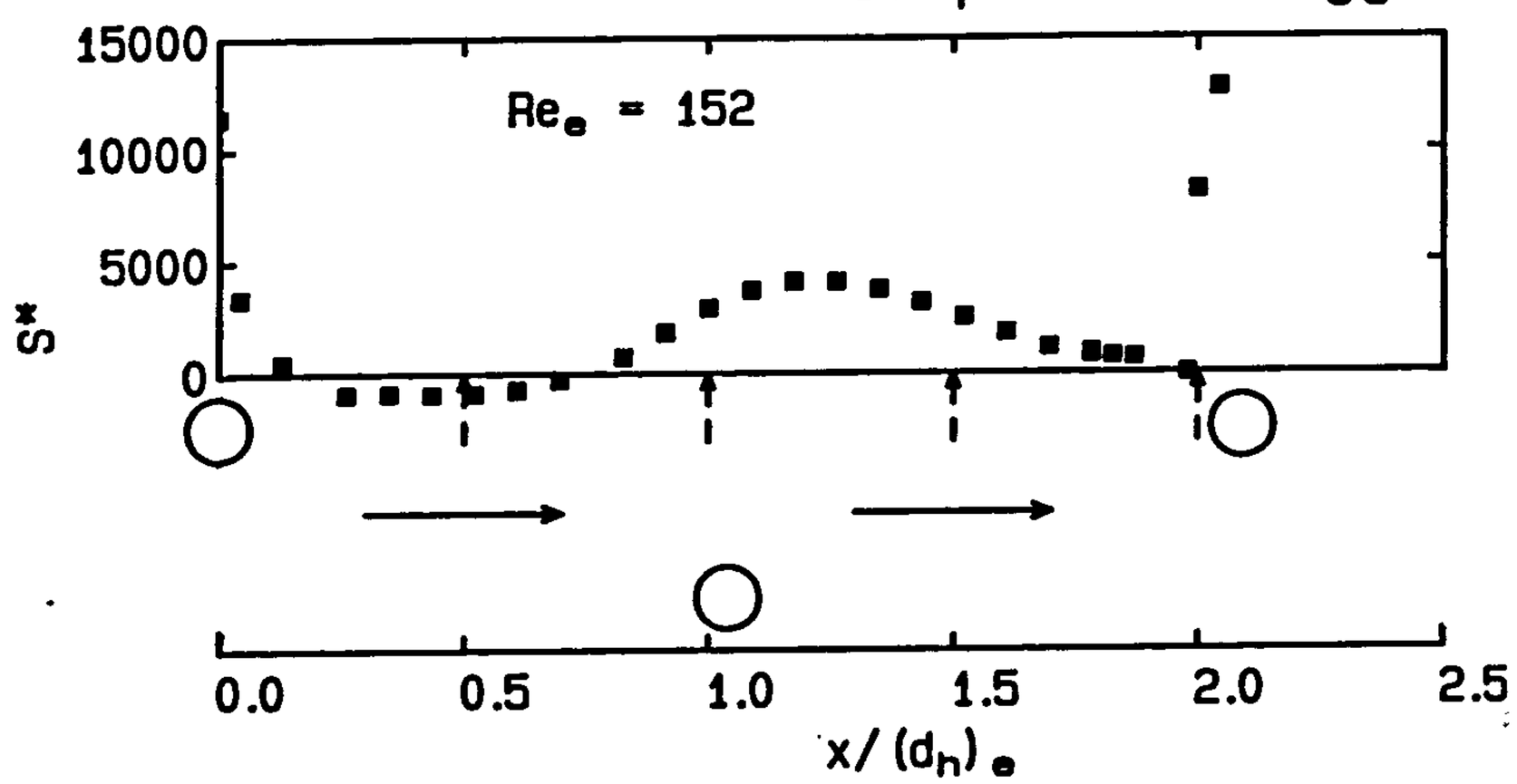

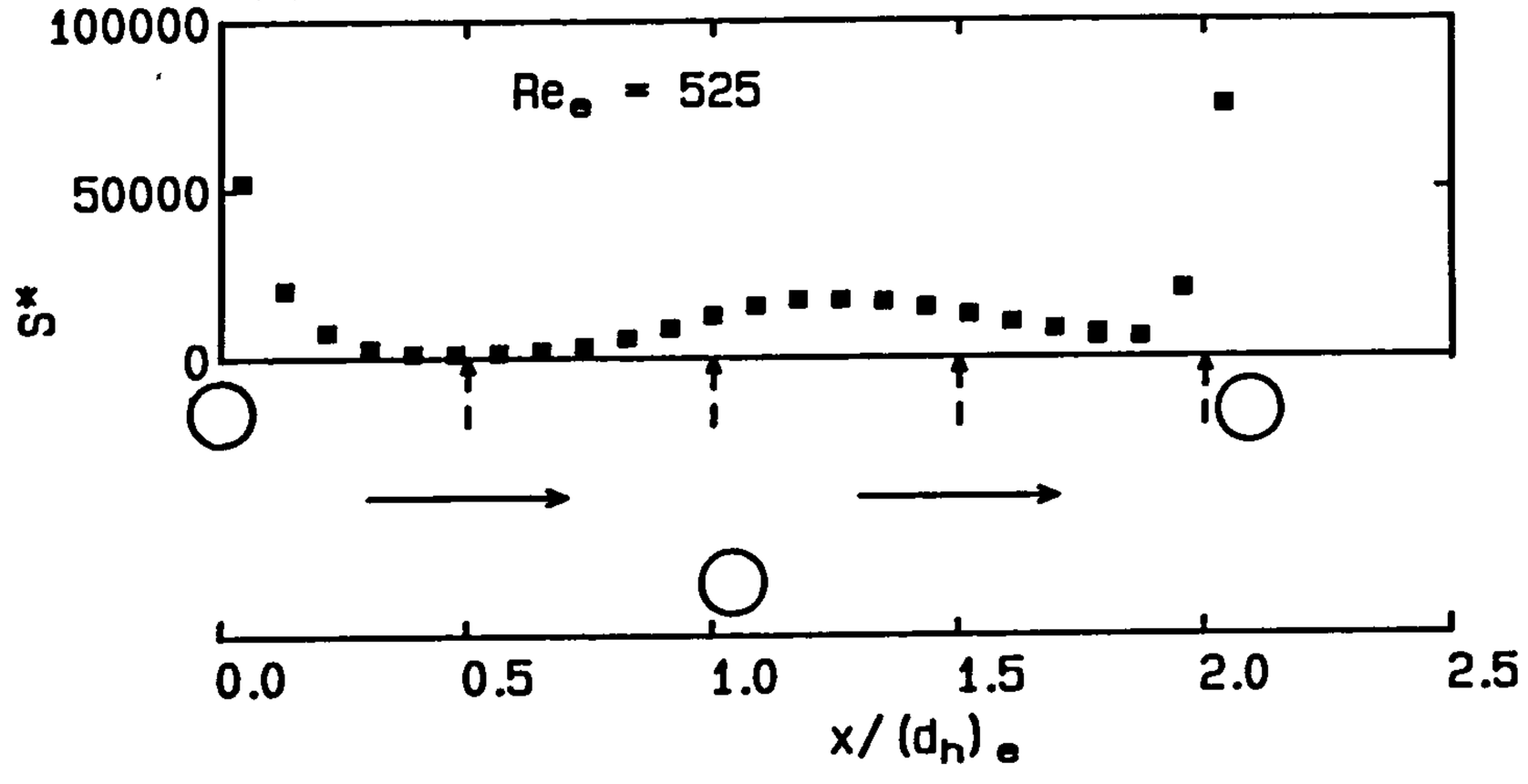

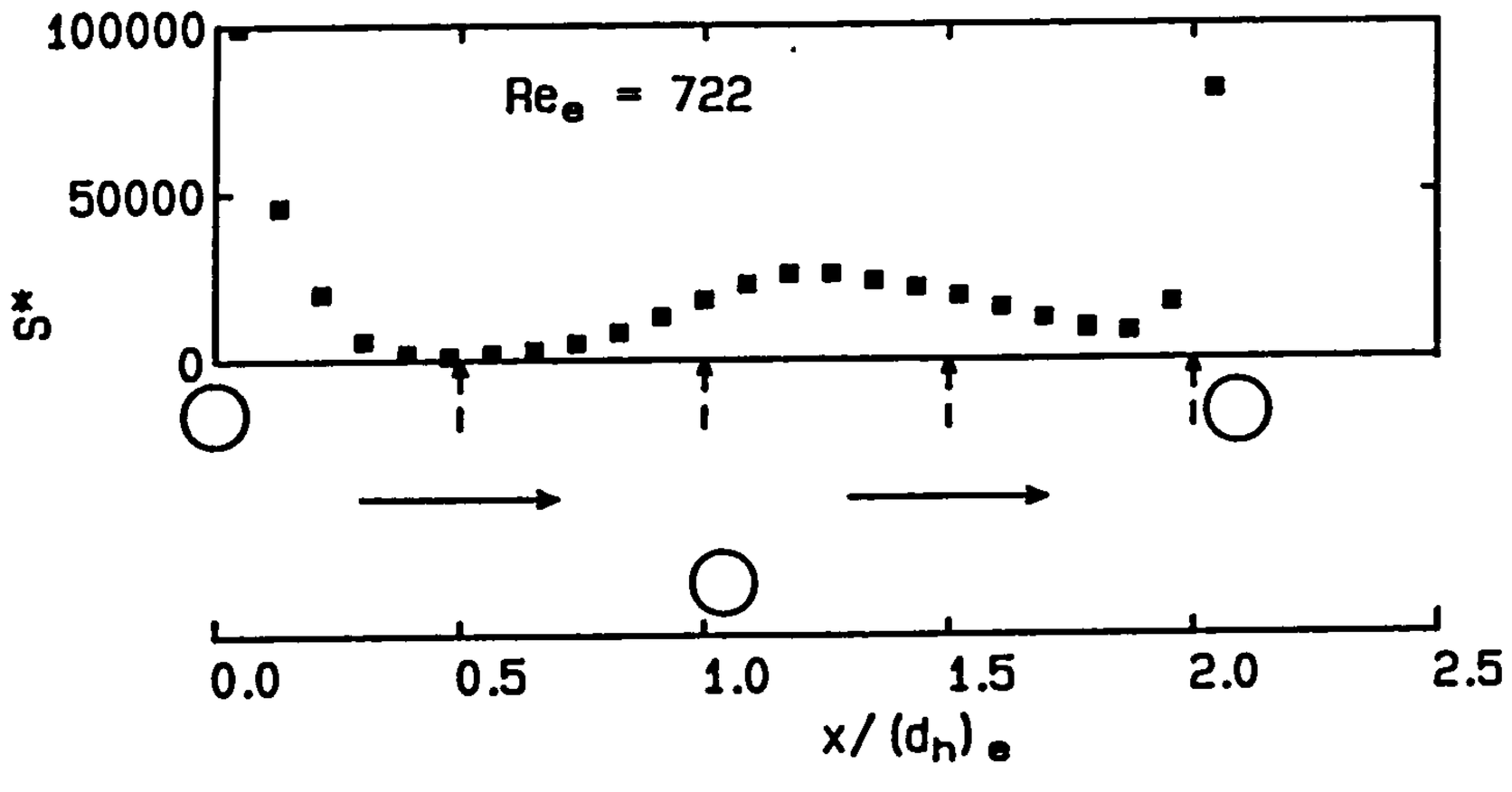

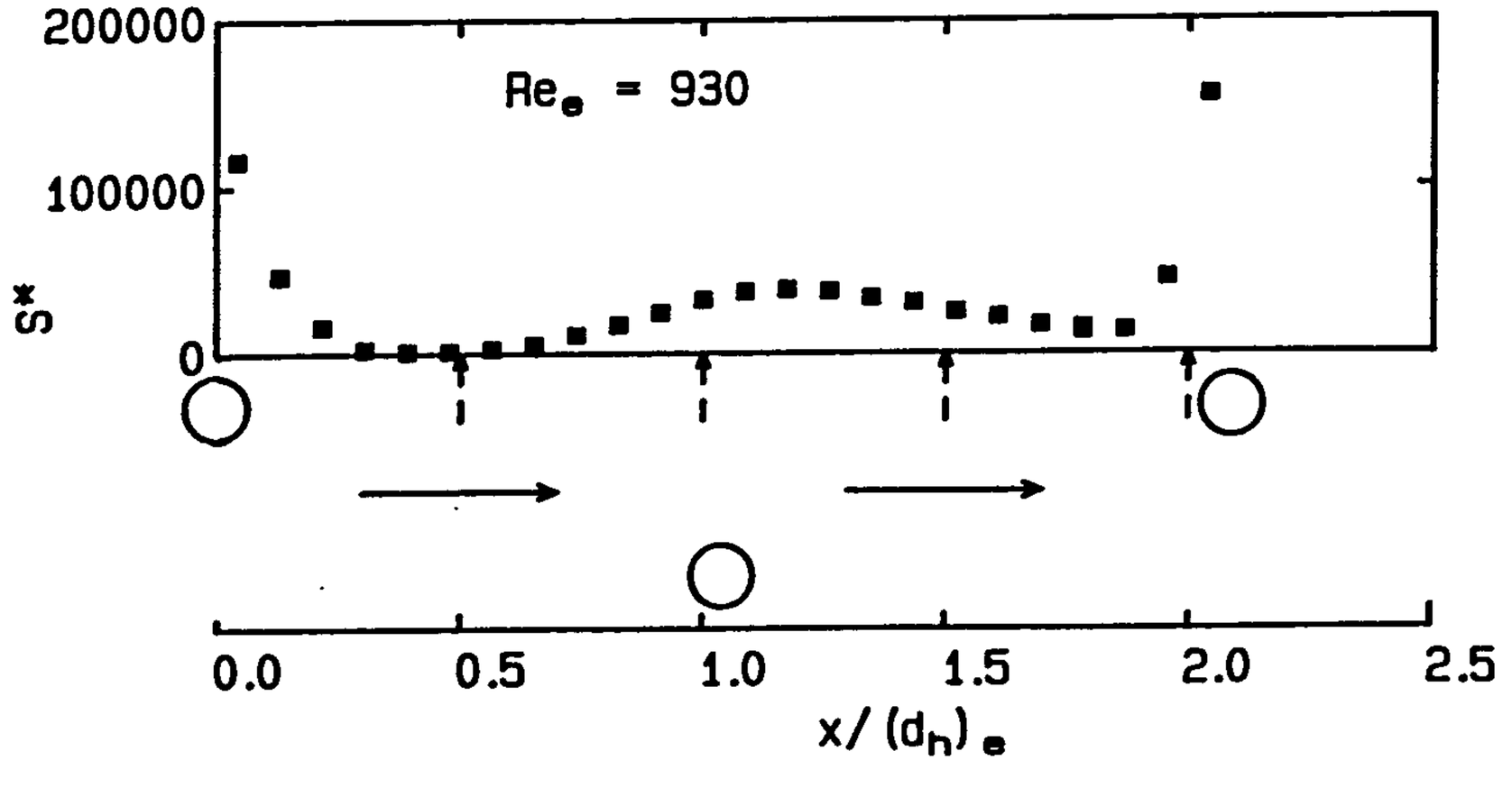

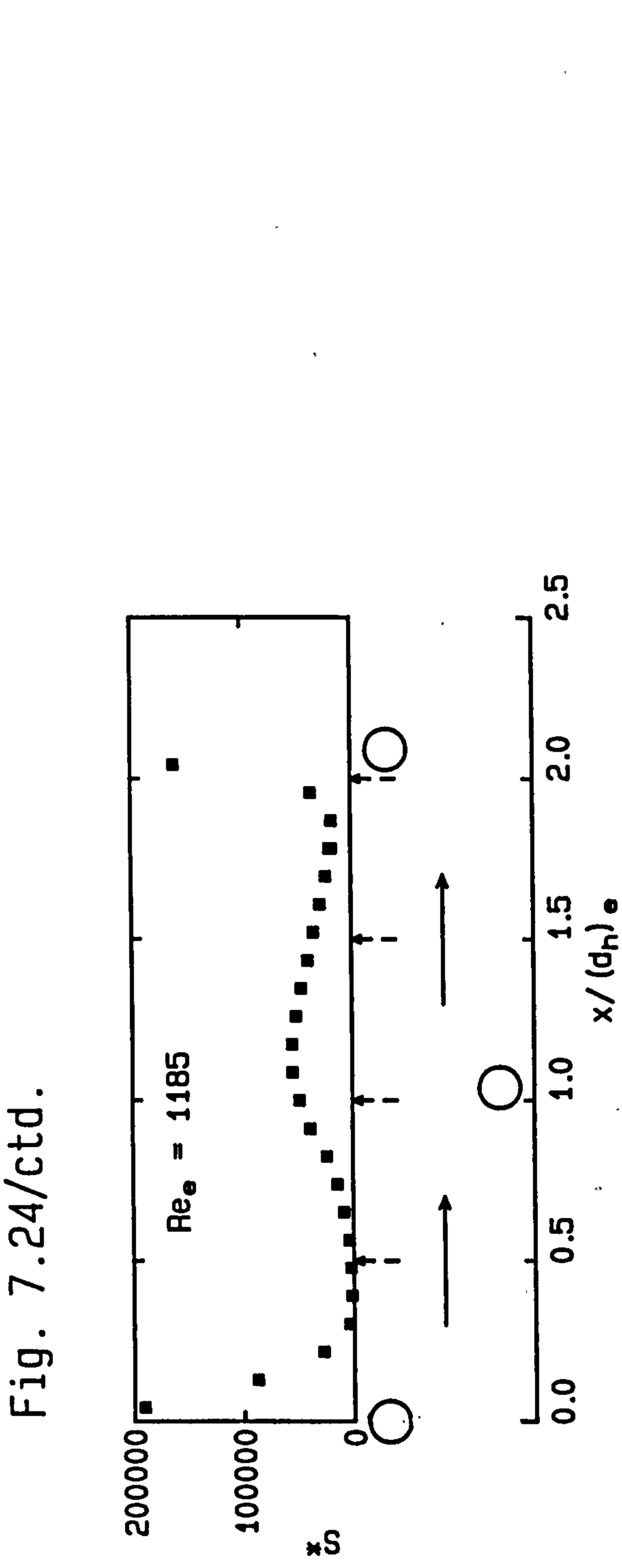
Fig. 7.24/ctd.
Re_e = 1185
200000
100000
0
xS
1.0
1.5
2.0
2.5
$x/(d_h)_e$
0.0
0.5

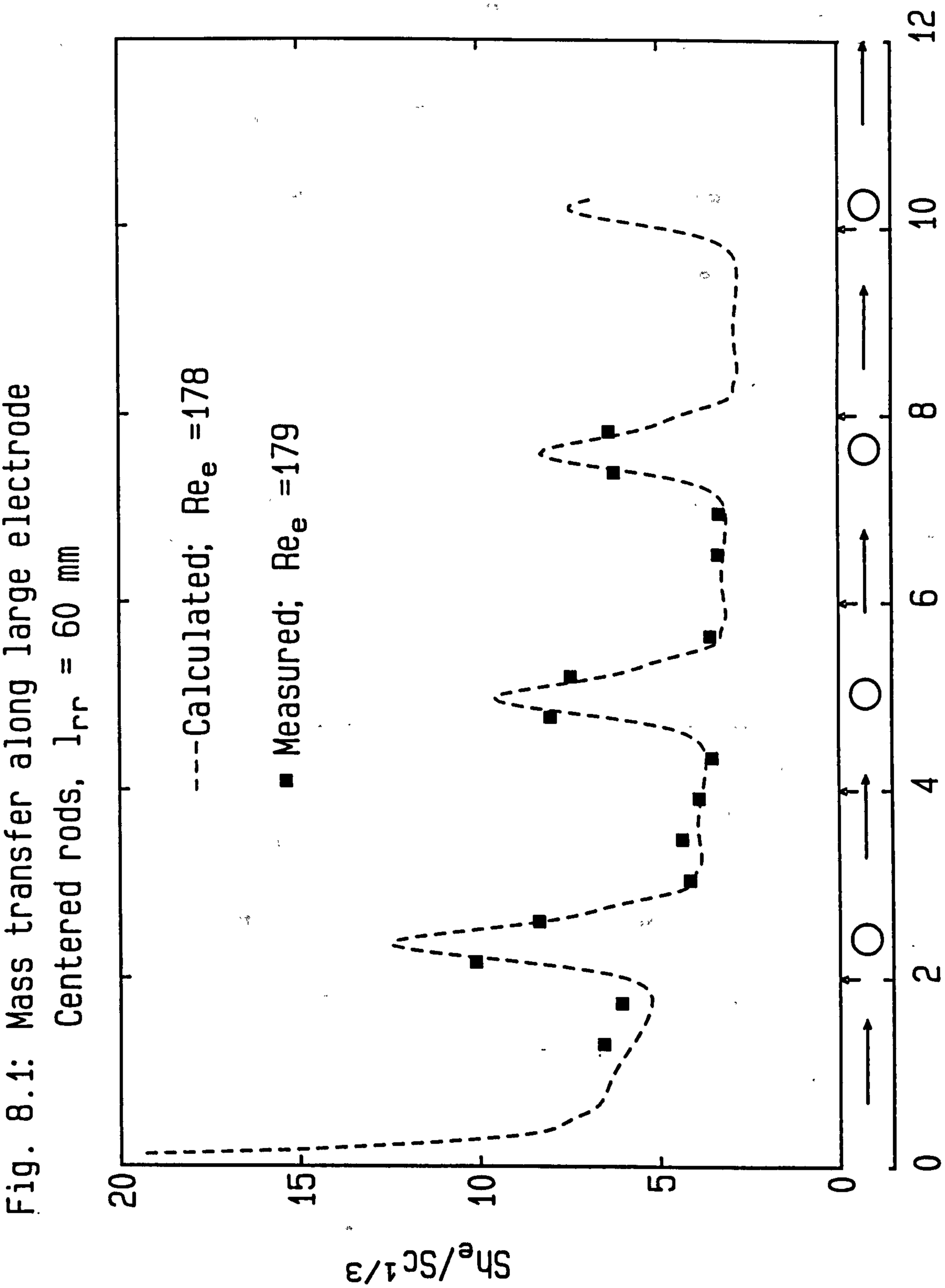
Fig. 8.1: Mass transfer along large electrode
Centered rods, l_{rr} = 60 mm
---Calculated; Re_e =178
■ Measured; Re_e =179
$Sh_e/Sc^{1/3}$
$x/(d_h)_e$
0
2
4
6
8
10
12
20
15
10
5
0

Fig. 8.2: Mass transfer between rods (calculation and measurement)
Centered rods, l_{rr} = 60 mm

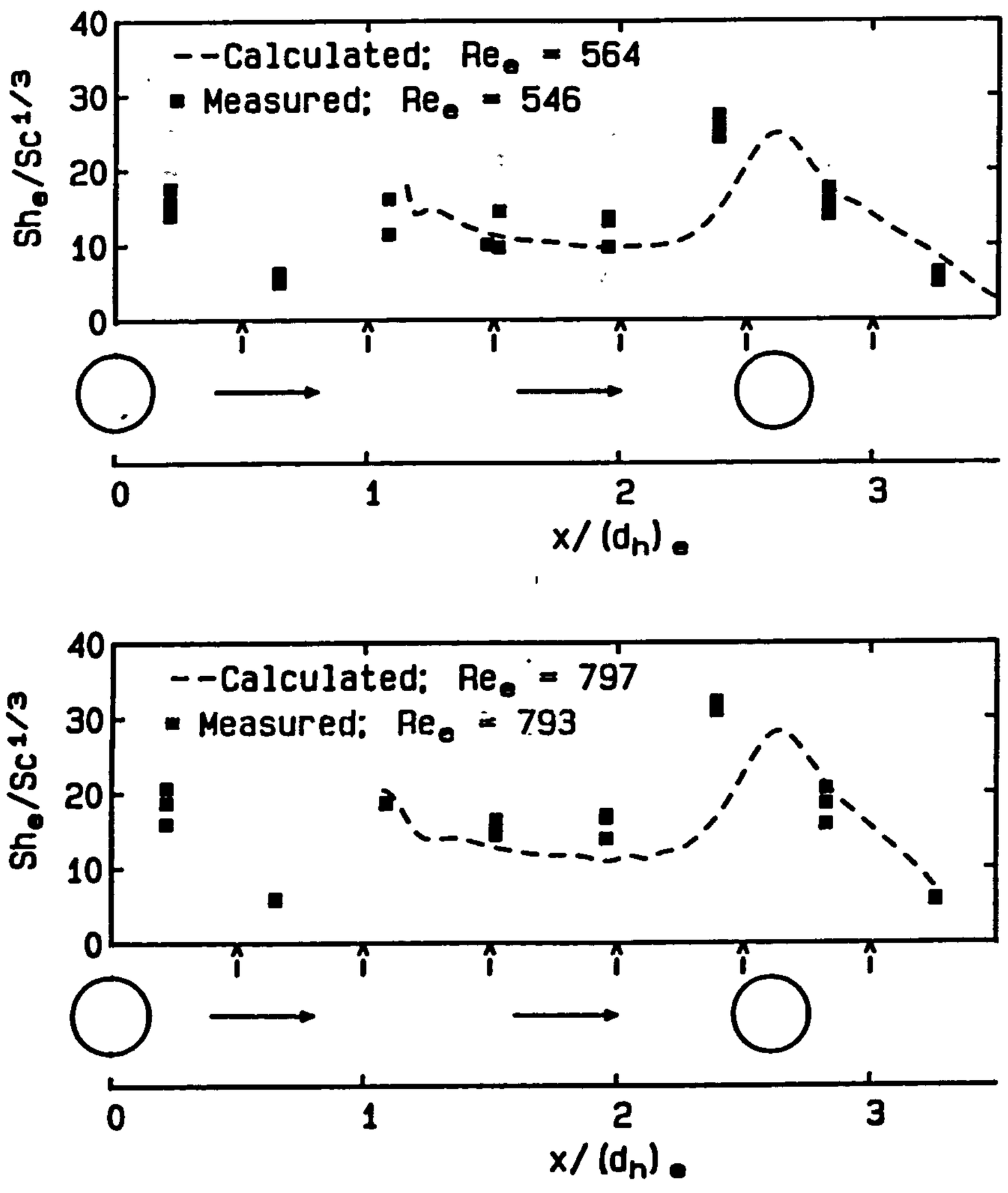

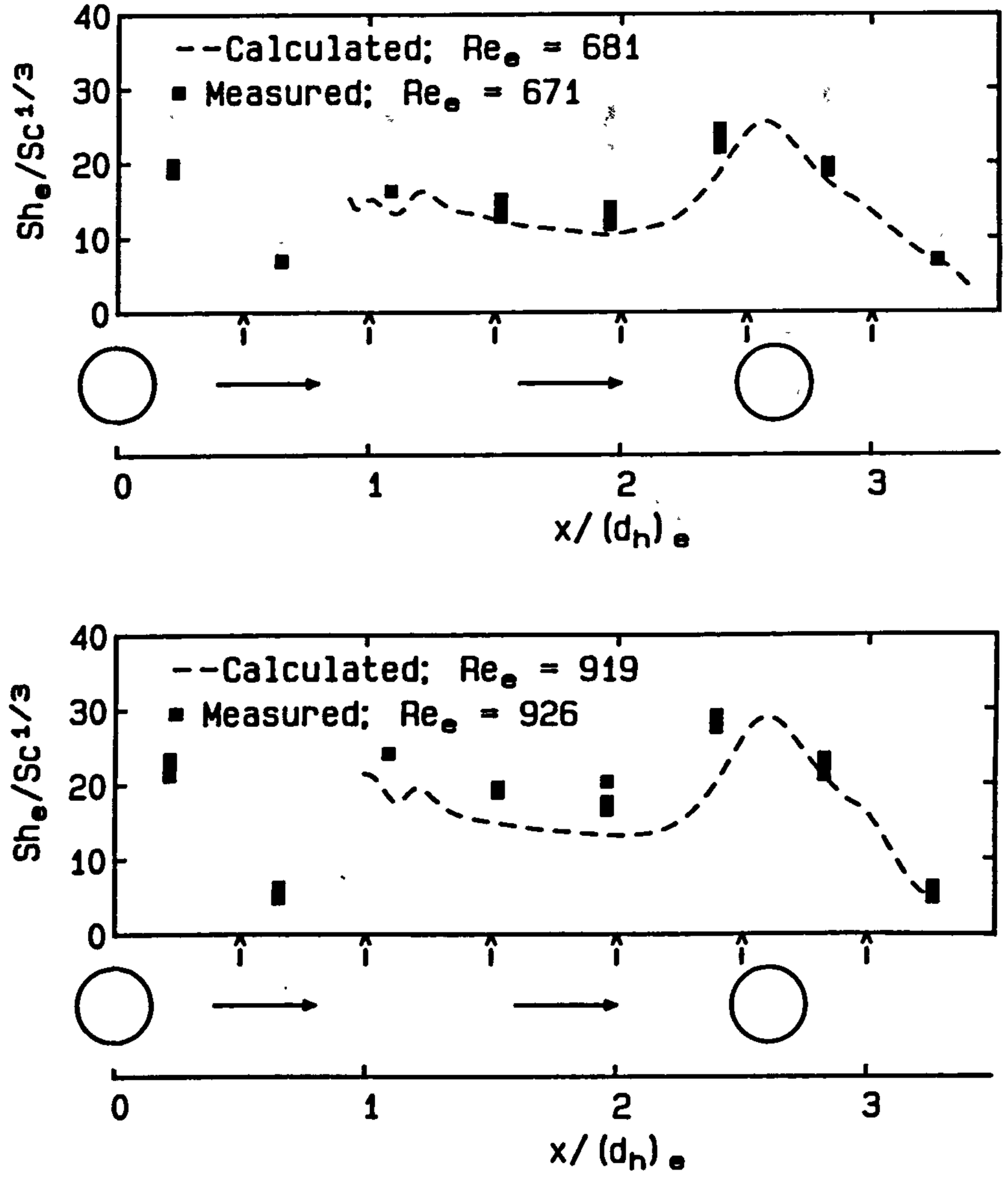

Fig. 8.2/ctd.

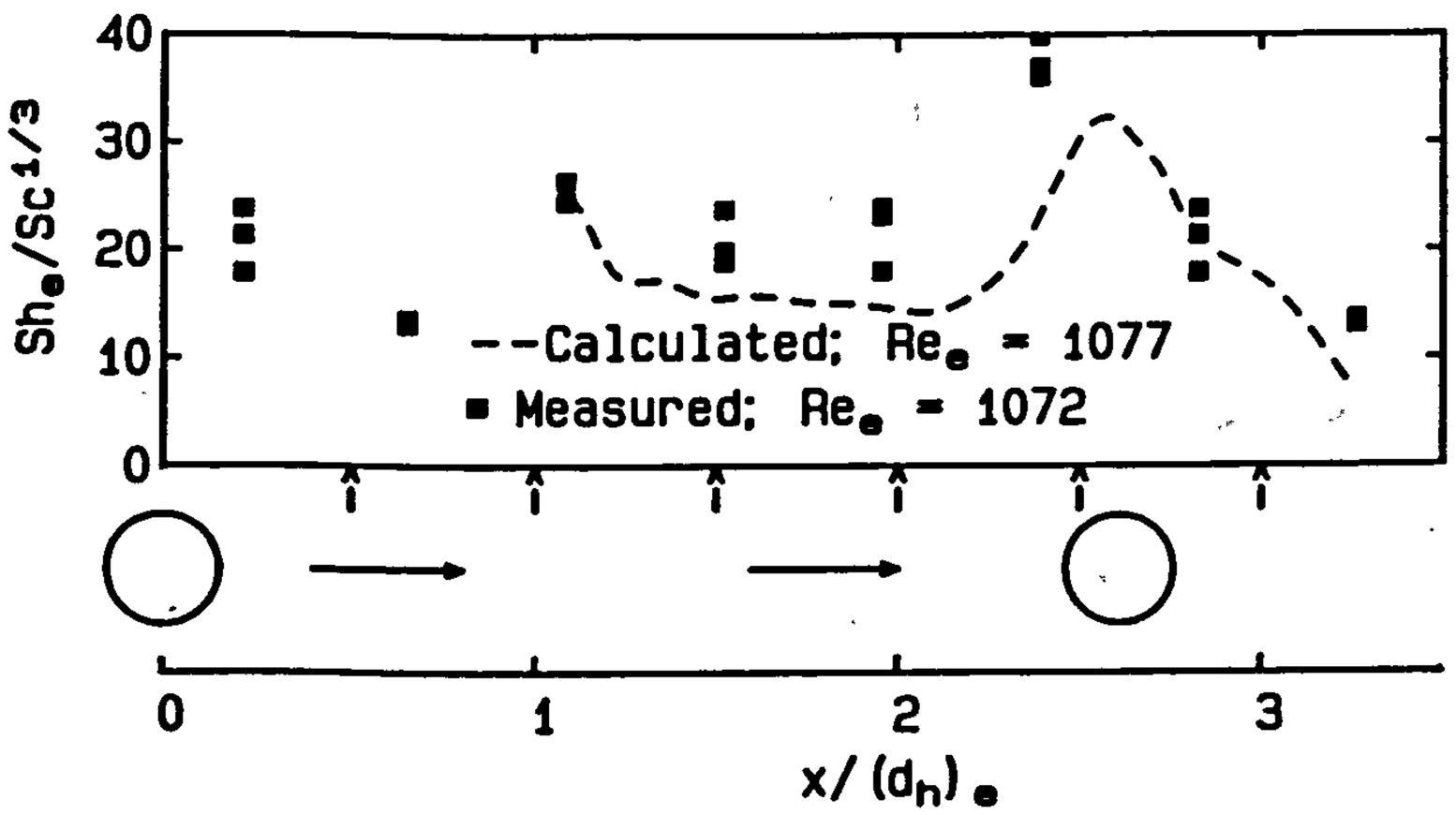
$Sh_e/Sc^{1/3}$
40
30
20
10
0
--Calculated; Re_e = 1077
Measured; Re_e = 1072
0
1
2
3
$x/(d_h)_e$

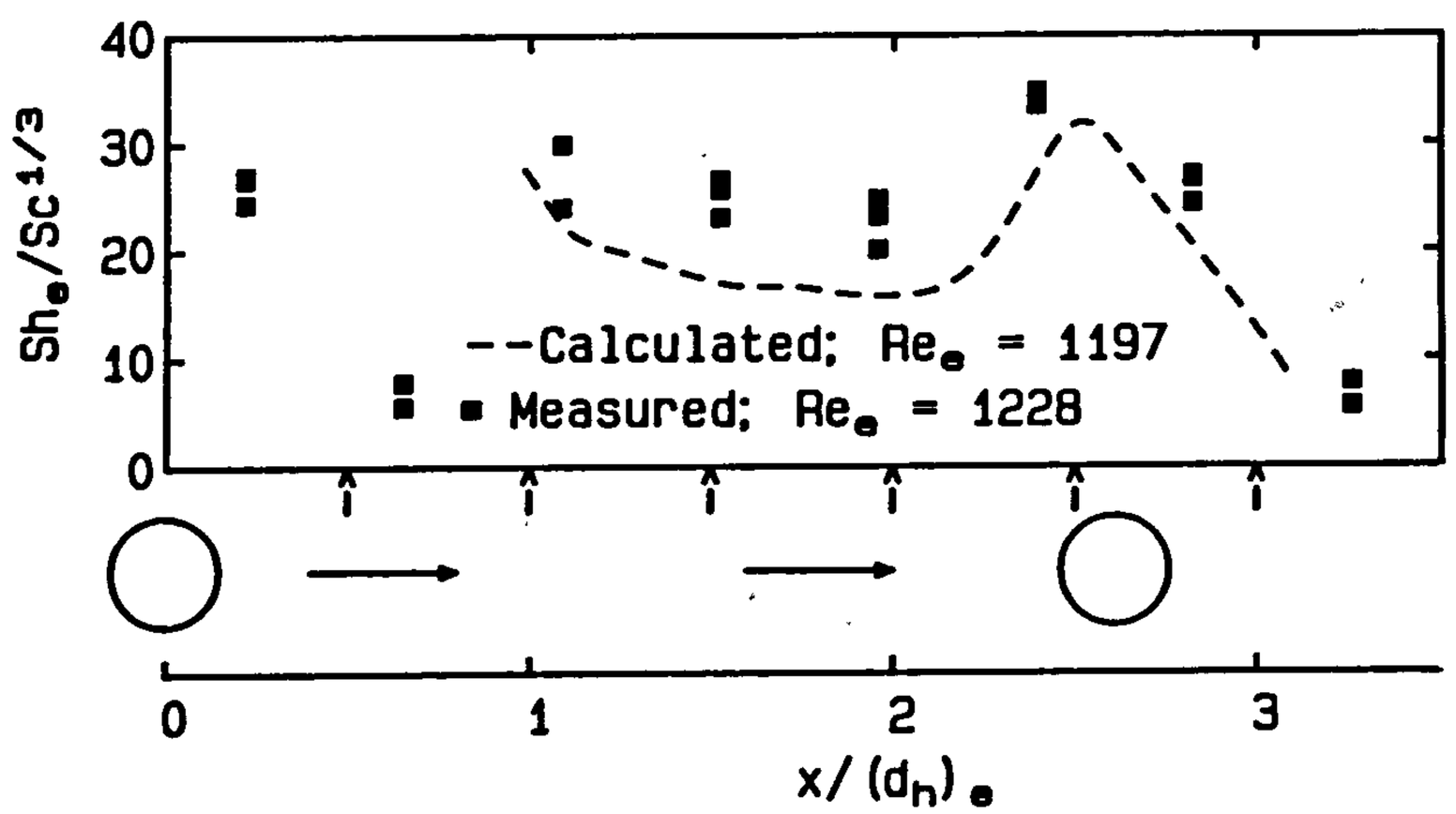
$Sh_e/Sc^{1/3}$
40
30
20
10
0
--Calculated; Re_e = 1197
Measured; Re_e = 1228
0
1
2
3
$x/(d_h)_e$

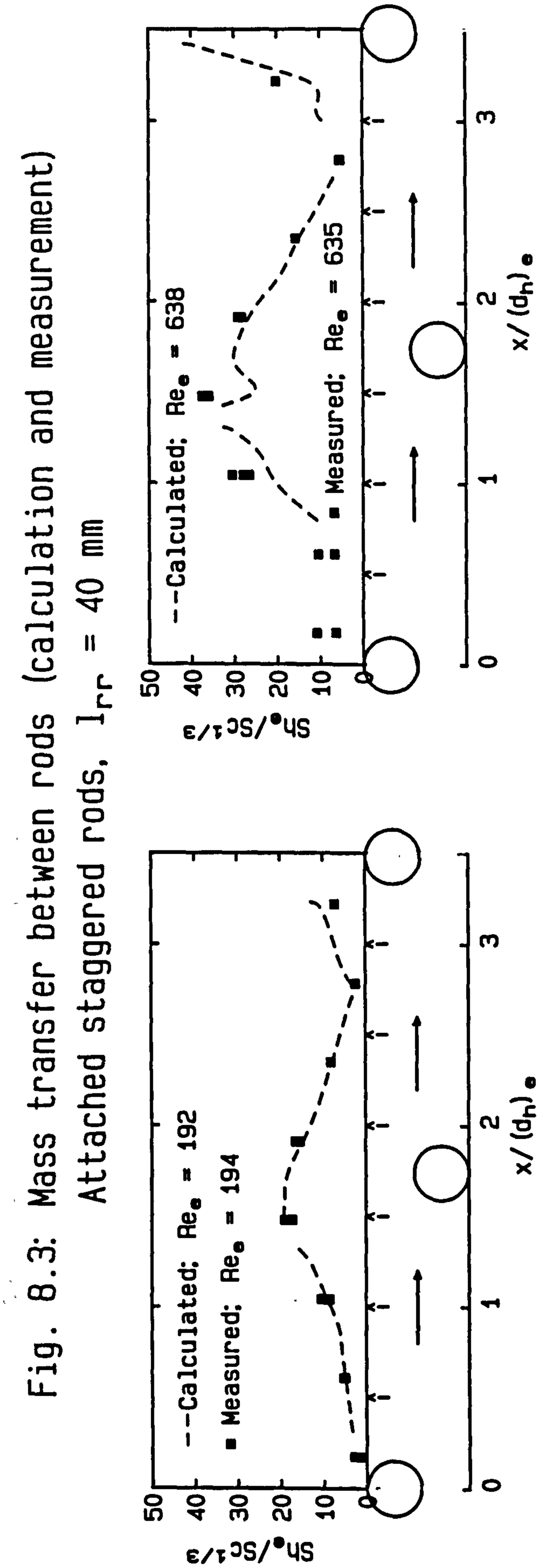

Fig. 8.3: Mass transfer between Attached staggered rods (calculation and measurement)

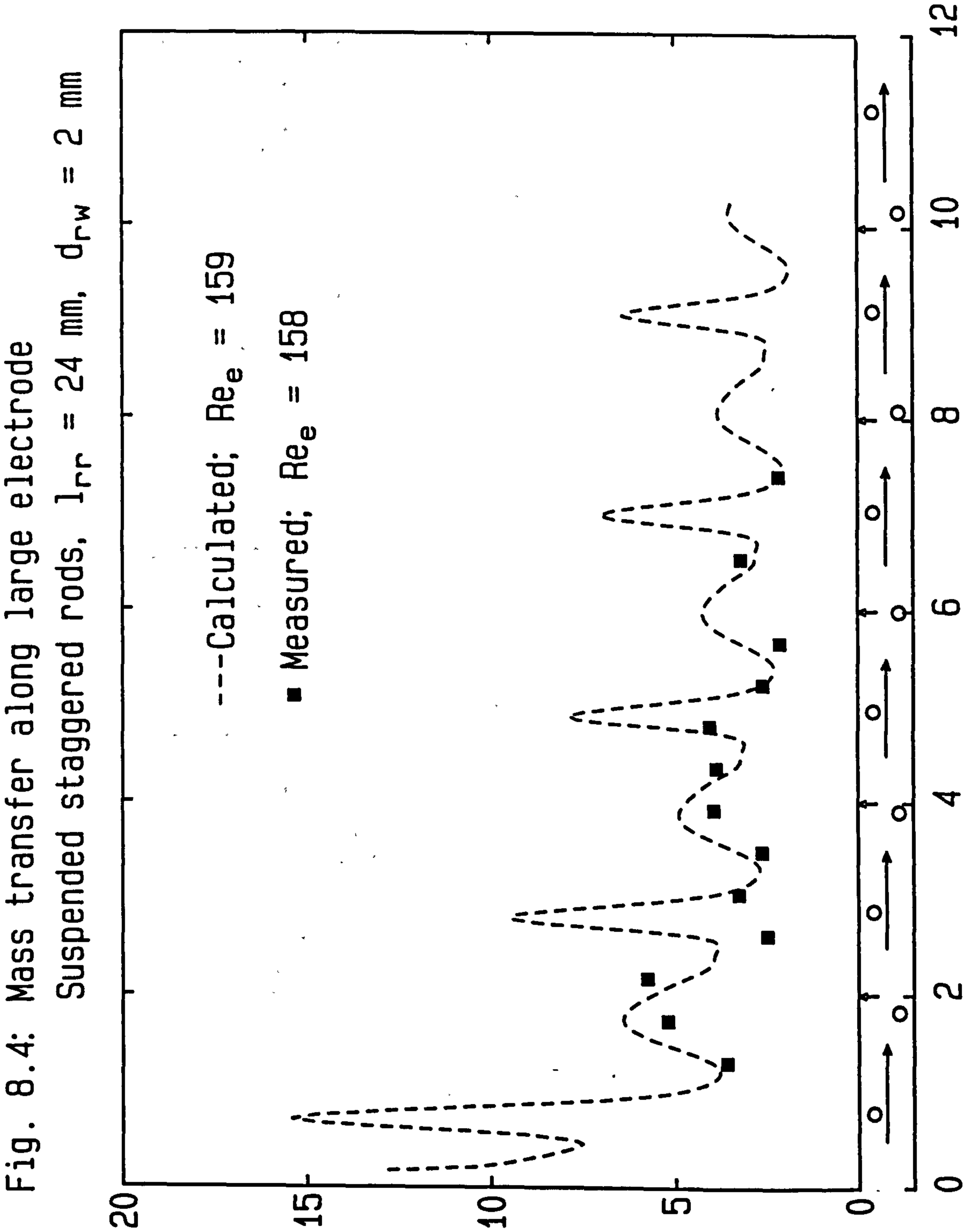

Fig. 8.4: Mass transfer along the large electrode
Suspended staggered rods, l_{rr} = 24 mm, d_{rw} = 2 mm

---Calculated; Re_e = 159

■ Measured; Re_e = 158

$Sh_e/Sc^{1/3}$

$x/(d_h)_e$

Fig. 8.5: Mass transfer between rods (calculation and measurement)
Suspended staggered rods, l_{rr} = 24 mm, d_{rw} = 2 mm

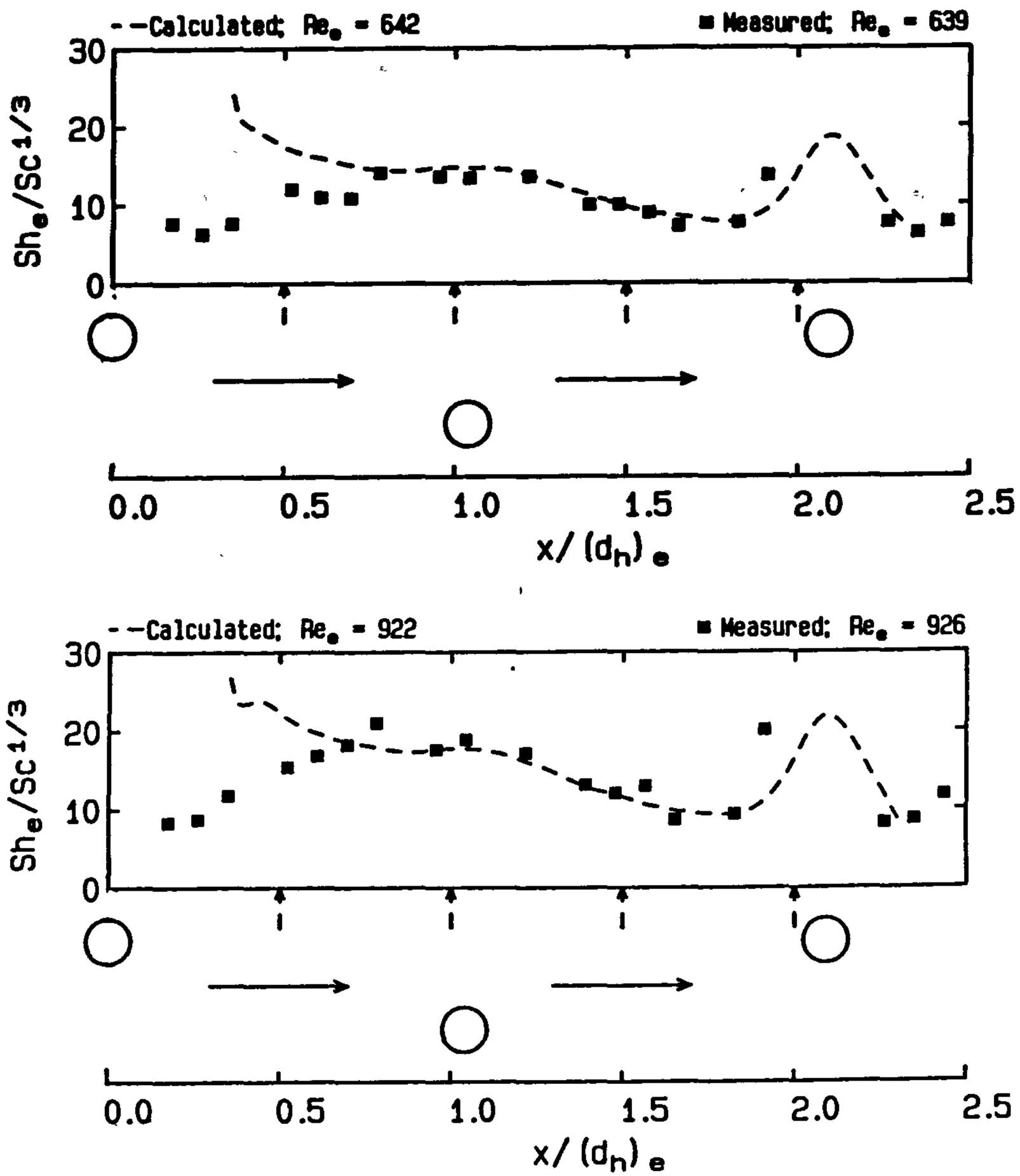

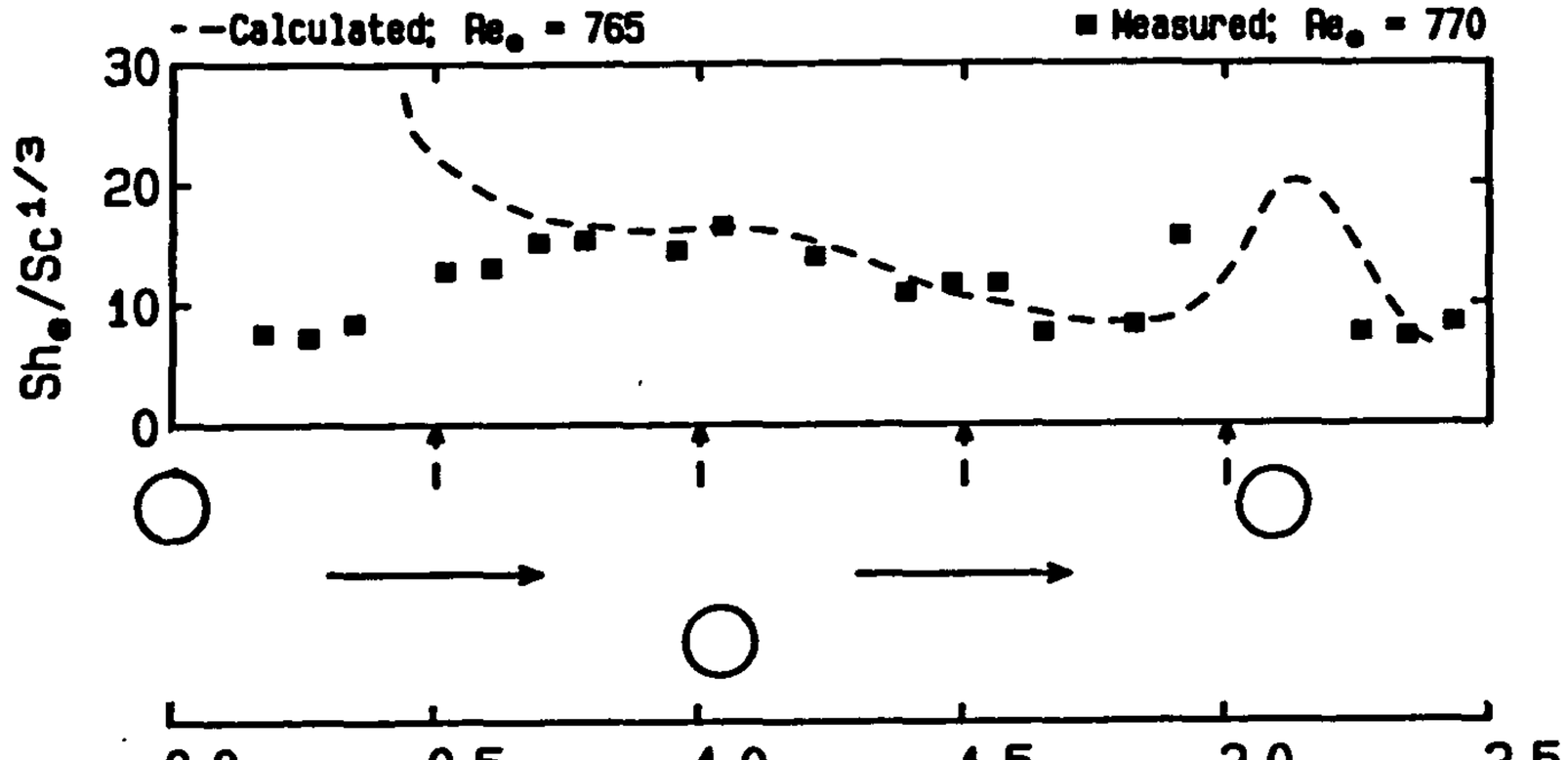

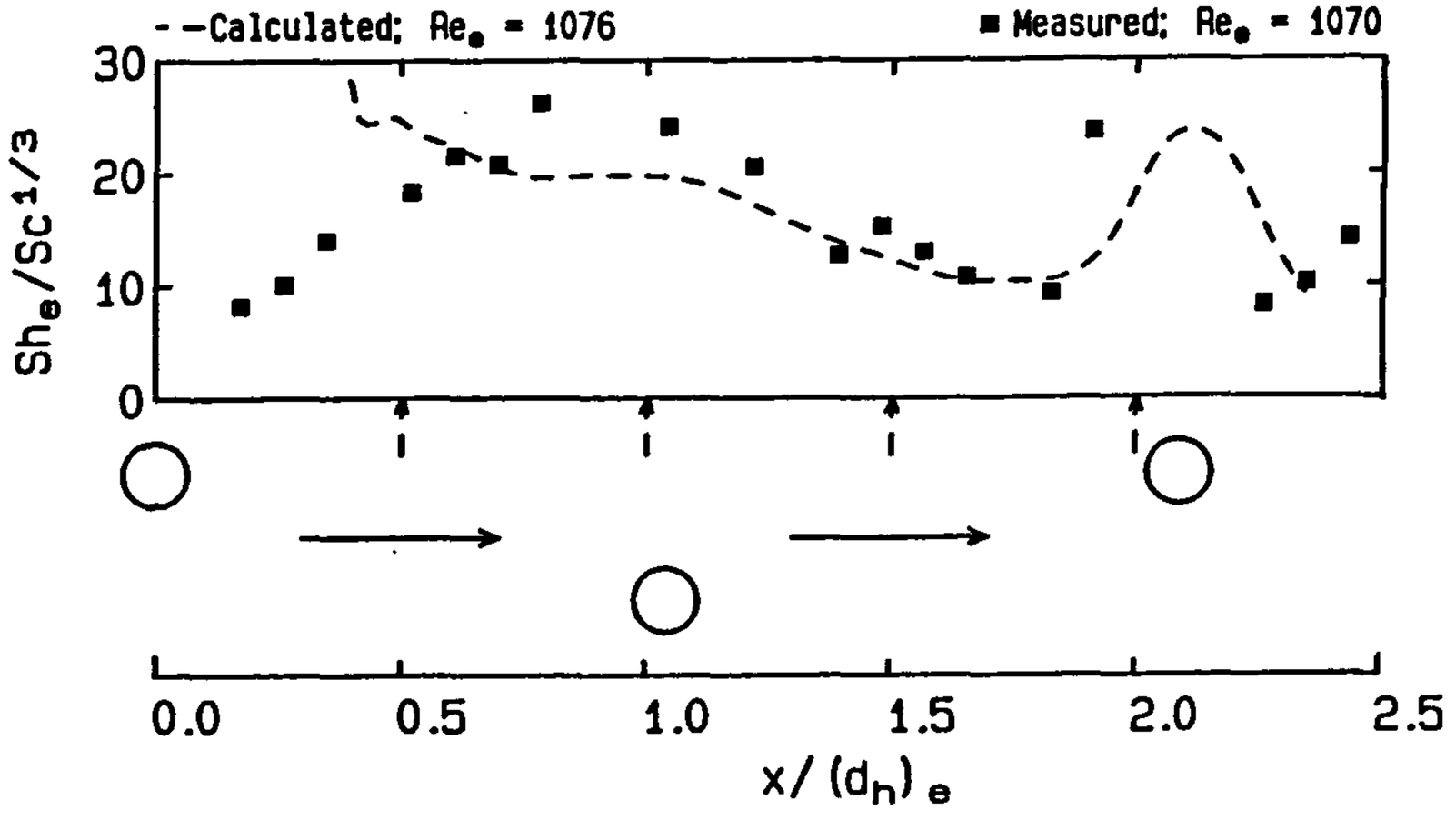

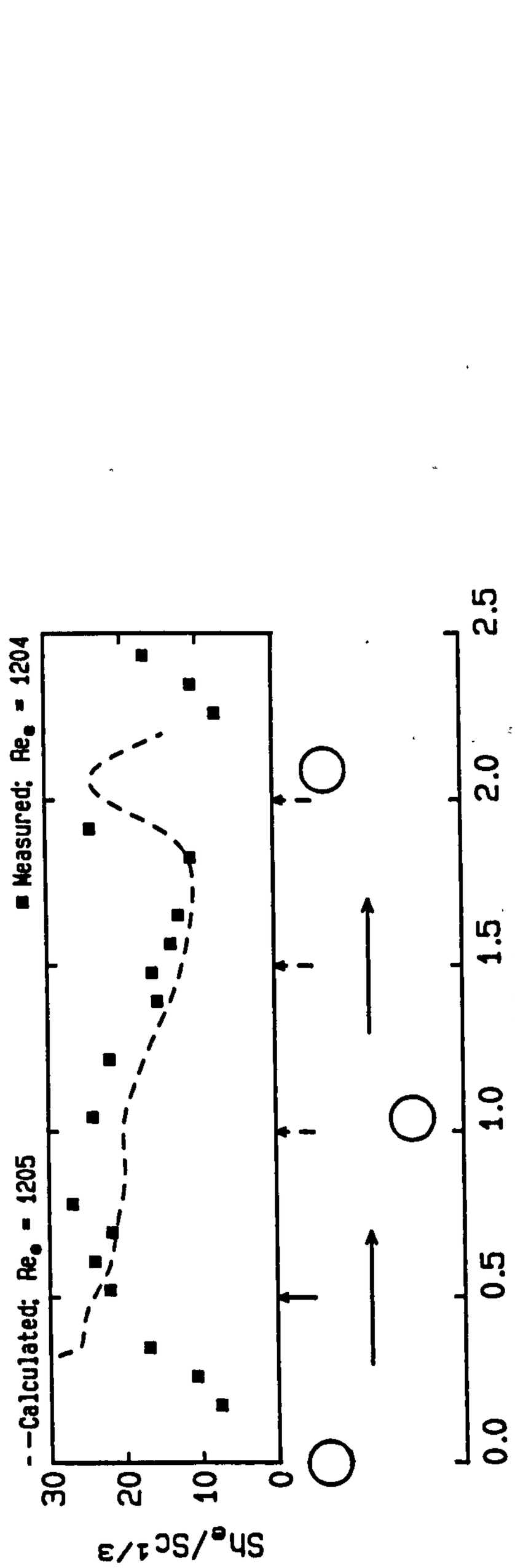
■ Measured; Re_e = 1204
--Calculated; Re_e = 1205
Sh_e/Sc^1/3
30
20
10
0
0.0
0.5
1.0
1.5
2.0
2.5
x/(d_h)_e

Fig. 8.5/ctd.

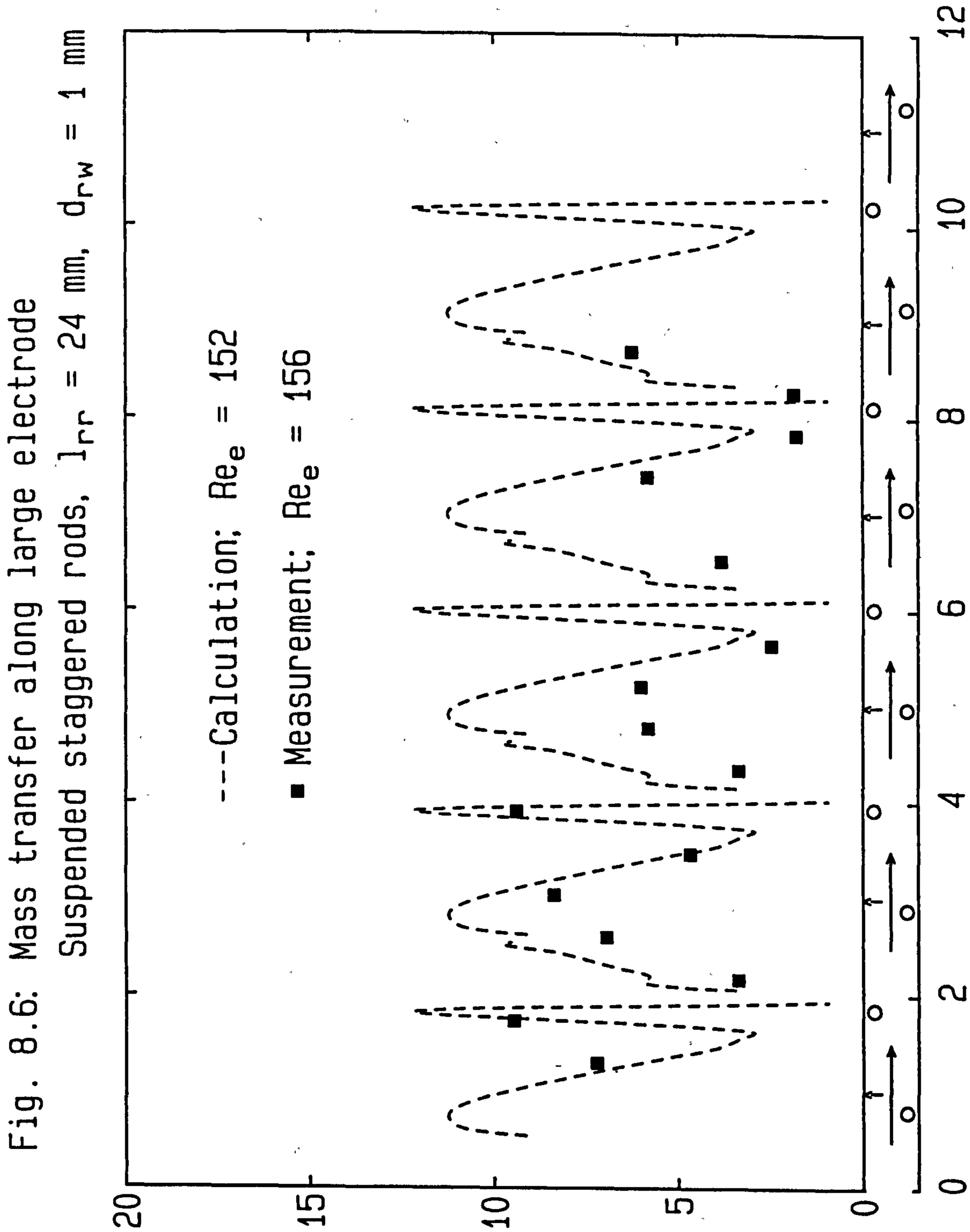
Sh_e/Sc^1/3
20
15
10
5
0
x/(d_h)_e
0
2
4
6
8
10
12
■ Measurement; Re_e = 156
---Calculation; Re_e = 152
d_rw = 1 mm
Suspended staggered rods, l_rr = 24 mm, d_r
Fig. 8.6: Mass transfer along large electrode

Fig. 8.7: Mass transfer between rods (calculation and measurement)
Suspended staggered rods, l_{rr} = 24 mm, d_{rw} = 1 mm

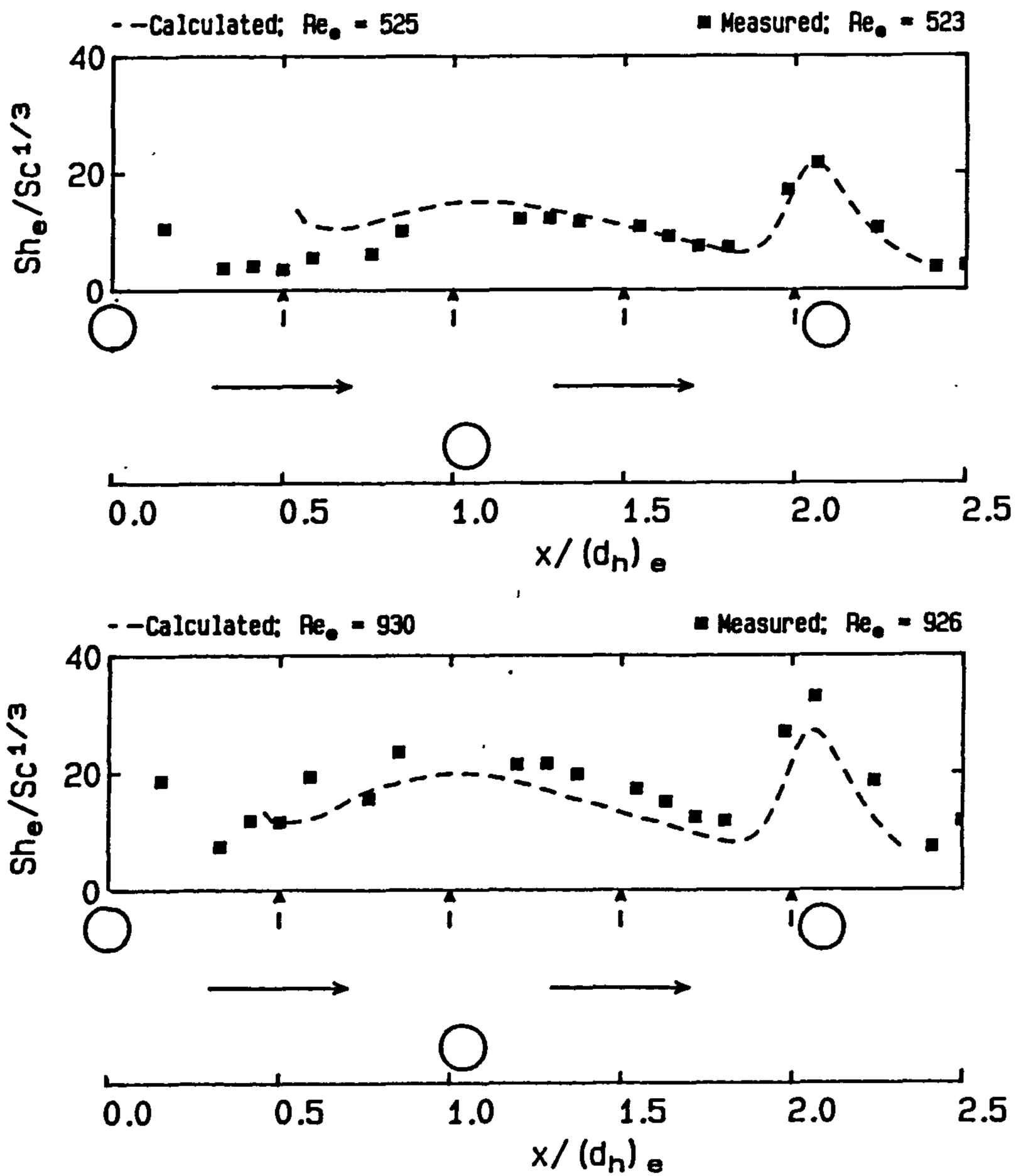

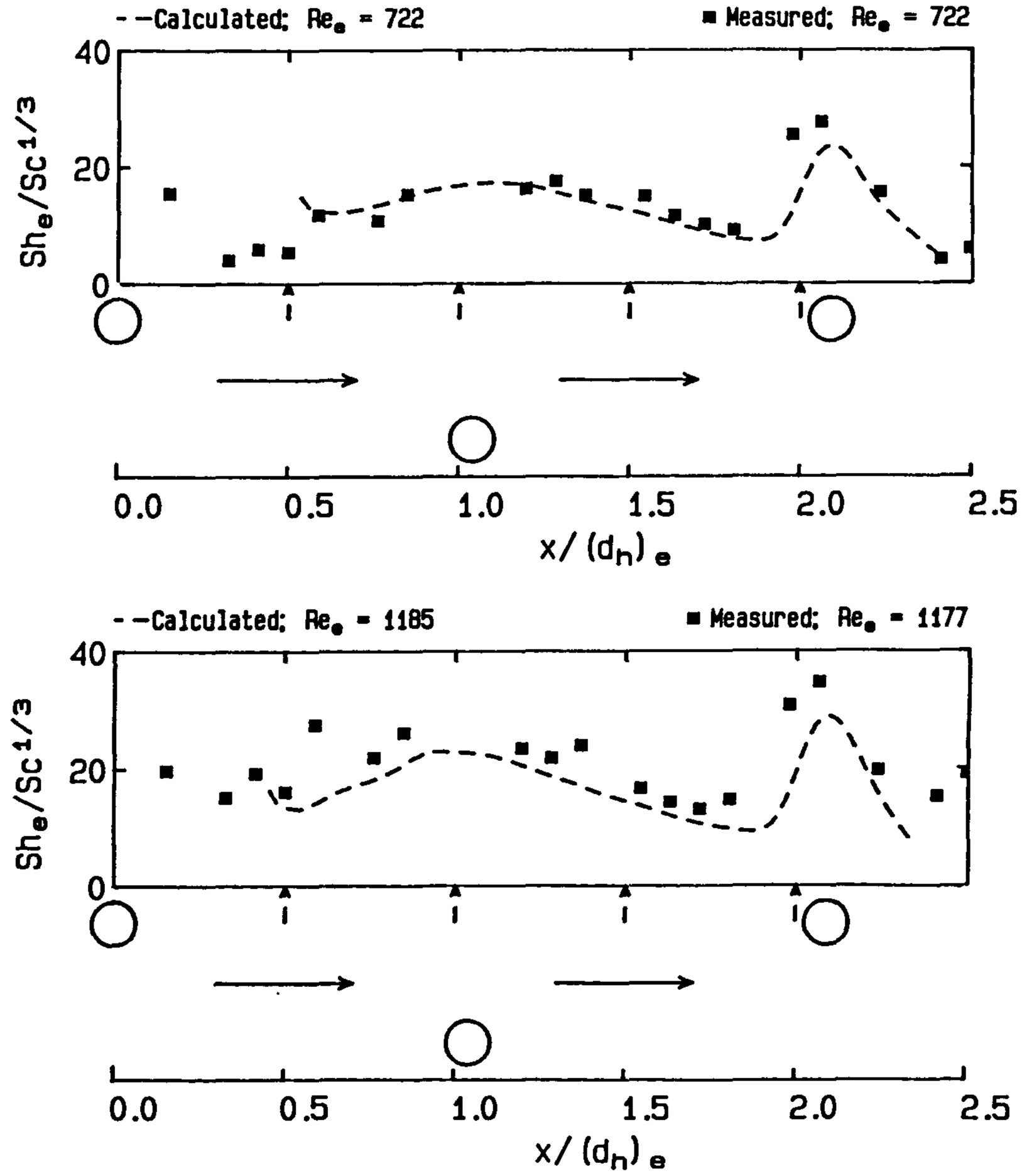

PLATES

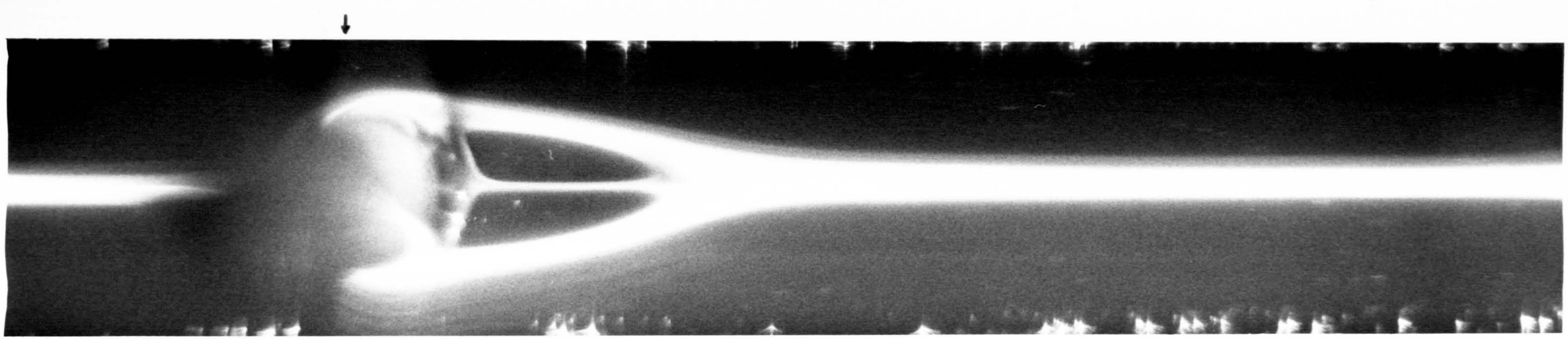

Plate 3.1: Centered rods, l_{rr} = 60 mm (↓ position of rod)

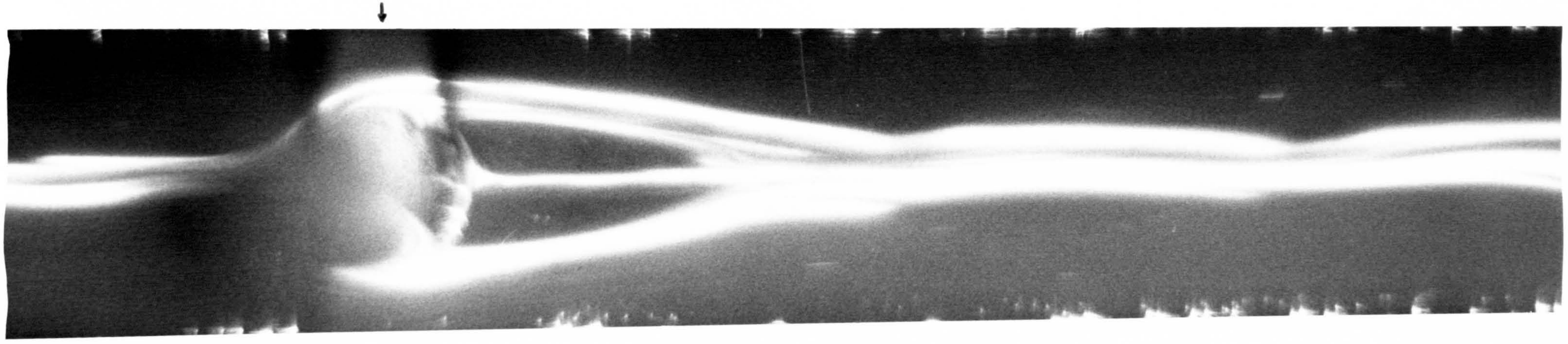

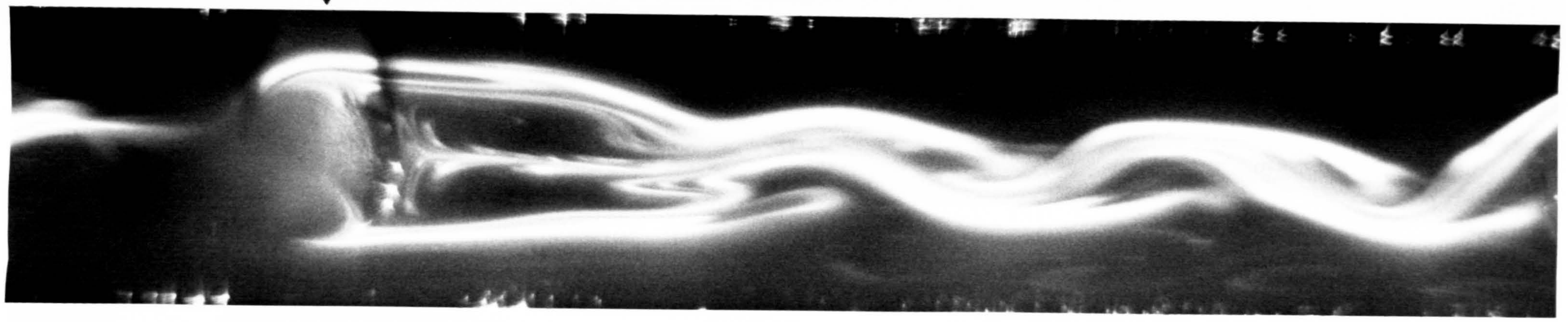

Flow ⟶

Re_e = 307

Plate 3.2: Centered rods, l_{rr} = 60 mm (↓ position of rod)

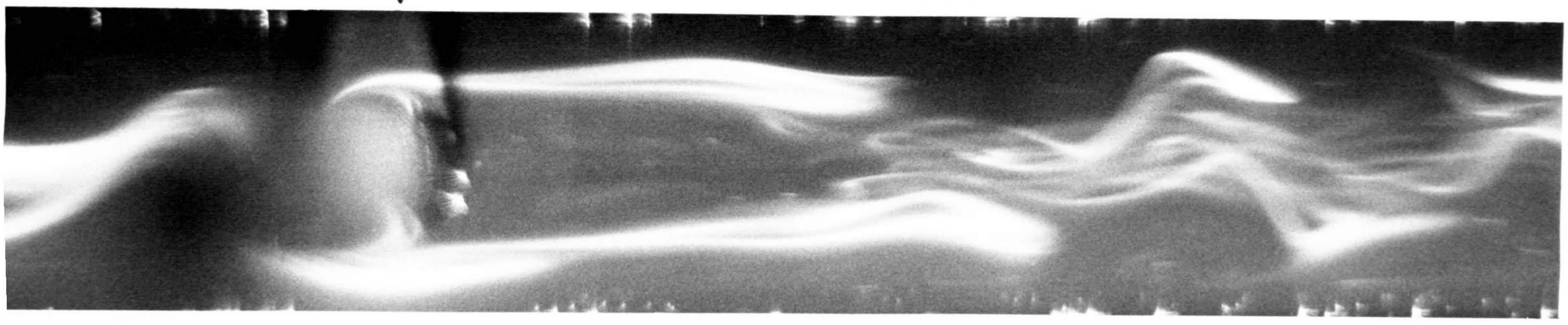

Flow ⟶

Re_e = 470

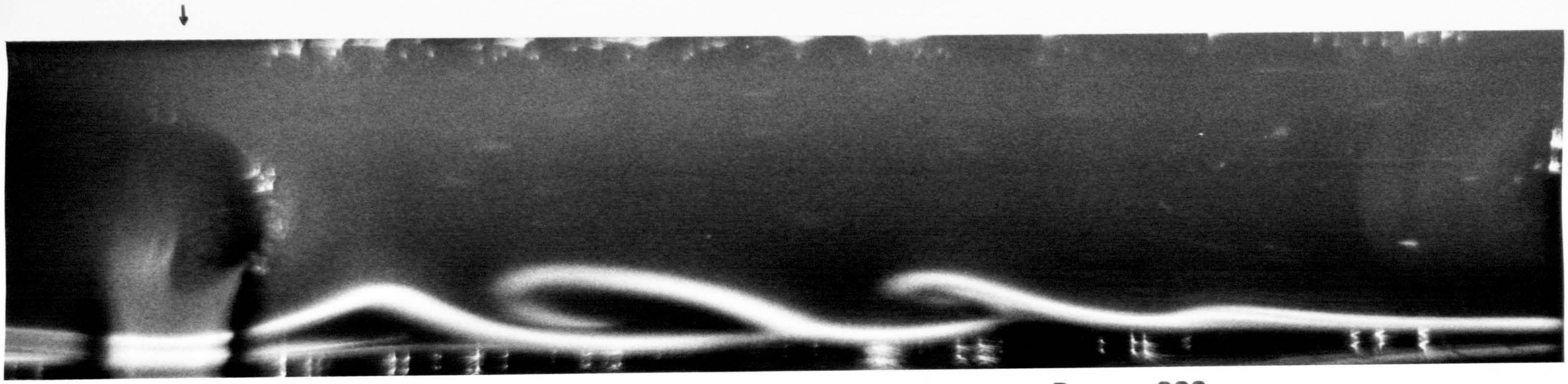

Plate. 3.3: Centered rods, l_{rr} = 60 mm (↓ position of rod)

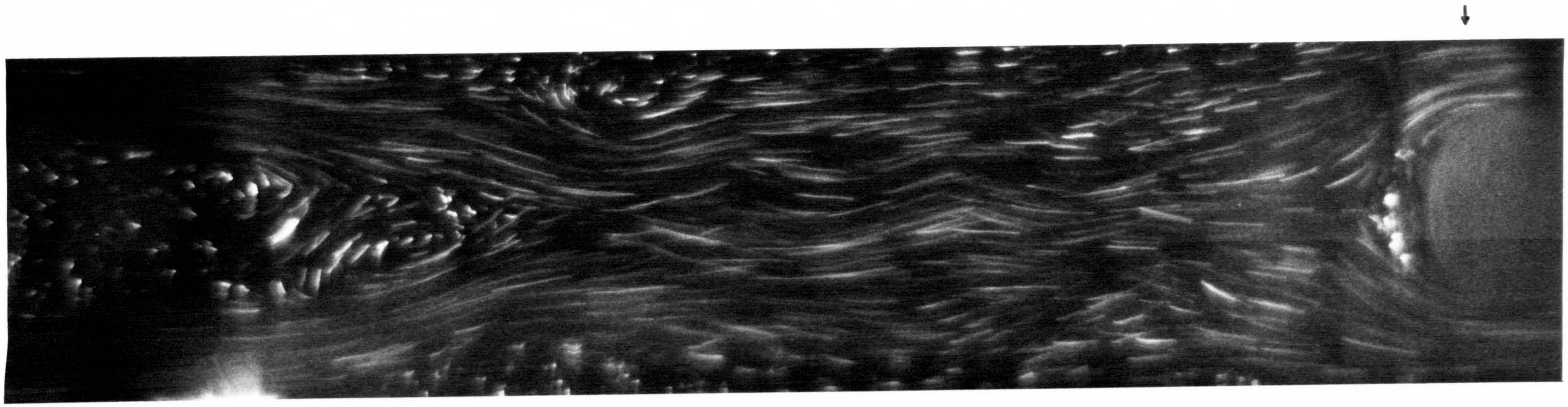

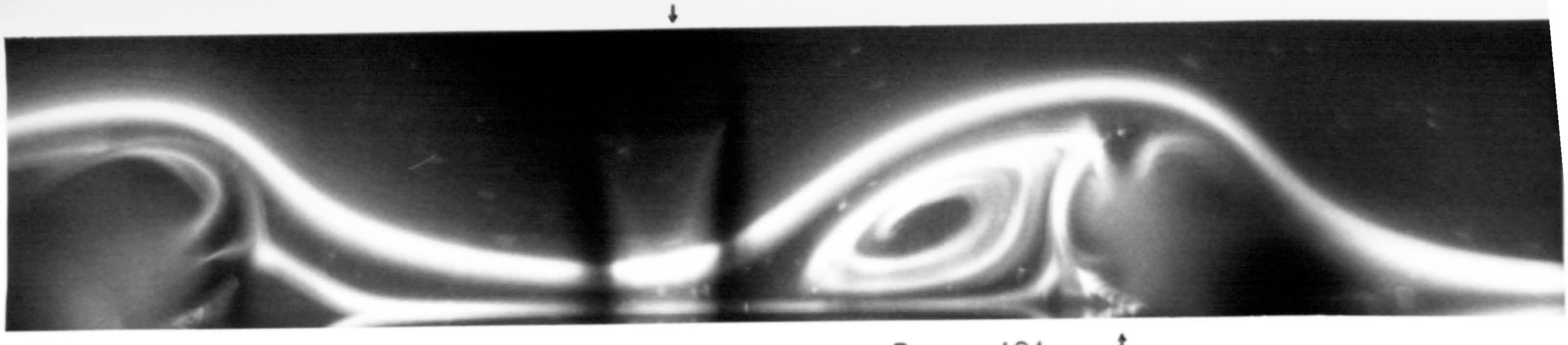

Plate 3.4: Attached staggered rods, l_{rr} = 20 mm (↑↓ position of rod)

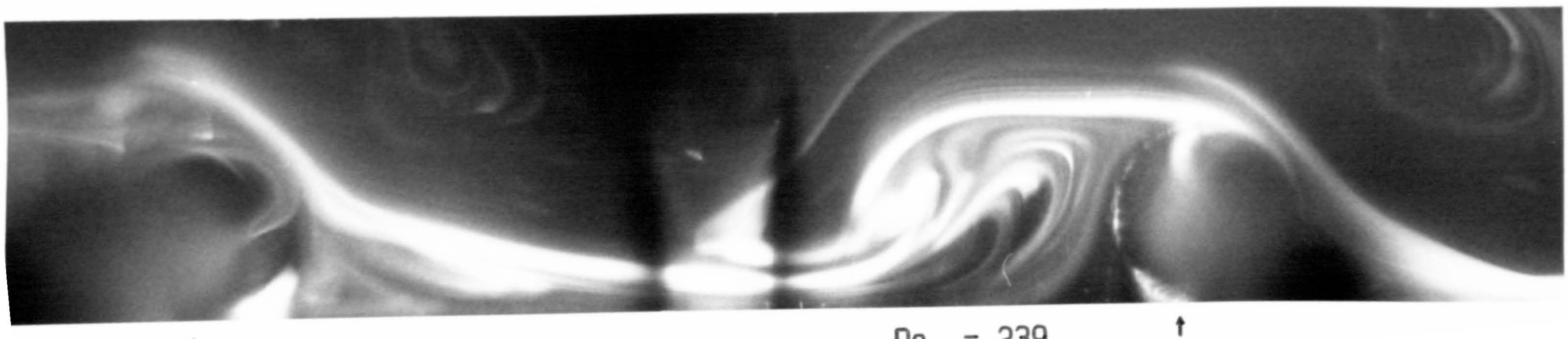

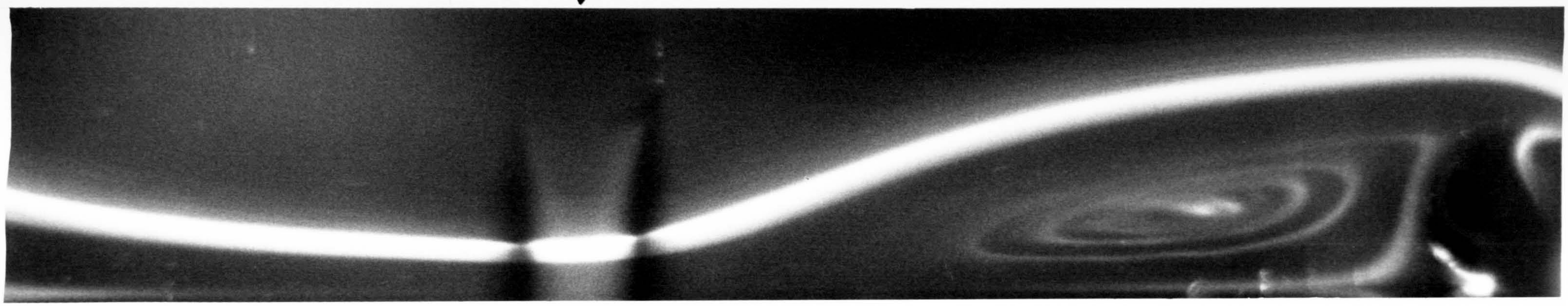

Flow ←

Re_e = 192

Plate 3.5: Attached staggered rods, l_{rr} = 40 mm (↑↓ position of rod)

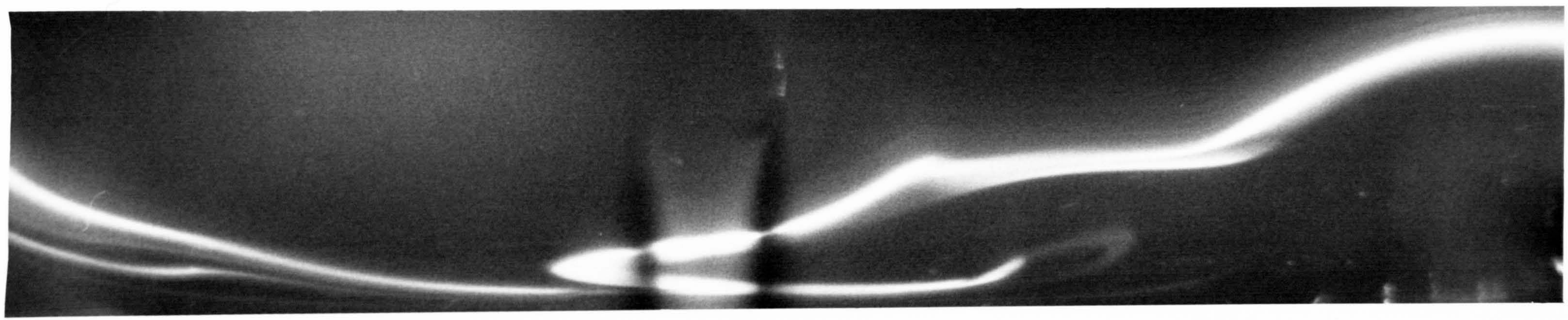

Flow ←

Re_e = 261

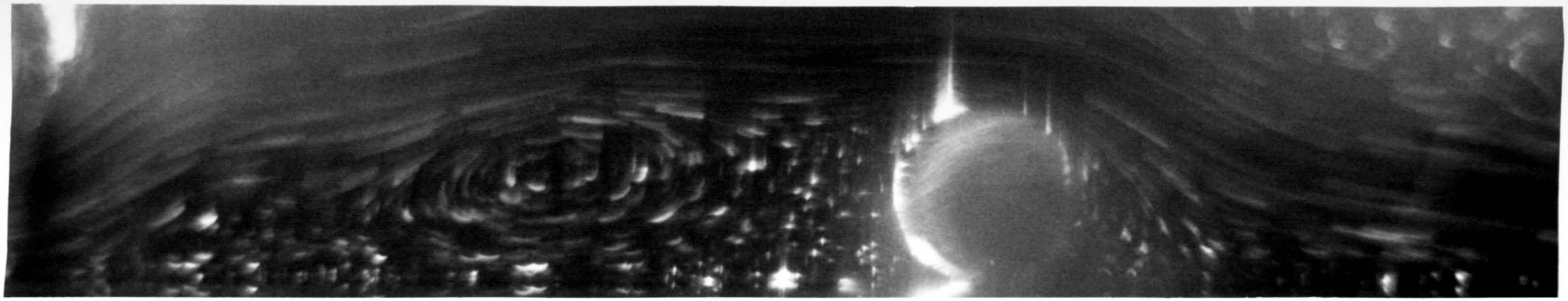

Flow ←

↑ Re_e = 273

Plate 3.6: Attached staggered rods, l_{rr} = 40 mm (↑↓ position of rod)

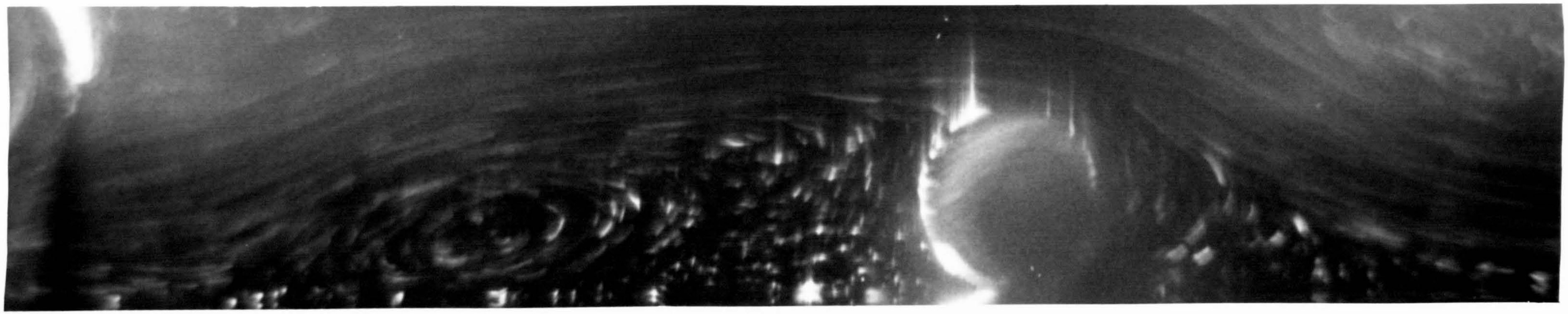

Flow ←

↑ Re_e = 347

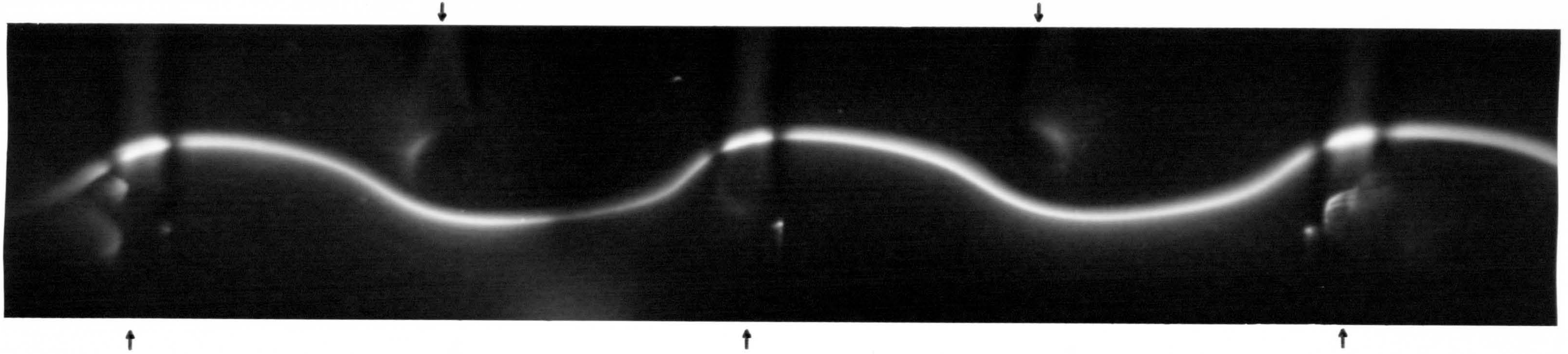

Flow ⟶

Re_e = 230

Plate 3.7: Suspended staggered rods (↓↑ position of rod)

l_{rr} = 12 mm, d_{rw} = 3 mm

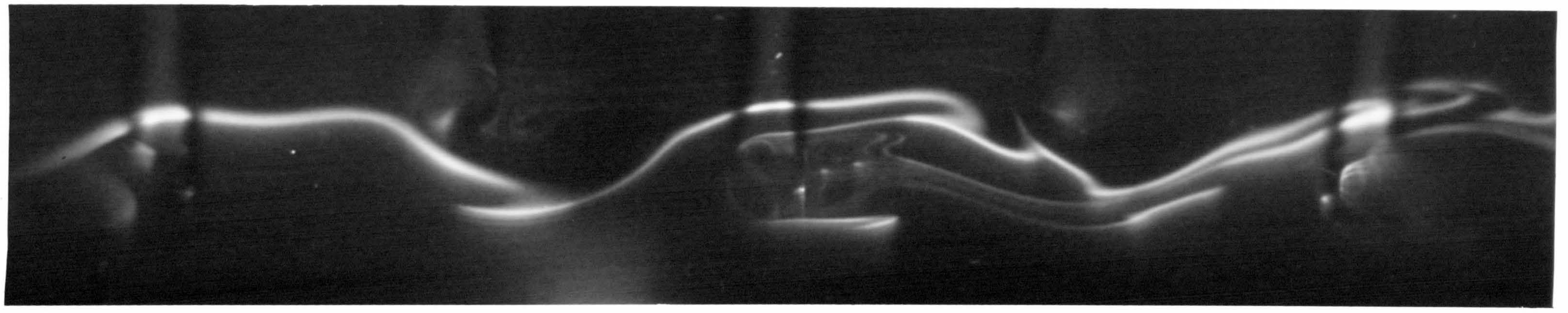

Flow ⟶

Re_e = 283

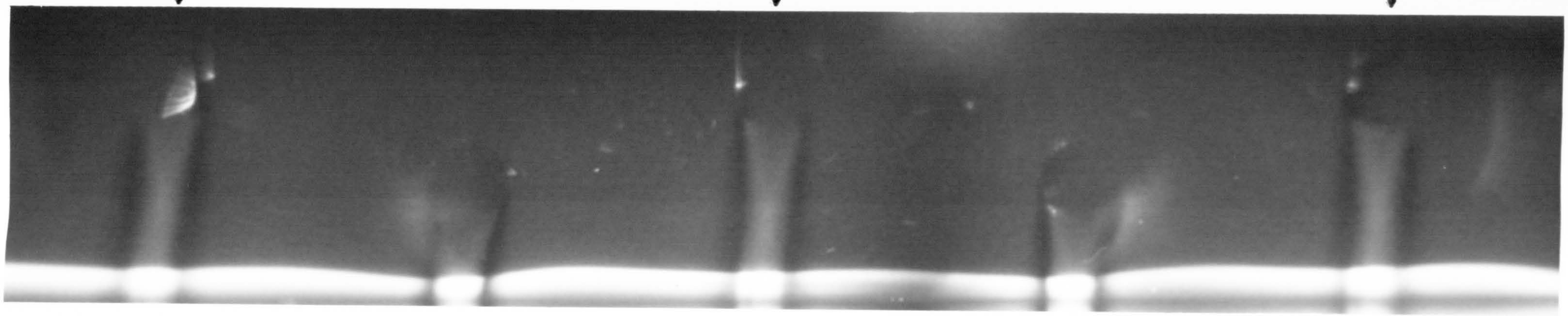

Flow ←

Re_e = 251

Plate 3.8: Suspended staggered rods (↓↑ position of rod)
l_{rr} = 12 mm, d_{rw} = 3 mm

Flow ←

Re_e = 345

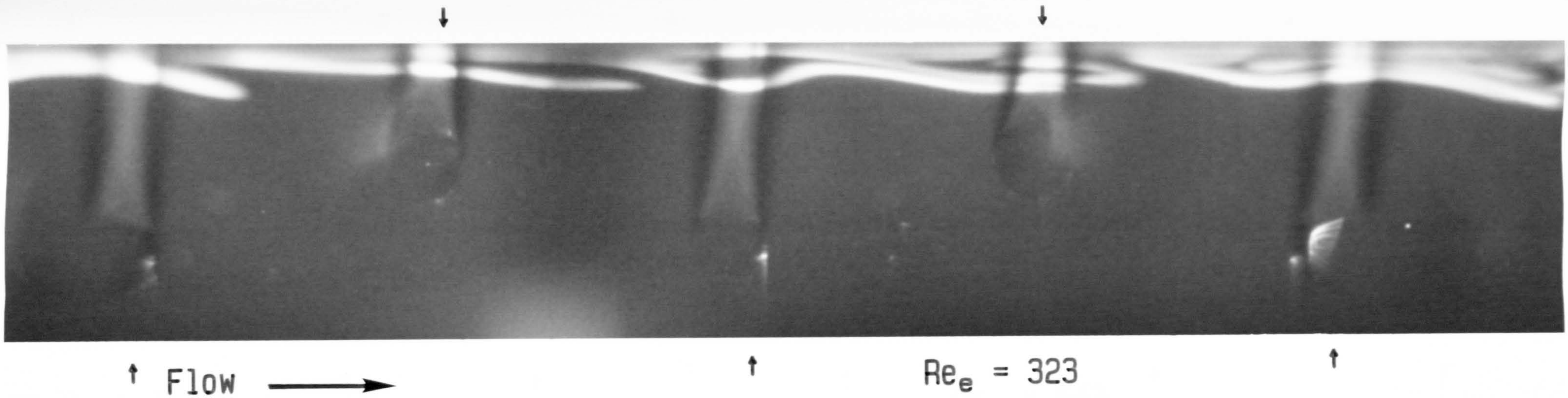

Plate 3.9: Suspended staggered rods (↓↑ position of rod)
l_{rr} = 12 mm, d_{rw} = 3 mm

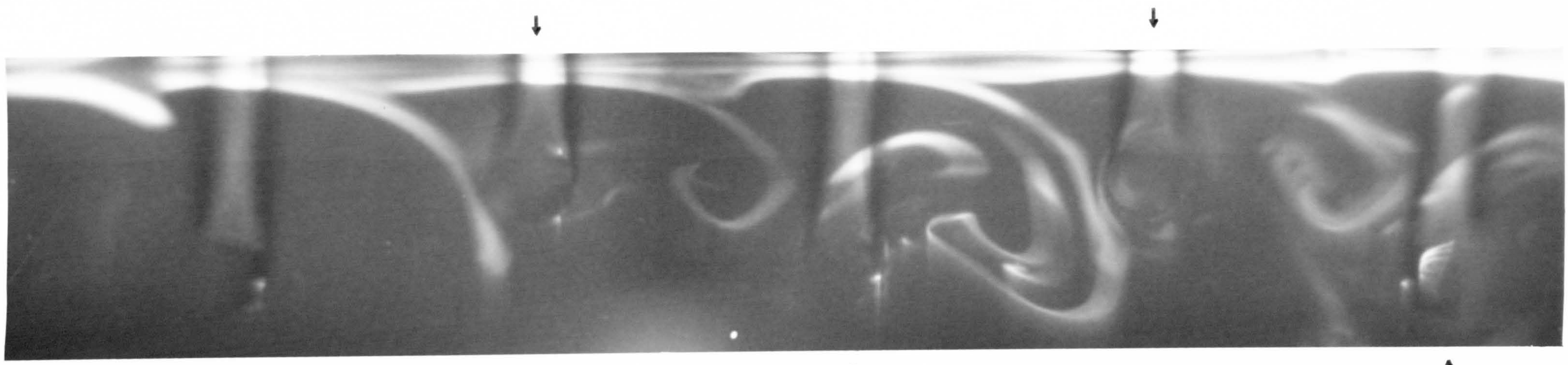

Flow → Re_e = 543

Plate 3.10: Suspended staggered rods (↓↑ position of rod)

l_{rr} = 6 mm, d_{rw} = 3 mm

Flow → Re_e = 778

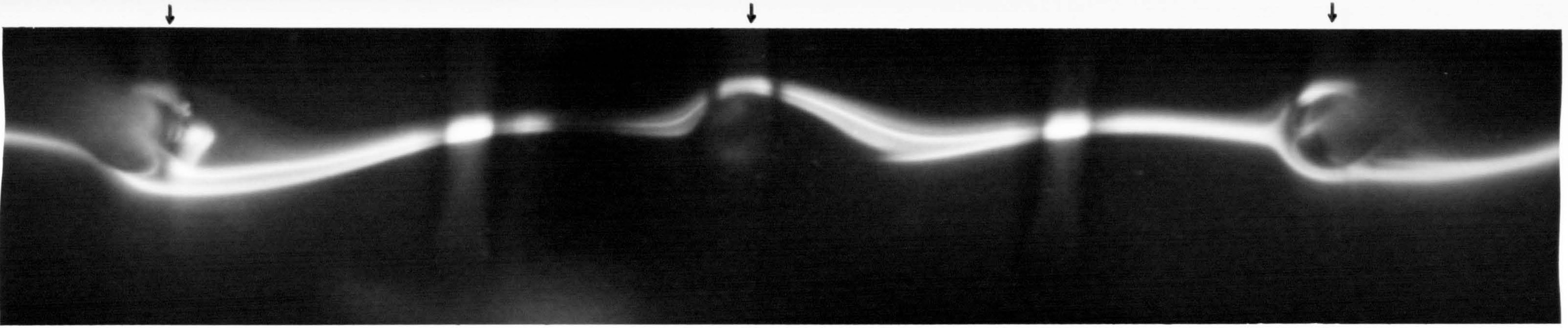

Flow ⟶ Re_e = 150

Plate 3.11: Suspended staggered rods (↓↑ positon of rod)
l_{rr} = 12 mm, d_{rw} = 2 mm

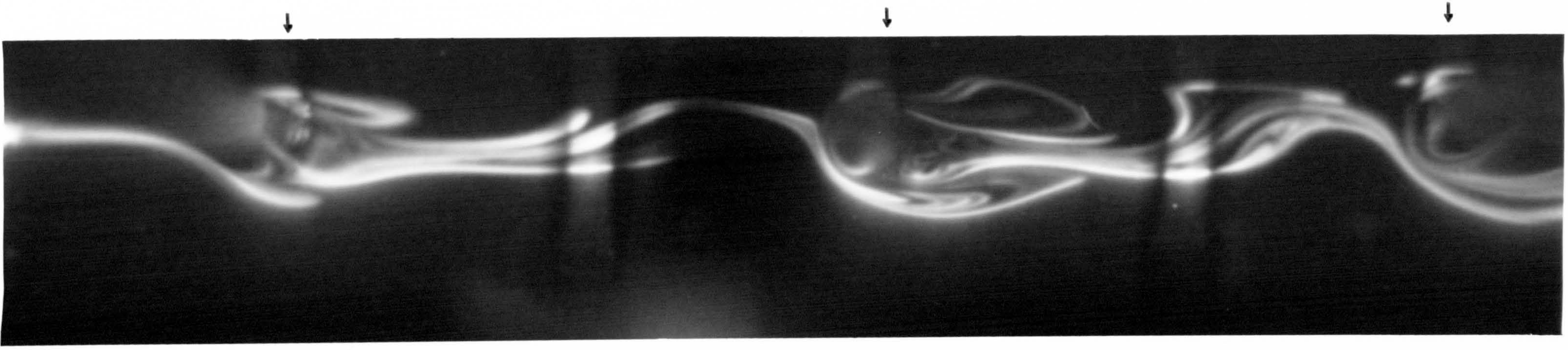

Flow ⟶ Re_e = 184

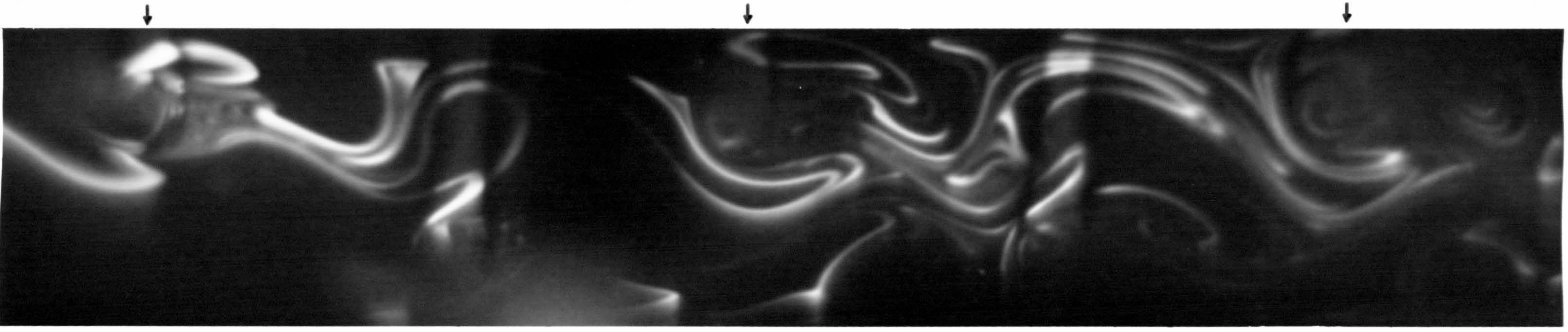

Plate 3.12: Suspended staggered rods (↓↑ position of rod)

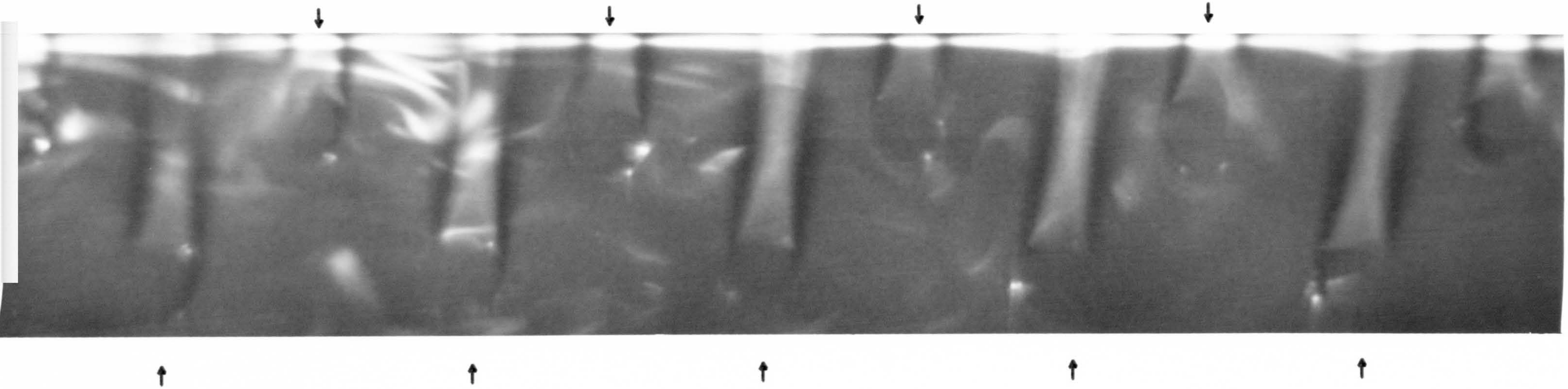

Flow ⟶ Plate 3.13: Suspended staggered rods (↓↑ position of rod)

l_{rr} = 12 mm, d_{rw} = 2 mm, Re_e = 338

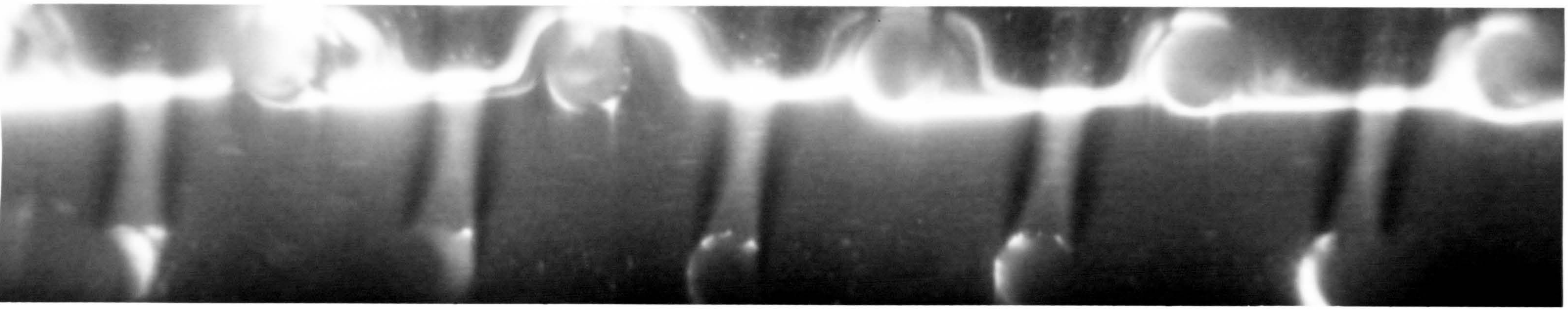

Flow ⟶

Re_e = 189

Plate 3.14: Suspended staggered rods (↓↑ position of rod)

l_{rr} = 6 mm, d_{rw} = 1 mm

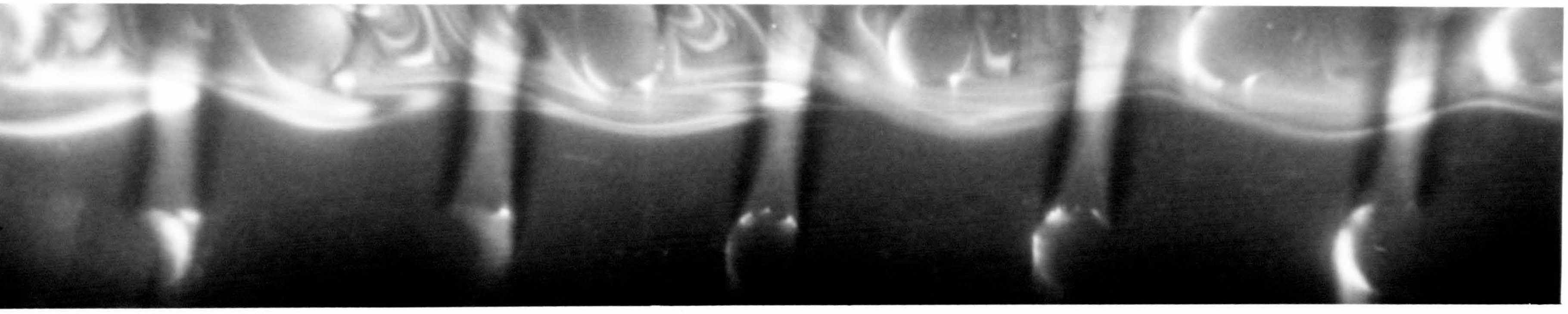

Flow ⟶

Re_e = 253

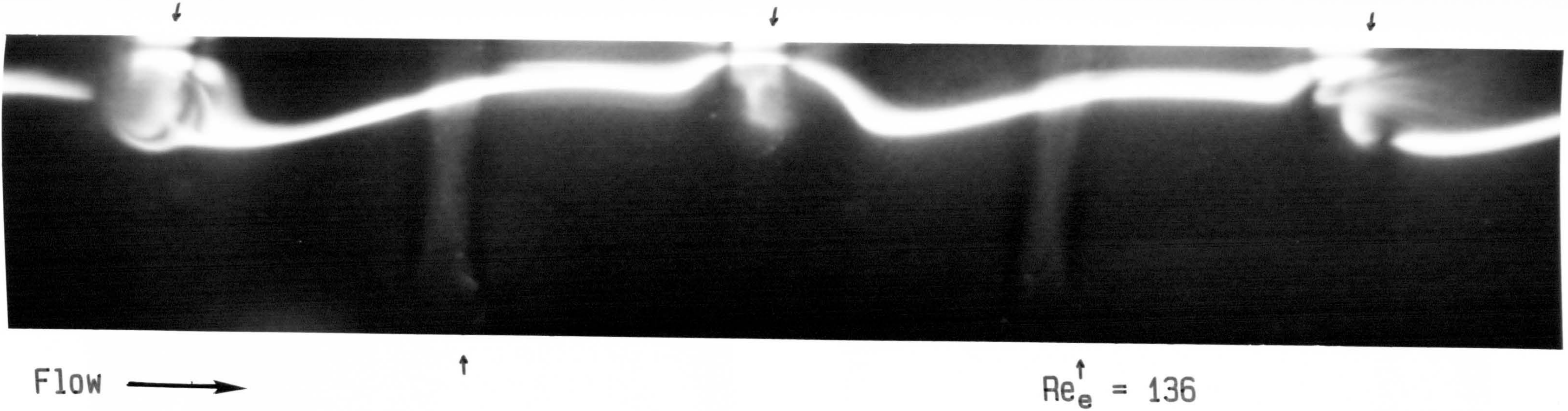

Plate 3.15: Suspended staggered rods (↓↑ position of rod)
l_{rr} = 12 mm, d_{rw} = 1 mm

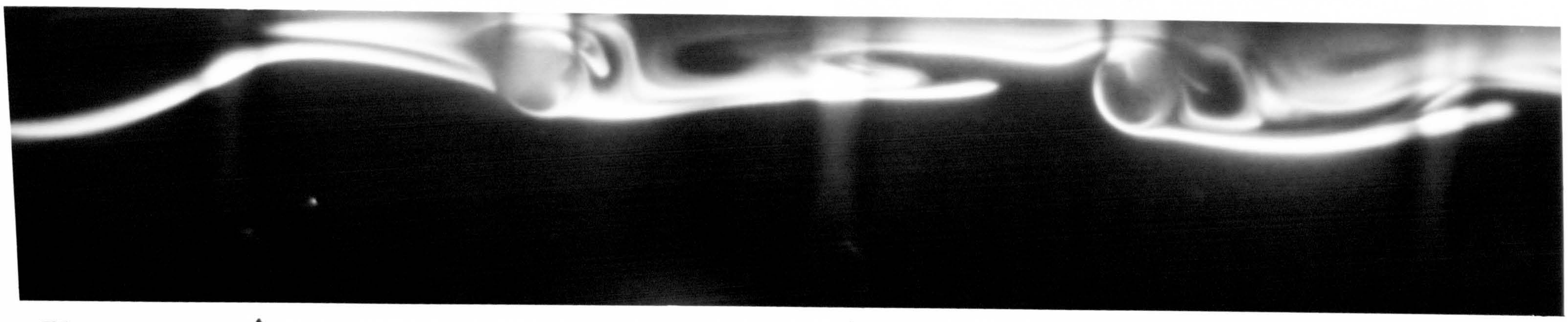

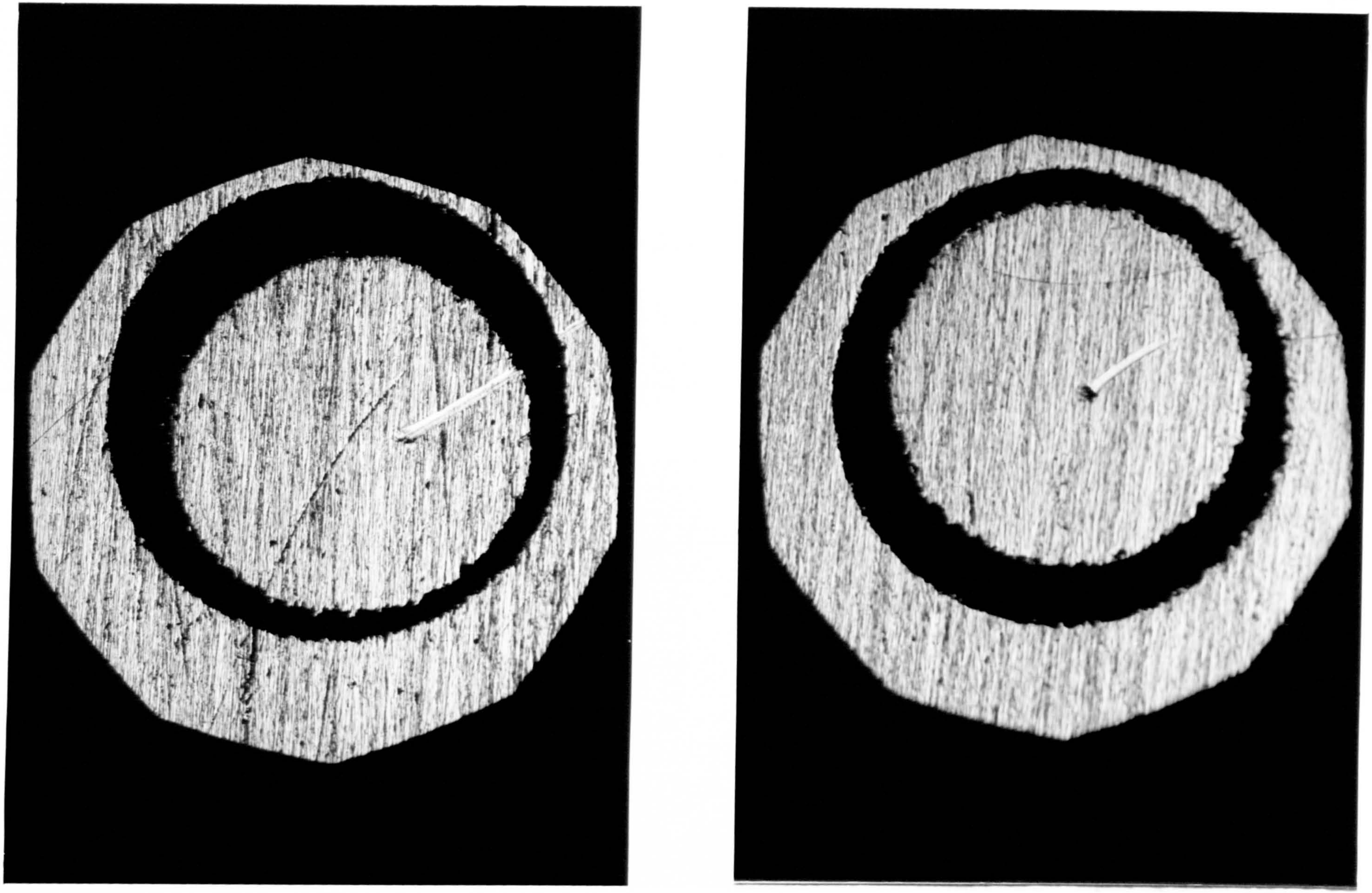

Plate 5.1: Mini-electrodes as seen through microscope (ø = 1 mm)

Plate 5.2: PVC flow tray with separator for electrochemical experiments